JAGIELLONIAN UNIVERSITY

THE FACULTY OF PHYSICS, ASTRONOMY
AND APPLIED COMPUTER SCIENCE
MARIAN SMOLUCHOWSKI INSTITUTE OF PHYSICS

VALIDATION OF SPALLATION MODELS

Sushil Sharma

PhD dissertation performed
in the Department of Nuclear Physics of Jagiellonian University
and in the Nuclear Physics Institute of the Research Center Jülich
Thesis supervisor : **Prof. dr. hab. Bogusław Kamys**

Cracow 2015

Contents

Abstract

The aim of the present work was to assess the model capabilities in describing the proton induced spallation reactions. To understand the reaction mechanism, different sets of observables must be investigated, inclusive as well as exclusive. Based on these criteria, the efforts were done to survey the scientific literature for the selection of representative data sets which fits the need. The selected data were rich in terms of production of various ejectiles: neutrons, light charged particles (LCP: p, d, t, ^{3}He, ^{4}He), intermediate mass fragments, i.e., the particles with atomic mass number ($A_{LCP} < A_{IMF} < A_{fission fragments}$), and target-like heavy residua. Several atomic nuclei from Al up to Pb were selected as representative for all the targets. The proton beam covered the broad range of energies from 180 MeV to 3000 MeV.

The spallation reaction was treated as a two stage process. In the first stage, the incident proton initiates the cascade of binary collisions with target nucleons leaving behind an excited remnant. The second stage consists in the decay of this excited remnant nucleus. The selection of best models to describe each of these two stages was done on the basis of previous benchmark efforts where INCL4.5 model was found to be the best to describe the first stage of the reaction. Therefore the newest version of this model - INCL4.6 was used in the present study. Four theoretical models different in approach to the reaction mechanism were chosen to realize the description of the second stage: ABLA07, GEMINI++, SMM, GEM2. Qualitative as well as quantitative comparisons of model calculations with experimental data were undertaken. To judge the quality of models the agreement in magnitude of different observables with model predictions as well as reproduction of the shape of the mass, angle and energy distributions of the cross sections were taken into account.

Various deviation factors were used for providing ranking and validation of the spallation models. The statistical properties of the test factors, i.e., their expectation value, variance and probability density function were studied carefully. Two new statistical deviation factors named $M-$factor and $A-$factor were proposed in the present work. They are equally good as the best factors used up to now in the literature but are more intuitive.

The ranking of models obtained by the application of the deviation factors were compared with the qualitative estimation of the data reproduction. It was found that all the studied models are able to reproduce the main characteristics of the data, however systematic deviations were observed and their interpretation was proposed.

Streszczenie

Celem obecnej pracy było określenie zdolności modeli do opisu reakcji spalacji wywołanych protonami. Dla zrozumienia mechanizmu reakcji muszą być badane różne *observable*, zarówno inkluzywne jak i ekskluzywne. Biorąc to pod uwagę zostały dołożone starania aby wykonać przegląd literatury naukowej dla wyboru reprezentatywnego zestawu danych, który odpowiada tym wymaganiom. Wybrany zestaw danych był zasobny w produkcję różnych produkowanych cząstek: neutronów, lekkich naładowanych cząstek: (LCP: p, d, t, ^{3}He, ^{4}He), fragmentów o masie pośredniej (IMF: $A_{LCP} < A_{IMF} < A_{\text{fragmenty rozszczepienia}}$) i tarczo-podobnych ciężkich jąder końcowych. Kilka jąder atomowych od Al do Pb zostało wybranych jako reprezentatywne dla wszystkich tarcz. Energia wiązki protonów pokrywała szeroki zakres od 180 MeV do 3000 MeV.

Reakcja spalacji była traktowana jako proces dwustopniowy. W pierwszym etapie padający proton wywołuje kaskadę binarnych zderzeń z nukleonami tarczy pozostawiając wzbudzone jądro końcowe. Drugi etap polega na rozpadzie wzbudzonego jądra końcowego. Wybór najlepszych modeli dla opisu każdegu z dwu etapów został wykonany w oparciu o poprzednie starania dla określenia wzorców gdzie stwierdzono, że model INCL4.5 został uznany za najlepiej opisujący pierwszy etap reakcji. Dlatego zastosowano w obecnych badaniach najnowszą wersję tego modelu - INCL4.6. Do realizacji opisu drugiego etapu wybrano cztery modele stosujące różne podejścia do mechanizmu reakcji: ABLA07, GEMINI++,SMM, GEM2. Podjęto jakościowe i ilościowe porównania obliczeń modelowych z danymi doświadczalnymi. Dla osądzenia jakości modeli brano pod uwagę zgodność wielkości różnych *observabli* z przewidywaniami modelowymi a także odtworzenie kształtu rozkładów masy, energii i kątów.

Zastosowano różne czynniki odchylenia, które zostały użyte dla zapewnienia rankingu i walidacji modeli spalacyjnych. Zbadano starannie statystyczne własności czynników testowych, t.j. ich wartości oczekiwane, wariancje i funkcje gęstości prawdopodobieństwa. W obecnej pracy zaproponowano dwa nowe czynniki odchylenia nazwane czynnikiem M i czynnikiem A. Są one równie dobre jak najlepsze czynniki używane do tej pory w literaturze ale są bardziej intuicyjne.

Rankingi modeli otrzymane przez zastosowanie czynników odchylenia zostały porównane z jakościowym oszacowaniem odtworzenia danych. Stwierdzono, że wszystkie badane modele są w stanie odtworzyć główne charakterystyki danych jednakże zaobserwowano systematyczne odchylenia i zaproponowano ich interpretację.

Chapter 1

Introduction

Proton induced spallation reactions are of indisputable importance due to their applications in wide range of fields. These reactions are considered as an optimal source of high energy neutrons which can be used for many purposes as e.g. in accelerator driven systems (ADS) in which long living nuclear waste could be burnt with simultaneous energy production [1]. Knowledge of the mechanism of the spallation reactions is necessary *inter alia* for interpretation of the cosmic rays interaction with terrestrial and extraterrestrial matter, for astrophysics, nucleosynthesis and for medical purposes. The last but not least, the knowledge of the mechanism of proton induced spallation reactions should help to understand much more complicated mechanism of interaction between heavy ions.

The efficient application of the spallation reactions demands knowledge of integral and differential cross sections over a broad range of the proton beam energies and of the atomic nuclei. It is easy to perceive that the experimental determination of cross sections for all possible targets in a broad range of proton energies and for large amount of products is practically not possible because of the technical reasons (e.g. short living unstable target nuclei) as well as of the time constraints for necessary experiments. Therefore it is necessary to rely on the theoretically predicted values of the cross sections. The simplified models must be used for this purpose since the theoretical description of the spallation reactions involves solution of many-body quantum mechanical problem which still cannot be exactly solved by the present day theory. A large number of efforts has been made for development of the models and corresponding computer codes which could be used as a standalone version in describing all nuclear data sets at all projectile energies and with all targets. The overview of the most important models of the spallation reactions is presented in the second chapter of the thesis (first section).

The experimental data must be confronted with results of the calculations performed by means of the theoretical models to judge their predictive power. For this purpose the most important observables have to be selected as well as the set of reliable data has to be chosen and compared with results of existing models. There is a general agreement that the neutron data, the data for production of LCP, i.e., light charged particles (p,d,t,^{3}He and ^{4}He) and the data on production of heavy target residua are crucial for this purpose. The efforts of the international scientific community undertaken to look for such data and to estimate quality of their reproduction by different models are described in the next (second) section of the second chapter. The conclusions which stem from these efforts allowed to select several most promising models to be used in the present work for analysis of the extended set of the data.

The success of selected models to reproduce the experimental data enables one to use these models in many practical applications but also helps to tag the fundamental approach to deal with the processes involved in the spallation reactions. The set of the representative data which can be used as benchmarks in such a procedure is discussed in the last (third) section of the second chapter.

The physical background and the details of the models selected for further analysis is presented in the third chapter. The INCL4.6 model - used to describe the first, fast stage of the reaction induced by protons on atomic nuclei is discussed in the first section. Four models of the second, slow stage of the reaction; GEM2, GEMINI++, SMM and ABLA07 are presented in the following sections.

The main subject of the present thesis, i.e., validation of the spallation models needs introduction of several definitions. First of them is a meaning of the term *validation of the model.* Experimentally determined observables are biased by some uncertainty which frequently is introduced by method of measurements but *always* is caused by a statistical nature of the number of observed reaction events. Therefore the measured cross sections are random variables and the exact equality of data and model predictions may be realized only incidentally. The term *"perfect agreement"* between the data σ^{exp} and model cross section σ^{cal} means that the expectation value of the random experimental observable is equal to the calculated, model value:

$$\boxed{E(\sigma^{exp}) = \sigma^{cal}. \qquad (1.1)}$$

The question arises how to determine quantitatively whether this situation takes place. For this purpose various *deviation factors*, i.e., functions of the model and experimental cross sections measuring the distance between them are proposed. Due to the random character of the data the deviation factors are also random variables. Then the condition (1.1) may be treated as a *null statistical hypothesis* H_0 [2] and may be tested by statistical methods against an *alternative hypothesis* H_1 which negates H_0 on the basis of values of the deviation factors. Deviation factor becomes *test statistic* and a range of its most unlikely values for true H_0 forms a *critical region.* Falling the deviation factor into this region is treated as indication that the null hypothesis is not true. It is therefore very important to know probability distribution function of the deviation factor used as a test statistic for testing the null hypothesis. Most popular deviation factors and their statistical properties are discussed in the first section of the fourth chapter of the thesis.

It frequently happens that the theoretical models do not fulfill the condition (1.1) i.e. none of them leads to the perfect description of the data but it is important to know which of them is *better* in reproduction of the data. Such a *ranking of models* may be done comparing values of the deviation factor evaluated by using different models for the same data.

Each deviation factor has a specific value corresponding to the situation when all measured cross sections are exactly equal to appropriate model cross sections. The proximity of the deviation factor to such a *reference value* determines the rank of the model. The model with value of the deviation factor closest to this specific value has the rank equal to one, other models which provide larger distance of the deviation factor from this value obtain the ranks equal to two, to three, etc. The models which lead to the same value of the deviation factor (within a reasonable range) are treated as equally good and usually they obtain so called *tied rank* i.e. the rank equal to the arithmetic average of their ranks which would be attributed to these models in situation of small differences between corresponding deviation factors.

It should be noted that the reference value of the deviation factor discussed above may differ from its expectation value or from its most probable value. For example the popular H-deviation factor :

$$\boxed{H \equiv \left[\frac{1}{N} \sum_{i=1}^{N} \left(\frac{\sigma_i^{\exp} - \sigma_i^{calc}}{\Delta\sigma_i^{\exp}} \right)^2 \right]^{1/2} \qquad (1.2)}$$

where $\Delta\sigma_i^{\exp}$ denotes the error of experimental cross section, has always non negative values thus its most probable value as well as its expectation value has to be larger than zero. It is shown in the Appendix A that they are both close to unity for the perfect agreement (1.1) of the model and experimental cross sections. However, the H- deviation factor would be exactly equal to zero when all experimental cross sections σ_i^{exp} are equal to the calculated cross sections σ_i^{cal}. Thus, the zero value of the H-factor is used in the ranking as a reference value in spite of the fact that it may appear only with the probability equal to zero. *The advantage of using a reference value consists in the fact, that this value may be easily found without knowledge of the probability distribution of the deviation factor.*

In the second section of the fourth chapter two new deviation factors (M-factor and A-factor) are proposed and their properties are discussed.

The application of the selected theoretical models to analyze the large set of inclusive and exclusive experimental data is described in the fifth chapter . The qualitative estimation of the agreement of the theoretical predictions with data is confronted with quantitative results of the statistical tests used for the validation and ranking of the models.

The summary and conclusions are presented in the sixth chapter, whereas the details of the calculations and derivation of some formulae are described in Appendices.

Chapter 2

Status of investigations of proton induced spallation reactions

Proton induced spallation reactions are of extreme importance for understanding the mechanism of nucleon-nucleus interaction and have very broad range of direct applications, e.g., for creation of neutron sources, transmutation of nuclear waste, production of radioactive ion beams, evaluation of damages caused by cosmic rays in space crafts, for accelerator driven systems to feed the subcritical reactors, and in the field of medical and biological science. All these subjects require the knowledge of the cross sections for such reactions in a broad range of the proton beam energies and target masses. It is not possible (technically as well as from economical reasons) to measure all the reaction observables for all possible combinations of targets and beam energies. Therefore, one has to rely on nuclear model predictions to extrapolate or interpolate the experimental data for the systems which are not accessible experimentally, e.g. for the unstable target nuclei. More than half a century, different scientific groups have been involved in developing various models to describe the complete reaction mechanism in proton induced spallation processes. It is obvious that the procedure to improve the quality of the models should consists of iterative steps. This involves the consecutive development of the models and the validation of their quality by making comparisons with the available experimental data.

It is widely accepted that the proton induced spallation reaction can be described as a two stage process. The first step (fast stage) corresponds to an intranuclear cascade of nucleon-nucleon and nucleon-meson collisions followed in the second step by de-excitation of the equilibrated target's remnants. This second - slow stage may proceed via evaporation / fission or/and multi-fragmentation. There are also attempts to involve some intermediate stage of the reaction which takes into consideration a possibility of emission of particles during pre-equilibrium stage of the reaction. In the next section, the most popular reaction models are briefly described whereas in the following sections the latest benchmark data and their application to validate the reaction models are discussed.

2.1 The theoretical models of the spallation reactions

The modeling of first stage in high energy nucleon induced reactions is described mainly by two approaches. One approach is founded on the Serber's idea [3] where high energy nucleon ($\approx$ 100 - 150 MeV) has wavelength $\leq 10^{-14}$ fm which is smaller than the average distance between nucleons in the nucleus and hence smaller than the mean free path of nucleons inside the target. Thus, interactions of nucleon with target's nucleons can be visualized as the cascade of successive binary-collisions which leads to the emission of high energetic nucleons, pions and finally leaves behind the excited target's remnant. This process is called Intranuclear Cascade (INC) stage of the spallation reaction. In second approach, models based on the idea of time-evolution of the one-body phase space distribution or which follow the n-body molecular dynamics provide the alternatives. We are going to discuss the main properties of the models based on these two approaches.

2.1.1 Intranuclear cascade models - INC

There are several INC models following the Serber's approach with the oldest one of BERTINI [4–6] dating back to 1963. The other well know INC models are ISABEL [7] developed by Y. Yariv and INCL [8–23] developed and modified by J. Cugnon and collaborators. All these models impose specific physical assumptions concerning various aspects of the reaction mechanism besides the main assumption of the dominance of the nucleon-nucleon collisions over other possible mechanisms: (1) In all models the interference effects are completely ignored, thus the cascade of the collisions is treated classically. (2) The nucleon-nucleon cross sections are basically provided by the experimental information on free nucleon-nucleon collisions. (3) The presence of other nucleons (besides those participating in two-body collisions) is taken into account by hindering of low energy transfer collisions by the Pauli principle, and (4) by effect of the reflection/transmission of nucleons through the barrier created due to the presence of the surface of the target nucleus.

The models differ in treatment of (1) the spatial and/or momentum distribution of the target nucleons, (2) the criterion of appearing the nucleon-nucleon collision, (3) the stopping criterion of the cascade, (4) the nucleon-nucleon cross section parameterizations, etc. The last versions of the INCL model, i.e., INCL4.3, INCL4.5 and newer allow for emission of complex particles from the fast stage of the reaction due to specific mechanism - the coalescence. Such an effect is not present in other INC models.

The differences in these models are summarized in the table 2.1.

The details of the INC models are described in the above mentioned references.

In the INCL code, the nucleon density is sampled according to the Woods-Saxon distribution and the nucleus is considered to be composed of individual nucleons moving in a fixed potential well. Unlike to INCL, Bertini and ISABEL code approach is based on the continuous medium in which the whole nucleus is divided into 3 (8 or 16 in case of ISABEL) concentric spheres, each with uniform nucleon density such that the density decreases with increasing radius. Two different approaches are implemented to describe the collision criteria in these codes:

Table 2.1: Comparison between the INC models in terms of basic ingredients.

Physical ingredients	INCL	BERTINI	ISABEL
Target density	Saxon - Woods	3-density regions	16-density regions
Medium	Discrete	Continuous	Continuous
Collision criterion	Min. dist. approach	Mean-free path	Mean-free path
Pauli-blocking	Statistical	Strict	Statistical or Strict
Stopping criterion	Time	Energy	Energy

- First (used in INCL) bases on the minimum distance approach; when two nucleons come closer than the distance $d_{min}=\sqrt{\sigma_{tot}/\pi}$, a collision occurs.
- Second approach (used in BERTINI and ISABEL) is based on the continuous medium assumption, i.e., it uses the mean free path to decide whether the collision occurs. The time interval between two collision is calculated as

  $$\Delta\tau = \min\left[\frac{\langle\lambda_i\rangle}{n\beta_i}\right]$$

  where $\langle\lambda_i\rangle$ represents the mean free path of i_{th} cascade nucleon and β is its velocity, n is a parameter fixed to value 20.

The collision can appear only in the case when it is not prohibited by the Pauli principle, i.e. when the momenta of the scattered nucleons are over the Fermi level. This is so called "strict" Pauli principle applied in ISABEL (optionally) and BERTINI codes. On the contrary it may happen that previous collisions removed one or more nucleons from the Fermi see creating empty states for nucleons. The INCL code and Isabel (optionally) takes this situation into consideration allowing for so called "statistic Pauli principle", i.e., it accepts with appropriate probability the collision which ends with the nucleon momentum below the Fermi level [24, 25].

The cascade stopping criteria are also different in different models. The INCL stops after the time which is depending on the target mass [16]. A different stopping condition is employed in BERTINI and ISABEL codes. It depends on the available energy of nucleons inside the target, i.e., when the energy of nucleons becomes lower than a definite threshold energy E_{cut}, cascade stage stops.

The INCL model which is used in the present thesis as the representative of all models of the fast stage of the proton-nucleus collisions is described in detail in section 3.1.1.

The other microscopic models which follow the second approach can be generally addressed as cascade plus nuclear mean field models, e.g., Boltzmann-Uehling-Uhlenbeck (BUU) and Quantum Molecular Dynamics (QMD) models. They are discussed below.

2.1.2 Boltzmann-Uehling-Uhlenbeck model - BUU

Boltzmann-Uehling-Uhlenbeck transport code is originated from the classical Boltzmann equation developed by Ludwig Boltzmann in 1872 to describe the dynamics of the gas which motion is mediated by the external force F and by collision processes between pairs of the gas molecules:

$$\boxed{\frac{\partial f}{\partial t} + v\frac{\partial f}{\partial x} + \frac{F}{m}\frac{\partial f}{\partial v} = \frac{\partial f}{\partial t}\Big|_{Collision} \qquad (2.1)}$$

f represents the single-particle distribution function at position x in a given moment of time t, v is the average velocity of particles in gas, m is the mass of the gas molecule. The evolution of phase space density distribution in time is termed as Boltzmann transport equation where x and v should be treated as vector variables. Later in 1933, Uehling and Uhlenbeck modified the equation by adding the Pauli-blocking factor in collision term (r.h.s. of eq. 2.1) for particles being the subject of the Fermi-Dirac statistics which leads to the current form of the equation called Boltzmann-Uehling-Uhlenbeck (BUU) equation. For a detailed description of BUU equation see the refs. [26–29]. The BUU equation is described as:

$$\boxed{\left[\frac{\partial}{\partial t} + \vec{v} \bullet \vec{\nabla}_r - \vec{\nabla}_r U \bullet \vec{\nabla}_p\right] f_1 = I_{collision} \qquad (2.2)}$$

where $I_{collision}$

$$= \frac{1}{(2\pi)^3}\int d^3\vec{p}_2 d^3\vec{p}_4 d\Omega \frac{d\sigma}{d\Omega} v_{12}\delta^3\left(\vec{p}_1 + \vec{p}_2 - \vec{p}_3 - \vec{p}_4\right)$$
$$\times \left[f_3 f_4 \left(1 - f_1\right)\left(1 - f_2\right) - f_1 f_2 \left(1 - f_3\right)\left(1 - f_4\right)\right]$$

The l.h.s. of eq. (2.2) describes the time evolution of the single particle phase space density distribution ($f(\vec{r}, \vec{p}, t) \equiv f_1$) of nucleons. U is the mean field felt by a given nucleon due to the presence of other nucleons. The collision term depends on the nucleon-nucleon cross section $\frac{d\sigma}{d\Omega}$, the relative velocity of the colliding nucleons v_{12} which move with momenta

p_1 and p_2 before the collision and with momenta p_3 and p_4 after collision. Conservation of momentum is assured by the δ^3 term. The Pauli-blocking is taken into account by using the factors f_i and $(1-f_i)$, i=1,2,3,4 which give information on the presence and absence of the $i-$the nucleon at given position, momentum and time, respectively.

The seven dimensional BUU transport equation cannot be solved analytically. Therefore, one has to rely on the numerical methods. The Monte Carlo method is used as a standard tool for this purpose. Here the realization of this method described in ref. [30] will be presented. This is done via a test particle method (each nucleon is represented by N test particles) to calculate the time evolution of a one-body phase space density distribution function after each fixed time interval δt.

$$\boxed{f\left(\vec{r},\vec{p},t\right)=\frac{1}{N}\sum_{i=1}^{N.A(t)}\delta^3\left(\vec{r}-\vec{r}_i\left(t\right)\right)\delta^3\left(\vec{p}-\vec{p}_i\left(t\right)\right) \qquad (2.3)}$$

N is the number of assumed test particles per physical nucleon whereas $A(t)$ is the number of real nucleons at the time t in target nucleus. Test particles are divided into N independent ensembles each representing $A(t)$ nucleons. Thus, collision between nucleons can be considered as to simulate N independent nuclear reactions in parallel. Final outcome is achieved by averaging over all N ensembles of the test particles. In proton induced reactions, the test particles representing the proton are distributed homogeneously in a cylinder with axis parallel to the proton beam momentum and radius equal to the radius of target nucleus. This choice allows such a distribution of the test particles which assures the results of calculations averaged over all impact parameters. Initially, the distribution of target nucleons in position space has the form of Woods-Saxon distribution or Gauss distribution assuming the same density distribution for protons and neutrons. The momentum distribution of nucleons is assigned homogenously in the Fermi sphere with the radius p_F(r) corresponding to the local spatial nucleon density.

- The Woods-Saxon spatial distribution of nucleons has the form:

$$\rho\left(r\right)=\rho_0\Big/\left[1+\exp\left(\frac{r-R_0}{a}\right)\right]$$

with the parameters: central density ρ_0 = 0.168 nucleon/fm^3, radius of half density R$_0$=1.124A$^{1/3}$ fm and diffuseness a = 0.025 A$^{1/3}$ + 0.29 fm.

- Momentum distribution of nucleons:

$$p_F\left(r\right)=\left(\frac{3\pi^2\rho\left(r\right)}{2}\right)^{1/3}$$

The test particles move in a dynamically changing mean field as described in ref. [26].

The collision criteria are the same as being adopted in the INCL model, i.e., collision takes place when two test particles (allowed only for test particles representing different nucleons) come closer than a minimum distance d$_{min}$ = $\sqrt{\sigma_{tot}/\pi}$ [31] in a given time step δt. Particles follow the straight line path between collisions according to classical Hamilton's equations of motion

$$\boxed{\dot{\vec{p_i}} = -\frac{\partial U\left(\vec{r_i}, \vec{p_i}, t\right)}{\partial \vec{r_i}} \qquad (2.4)}$$

$$\boxed{\dot{\vec{r_i}} = \frac{\vec{p_i}}{\sqrt{m^2 + p_i^2}} + \frac{\partial U\left(\vec{r_i}, \vec{p_i}, t\right)}{\partial \vec{p_i}} \qquad (2.5)}$$

The probability of interaction between nucleons is calculated as σ_{NN}/N. Only those collisions are allowed which lead to the unoccupied or partially occupied states. Unlike only Δ resonance and pion production in INCL model, BUU allows for the production of various resonances Δ, N(1440), N(1535) and η mesons for nucleon-nucleon collisions. One of the main important features of the BUU model is to include the possibility to decay for the unstable particle (mainly the resonances). The decay probability of a particle with mass m and energy E during a time step Δt is calculated as

$$\boxed{P_{dec} = 1 - \exp\left(-\frac{\Gamma(m)}{\gamma}\Delta t\right) \qquad (2.6)}$$

where γ=E/m is the Lorentz factor and Γ denotes the decay width of the particle in its rest frame. The flight direction of remnants of the decaying particle is sampled by Monte Carlo assuming the isotropic decay. Advantage of using the test particles method in BUU is the possibility to describe collective effects e.g., giant resonances since the averaging over ensemble of N test particles allows for good determination of the density distribution of the nucleons. However, this method reduces possibility to produce high energy tails observed in experimental spectra of nucleons due to less fluctuation in nuclear matter.

More detailed description of the BUU models, may be found in [26, 27, 30] references.

2.1.3 Quantum molecular dynamics model - QMD

In the present section the JQMD model is described as a typical representative of QMD models.

The JQMD code is founded on the principles of Quantum Molecular Dynamics (QMD) and follows a semi-classical approach based on Monte-Carlo simulation. The JQMD model was originally formulated by Niitta et al. [32] to analyze various aspects of heavy ion reactions. Later it was extended to study the nucleon induced reactions by Chiba et al. [33,34] and combined with Statistical Decay Model (SDM) to describe the de-excitation of the residue from the pre-equilibrium stage of the reaction.

In JQMD each nucleon state is represented by a Gaussian wave packet in space as well as in momentum coordinates as shown below

$$\boxed{f_i\left(\vec{r},\vec{p}\right) = 8\exp\left[-\frac{\left(\vec{r}-\vec{R_i}\right)^2}{4L} - \frac{2L\left(\vec{p}-\vec{P_i}\right)^2}{\hbar^2}\right] \qquad (2.7)}$$

where L is the spatial spread of the wave packet, $\vec{R_i}$ and $\vec{P_i}$ are the centers of wave packet in the coordinate and momentum space, respectively. Thus one-body density distribution function can be represented as

$$\begin{aligned} f_i\left(\vec{r},\vec{p},t\right) &\equiv \prod_i f_i\left(\vec{r},\vec{p},t\right) \\ &= \prod_i 8\exp\left[-\frac{\left(\vec{r}-\vec{R_i}\right)^2}{4L} - \frac{2L\left(\vec{p}-\vec{P_i}\right)^2}{\hbar^2}\right] \end{aligned} \tag{2.8}$$

Time evolution of density distribution in terms of $\vec{R_i(t)}$ and $\vec{P_i(t)}$ is described by Newtonian's equation of motion derived on the basis of the time-dependent variational principle [35] as following:

$$\dot{\vec{R_i}} = \frac{\partial H}{\partial \vec{P_i}}$$

$$\dot{\vec{P_i}} = -\frac{\partial H}{\partial \vec{R_i}}$$

Here, hamiltonian H consist of both, single particle plus two-body interaction energy.

$$\begin{aligned} H = &\sum_i \sqrt{m_i^2 + P_i^2} \\ &+\tfrac{1}{2}\tfrac{A}{\rho_0}\sum_i \langle p_i\rangle + \tfrac{1}{1+\sigma}\tfrac{B}{\rho_0^\sigma}\sum_i \langle\rho\rangle^\sigma \\ &\quad+\tfrac{1}{2}\sum_{i,j\neq i} c_i c_j \tfrac{e^2}{\left|\vec{R_i}-\vec{R_j}\right|} erf\left(\left|\vec{R_i}-\vec{R_j}\right|/\sqrt{4L}\right) \\ &\quad+\tfrac{C_s}{2\rho_0}\sum_{i,j\neq i}(1-2\left|c_i-c_j\right|)\rho_{ij} \end{aligned} \tag{2.9}$$

The first term corresponds to free particle energy, the second and third term represent Skyrme-type N-N interaction [36], the fourth term is responsible for Coulomb interaction and the fifth one is for the symmetry energy. The constant c$_i$ is unity for protons, zero for neutrons and the symmetry energy parameter C_s is equal to 25 MeV. The detailed information about the parameters of the Skyrme type interaction term can be found in ref. [36]. Wave packet width parameter L is fixed, equal to 2 fm^2. Information on the other symbols used in eq. (2.9) can be found in ref. [32, 33].

The collision criteria of nucleons in QMD are the same as in the case of INCL and BUU models based on the minimum distance approach i.e. $d_{min}=\sqrt{\sigma_{tot}/\pi}$. Like BUU model, Δ's and N* resonances are also in case of high bombarding energies to account for in-elastic reactions. The Pauli-exclusion principle is implemented in the similar wasy as in

BUU code by including the Pauli-blocking factor [1-f($\vec{r}$, $\vec{p}$,t)]. For the detailed description of the fate of resonances, see ref. [32].

The sampling of phase space distribution of nucleons inside the target is an important ingredient of QMD model. To achieve a stable ground state configuration of target nucleus the following parameters and constrains are employed in the model:

- The central position $\vec{R}_i$ of the wave packet referred to the individual nucleon is randomly chosen [37] following the Woods-Saxon distribution of radius R_0=1.124$A^{1/3}$-0.5 fm and diffuseness parameter a = 0.2 fm. Additional constraint is set to cut off the Woods-Saxon tail at R_{max}=1.124$A^{1/3}$.

- To assure, not to have large spatial density fluctuations, the distance between the centers of Gaussian wave packets was kept to be larger than 1.5 fm for proton-proton and neutron-neutron pairs and larger than 1.0 fm proton-neutron pair.

- The center of wave packet in momentum space $\vec{P}_i$ is randomly sampled from the sphere of radius $p_F(\vec{R}_i)$ obtained by the local Thomas-Fermi approximation.

- The sampling for nucleon in phase space density of target is accepted only if it satisfies the following criteria:

  1. Sum of kinetic and potential energies of sampled nucleon is negative (bound nucleon).
  2. Phase space factor f($\vec{r}_i, \vec{p}_i$) obey the Pauli-exclusion principle.

- Finally, to consider the "constructed" nucleus as the real nucleus in its ground state by comparing its binding energy with the simple mass formula [38].

  $$E_{bind} = -15.56 + 17.23A^{2/3} + 46.57\frac{(N-Z)^2}{2A} + \frac{3}{5}\frac{Z^2e^2}{1.24A^{1/3}}$$

  If E_{bind}/A lies within the range E_{bind}± 0.5 MeV, the sampled nucleus is considered as a good approximation for the nucleus in its ground state. However, for group of fermions, ground state energy is not the minimum energy state, therefore only 70% of the collisions are blocked by employing the final state Pauli - blocking. This may lead to the spontaneous emission of nucleons as a result of possible collisions between target nucleons themselves due to the presence of fluctuation in such configuration. The technical constraint that collision may take place only with the beam proton or with the participant nucleons solves the problem of spontaneous emission of nucleon from the configured ground state nucleus to great extent (up to 1%).

The advantage of JQMD over BUU model approach is that there is a possibility to calculate nucleon correlations leading to density distortion, nuclear shape changing and composite particles emission as excited clusters. Examples of these effects can be found in ref. [35].

2.1.4 Cascade-Exciton model - CEM

The Cascade-Exciton Model (CEM) approach follows the different recipe than other spallation models. The CEM treats the spallation reaction process as sequence of three steps instead of two. The main difference introduced is to sandwich a pre-equilibrium stage between cascade and equilibrium processes. First time, the CEM was developed by Mashnik, Gudima and Toneev in JINR, Dubna during 1980's [39] and still being developed by S. Mashnik and co-workers [40–48] in LANL. The latest version of CEM are CEM03.03 and and LAQGSM03. The newer versions of this code are not only able to be employed to simulate the proton induced spallation reactions but also to describe the nucleus-nucleus interactions. The cascade stage of CEM inherits the basic postulates from the standard DUBNA model. The further recipe is applied in terms of inclusion the better systematics for np, pp, and nn interactions published by Boudard et. al. [16] and BRIC code[DUA00A,DUA07A], better energy-momentum conservation and the only attachment to quantum approach, i.e., Pauli-blocking to decide the acceptance of collisions.

To describe the emission of LCP, CEM incorporates the coalescence model [49] based on the final-state interaction of the cascade particles. The subsequent step is considered as a pre-equilibrium decay state of the excited remnant of the cascade. It is treated by an improved version of the Modified Extension Model(MEM) described in ref. [39], MODEX [50,51] to complete the so-called first stage of reaction. The decay of equilibrated remnants can be described either by using Generalized Evaporation Model GEM2 [52,53] or GEMINI [54]. If remnants have mass A<12, the possibility to use Fermi-break up model is also embedded in CEM03 package.

The second stage of reaction refers to the situation when the equilibrated excited remnant from the first stage de-excites via different possible reaction mechanisms. Several models have been reported in literature which follows different recipes to describe the fate of this excited remnant. The well known models are Generalized Evaporation Model (GEM2), Statistical Multi-fragmentation Model (SMM), ablation process based code (ABLA07) and sequential-fission based code (GEMINI). These models are described in detail in the chapter 3.

2.2 Benchmarks and selection of the models

The scientific community has organized during last two decades several benchmark studies with the aim to select a set of the experimental data to be compared to various spallation models. The ambitious goal of these studies is to find most reliable nuclear models which can be used to describe the representative set of the reaction products. This is quite a difficult task because it must involve both, broad range of the proton beam energies and the nuclear targets as well as various observables which are able to put severe constraints to the assumed reaction mechanism.

It is obvious that the condition *sine qua non* of the acceptance of given reaction model is the reproduction of the integral observables, such as ***total production cross sections of heavy residua*** of the reactions since each proton-nucleus collision at proton beam energies up to several GeV is accompanied by appearing of heavy products. However, the model which well reproduces selected integral quantities as residue mass and charge distributions may be not adequate for other integral observables, e.g., for isotope distributions. Then such a model also cannot be treated as a reliable tool to compute the production yields of the spallation reactions. Furthermore, it is necessary to investigate the abilities of the models to predict reliably excitation functions of various production yields since this has twofold consequences: (i) these yields may be relevant for a wide domain of applications, and (ii) such an ability may be used as the argument in favor of the reaction mechanism taken into account in the specific model.

Besides the heavy residua of the reaction there is another group of particles, which is always very abundant in all proton - nucleus collisions. This group consists of ***neutrons and light charged particles (LCP)***, i.e. protons, deuterons, tritons, ^{3}He, and ^{4}He. Thus all spallation models should be tested using the observables determined experimentally for these particles. First benchmark task was undertaken in 1994 [55], which was limited to the production of protons and neutrons only. Second exercise was organized in 1997 [56] devoted to excitation functions of residue production. Model predictions were tested not only qualitatively but also quantitatively by using the statistical deviation factors [56]. A significant discrepancies were observed between:

- experimental data and model predictions,
- the descriptions provided by different models themselves.

These conclusions provided the ground to measure the high quality data sets for e.g., ***mass, charge, isotopic distribution and residue production cross sections*** for many nuclear systems were measured by using the reverse kinematics in the Fragment Separator at GSI [24, 57–67], ***double differential cross sections***(DDXS) of ***Light Charged Particles***(LCP: $Z \leq 2$) and ***Intermediate Mass Fragments***(IMF: $Z > 2$) were also measured for a large range of target masses and beam energies by NESSI [68–71] and PISA collaboration [72–79] in the efforts to understand the reaction mechanism in proton induced spallation reactions. ***New neutron data*** for differential cross sections were also reported by various authors [80, 81]. In parallel efforts, model developers modified the physics ingredients in their existing models or proposed new models tested on selected set of experimental data. Thus a need appeared to validate the predictive capabilities of modified models with the old and newly measured experimental data. A new benchmark exercise was proposed and organized in 2008 [82] under auspices of the International Atomic Energy Agency(IAEA) with two main goals:

1. To judge the predictions of spallation models that could be used for the simulation not only in the existing spallation based facilities (ISIS, SINQ, JNS, J-PARC) but also in new facilities for designing and construction of spallation sources in Europe(ESS) and China(CSNS).
2. To give a deep cognizance on the reasons for the successes or deficiencies of the models in terms of ingredients based on physical ideas or experimentally tested parameterizations used in them.

Later in 2010, a workshop was organized dedicated mainly to the benchmark analysis. The judgements on the successes and shortcomings of different models were made individually for different ejectiles and specific observables. Results of the analysis are presented on the IAEA web site [82] and published in scientific literature [83, 84].

The short summary of the results for different observables corresponding to various reaction products is presented below in order to select the best suitable models for the present investigations. To fulfill this requirement the selected figures [2.1, 2.4, 2.5] are reproduced by using the benchmark tools provided on IAEA page dedicated to Benchmark of spallation models [82], and other figures [figs. 2.3, 2.2, 2.6, 2.7(a), 2.7(b), 2.7(c), 2.8] of final ratings for neutrons, LCP and residue production are adapted from the various reference [[83–85]]. All figures presented here are used only as the illustrative examples and for the qualitative comparisons.

NEUTRONS:

To assess the neutron production in spallation reactions is of high importance for reactor physics as well as for neutron sources. The observable which is directly related to the total neutron production is the averaged (over energy) multiplicity of neutrons. Another observable, which gives information on the energy and angle distribution of the produced neutrons is the double differential cross section $d\sigma/d\Omega dE$ (DDXS). Here we present only these two observables which have been studied for neutrons. An additional observable - multiplicity distribution of neutrons was also studied [82], which is not discussed here. Method of rating based on the model performance for the DDXS of neutrons is shown in Table 2.2.

Table 2.2: Rating criteria used to analyze the benchmark results [83] for neutrons and residue productions.

Quality	Points
Good	2
Moderately good, minor problems	1
Moderately bad, particular problems	-1
Unacceptably bad, systematically wrong	-2

The neutron spectra were divided into four energy regions,each one represents a single physics process leading to the neutron production: Evaporation, Pre-equilibrium, Pure cascade and Quasi-inelastic regions.

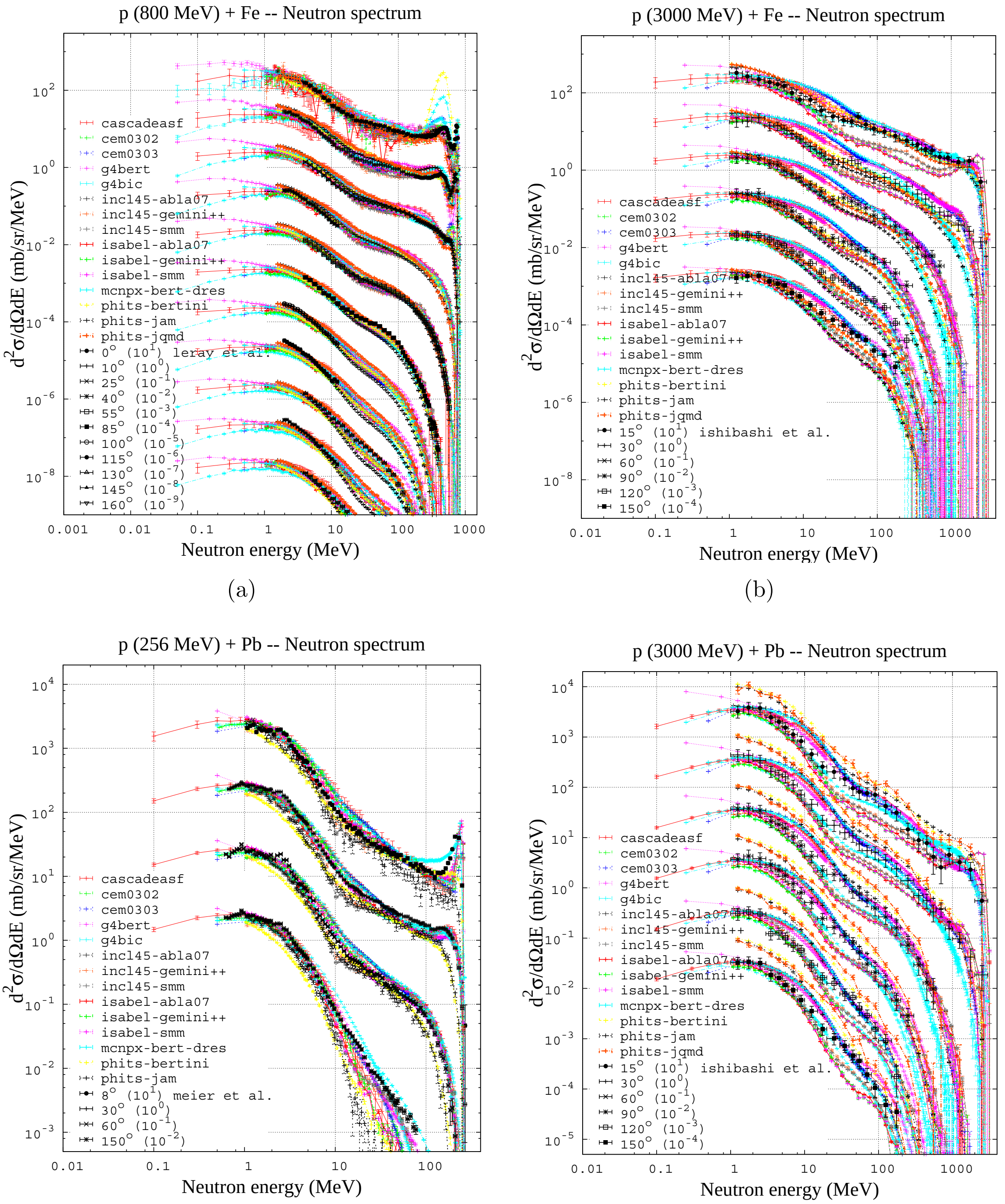

(a)

(b)

(c)

(d)

Figure 2.1: Neutron DDXS representative figures for the qualitative comparison of all participants models and experimental data for two targets: Fe and Pb at four different angles. The figure was adapted from ref. [82].

The comparison of model predictions with differential data for neutrons were done for Fe and Pb targets at many proton beam energies [82]. Qualitative comparisons between model predictions and experimental data are illustrated in fig. 2.1. Nearly all models are able to reproduce main properties of the experimental data. However, one can observe the energy regions where all models need to be further improved. For example, at high energies the quasi-elastic peak and quasi-inelastic peak are not always at the right position and not always have the proper magnitude. The region which is mainly contributed by the pre-equilibrium processes (around 30-120 MeV) is not well reproduced by most of the models.

The final ratings evaluated for neutrons DDXS which can indicated the models performance objectively is shown in fig. 2.2 [83].

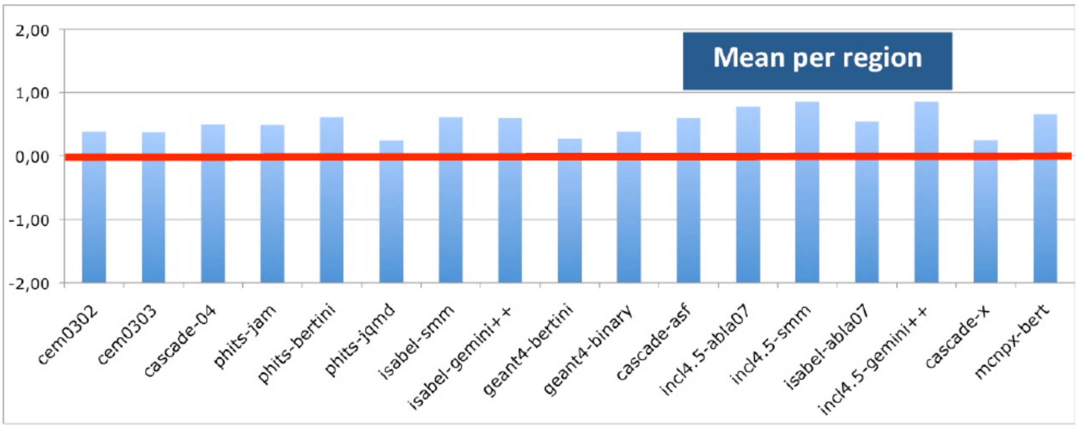

Figure 2.2: Ratings provided to different models using the method shown in Table 2.2 for neutron double differential cross sections. The figure was adapted from ref. [83].

The prediction capabilities of models to calculate the excitation functions of the average multiplicity of neutrons were also tested with the same two targets: Fe and Pb at three different projectile energies: 800, 1200 and 1600 MeV. The energy range of the emitted neutrons was divided in two parts: the low (E < 20 MeV) and the high (E > 20 MeV) energies.

The qualitative comparison between experimental data and different models is shown in figure 2.3. Model predictions for Pb were found close to experimental data but the situation for Fe was less satisfactory for most of the models.

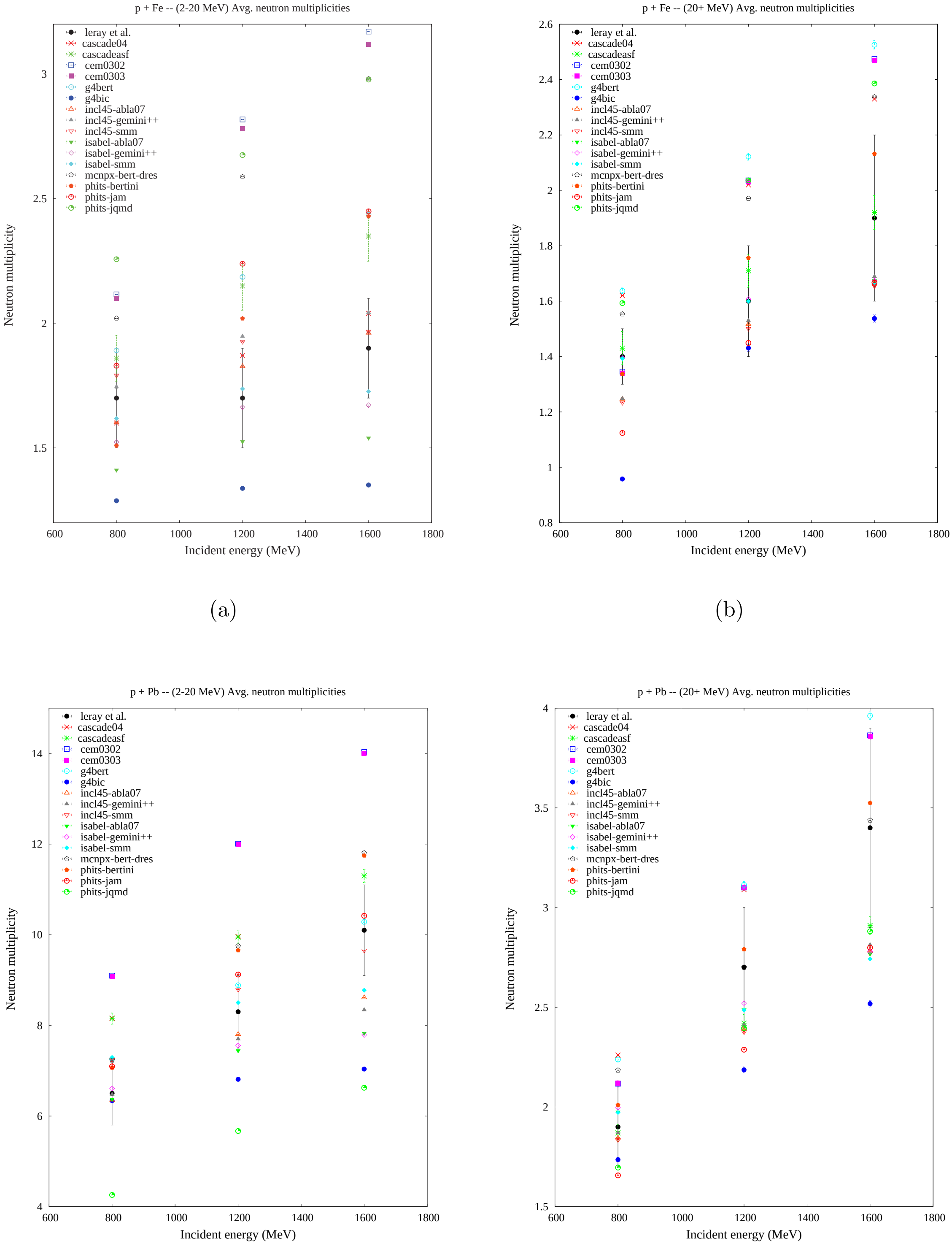

(a) (b)

(c) (d)

Figure 2.3: Experimental energy dependence of average multiplicities of low energy neutrons for Fe [2.3(a), 2.3(b)] and Pb [2.3(c), 2.3(d) targets compared with predictions of different spallation models. The figure was adapted from ref. [82].

LIGHT CHARGED PARTICLES:

Light charged particles are of unavoidable concern for calculating the material damage issues. For example, Helium can cause swelling in the structure materials separating the accelerator vacuum from the spallation target. Tritium, which is a beta emitter with half life ∼ 12 years, can contribute significantly to the target radioactivity in the spallation source and hence an issue arises (to estimate its production) from the point of view of radio protection. Therefore, in the benchmark exercise, model predictions were also confronted with experimental data for the production of LCP DDXS. The rating terminology for evacuating the successes of models for describing the LCP is shown in Table 2.3.

Table 2.3: Rating criteria used to analyze the benchmark results [83] for LCP DDXS.

Acceptance band [eval/x;eval*x]	Points
x=5	1
x=3	2
x=2	3
x=1.4	4

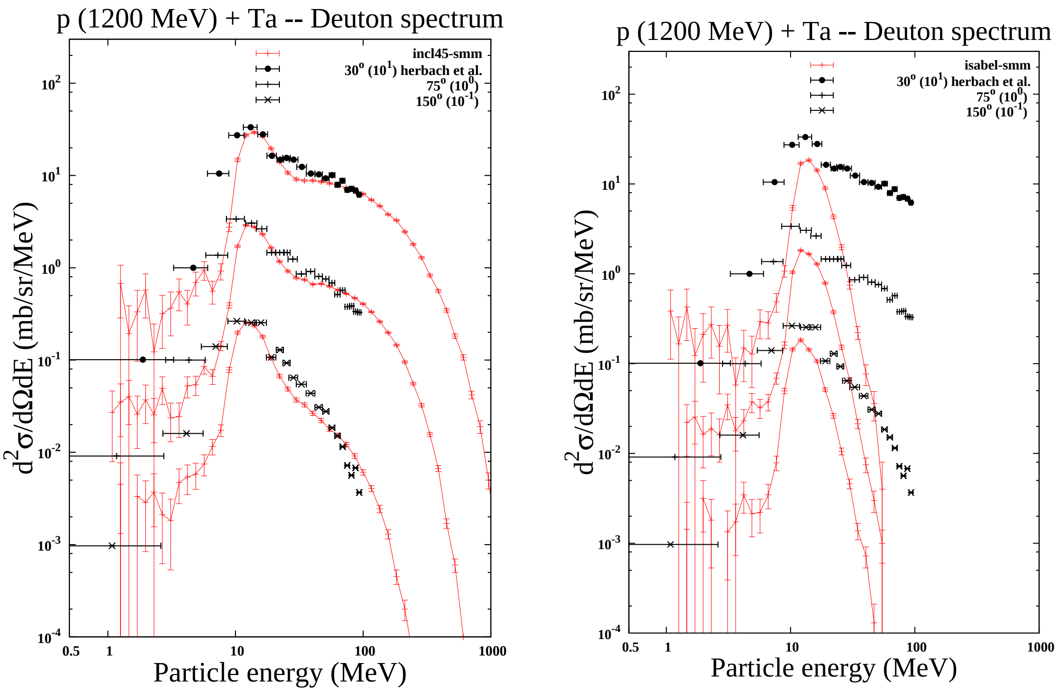

(a) (b)

Figure 2.4: Comparison of experimental DDXS for deuteron emission from p(1200)+Ta reaction at three different angles: 30^0, 75^0, 150^0 with two different models. INCL4.5 (which includes possibility of emission of energetic clusters)+SMM (left panel) and ISABEL (restricted to the emission of protons and neutrons)+SMM (right panel). The figure was adapted from ref. [82].

It was reported that a high energy tail was present in the measured energy spectra of the composite particles (deuteron - alpha), which seems far away from the scope of de-excitation models predictions. Such contribution can be interpreted as the emission of these particles during the fast stage (proton(beam)+nucleus interaction) of the reaction. So, only those models are qualified to compare with experimental data which take into consideration such an embedded mechanism in their physical ingredients.

This effect is emphasized clearly in the fig. 2.4 where fig. 2.4(a) shows the comparison of experimental data for emission of deuterons in p(1200 MeV)+Ta reaction with intranuclear cascade model INCL4.5 which includes explicitly the possibility of the emission of composite particles as the results of surface coalescence, whereas fig. 2.4(b) shows the comparison of same data set with the model of those categories which doesn't include it. The same deexcitation model was used intentionally to highlight the differences between the predictions of such two models for describing the fast stage of reaction. The necessity is obvious to include the required mechanism into the models for the reproduction of high energy tails of energy spectra, cf. fig. 2.4(a).

Before the final rating for LCP DDXS, it is interesting to see how closely the different models are able to describe the experimental data. It has been shown for p(1200 MeV)+Ta reaction. Only those models were included in comparison with experimental data which include the recipe responsible for the emission of composite particles along with protons; see fig. 2.5.

A closer look to qualitative comparisons between different model predictions and experimental data gives an impression that in all cases when INCL4.5 model is chosen to describe the first stage of reaction the high energy tails of spectra for composite particles are reproduced. The other candidates which also fulfill this criteria are cascade-asf and cascade-exciton models(cem-03-03,cem03-03) but they are clearly overestimating the production of low energy particles. On the contrary, INCL4.5 coupled with abla07/gemini++/smm seems better in reproducing the full energy spectra for all particles.

With the undertaken example, It is evident from the rating patterns for different particles that there is significant discrepancies among the models themselves in the prediction of LCP. The same terminology of rating was extended to other nuclear systems and finally the results averaged over all the models are calculated to estimates the model performances see Table 2.4.

Table 2.4: Rating results from the benchmark exercise for the LCP DDXS [83].

Light Charged Particles	Averaged rating (Models)	
Protons	2.4	agreement within a factor 2-3
Deuterons	1.2	agreement within a factor 4
Tritons	1.2	agreement within a factor 4
He-3	0.9	agreement within a factor 5
alpha	1.3	agreement within a factor 4

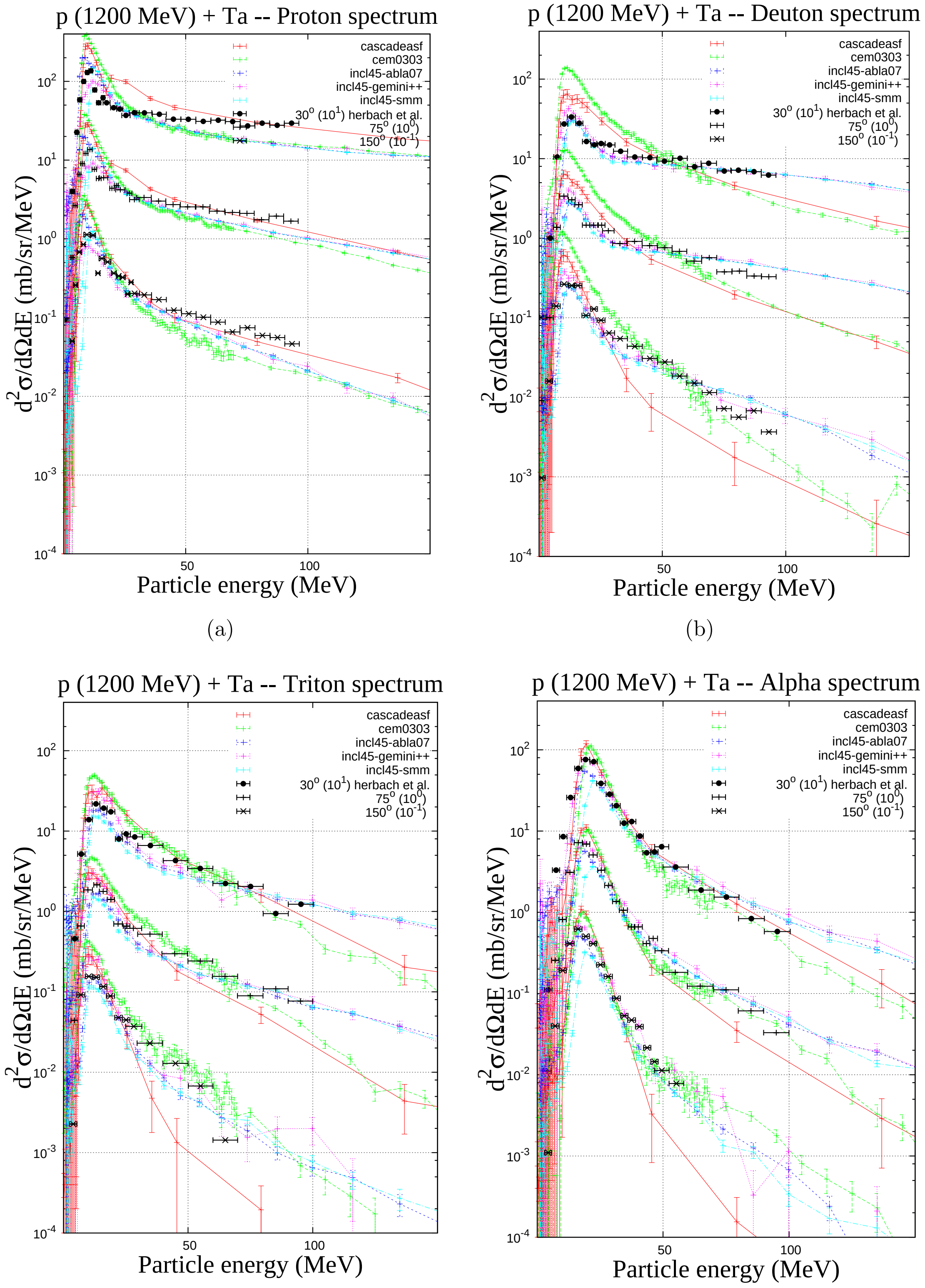

(a) (b)

(c) (d)

Figure 2.5: Comparison of experimental data for p(1200)+Ta reaction 2.4 at three angles with those models only which are able to emit composite LCP. The figure was adapted from ref. [82].

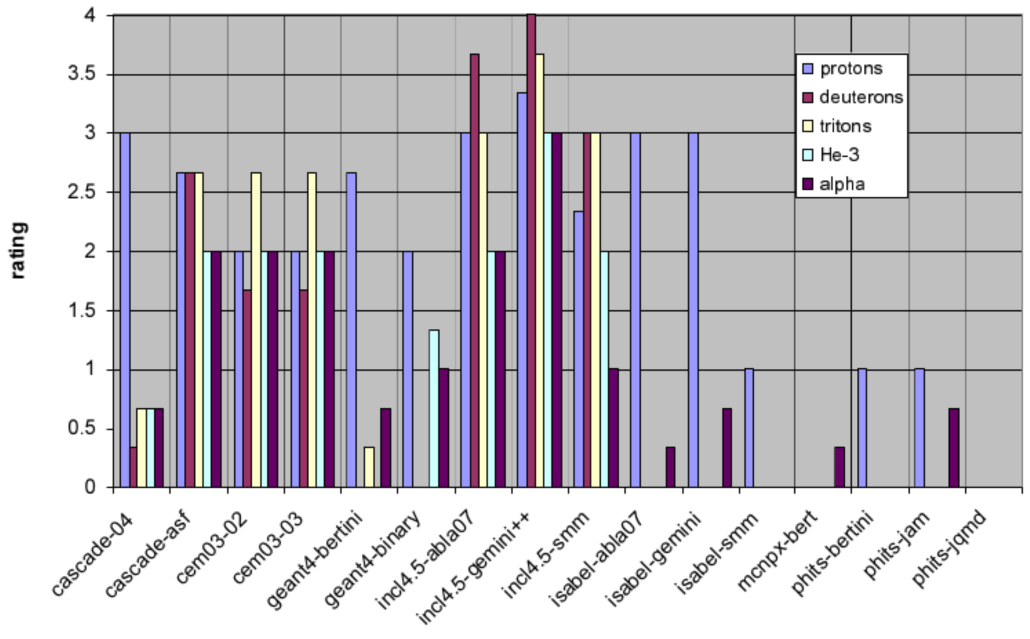

Figure 2.6: Ratings provided to different models for different particles for the production of LCP DDXS for p(1200 MeV)+Ta reaction. The figure was adapted from ref. [84].

SPALLATION RESIDUA:

It is of utmost importance to check the models predictions to evaluate the production of radionuclides in spallation reactions. The knowledge of spallation residue can be used to assess the radioactivity and damages.

Predictions for the residue production are more difficult to fit the experimental data than neutrons. This is caused by the fact that it is difficult to completely remove the possibility of heavy ions to stuck inside the target thickness. Such effects are crucial for thick targets but may be frequently neglected for thin targets.

In last decades, a large efforts were done to measure excitation functions, mass and charge distributions of the identified isotopes. Residue spectra were divided into four nuclide regions: target like products, spallation products, fission products and light products (d-alpha and IMF) with masses smaller than the fission products. The process followed to assign the rating for residua is same as used for neutrons 2.2.

A very large discrepancies were observed between inter-model predictions and with experimental data in describing the different observables of residue: mass, charge and isotopic distributions. A qualitative comparison for only the residua mass distribution measured for p(1GeV)+^{56}Fe (light target representative) and ^{208}Pb (heavy target representative) target is presented here in fig 2.7(a) and 2.7(b).

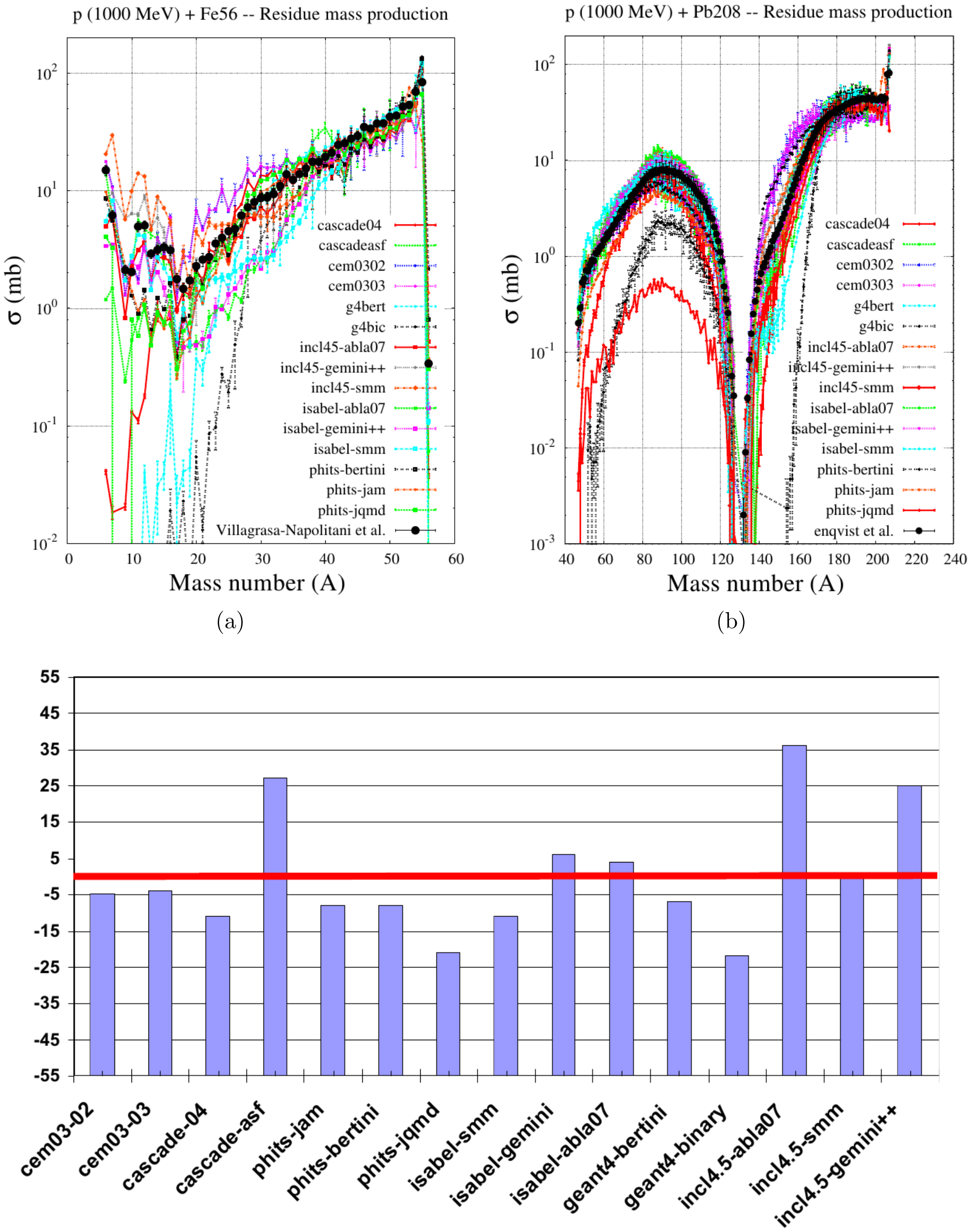

(a) (b)

(c)

Figure 2.7: Rating results for mass and charge distribution of 15 participant models for residua measured by inverse kinematics for iron, lead, and uranium at all energies included in the benchmark [82]. Fig. 2.7(a) and 2.7(b) are adapted from ref. [84] where, similarly as the fig. 2.7(c) were taken from ref. [85].

It is clearly visible that there is huge differences in the predictions of models themselves.

The situation gets worse for lighter targets. In case of Pb, the comparison is restricted upto the fission products but for lighter target Fe, we can see maximum disagreement is observed for IMF. Some models are clearly failed in describing the mass-distribution of residue and demands for the conceptual improvements. A collective rating is provided to different models based on their performance in reproducing the mass and charge distributions of residua - cf. fig. 2.7(c).
The task of rating to different models in describing isotopic distributions is done separately from mass and charge distribution of residue cf. fig. 2.8.

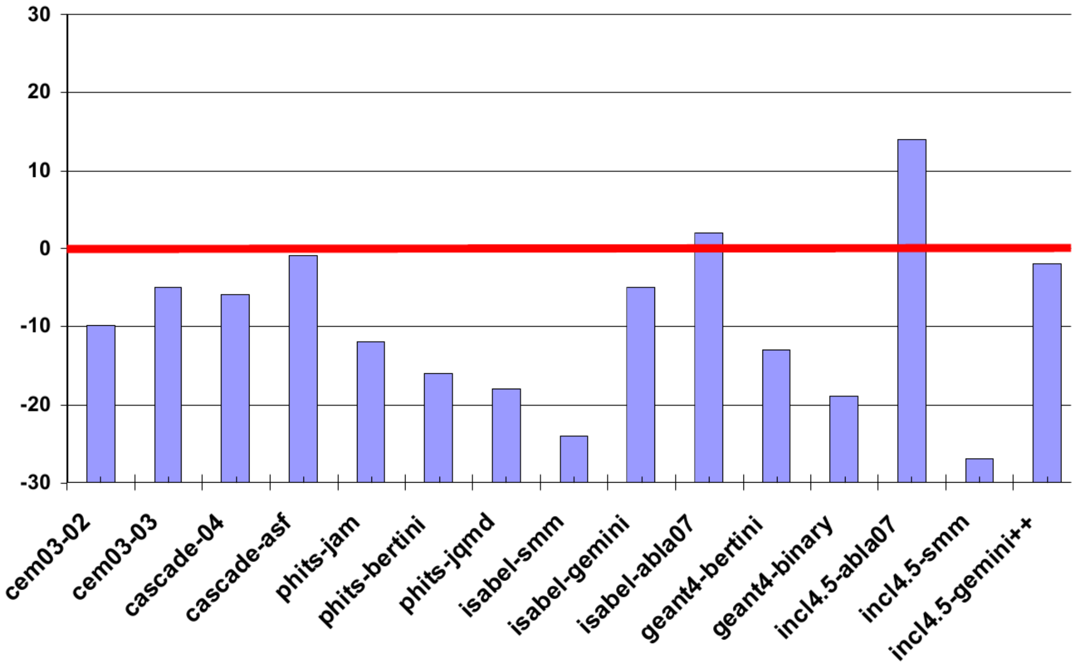

Figure 2.8: Same as on fig. 2.7 but for isotopic distribution. The figure was adapted from ref. [85].

In summary, the benchmark exercise was a successful effort to highlight the advantages and deficiencies of the participated theoretical models over the selected set of data and observables which are important to understand the reaction mechanism in proton induced spallation reactions. Model predictions are found surely improved in interpreting the various reaction observables for different ejectiles as compared to previous benchmark exercises [55, 56]. However, certain discrepancies are still present in all the models as discussed above in the inline text, which must be treated to achieve the goal of the single reliable model for all reaction products and corresponding observable. So one can conclude the following points:

- The maximal disagreement was found in the interpretation of intermediate mass fragment cross sections, cf. fig. 2.7(a) which were not included in the present benchmark explicitly to check the model abilities to produce them mainly due to the lacking of reliable data.

- Few models [e.g., cascade-asf, INCL4.5+(de-excitation code), cem-03-02, cem-03-03], cf. fig. 2.5 were able to reproduce the general properties of LCP DDXS tested on limited (not systematic) data sets. However, still is a need of improvements to describe data in magnitude and the shape of the energy spectra. Furthermore, it is mandatory to judge the model predictions for the systematic study for different target masses and proton beam energies to have more close insight on the missing mechanism.

- Nearly all models predicted the emission of isotopic distribution [83] of reaction products worst as the final rating to different models. The inspection of fig. 2.8 confirms this.

- While using same fast stage model (INCL4.5) coupled with different de-excitation models performs significantly different, cf. fig. 2.8. This indicates the different treatment by the de-excitation models for the same residue inputs and eventually the involved physical ingredients to describe the reaction mechanism.

- All models were nearly equally good in the description of neutron production 2.1, still the interpretation for the selected regions is needed to be improved in all the models.

SELECTION OF MODELS FOR FURTHER INVESTIGATIONS

The above review of benchmark data and their comparison with most frequently used spallation models indicate that the Liége version of the intranuclear cascade, i.e., the INCL model, coupled with different models describing the second stage of the reaction is in average producing the best agreement. Furthermore, there is no evidence of improvement when the two-step model of the reaction is extended to the three-step model by inclusion of preequilibrium stage of the reactions. Thus in the present thesis the two-step model is selected for further analysis with the first step of the reaction described by the newest version of the INCL model, namely **INCL4.6** [23].

Three different models; **ABLA07** [86], **GEMINI++** [54], and the **SMM** [87] were used for description of the second step of the reaction in the above benchmark studies. It was found that the quality of data reproduction changed from one set of data to another in favor of each of these models. Thus all three models were used in the present thesis with a hope to find more information on their predictive power from the study of the extended set of the data. The ABLA07 and SMM models take into account the evaporation of particles, the simultaneous multifragmentation of excited nuclei as well as fission of heaviest of them. The GEMINI++ treats the emission of particles from excited residua of the first stage of the reaction in different manner. It is calculated as series of transmissions through the barrier which is evaluated in analogous way to the transmission barrier for fission. It is thus interesting to check which of these mechanisms is working better in reproduction of the data. The **GEM2** model [52, 53] has been also applied as the model of the second stage of the reaction since its approach to the deexcitation of the nuclei consists only in evaporation of particles and (for heavy nuclei) in their fission.

Comparison of results obtained with these four different models of the reaction may shed some light on the mechanism of the deexcitation of heavy residua from the intranuclear cascade.

2.3 Benchmark data used in the present thesis

In previous chapter, the selection of spallation models for the present study was done based on their ranking in describing well the experimental data. A wide range of data sets for different observables were used to judge the model performances. An idea to include both inclusive as well as exclusive observables must be opted in such kind of benchmark studies. All applications of the spallation reactions require knowledge of the inclusive observables because they decide about yield of any process. However, to verify that the assumed mechanism of the reaction is realistic the reproduction of inclusive observables alone is not stringent enough. For this purpose also the exclusive observables have to be reproduced by the model. From the knowledge of last benchmark, one of the main conclusions was that spallation models were improved significantly in describing the production of neutrons and residua in respect to previous benchmarks. However, models were not found in the equally good agreement for the production of light charged particles (p,d,t,^{3}He,^{4}He) and especially intermediate mass fragments (LCP<A<fission fragments) which were secluded from such studies up to now. In previous benchmark [82], selected data sets for LCP were included to check the predictions of the models. It was found that specific model predictions were better for one set of target mass and projectile energy but didn't repeat the success to describe other data set. This behavior pointed out the need to perform a systematic studies in terms of target masses and projectile energies of protons. To understand full reaction mechanism and use the knowledge of spallation reactions in various applications, it is mandatory to estimate the production of all possible nuclides including LCP and IMF.

In the present study, all these points were taken into consideration specifically. The predictions of selected models were tested over different data sets starting from total cross-sections, isotopic production cross sections, isobaric production cross sections and differential cross section for various ejectiles.

Table 2.5: Inclusive data sets selected from literature for the validation of spallation models. The data for isobaric production cross section for proton induced reaction with Al target at 180 MeV energy is taken from ref. [88], isotopic production cross section for p(500 MeV)+^{136}Xe is measured by Giot et al. [89], data for angular asymmetry in F/B emission of recoil nuclides was taken from ref. [90].

Energy in MeV	**Targets**		
	Al	**Xe**	**Au**
180	Isobaric distributuion σ(A) angular and energy		
500		Isotopic distribution $\sigma\ (\mathrm{A}\vert\mathrm{Z})$ Z=41 to Z=56	
1000 and 3000			Forward/Backward asymmetry

For the validation of spallation models, proton induced reaction at 180 MeV on Al target is chosen purposely. Various observables were measured, e.g., isobaric (summed over elements) cross sections starting with A=6 to A=25, angular distributions of selected isobars (A=7, 12, 16, 22, 24, 25) and energy spectra for three isobars A=7, 16, 22 at different angles. We consider this data set as representative of integral observables. The main motive to analyze this data was to validate the models applicability towards the low projectile energy (180 MeV) and with light target mass (Al) where the INCL4.6 may not work properly.

Another set of data is the isotopic production of various elements starting from element Z=41 to Z=56 (Table.2.5) for proton induced reactions with ^{136}Xe target at beam energy 500 MeV. It is very important to check the prediction capabilities of models in describing the isotopic distribution to estimate the possibilities for production of the radionuclides with large life time and may be the concern of radioactivity issues.

The third data set is specific in the sense that it can be treated as a measure of angular asymmetry in the production of nuclides in proton induced reaction, however, without measuring detailed angular distributions. Angular asymmetry can be defined as the ratio of nuclides emitted in the forward direction (angle$<$90°) to the nuclides which are emitted in the backward hemi-sphere(angle $>$ 90°). The main motive to choose this data set was to check the model predictions in reproducing the nuclide mass and beam energy dependence for this observable.

Table 2.6: Data sets are chosen to check the description of double differential cross sections by the selected spallation models. Where n stands for neutrons, LCP for light charged particles and IMF for intermediate mass fragments.

Energy in MeV	**Targets**				
	Al	**Ag**	**In**	**Au**	**Pb**
256	**n**				**n**
480		**IMF**			
590			**n**		
1200	**n, LCP, IMF**	**n, LCP, IMF**		**n, LCP, IMF**	
1500			**n**		
1900	**n, LCP, IMF**	**n, LCP, IMF**		**n, LCP, IMF**	
2500	**n, LCP, IMF**	**n, LCP, IMF**		**n, LCP, IMF**	
3000	**n**		**n**		**n**

As the representative of the exclusive observables, measurements performed by PISA collaboration [74–78] for:

- three different targets: Al, Ag, Au,
- three different proton beam energies: 1.2, 1.9 and 2.5 GeV,
- various isotopically identified ejectiles in the range of atomic number from Z=1 to Z=5

provide the possibility to perform systematic study for the production of LCP and IMF using five different theoretical models.

In the present investigations are also included the data measured by Green el al. [93], for nuclear system p(480MeV)+Ag. These data are specific in the sense that they consists the double differential cross sections for quite a broad range of isotopically identified IMF starting from element Z=3 to Z=12 at different angles. Furthermore, the Ag target is close to Xe target for which inclusive data are studied in the present thesis at almost the same proton beam energy (500 MeV) - cf. table 2.5. The above listed 10 combinations of target masses and projectile energies surely can be claimed to establish the important contribution to the benchmark studies [82], where the IMF were completely not taken into consideration and LCP data were partially used.

As it is well known the production of neutrons is of utmost importance because of their wide range of applications. In previous benchmark [82], nearly all models were proved to be satisfactory in describing the production of neutrons. To complete the set of ejectiles, the validation of selected models for the production of neutrons is also taken into consideration in the present study. For the systematic investigations like in case of LCP and IMF, neutron data (double differential cross sections) were taken for three targets:

- Al [80, 81, 91] at 256, 1200 and 3000 MeV proton beam energy,
- In [80, 92] at 585, 1500 and 3000 MeV, and

- Pb [80, 81, 91] at 256, 1200 and 3000 MeV.

In summary, the inclusive as well as exclusive observables were chosen for validation of selected models using data for various nuclear systems at several proton beam energies. These data were not included in previous benchmark activities (with exception of neutrons and some LCP) thus the present investigations are valuable as extension of previous studies.

Chapter 3

Description of the selected theoretical models

3.1 Model to describe first stage of reaction - fast stage

3.1.1 Intra nuclear cascade of Liège University - INCL

The INCL model was developed during last thirty years. Short history of this development is presented below:

1981 : First version of the code was presented in 1981 [8] to study reactions involved by heavy ion collisions at energies around 1 GeV. In this version of the model only nucleon degrees of freedom have been taken into account.

1982 : Next year, in the context of cascade calculations the production of pions due to excitation of nucleons to the Δ resonances was introduced. The only source of production was the decay of $\Delta-$resonances which can be potentially formed due to nucleon - nucleon collisions [9].

1987 : First version of model for nucleon-nucleus case was introduced [10]. Model calculations were performed for broad energy range of the proton beam from 100 MeV up to 20 000 MeV. Authors mainly studied the energy loss of incident proton in the target medium. The effort was to calculate the nuclear stopping power.

1988 : Role of target medium was discussed for the production of pions. For this three different possible cases: proton-nucleus, pion-nucleus and heavy ion collision reaction were studied [11].

1997 : In 1997, an improved version of INCL [14] was studied thoroughly with main emphasis on different physical ingredients e.g., in-medium cross sections, stopping time for cascade, Pauli-blocking, surface diffuseness of the target nucleus etc. The cross-sections for possible interactions during cascade stage are parameterized as described in ref. [13].

2002 : After few years, a detailed version of INCL code (INCL4.2) for comprehensive description of spallation reaction data was published [16]. This version could simulate not only the nucleon/pions induced reactions but also light ion (with A $\leq$ 4) induced reactions.

Basic assumptions of the INCL4.2 model:

1. De-Broglie wavelength of the incident particle should be smaller than the average distance of nucleons in the nucleus(d $\approx$1.3 fm) and its mean free path length L in nuclear matter i.e., only binary collisions are allowed.
2. The interaction radius is smaller than the mean free path length L, which allows only to collide with single nucleon at a time. Interaction takes place between the nucleons when minimal distance of approach is $d_{min} = \sqrt{\sigma/\pi}$.
3. To assure the existence of static potential through out the collision, number of participants should be considerably smaller than number of target nucleons A_t.

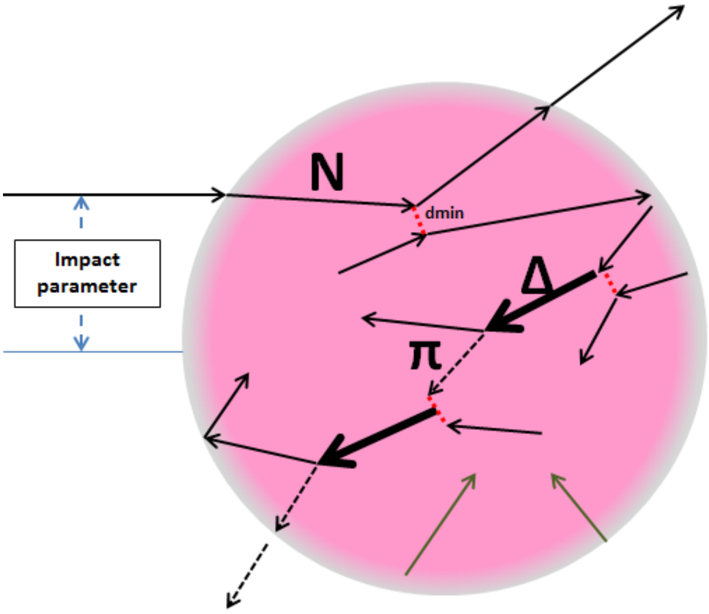

Figure 3.1: Representation of intra nuclear cascade

Initially, target nucleons are positioned according to Saxon-Woods distribution as follow:

$$\rho(r) = \begin{cases} \frac{1}{1+\exp\frac{r-R_0}{a}} & \text{for r} \leq \text{R}_{\text{max}} \\ 0 & \text{for r} > \text{R}_{\text{max}} \end{cases}$$

where R_{max}=R_0+8a , where R_0 and a(diffuseness parameter) have been parametrised as function of target mass A:

$$R_0 = (1.063 + 2.745E - 4.A).A^{1/3}$$
$$a = 0.510 + 1.63E - 4.A$$

This form of density distribution is followed for the target masses A $>$ 27. For target masses between 5 - 27, the modified harmonic oscillator was used as described below:

$$\rho(r) = 1 + R_0.\left(\frac{r}{a}\right)^2).\exp(-\left(\frac{r}{a}\right)^2)$$

for which value of R_0 and a are explicitly tabulated in model. For lighter targets A<6, Gaussian distribution with tabulated values of root mean square is being used.

The momentum of nucleons is generated in a Fermi sphere of radius equal to Fermi momentum p_F. It is assumed that a nucleon with a large momentum will cover a larger radial distance than a nucleon with a lesser momentum. This implies that a nucleon with a momentum p can reach to a maximal distance R(p). Thus, a r-p correlation is followed for the distribution of nucleons inside the target nucleus. This radial - momentum correlation confirms that a nucleon with a momentum between p and p+dp should be placed with a constant uniform probability, in a sphere of radius R(p). Based on this hypothesis, the radius of a nucleon with momentum p can be deduced by assuming that the number of nucleons populating the layer of density profile ρ(R(p)) and ρ(R(p+dp)) are the same as the number of nucleons in the range of momentum p and p+dp:

$$A_T \frac{4\pi p^2 dp}{\frac{4}{3}\pi p_F^3} = \frac{4}{3}\pi R^3(p) d\rho$$

By doing integration of above equation using the boundary limit conditions for R(0)=0 and R(p_F)=R_{max} :

$$\left(\frac{p}{p_F}\right)^3 = \frac{4\pi}{3A_T}\int_0^{R(p)} \frac{d\rho(r)}{dr} r^3 dr$$

This implies:

$$\left(\frac{p}{p_F}\right)^3 = F(R(p))$$

The impact parameter of the incident particle on the target nucleus is simulated. Particle moves in straight line until it encounters the target's nucleon at a distance closer than d$_{min}$ and thus go through the nucleon-nucleon binary collision. Thus it forms the cascade of binary collisions and can opt the following possible interactions: $NN \rightarrow NN$, $NN \leftrightarrows N\Delta$, $N\Delta \rightarrow N\Delta$, $\Delta\Delta \rightarrow \Delta\Delta$ and $\Delta \rightleftarrows \pi$N. Pauli-blocking is introduced for the possible collisions, only those collisions are allowed which leads to the final states when nucleons momenta are greater than Fermi-momentum. Collisions are allowed only in-between the participants nucleons which is on contrary forbid between the spectators. Finally, the particles can tunnel through the assumed square potential of target nucleus or reflected back based on the calculated transmission probability. Delta resonances decay to nucleons and pions either based on their life time or forced to decay after the stopping time of cascade. Stopping time of the cascade is determined self-consistently as a function of target mass

$$t_{stop} = f_{stop} t_0 \left(\frac{A_T}{208}\right)^{0.16}$$

where t$_0$ = 70fm/c and f$_{stop}$ is a free parameter usually taken equal to unity. Conservation of mass, charge, energy, momentum and angular momentum is respected by the simulation of each event. For the detailed information see in Ref. [16].

2004-2013 : During this time period continuous improvements were introduced in the model e.g.,

i Production of light charged particles(LCP: d, t, 3He, 4He) [18],

ii Energy and isospin dependent potential well for nucleons [19].

iii Modification in pion physics [21].

iv Deflection of incoming and outgoing charged particles due to Coulomb field.

v A strict Pauli-blocking to the first collision - only those collisions are allowed which leads to the final state of nucleons outside the fermi-sea, and stochastically pauli-blocking for the subsequent ones.

vi Modified treatment to soft-collisions. C.M energy ($\sqrt{s}$) for such collisions reduced from 1925 MeV to 1910 MeV. The effect of this change is mainly visible in low energy collisions.

vii Modification in the status of participants and spectators.

viii Modified value of R$_{max}$ mainly to be taken into consideration the increased range of interaction for nucleons impinging at low energies. So, an interaction term depending the total cross-section is also added in the previous value of R$_{max}$, which becomes now:

$$R_{max} = R_0 + 8a + r_{int}$$

where $r_{int} = \sqrt{\sigma^{tot}_{NN}/\pi}$ and σ^{tot}_{NN} is the nucleon-nucleon total cross section at the incident energy.

ix Experimental threshold (separation energy S$_n$) is used for the emission of nucleons in INCL4.6 instead of fixed values for a given target as used in in its predecessor versions.

For the detailed descriptions of all the parameter, one can look in ref [23].

The recent official version of INCL code (INCL4.6) contains all earlier introduced modifications with some additional improvements [23] which will be discussed below, mainly the improved algorithm for the production of clusters with mass heavier than A = 4. For the pion physics, there has been developed a separate extension of INCL4.2 code at incident energies between 2GeV - 12 GeV [94].

Coalescence model: The coalescence algorithm embedded in INCL4.6 [23] for the emission of complex fragments based on the idea suggested by Butler and Pearson [95].

1. Each outgoing nucleon is checked either it is capable to cross the potential barrier at surface or not. If it can, the criteria to select a leading nucleon which is going to form cluster with neighboring nucleons is fulfilled irrespective to the number of collision it made earlier. Otherwise, it is reflected back in nuclear medium.

2. The selected leading nucleon is trace back (straight line) to a radial distance D = R_0 + h. Where h is fix parameter (1.0 fm) once for all nuclear systems and R_0 is half-density ($\rho/\rho_0 = 1/2$) radius. It is assumed that the cluster (A > 1) is built by carrying along all those nucleons which come in close vicinity of leading nucleons and satisfy the following conditions.

   $$r_i, [i-1] p_i, [i-1] \leq h_0(A_{cl}); i = 2, 3, 4, .., A_{cl}$$

   Where h_0 is phase volume as a function of mass number of cluster(A_{cl}). Here, $r_i, [i-1]$ and $p_i, [i-1]$ are the spatial and momentum Jacobian co-ordinates of the i_{th} nucleon (leading) with respect to the subgroup constituted of the [i-1] nucleons. Value of phase volume for different potential cluster is as follows:

$h_0(A_{cl} = 2)$	$h_0(A_{cl} = 3)$	$h_0(A_{cl} = 4)$	$h_0(A_{cl} > 4)$
424	300	300	$200A_{cl}^{1/3}$

3. The most stable cluster (up to Z = 5, A_{cl}^{max} = 8 with default options) is preferred. Let $\sqrt{s}$ is the c.m. energy of the glued nucleons forming the cluster and B_{cl} is its binding energy , the cluster with minimum values of the quantity ($\sqrt{s} - \sum m_N$ - B_{cl}(A,Z))/A_{cl} is chosen.

4. This cluster is allowed to emit only if it satisfies the following three conditions:

   (a) It should have energy above the threshold ($\sum(T_i - V_i) - B_{cl} > 0$) energy.

   (b) Able to penetrate through the Coulomb barrier (transmission co-efficient is positive).

   (c) Cluster can't emit after the range of angle between the direction of emission and radial outward direction passing by the center of mass of the constructed cluster i.e., cos$\theta < 45^0$.

If, these tests are not successful, only leading nucleon will emit out providing it satisfies the condition to tunnel through the Coulomb barrier.

5. At the end of cascade, unstable clusters (life time < 1 ms) are forced to decay isotropically. The list of detectable and unstable clusters are shown in Fig. 1 of ref. [23].

3.2 Models to describe the de-excitation stage - Slow stage

3.2.1 Generalized Evaporation Model - GEM2

The GEM2 is the statistical code developed by S.Furihata to describe the de-excitation stage of the residual nucleus by means of two processes: (1). Evaporation (2). Fission. Generalized evaporation model (GEM2) by Furihata [52, 53] is based on the Weisskopf-Ewing's formulation [96], whereas fission is based on the Atchison's [97] fission model.

(1). Evaporation: According to Weisskopf-Ewing approach, the probability for the emission of j_{th} particle from i_{th} parent nucleus with the center of mass kinetic energy ε inside the interval ε+dε is

$$\boxed{P_j\left(\varepsilon\right) d\varepsilon = g_j\ \sigma_{inv}\left(\varepsilon\right) \frac{\rho_d\left(E - Q - \varepsilon\right)}{\rho_i\left(E\right)} \varepsilon d\varepsilon \qquad (3.1)}$$

where ρ_d and ρ_i are level densities (MeV^{-1}) of the daughter and the parent nuclei, respectively. They are evaluated according to the Fermi-gas model of Gilbert and Cameron [98]. The E symbol represents excitation energy of the parent nucleus and Q is the Q-value of the reaction. The g_j term is: $g_j = \left(2S_j + 1\right) m_j / \pi^2 \hbar^2$ where S_j and m_j represent the spin and mass of the emitted particle, respectively. The σ_{inv} is the cross section for inverse reaction taken in the following form

$$\sigma_{inv}\left(\varepsilon\right) = \sigma_g \alpha \left(1 + \frac{\beta}{\varepsilon}\right) \equiv \left\{ \begin{array}{c} \sigma_g c_n (1 + b/\varepsilon) - \text{ for neutrons} \\ \sigma_g c_i (1 - V/\varepsilon) - \text{for charged particles} \end{array} \right. \tag{3.2}$$

where α[MeV^{-1}] is the level density parameter, σ_g=πR_b^2 [fm^2] is the geometric cross section, V represents Coulomb barrier, whereas c_n, c_i, and b are the parameters [52, 53].

The total decay width for the j_{th} particle can be calculated by integrating formula (3.1) over total kinetic energy up to E-Q :

$$\boxed{\Gamma_j = \frac{g_j \sigma_g \alpha}{\rho_i\left(E\right)} \int\limits_V^{E-Q} \varepsilon \left(1 + \frac{\beta}{\varepsilon}\right) \rho_d\left(E - Q - \varepsilon\right) d\varepsilon \qquad (3.3)}$$

The production of jth particle is selected according to the probability distribution $p_j = \Gamma_j / \sum_j \Gamma_j$ using the Monte Carlo sampling. The total kinetic energy ϵ is sampled from the eq. (3.1), direction of motion is chosen isotropically in the centre of mass of the parent nucleus.

GEM2 calculates the emission of total 66 nuclides based on the following criteria:

1. Atomic number Z≤12
2. Naturally existing isotopes or those which lay close to the stability line
3. Isotopes with half-life larger than 1 ms.

The table of nuclides which satisfy the above mentioned conditions:

Z_j	Isotopes						
0	n						
1	p	d	t				
2	^{3}He	^{4}He	^{6}He				
3	^{6}Li	^{7}Li	^{8}Li	^{9}Li			
4	^{7}Be	^{9}Be	^{10}Be	^{11}Be	^{12}Be		
5	^{8}B	^{10}B	^{11}B	^{12}B	^{13}B		
6	^{10}C	^{11}C	^{12}C	^{13}C	^{14}C	^{15}C	^{16}C
7	^{12}N	^{13}N	^{14}N	^{15}N	^{16}N	^{17}N	
8	^{14}O	^{15}O	^{16}O	^{17}O	^{18}O	^{19}O	^{20}O
9	^{17}F	^{18}F	^{19}F	^{20}F	^{21}F		
10	^{18}Ne	^{19}Ne	^{20}Ne	^{21}Ne	^{22}Ne	^{23}Ne	^{24}Ne
11	^{21}Na	^{22}Na	^{23}Na	^{24}Na	^{25}Na		
12	^{22}Mg	^{23}Mg	^{24}Mg	^{25}Mg	^{26}Mg	^{27}Mg	^{28}Mg

The GEM2 code takes into consideration all the nuclides not only in their ground state but also in excited states. Only those excited states are included which fulfill the following condition:

$$\frac{T_{1/2}}{\ln 2} > \frac{\hbar}{\Gamma_j^*} \tag{3.4}$$

where $T_{1/2}$ [sec] is half lifetime of excited state and Γ_j^* represents the decay width of the resonance emission. It can be calculated in the same way as for a ground state particle emission.

In the GEM2 program the emission of resonances is not treated explicitly but it is taken into account by redefinition of the ground state decay width Γ_j in the following way:

$$\Gamma_j = \Gamma_j^0 + \sum_n \Gamma_j^n$$

where Γ_j^0 is the decay width for the emission of particle j in the ground state, and Γ_j^n corresponds to the emission of particles in n^{th} excited state.

(2). Fission: Fission sub-module embedded in GEM2 is based on Atchison [97] approach which assumes that at each stage of the de-excitation of excited nucleus with atomic number $Z \geq 70$, fission competes with neutron emission. The fission probability P_f is calculated as:

$$\boxed{P_f \approx \frac{\Gamma_f}{\Gamma_f + \Gamma_n} = \frac{1}{1 + \Gamma_n/\Gamma_f} \qquad (3.5)}$$

where Γ_f and Γ_n are the total neutron emission and fission width, respectively.

For nuclei with $70 \leq Z_i < 89$ the neutron emission width and the fission width are calculated separately. The fission width Γ_f:

$$\boxed{\Gamma_f = \frac{(s_f - 1)\exp(s_f) + 1}{a_f} \qquad (3.6)}$$

where

$$\begin{aligned}
s_f &= 2\sqrt{a_f\left(E - B_f - \delta\right)} \\
a_f &= a_n\left[1.09 + 0.011\left(Z_i^2/A_i - 31.09\right)^2\right] \\
B_f &= Q_n + 321.2 - 16.7\frac{Z_i^2}{A_i} + 0.218\left(\frac{Z_i^2}{A_i}\right)^2 \\
a_n &= (A_i - 1)/8.
\end{aligned}$$

The neutron width Γ_n:

$$\boxed{\Gamma_n = 0.352\left[1.68J_0 + 1.93A_i^{1/3}J_1 + A_i^{2/3}\left(0.76J_1 - 0.05J_0\right)\right] \qquad (3.7)}$$

where

$$\begin{aligned}
J_0 &= \frac{(s_n - 1)\exp(s_n) + 1}{2a_n} \\
J_1 &= \frac{(2s_n^2 - 6s_n + 6)\exp(s_n) + s_n^2 - 6}{8a_n^2} \\
s_n &= 2\sqrt{a_n\left(E - Q_n - \delta\right)}
\end{aligned}$$

It should be emphasized, that the above defined values of the neutron emission width Γ_n and the level density parameter a_n are different from those used in the evaporation part of the GEM2 model. Nevertheless just these values were proposed by Atchison and they remained unchanged in the GEM2 program.

For nuclei with $89 \leq Z_i \leq 100$ the ratio Γ_n/Γ_f was parameterized according to semi-empirical expression proposed by Vandenbosch and Huizenga [99]:

$$\boxed{\log\left(\frac{\Gamma_n}{\Gamma_f}\right) = \Phi(Z_i)\,(A_i - \Psi(Z_i)) \qquad (3.8)}$$

The functions $\Phi(Z_i)$ and $\Psi(Z_i)$ are tabulated in ref. [52].

It should be pointed out that the fission probability represented by formula (3.8) is independent of the excitation energy of the pre-fission nucleus whereas the fission width (3.6) and the neutron width (3.7) for nuclei with $70 \leq Z_i < 89$ are apparently energy dependent.

The condition to decide either the residual nuclei will follow symmetric or asymmetric fission is decided by term ($\mathrm{Z}_i^2/\mathrm{A}_i$). If this expression is larger than 35, both symmetric and asymmetric fission are possible, otherwise only symmetric. In the former case, the decision that which mechanism is taken into consideration is based on the calculated asymmetric fission probability P_{asy}

$$\boxed{P_{asy} = \frac{487e^{-0.36E}}{1 + 487e^{-0.36E}} \qquad (3.9)}$$

where E is excitation energy of pre-fission nucleus.

The mass of one of the post-fission fragments A_1 is selected from a Gaussian distribution which parameters depend on the previous decision - whether the symmetric or asymmetric fission appears. The mass of the second post-fission fragment A_2 is taken as a difference $A_2 = A_i - A_1$.

The charge of the fission fragments as well as kinetic energy of the fragments is sampled from Gaussian distributions with the parameters determined from previous studies of Atchison [97] and Furihata [52]. Values found by Furihata are taken as default.

The details of the above parameterizations may be found in Refs. [52,53,97,99].

3.2.2 Statistical multi-fragmentation - SMM

After the first dynamical stage of proton induced spallation reaction when high energy particles leave the interaction region the remaining nuclear system evolves towards equilibrium. The fate of this target's remnant depends mainly on its excitation energy and the mass number. At low excitation energy the residual nucleus is able to achieve the thermal equilibrium before emission of any particle. Then, in the case of light nucleus a sequential evaporation of nucleons and composite particles appears whereas for heavy excited nucleus a fission process may compete with emission of light particles. However, at high energies (~ 3 MeV/nucleon), the order of time interval between two adjacent emissions of fragments - estimated within the evaporation models [100] - falls too short to allow for achieving equilibration of the excited nucleus. Thus the sequential emission from compound nucleus seems not longer be a reasonable approach. It is predicted by statistical models (e.g. [101]) that for energies larger than 2 - 4 MeV/nucleon the break-up of the excited nucleus into several intermediate mass fragments becomes more probable. Such a process is known as nuclear multifragmentation.

The process of multifragmentation may be described by different models based on statistical or dynamical approaches. The conceptual differences and overview of the models may be found in ref. [102].

Here the short description of SMM (Statistical Multifragmentation Model) - one of the most popular models of nuclear multifragmentation - is outlined. Detailed formulation of this model is presented in review article of Bondorf et al. [87]. SMM assumes that the de-excitation process proceeds in two steps. In the first step, the equilibrated excited target's remnant expands within a fixed freeze-out volume, which is defined as a volume in which the nuclear interactions between fragments cease and the fragments only move in the mutual Coulomb field. Then the nucleus breaks up into nucleons and hot fragments. All breakup channels allowed by conservation laws are taken into consideration. The probability W_j of a specific channel j of the nucleus deexcitation is assumed to be proportional to the exponential function of the entropy S_j of the selected decay channel:

$$\boxed{W_j \propto \exp(S_j) \qquad (3.10)}$$

where, S_j depends on the number of fragments, excitation energy, mass, charge and freeze-out volume of the system. The formation of the compound nucleus and its de-excitation via conventional evaporation or fission processes is considered as one of the possible channels. Thus this process is treated on the equal footing as all other processes. Due to this the transition from evaporation at low excitation energies to fragmentation at high energies is decided on the basis of the available phase space.

SMM treats the light fragments with mass number A $\leq$ 4 and atomic number Z $\leq$ 2 as structureless particles i.e, only translational degrees of freedom of these particles contribute to the entropy of the system. The heavier fragments are treated as heated drops of nuclear liquid and their individual free energies F_{AZ} are parametrized according to liquid drop model as a sum of the bulk, surface, Coulomb and symmetry energy contributions.

$$F_{AZ} = F^B_{AZ} + F^S_{AZ} + E^C_{AZ} + E^{sym}_{AZ}.$$

Coulomb interaction in-between the fragments is taken into account as per the Wigner-Seitz approximation. The detailed description of the individual terms and the parameters of the model is provided by Refs. [87, 102]. After the simultaneous break-up, Coulomb repulsion and hence acceleration of the fragments is calculated by solving the Hamilton equation of motion for fragments.

In the second stage, de-excitation of the hot fragments depends on the mass of the fragment. Light fragments (A $\leq$ 16) decay in several small clusters as their excitation energy may be large enough to be comparable with their total binding energy. This decay is described by the Fermi-break up model [87,103]. Heavy fragments de-excite according to a modified Weisskopf-Ewing formula (3.1) with the possibility of the emission of ejectiles up to ^{18}O.

For heavier residual nuclei (A > 100), a fission is another important decay channel. This process is described according to formalism based on the Bohr-Wheeler statistical formula [104]. According to Bohr-Wheeler approximation, the partial width for the compound nucleus to undergo fission is proportional to the level density ρ_{sp} at respective saddle point

$$\boxed{\Gamma_f = \frac{1}{2\pi\rho_{AZ}(E^*_{AZ})} \int\limits_{0}^{E^*_{AZ}-B_f} \rho_{sp}\,(E^*_{AZ} - B_f - E)dE \qquad (3.11)}$$

where the symbol ρ_{AZ} represents the level density of the decaying, excited nucleus and B_f is the height of the fission barrier determined by Myers-Swiatecki approximation [105].

For the detailed descriptions of implemented modes in the framework of SMM code and information about the parameters see Ref. [87, 102, 103].

3.2.3 GEMINI++

The GEMINI++ is the statistical code developed by R.J.Charity to describe the nuclear de-excitation as a series of sequential binary decays (no multi-fragmentation allowed strictly). It uses different formalisms: (1) the Hauser-Feshbach formalism [106] for very asymmetric decays, i.e., for emission of neutrons, light charged particles and light intermediate mass fragments, (2) the Bohr-Wheeler formalism [104] for symmetric fission of very heavy systems, and (3) the Moretto's generalized transition-state formalism [107] for other decays.

(1). Very asymmetric decays:

The approach which makes it different from other statistical de-excitation codes lays in the implementation of the Hauser-Feshbach formalism [106] instead of the Weisskopf-Ewing [96] to describe the emission of light fragments Z ≤ (user's choice : Z= 3,4,5). This method is considered to be the best in a situation when target's residua are produced with high spin. The partial decay width of an excited nucleus with energy E*, spin S$_{CN}$ and level density ρ_{CN} for the evaporation of i$_{th}$ particle is described according to Hauser-Feshbach formalism as:

$$\boxed{\Gamma_i^{HF} = \frac{1}{2\pi\rho_{CN}\,(E^*, S_{CN})} \int d\varepsilon \sum_{S_d=0}^{\infty} \sum_{J=|S_{CN}-S_d|}^{S_{CN}+Sd} \sum_{l=|J-S_i|}^{J+S_i} T_l\,(\varepsilon)\rho_d\,(E^* - B_i - \epsilon, S_d) \qquad (3.12)}$$

where S$_d$ and ρ_d are the spin and level density of daughter nucleus, whereas S$_i$, J, l, ϵ, B$_i$ are the spin, total angular momentum, orbital angular momentum, kinetic energy and separation energy of evaporated particle/fragment, respectively. T_l is the transmission co-efficient. The Hauser-Feshbach approach calculates explicitly all angular momentum couplings between initial and final states but the cost of this treatment is a large computation time.

(2). Symmetric fission of very heavy systems:

The Bohr-Wheeler (1- Dimension) [104] transition-state decay width for symmetric fission is implemented which is calculated as:

$$\boxed{\Gamma_{BW} = \frac{1}{2\pi\rho_{CN}\left(E^{*}, S_{CN}\right)} \int \rho_{sp}\left(E^{*} - B_f\left(S_{CN}\right) - \varepsilon\right) d\varepsilon \qquad (3.13)}$$

where ρ_{sp} is the level density at saddle point, $B_f(S_{CN})$ is a saddle point energy (i.e. the fission barrier plus ground-state rotational energy) as a function of spin of nucleus and ε is the kinetic energy in the fission degree of freedom. The value of fission barrier is taken from Sierk's Finite-Range Model [108] calculated after including the shell δW and pairing δP corrections, i.e., $B_f(S_{CN})=B_f^{Sierk}(S_{CN})$ - δW - δP.

(3). Asymmetric division of light and heavy nuclei:

Moretto and Wozniak [107] proposed a formalism which allows to calculate the fragments decay width for distinct mass and charge splits where conditional barrier terms include both the mass and charge asymmetries:

$$\boxed{\Gamma_{Z,A} = \frac{1}{2\pi\rho_{CN}\left(E^{*}, S_{CN}\right)} \int \rho_{sp}\left(E^{*} - B_{Z,A}\left(S_{CN}\right) - \varepsilon\right) d\varepsilon \qquad (3.14)}$$

The new refined conditional barrier can be represented as:

$$B_{Z,A}(S_{CN}) = B_A^{Sierk}(S_{CN}) + \Delta M + \Delta E_{coul} - \delta W - \delta P$$

where $B_A^{Sierk}(S_{CN})$ is interpolated from the Sierk's Final-Range model calculations for the specified mass asymmetry. Since in the Sierk calculations the two nascent fragments have the same Z/A ratio, one has to introduce some corrections for the case of different Z/A ratios of the two fragments. This is realized by introducing the ΔM and ΔE_{coul} terms.

Further details on the GEMINI++ model may be found e.g. in ref. [54].

3.2.4 ABLA07

Like other statistical model codes ABLA07 follows a specific recipes to describe the de-excitation process of thermalised nucleus in terms of particle evaporation, nuclear multifragmentation and fission. If the excitation energy per nucleon of the nucleus exceeds a limiting value (default 4.2 MeV/nucleon) then the extra excitation energy causes the simultaneous break-up of the nucleus. For smaller excitation energies the de-excitation of the nucleus proceeds through sequential evaporation and/or fission.

(1). Multifragmentation: The calculation of the break-up process in ABLA07 is divided into two steps. In the first step it is estimated how large is the mass loss of the excited nucleus if the heaviest fragment appearing due to the fragmentation has excitation energy per nucleon corresponding to the limiting value. An assumption is made that the energy used to lose one unit of mass varies from 10 MeV for an initial excitation energy of 2.9 MeV/nucleon to 5 MeV for an initial excitation energy of 11.8 MeV/nucleon. The mass number A and atomic number Z of heaviest created nucleus may be obtained due to the additional assumption that the break-up product has the same N/Z ratio as the initial excited nucleus. The mass numbers of lighter fragments A_{IMF} appearing in the fragmentation are found by Monte Carlo sampling according to the empirical power law:

$$\frac{d\sigma}{dA_{IMF}} \propto A_{IMF}^{-\tau} \tag{3.15}$$

where the exponent $\tau \approx 2$. The sampling is terminated when the maximum available mass is exhausted.

The atomic number Z_{IMF} of the fragment is sampled from a Gaussian distribution centered around a value Z_{MEAN} which is determined by assuming that the value of A/Z ratio is the same as for the hot remnant. The standard deviation of this distribution is evaluated from the following formula

$$\sigma^2_{Z_{IMF}} = \frac{T_{freeze-out}}{C_{sym}} = \frac{5.5\ MeV}{14.0\ MeV} = 0.3929 \tag{3.16}$$

The symbol C_{sym} represents the symmetry term of the nuclear equation of state [109] and $T_{freez-out}$ is so called freeze-out temperature [110]. Values of the C_{sym} and $T_{freez-out}$ are taken from refs. [109] and [110], respectively.

The method of evaluation of the kinetic energy of fragments evolved in simultaneous break-up of nucleus depends on the time-scale of the break-up process. If the time scale is too short to establish the thermal equilibrium, i.e., < 100 fm/c, the decay is governed by the Fermi-motion of nucleons in the break-up system. The width σ of the momentum distribution of a produced fragment can be calculated using the Fermi-gas model [111]

$$\boxed{\sigma^2 = \sigma_0^2 . \frac{A_{frag} . \left(A_{init}^{spectator} - A_{frag}\right)}{A_{init}^{spectator} - 1} \qquad (3.17)}$$

where $A_{init}^{spectator}$ is the mass number of the excited nucleus at the starting point of ABLA07, A_{frag} is the mass of fragment, and σ_0 is a parameter amounting to $\sim$ 118 MeV/c for heavy nuclei. This parameter has to account for the effects of internal motion of nucleons inside the fragment [112] and for thermal expansion of the break-up source [113].

On contrary, when time scale is large enough to attain the equilibrium of break-up system then the thermal motion of fragments plays a decisive role. Equation for the width of the momentum distribution of the fragment can be described as

$$\boxed{\sigma^2 = m_n.A_{frag}.T_{freeze-out}.\frac{\left(A_{init}^{spectator} - A_{frag}\right)}{A_{init}^{spectator}} \qquad (3.18)}$$

where m$_n$ is the nucleon mass. The Coulomb repulsion among nascent fragments is also accounted for calculating their velocities [114].

(2). Evaporation

If the excitation energy is not large enough to trigger the multi-fragmentation modules, the compound nucleus directly enters into the alternative de-excitation process. In this, emission of stable nucleus up to half the mass of compound nucleus is described by Weisskopf-Ewing formalism [96]. The decay width of a particular channel by emitting an ith particle with kinetic energy ϵ_i is given as:

$$\boxed{\Gamma_i\left(E_p\right) = \frac{2s_i+1}{2\pi\rho_p\left(E_p\right)} \cdot \frac{2m_i}{\pi\hbar^2} \int\limits_0^{E_p-S_i-B_i} \sigma_c\left(\varepsilon_i\right).\rho_d\left(E_d\right)\left(\varepsilon_i - B_i\right)dE_d \qquad (3.19)}$$

where s$_i$ is the spin and m$_i$ the mass of the emitted particle, respectively. B$_i$ is the Coulomb barrier and σ_c is the inverse cross section for the emission of particle, ρ_p and ρ_d represents the level densities for parent and daughter nucleus, respectively. All these parameters play a significant role to calculate the probability of a certain decay channel. For IMF the barrier B$_i$ was calculated by using the empirical fusion nuclear potential of Bass [115]. In the case of light charged particles different parameters of the barrier have been used. All nuclei below the Businaro-Gallone maximum of the mass-asymmetry dependent barrier are taken into account in the evaporation process. Above the Businaro-Gallone point, emission of IMF through evaporation from a heavy nucleus competing with fission process as an asymmetric mass-split is treated dynamically based on the solution of the Fokker-Plank equation for collective deformation of system over the fission barrier.

(3). Fission

Fission is an important and very sophisticated decay channel introduced in ABLA07. It is of significant importance to describe the decay of heavy excited nuclei produced in proton collisions with heavy targets. In the ABLA07, fission is handled by an inbuilt program called PROFI [116–118] which allows only independent binary decays. It calculates the atomic masses, charges, excitation energies and velocity of two fission fragments. ABLA07 code calculates the fission decay width using a time-dependent approach [119–121]. In the code, there is possibility to calculate the emission of particles at different fission stages. It starts from the expansion of excited nucleus to the saddle point, from saddle to scission point, and finally from two separated fission products. Only emission of neutrons and LCP is possible during saddle-to-scission period. After scission, the system breaks into two fragments.

The detailed description of the ABLA07 code may be found in Ref. [86] and references cited therein.

Chapter 4

Statistical properties of tests used in validation of the spallation models

As it was mentioned in the introduction, the validation of models may be treated as the testing of the statistical hypothesis which claims that the expectation value of the experimental cross section σ^{exp} is equal to the calculated cross section σ^{cal} (1.1):

$$E(\sigma^{exp}) = \sigma^{cal}.$$

This can be realized by introduction of the deviation factors which are functions of both, experimental and theoretical cross sections measuring distance between the data and calculated values. Knowledge of the probability density function of the deviation factor constructed under assumption that the above equality is fulfilled allows to check whether the observed value of the deviation factor is sufficiently close to its expectation value. In such a case one is allowed to state that the perfect agreement is achieved, or more precisely that there is no evidence against such a statement.

There are many deviation factors proposed in the literature for the quantificationof the agreement between calculated cross-sections and experimental data (see e.g. ref. [122]). It is unfortunate that their probability density functions are usually not known. In such a situation the method of validation as described above cannot be applied and the deviation factors can be used only to perform ranking of the models. Thus in the present section an attempt is made to find the probability density functions of the deviation factors analytically or by applying the Monte Carlo method.

In these investigations a fact should be taken into consideration that most of the modern theoretical models of the spallation reactions evaluate the cross sections by performing an event-by-event Monte Carlo imitation of the collision processes. *In such a situation the theoretical cross sections are also random variables.* Therefore the perfect agreement between the theory and the experiment should be rather formulated as the equality of expectation values of the experimental and calculated cross sections:

$$\boxed{E(\sigma^{exp}) = E(\sigma^{cal}). \quad (4.1)}$$

Then the spread of Monte Carlo results around their expectation values should be taken into account to judge how well the above equality is fulfilled. To our knowledge this effect was not treated explicitly in the literature.

In the first section of the present chapter the most frequently used deviation factors are presented in their standard form used in the literature (i.e. without taking into account a possible random character of the model cross sections) and their statistical properties are studied.

In the second section the desirable features of the statistical test used for validation of the reaction models are discussed and new deviation factors are proposed together with recommendation of some previously used factors. In their definition the random character of model cross sections calculated by Monte Carlo method is taken into account.

In all statistical concepts used here a common tacit assumption is that the statistical properties of the cross sections can be well described by Gaussian probability density distributions. Since the cross sections are positive the Gaussian distribution centered at positive x_0 with relatively small standard deviation σ has to be used in all considerations. Thus the following conditions should be fulfilled in simulation of the probability density distribution of the cross sections:

$$x_0 > 0 \bigcap \sigma << x_0. \tag{4.2}$$

However, it has to be taken into consideration that the second condition is not realized for poor statistics measurements. Then the Gaussian approximation should be abandoned and the Poisson distribution of the number of events (properly normalized to obtain the cross sections) has to be applied. This fact is taken into account in the presented study.

4.1 The literature deviation factors

In this section the most popular deviation factors, used in the literature for the validation of the spallation models are presented and their statistical properties are studied analytically or by means of the Monte Carlo simulation.

Following assumptions are made for analytical considerations:

1. The $\sigma_i^{\exp}$ variable has a Gaussian probability distribution with the expectation value and the variance equal to:

$$\boxed{\begin{aligned} E\left(\sigma_i^{\exp}\right) &= \sigma_i^{calc} \qquad (4.3) \\ var\left(\sigma_i^{\exp}\right) &= \left(\Delta\sigma_i^{\exp}\right)^2 \end{aligned}}$$

Here symbols $\sigma_i^{\exp}, \sigma_i^{calc}$, and $\Delta\sigma_i^{\exp}$ denote the experimental cross section, the calculated cross section, and the error of the experimental cross section, respectively.

2. The variables $\sigma_i^{\exp}$, $i = 1, 2, \ldots N$ are statistically independent
3. The possibility that model cross sections are also random variables is not taken into account.

The experimental cross section is proportional to the number of detected events which is the Poisson random variable. For experiments performed with a good statistics, i.e., with small relative statistical errors the Poisson distribution is well approximated by the Gaussian distribution [2] thus the above assumption is justified.

For the poor statistics data the approximation of the Poisson variables by Gauss variables is not justified. Therefore in the Monte Carlo study the data with relative statistical uncertainty $\Delta\sigma_i^{exp}/\sigma_i^{exp} > 1/6$ are treated as the Poisson random variables.

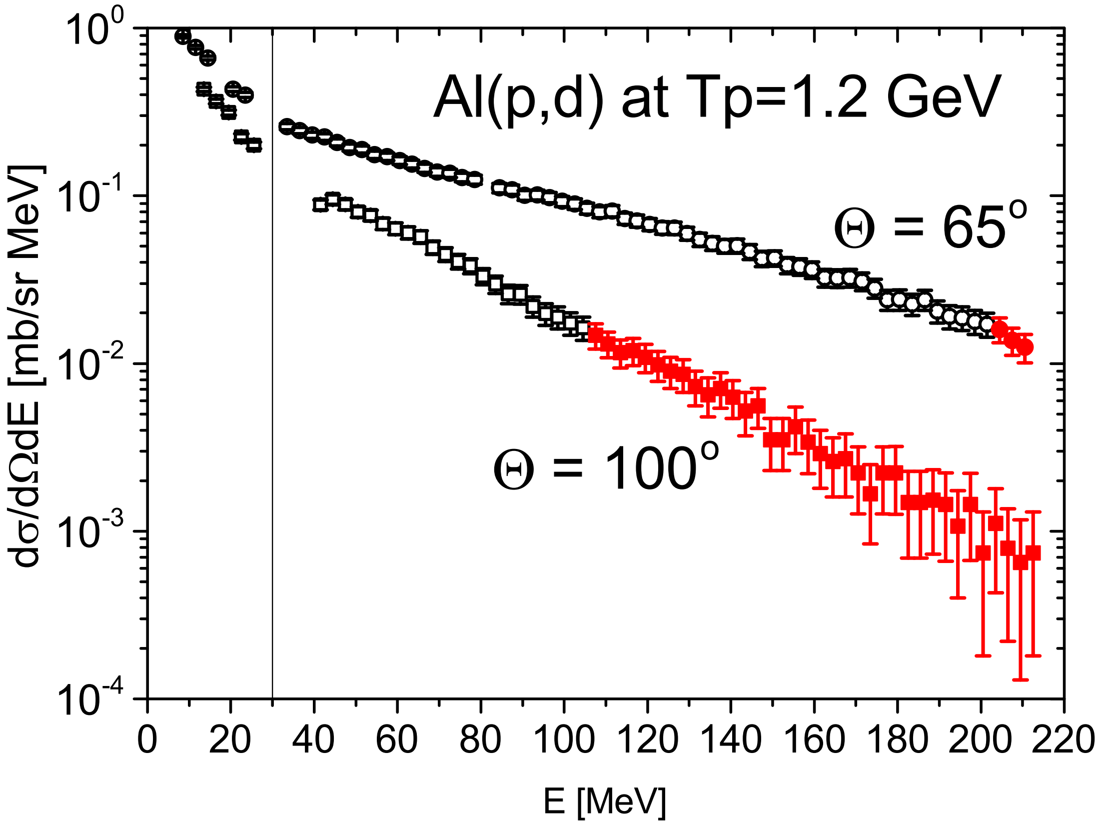

Figure 4.1: Typical energy spectra of the deuterons - spallation products from p+Al collisions at proton beam energy equal to 1.2 GeV [78]. These data were used in the present study for presenting statistical properties of different deviation factors applied in the literature for validation of spallation models.

For the present study, the typical experimental data of the spallation reactions induced by protons have been selected. There are the data obtained by PISA collaboration for emission of deuterons at two scattering angles: 65° and 100° from the reactions induced by 1.2 GeV protons impinging on to aluminium target [78]. The spectra at these two scattering angles - shown on fig. 4.1 - represent the following different types of the cross sections:

- The data for ejectile energies smaller than 30 MeV correspond mainly to the evaporated particles, thus they are usually measured with good statistics because the evaporation cross sections are relatively the largest. These cross sections change in very similar manner with the energy for all scattering angles.
- The data for energies larger than 30 MeV show an exponential fall off which is faster for larger scattering angles. Therefore the tests used for validation of the theoretical models may indicate angle dependent behaviour.
- Decreasing of the cross sections for large scattering angles is so fast that the data at largest energies are measured with much poorer statistics than those for the evaporation region. For such data the Gaussian approximation to the probability distribution of the experimental cross sections may be not satisfactory. The Poisson distribution should be applied then. This may significantly influence statistical properties of the deviation factors derived under assumption of Gaussian distributions of the cross sections. The selected data enable us to study this effect.

The open symbols in fig. 4.1 represent the cross sections which were measured with good statistics (the relative statistical error of the evaporation cross sections is of order of 5%). The full (red) symbols represent the cross sections which were obtained with poor statistics by accumulating in the experiment not more than 36 events per energy bin (relative error of 17 % or larger). The largest errors in these data correspond to 70% of the cross section, i.e. these cross sections were determined by collecting only 2 events. *The selected data put very demanding constraints on the statistical reasoning performed with the simplified assumption of the Gaussian instead the Poisson distribution of the data.* Thus, one can expect that the statistical methods working in such restrictive conditions will be also applicable to good statistics data.

4.1.1 H-deviation factor

The H-test mentioned in the Introduction (1.2) is defined by the formula [123]:

$$\boxed{H \equiv \left[\frac{1}{N}\sum_{i=1}^{N}\left(\frac{\sigma_i^{\exp}-\sigma_i^{calc}}{\Delta\sigma_i^{\exp}}\right)^2\right]^{1/2} \qquad (4.4)}$$

where $\sigma_i^{\exp}, \sigma_i^{calc}$, and $\Delta\sigma_i^{\exp}$ denote the experimental cross section, the calculated cross sections, and the error of the experimental cross section, respectively.

It can be shown (see Appendix A) that under the above assumptions the probability density function of the H-factor $f(H)$, its expectation value $E(H)$, the variance $var(H)$, and the mode H_m (i.e. a position of the maximum of $f(H)$) are equal to:

$$\begin{aligned}
f(H) &= \frac{N^{\frac{N}{2}}}{2^{\left(\frac{N}{2}\right)-1}\Gamma\left(\frac{N}{2}\right)}\exp\left(-\frac{NH^2}{2}\right)H^{N-1} && (4.5)\\
E(H) &= \sqrt{\frac{2}{N}}\frac{\Gamma\left(\frac{N+1}{2}\right)}{\Gamma\left(\frac{N}{2}\right)} && (4.6)\\
\mathrm{var}(H) &= 1-E\left(H\right)^2 && (4.7)\\
H_m &= \sqrt{\frac{N-1}{N}} && (4.8)
\end{aligned}$$

The probability density functions of the H deviation factor have been calculated for different groups of the data presented in fig. 4.1, i.e., for both scattering angles - separately for energies smaller than 30 MeV, larger than 30 MeV, and for the full spectra. The points in fig. 4.2 depict results of Monte Carlo simulations whereas the solid lines present values obtained according to the theoretical formulae (4.5) - (4.7). In the left column of panels in fig. 4.2 the probability density functions for 65° are shown, in the right one these functions are for 100°. The results for energies smaller than 30 MeV are depicted in the upper panels, those for energies larger than 30 MeV are shown in the middle ones whereas the lowest panels of the figure represents the full energy spectra.

The following properties of the H-test are evident from the inspection of figure 4.2:

- The theoretical probability density functions derived under assumption of the Gaussian distribution of the experimental cross sections reproduce well the histograms in all cases, even for the data at 100° and energies larger than 30 MeV where the Poisson distribution was used for generating the histograms.
- The width and the position of distribution depend strongly on the number of experimental cross sections. This has to be taken into account when the H-factor is used for validation and/or ranking of the models.

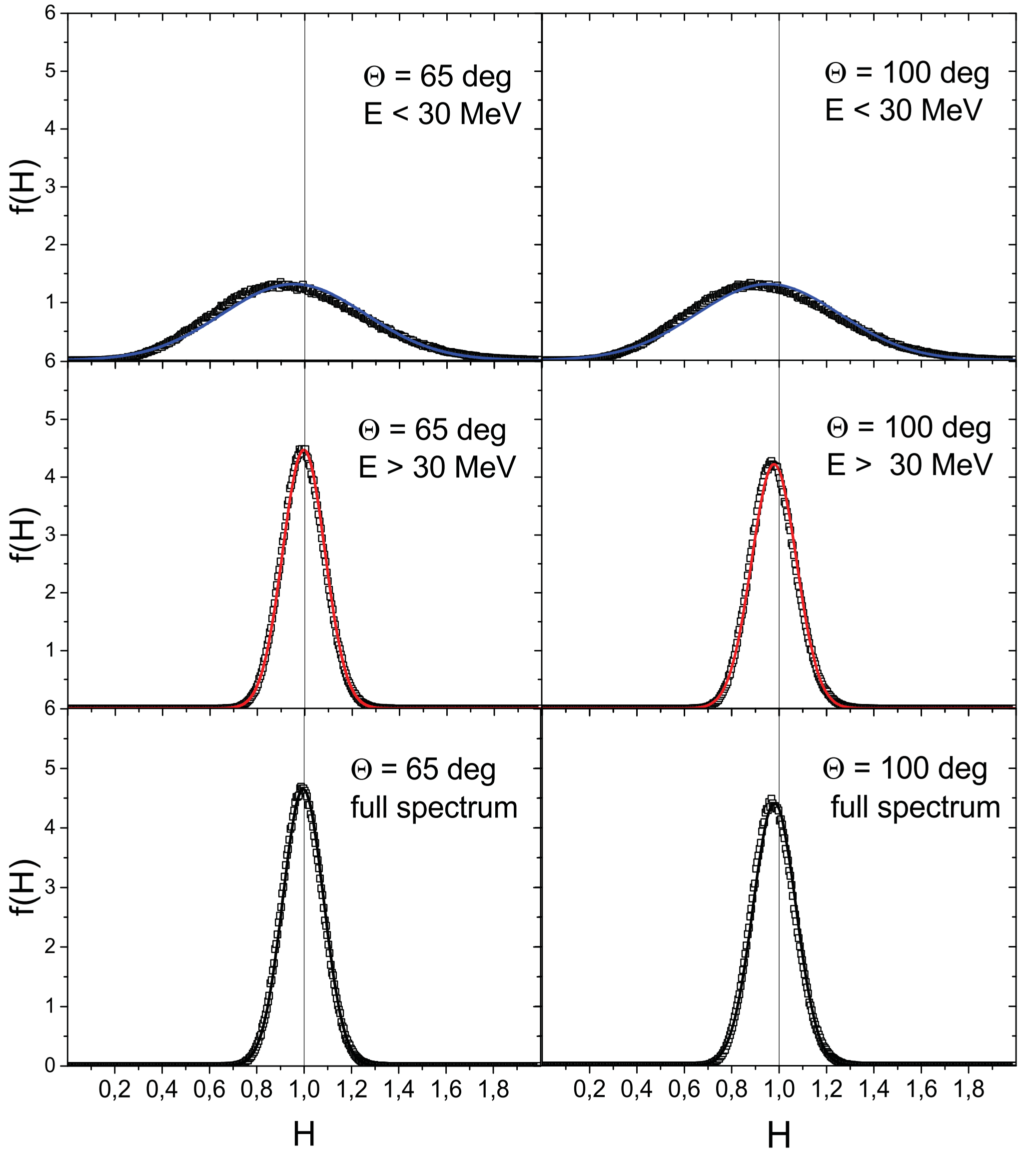

Figure 4.2: Probability density functions (lines) and histograms (circles) of the H-test calculated for the experimental spectrum of deuterons measured at angle 65° and 100° from the spallation reactions induced by 1.2 GeV protons on the Al target [78] (see fig. 4.1). The histograms were generated by Monte Carlo method assuming that $E(\sigma_i^{exp}) = \sigma_i^{cal}$ and the standard deviations of data are equal to statistical experimental errors $\Delta\sigma_i^{exp}$. The lines are theoretical probability functions calculated according to formulae (4.5) - (4.7). Vertical line present in all panels shows position of $H = 1$.

The reference value of the H-factor, used for ranking of models is equal to zero which is simultaneously equal to the absolute minimum of the factor. Its worth noting that the reference value is different from the expectation value $E(H)$ as well as from the most likely value H_m.

4.1.2 R^{EC} and R^{CE} deviation factors

These tests are defined as follows [122]:

$$\boxed{\begin{aligned} R^{EC} &\equiv \frac{1}{N}\sum_{i=1}^{N}\frac{\sigma_i^{\exp}}{\sigma_i^{cal}} \qquad (4.9)\\ R^{CE} &\equiv \frac{1}{N}\sum_{i=1}^{N}\frac{\sigma_i^{cal}}{\sigma_i^{\exp}} \qquad (4.10)\end{aligned}}$$

Using the same assumptions as those for the H-test it is easy to find that the R^{EC} test has a Gaussian distribution with the expectation value:

$$\boxed{E(R^{EC}) = 1 \qquad (4.11)}$$

This is because each term $\sigma_i^{\exp}/\sigma_i^{cal}$ in the sum (4.9) is a Gaussian random variable with the unit expectation value. It is known that the sum of independent Gaussian variables is a Gaussian variable with the expectation value equal to the sum of expectation values of individual terms in the sum [2]. The factor $1/N$ in front of the sum (4.9) assures that the expectation value of the R^{EC} is equal to one.

The variance of the R^{EC}-test is equal to the sum of variances for individual terms in the sum (4.9) divided by N^2. Thus it is equal to:

$$\boxed{\operatorname{var}\left(R^{EC}\right) = \frac{1}{N^2}\sum_{i=1}^{N}\left(\frac{\Delta\sigma_i^{\exp}}{\sigma_i^{cal}}\right)^2 \qquad (4.12)}$$

where the variance of $\sigma_i^{exp}/\sigma_i^{cal} = (\Delta\sigma_i^{\exp})^2/(\sigma^{cal})^2$ because the model cross section is treated here as a constant and the variance of σ_i^{exp} is equal to the square of the experimental error $(\Delta\sigma_i^{\exp})^2$. The relations (4.11) and (4.12) are exact.

Thus, the R^{EC}-test has similar properties as the H-test, i.e. it is unimodal with the mode $R_m^{EC} = 1$ and expectation value $E(R^{EC}) = 1$. However, as opposed to the H-test the variance of the R^{EC}-test is not determined only by the number N of the data but depends on the values of theoretical cross sections, thus it has to be found separately for each theoretical calculation. Of course, the calculated cross section is equal to the expectation value of the experimental cross section in the case of the perfect agreement (1.1) of model values with the data.

The reference value of the R^{EC}-factor is equal to one, i.e., it is equal to the expectation value and the mode of the factor.

The histograms for values of the R^{EC} factor were calculated for the perfect agreement of the calculated and experimental cross sections using the same assumptions as those applied for calculations of the histograms of the H-factor. The theoretical probability density distributions which are of the Gaussian shape were calculated with the expectation value and variance parameters taken from equations (4.11) and (4.12), respectively. Results of the calculations are presented in fig. 4.3.

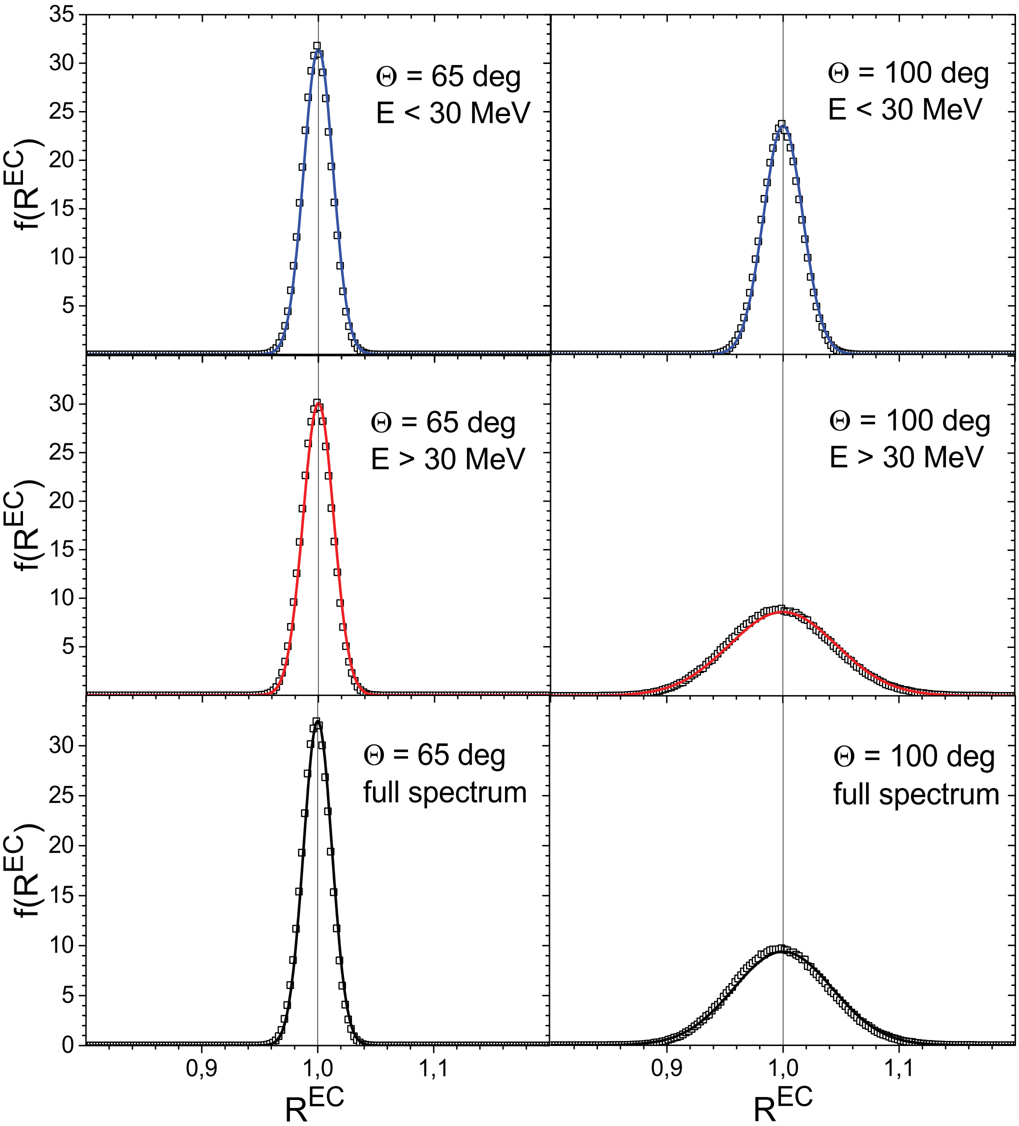

Figure 4.3: The open symbols represent probability density distributions of the R^{EC} deviation factor calculated by Monte Carlo method whereas the solid lines depict Gauss functions with parameters given by formulae (4.11) and (4.12). Vertical line present in all panels shows position of $R^{EC} = 1$.

It is evident from inspection of fig. 4.3 that

- For all the data the shape of histograms agrees perfectly with predicted Gaussian shape. Moreover, the lines calculated with the parameters predicted by the theory reproduce very well the histograms.

- This good agreement of the shape and magnitude of the theoretical probability density functions with the histograms generated by Monte Carlo method is preserved also for the data at 100° for energies larger than 30 MeV (middle - right panel of the figure) and for full spectrum (lower - right panel) where in both cases the data with poor statistics are abundant. For such data (red full symbols in figure 4.1) the Poisson probability distribution was used in the Monte Carlo calculations. In spite of this the results are in good agreement with theoretical predictions made for the cross sections ruled by the Gaussian distribution.

Since the R^{CE}-factor is defined as a sum of independent variables the probability density of this test should also have asymptotically (for large N) a Gaussian distribution. This is because **the central limit theorem** states that the sum of independent random variables has normal probability distribution in the limit of large N [2].

However, it is not easy to determine expectation value of the R^{CE} factor because expectation values of individual terms in the sum (4.10) may deviate from unity

$$E(\sigma_i^{cal}/\sigma_i^{exp}) \neq 1$$

even in the case of the perfect agreement between the model and experimental cross sections; $\sigma_i^{cal} = E(\sigma_i^{exp})$. This is due to *the nonlinear* dependence (reciprocal) of the ratio $\sigma_i^{cal}/\sigma_i^{exp}$ on the normal random variable σ_i^{exp}. Moreover, the deviation of expectation value $E(R^{CE})$ from unity depends on the relative experimental error $\Delta(\sigma_i^{exp})/\sigma_i^{cal}$ - see Appendix C. Thus the exact value of $E(R^{CE})$ is not known even for the perfect agreement of the model and experimental cross sections. This creates uncomfortable situation for testing the hypothesis of the perfect agreement of model and experimental cross sections. A possible solution of this problem may be found by Monte Carlo simulation of the R^{CE} probability density distribution for each individual set of the experimental cross sections with known errors.

In contrast to the expectation value the variance of the R^{CE}-test may be estimated in a simple way. It is equal to the sum of variances of individual terms in the sum (4.10) divided by N^2. Thus it may be calculated as

$$\boxed{\operatorname{var}\left(R^{CE}\right) \approx \frac{1}{N^2}\sum_{i=1}^{N}\left(\sigma_i^{cal}\cdot\frac{\Delta\sigma_i^{\text{exp}}}{(\sigma_i^{exp})^2}\right)^2. \qquad (4.13)}$$

Similarly as for the R^{EC}-factor the variance of the R^{CE}-factor depends not only on the experimental values but also on values of the model cross sections.

The reference value of the R^{CE}-factor for the ranking is also equal to one as for R^{EC}-factor.

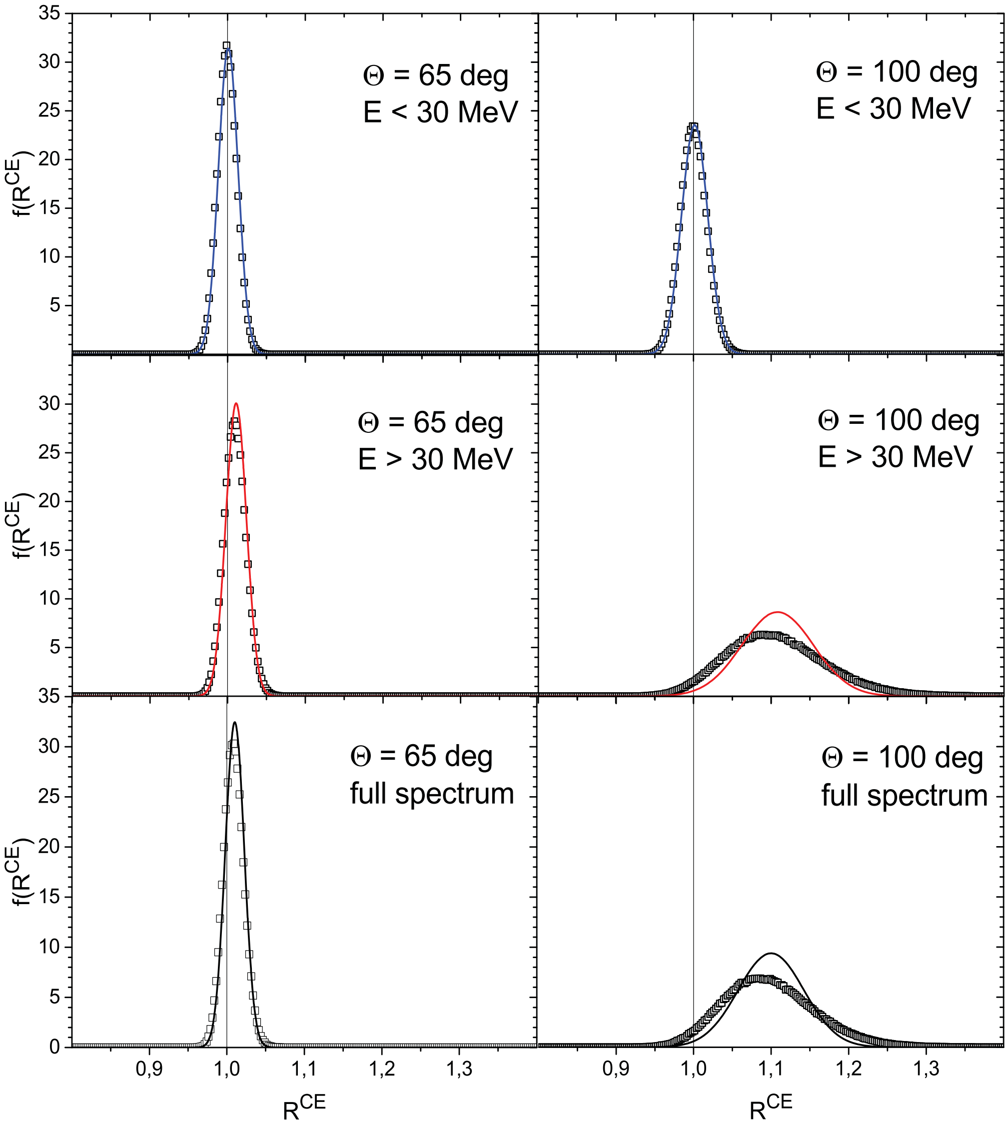

Figure 4.4: Probability density distributions of the R^{CE} deviation factor calculated by Monte Carlo method (the open symbols) and from analytical formulae (solid lines) for the data presented in fig. 4.1. The lines represent Gauss functions with expectation values $E(R^{CE})$ derived from the Monte Carlo histograms and the variances var(R^{CE}) calculated according to the formula (4.13). Vertical line present in all panels shows position of $R^{CE} = 1$.

The histograms of the R^{CE} deviation factor were calculatedfor the same data as for previously discussed factors and they are presented in fig. 4.4 together with Gaussian functions. The variances of the Gaussian functions were determined using the formula (4.13) with the approximation $\sigma_i^{cal} = \sigma_i^{exp}$ but the expectation values must be taken from the Monte Carlo histograms.

As can be seen in fig. 4.4:

- The shape of the histograms resembles the Gaussian function for good statistic data (left column of the figure and the upper panel of the right column). Moreover, the width of the histograms is well reproduced by the variance calculated according to the formula (4.13).
- However, for poor statistic data (the middle-right and lower-right panels of the figure) the shape of the histograms deviates from the Gauss function showing a positive skewness. Furthermore, the width of the histograms is larger than that predicted by the formula (4.13).

The definitions of the R^{EC} and R^{CE} factors have an obvious drawback. It consists in the fact that individual terms in the sums (4.9) and (4.10) are not symmetrical in respect to exchange of the calculated and experimental cross sections. An overestimation and underestimation of the data by the model leads to deviations of the ratio $\sigma_i^{exp}/\sigma_i^{cal}$ in opposite directions in respect to unity. It may thus happen that the model which strongly overestimates part of the data and simultaneously strongly underestimates another part of the data results in value of R^{EC} or R^{CE} factors quite close to unity - suggesting overall good agreement.

4.1.3 D^{EC} and D^{CE} deviation factors

These tests are determined by the following definitions [122]:

$$\boxed{\begin{aligned} D^{EC} &\equiv \frac{1}{N}\sum_{i=1}^{N}\left|\frac{\sigma_i^{\mathrm{exp}}-\sigma_i^{cal}}{\sigma_i^{cal}}\right| \qquad (4.14)\\ D^{CE} &\equiv \frac{1}{N}\sum_{i=1}^{N}\left|\frac{\sigma_i^{\mathrm{exp}}-\sigma_i^{cal}}{\sigma_i^{\mathrm{exp}}}\right| \qquad (4.15)\end{aligned}}$$

The D^{EC} factor is a sum of absolute values of the terms

$$\frac{\sigma_i^{\mathrm{exp}}}{\sigma_i^{cal}} - 1$$

which are very similar to those appearing in the definition of the R^{EC} factor. The only difference consists in subtracting of unity. Thus, the expectation value of each such a term is equal to zero (under assumption of perfect model description of the experiment $E(\sigma_i^{\mathrm{exp}}) = \sigma_i^{cal}$):

$$E\left(\frac{\sigma_i^{\mathrm{exp}}}{\sigma_i^{cal}} - 1\right) = 0$$

Furthermore, a variance of each term is equal to variance of the $\sigma_i^{\exp}/\sigma_i^{cal}$ because subtracting of the constant from the variable does not change its variance, namely

$$\mathrm{var}\left(\frac{\sigma_i^{\exp}}{\sigma_i^{cal}}-1\right)=\mathrm{var}\left(\frac{\sigma_i^{\exp}}{\sigma_i^{cal}}\right)=\left(\frac{\Delta\sigma_i^{\exp}}{\sigma_i^{cal}}\right)^2.$$

Since the experimental cross section may be treated as a normal random variable, each of the terms $\sigma_i^{\exp}/\sigma_i^{cal}-1$ has a normal distribution with the expectation value equal to zero and the standard deviation equal to $\sigma \equiv \Delta\sigma_i^{\exp}/\sigma_i^{cal}$.

The absolute values of such terms enter in the definition of the D^{EC}-factor which influences the expectation value and standard deviation discussed above. The symbol y will be used below for such a random variable ($y \equiv \sigma|z|$ where z is the standard normal variable). According to formulae derived in the Appendix B the probability density distribution of y is equal to

$$g\left(y\right)=\sqrt{\frac{2}{\pi\sigma^2}}\exp\left[-\frac{y^2}{2\sigma^2}\right]$$

with the expectation value and variance equal to:

$$\begin{aligned} E(y) &= \sqrt{\frac{2}{\pi}}\cdot\sigma \\ \mathrm{var(y)} &= \left(\frac{\pi-2}{\pi}\right)\sigma^2. \end{aligned}$$

Thus the expectation value and the variance of each term in the sum (4.14) is equal to:

$$\begin{aligned} E\left(\left|\frac{\sigma_i^{\exp}}{\sigma_i^{cal}}-1\right|\right) &= \sqrt{\frac{2}{\pi}}\cdot\left(\frac{\Delta\sigma_i^{\exp}}{\sigma_i^{cal}}\right) \\ \mathrm{var}\left(\left|\frac{\sigma_i^{\exp}}{\sigma_i^{cal}}-1\right|\right) &= \left(\frac{\pi-2}{\pi}\right)\cdot\left(\frac{\Delta\sigma_i^{\exp}}{\sigma_i^{cal}}\right)^2. \end{aligned}$$

Since the expectation value and variance of the sum of independent variables are equal to sums of expectation values and variances of individual terms, the following formulae held for the D^{EC} factor:

$$\boxed{\begin{aligned} E\left(D^{EC}\right) &= \frac{1}{N}\sqrt{\frac{2}{\pi}}\sum_{i=1}^{N}\left(\frac{\Delta\sigma_i^{\exp}}{\sigma_i^{cal}}\right) && (4.16) \\ \mathrm{var}\left(D^{EC}\right) &= \frac{1}{N^2}\left(\frac{\pi-2}{\pi}\right)\sum_{i=1}^{N}\left(\frac{\Delta\sigma_i^{\exp}}{\sigma_i^{cal}}\right)^2 && (4.17) \end{aligned}}$$

Of course, these formulae are valid only for the perfect description of data by model cross sections $E(\sigma^{exp}) = \sigma^{cal}$.

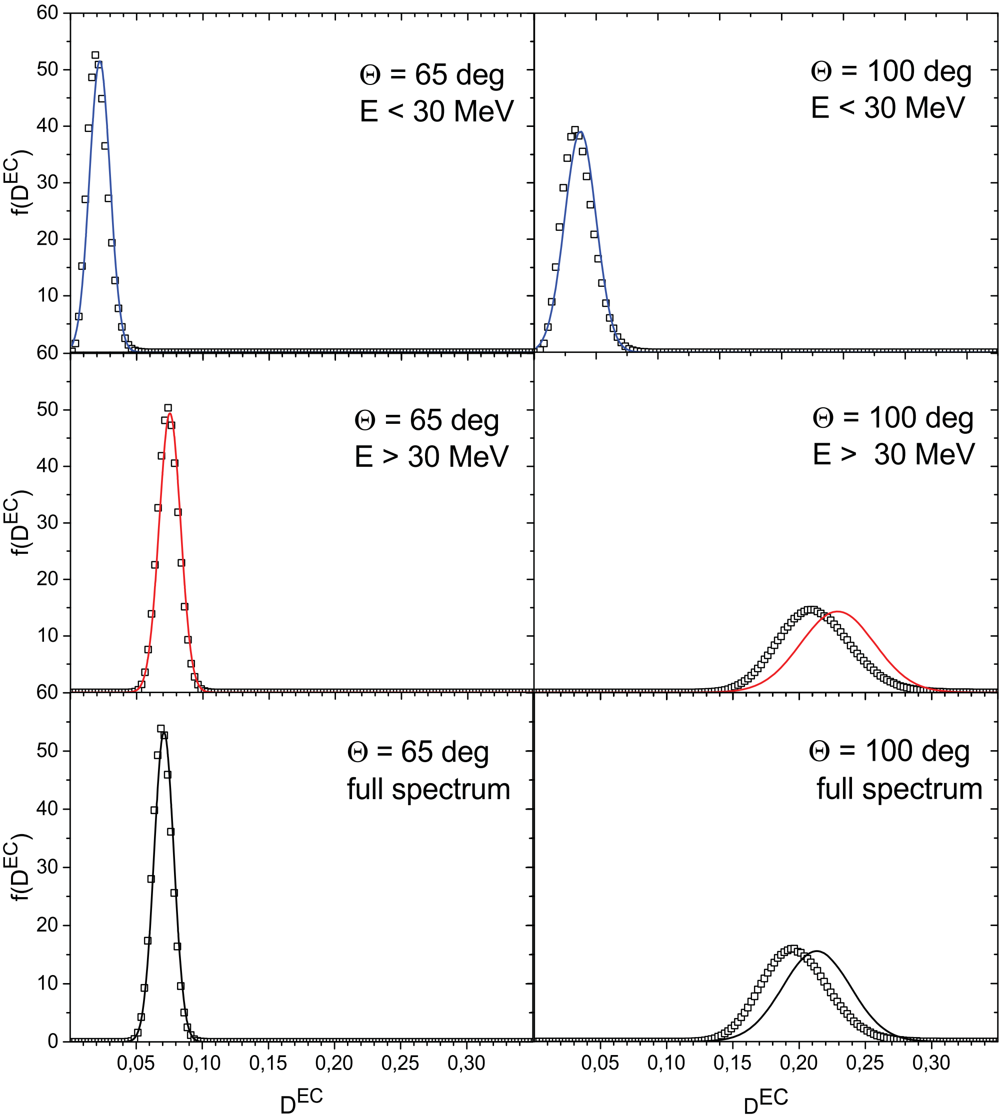

Figure 4.5: Probability density distributions of the D^{EC} deviation factor calculated by Monte Carlo method (the open symbols) and from analytical formulae (solid lines) for the data presented in fig. 4.1. The lines represent Gauss functions with expectation values $E(D^{EC})$ and variances var(D^{EC}) according to the formulae (4.16) and (4.17).

Histograms of the D^{EC} factor have been calculated for the data shown in fig. 4.1 in the same manner as for previous deviation factors. It means, the perfect agreement of the model and experimental data has been assumed. The probability distributions of the cross sections have been taken in the Gaussian form for good statistic data (at scattering angle 65° and for energies $E < 30$ MeV at scattering angle 100°), whereas the Poisson distributions have been applied for poor statistic data (the cross sections measured at 100°

at energies larger than 30 MeV - red, full symbols in fig. 4.1). The theoretical probability distribution functions were taken in the Gaussian form on the basis of the central limit theorem with the parameters determined by formulae: (4.16) and (4.17) for expectation value $E(D^{EC})$ and variance $\mathrm{var}(D^{EC})$, respectively. Results of the calculations are shown in fig. 4.5.

It can be seen that:

- The shape of the histograms is well reproduced by the Gauss function for all data. The centroids and widths of the histograms for good statistic data are also reproduced.
- However, the centroids of histograms are shifted to lower values of the D^{EC} factor for poor statistic data (middle and lower panel in the right column of fig. 4.5) in comparison to predictions of the formula (4.16). This means that the statistical properties of the D^{EC} factor predicted with the Gaussian distribution of the cross sections differ from those obtained with the Poisson distribution. Since for poor statistic data the Poisson distribution is adequate, one has to treat with caution the results (4.16) and (4.17) obtained with the Gaussian distributions.

The reference value of the D^{EC} factor for ranking of models is equal to zero, i.e. it differs from the expectation value and the most likely value what is evident from the figure 4.5.

The properties of the D^{CE} factor can be judged by analogy with the R^{CE} properties. Each term in definition (4.15) of D^{CE} is equal to the modulus of the corresponding term in definition (4.10) of the R^{CE} factor shifted to smaller values by unity. Since the expectation value of each term in definition of R^{CE} is slightly larger than unity (see appendix C) the expectation value of corresponding term in definition of D^{CE} should be slightly larger than zero. Unfortunately exact value may be found only numerically for each individual situation. This prohibits to find analytically the exact values of the expectation value and the variance for modulus of each term and therefore for total sum which defines the D^{CE} factor.

It seems that for the practical estimation of the probability distribution function of this factor the numerical, Monte Carlo simulations should be used. The generated histograms of D^{CE} factor (for the perfect agreement of the data and model cross sections) as well as the Gaussian functions with the parameters derived from the histograms are shown in fig. 4.6 below. The shape of the distributions differs from the Gaussian function, especially for poor statistic data (the middle and lower panel of the right column of panels in the figure). Furthermore, it is evident that the expectation value and the standard deviation of the D^{CE} factor for data measured with poor statistic significantly differ from those obtained for good statistic data.

The reference value of the D^{CE} - factor for the ranking of models is equal to zero, similarly as for the D^{EC} - factor.

The D^{EC} and D^{CE} factors are not symmetrical in respect to exchange the experimental and calculated cross sections similarly as it is the case for the R^{EC} and R^{CE} factors. This leads to the same conclusions, i.e., the D^{EC} and D^{CE} factors may erroneously suggest a good agreement of the theoretical and experimental cross section when the part of data is overestimated and another part is underestimated by model cross sections.

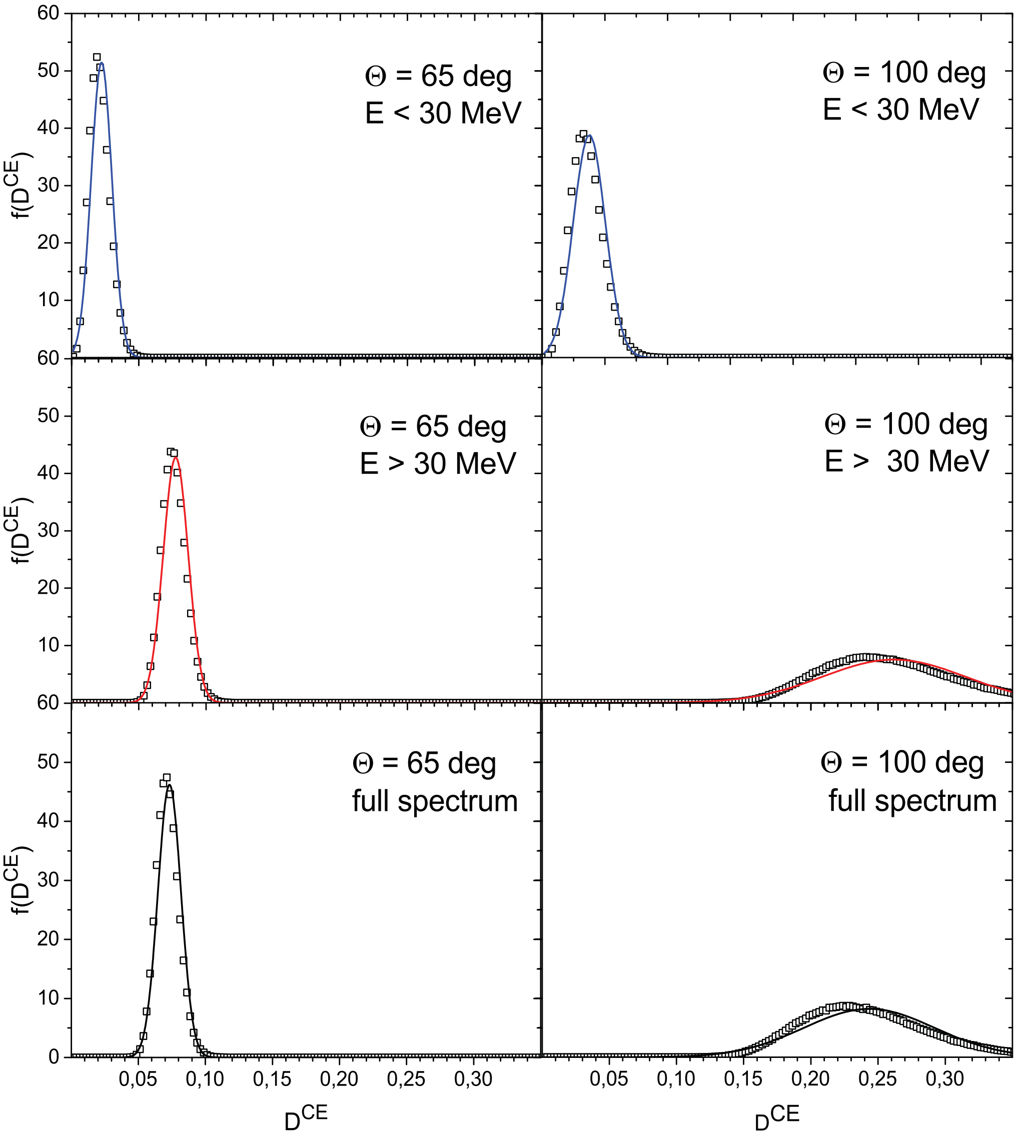

Figure 4.6: Open symbols represent the probability density distributions of the D^{CE} deviation factor calculated by Monte Carlo method whereas the lines represent Gauss functions with expectation values $E(D^{CE})$ and variances $\mathrm{var}(D^{CE})$ taken from histograms generated by Monte Carlo method. The calculations have been done for the data presented in fig. 4.1.

4.1.4 F_M deviation factor

The F_M test is defined by the formula [122]:

$$\boxed{F_M \equiv 10^{\frac{1}{N}\sum_{i=1}^{N}\log\left(\frac{\sigma_i^{\exp}}{\sigma_i^{cal}}\right)} \qquad (4.18)}$$

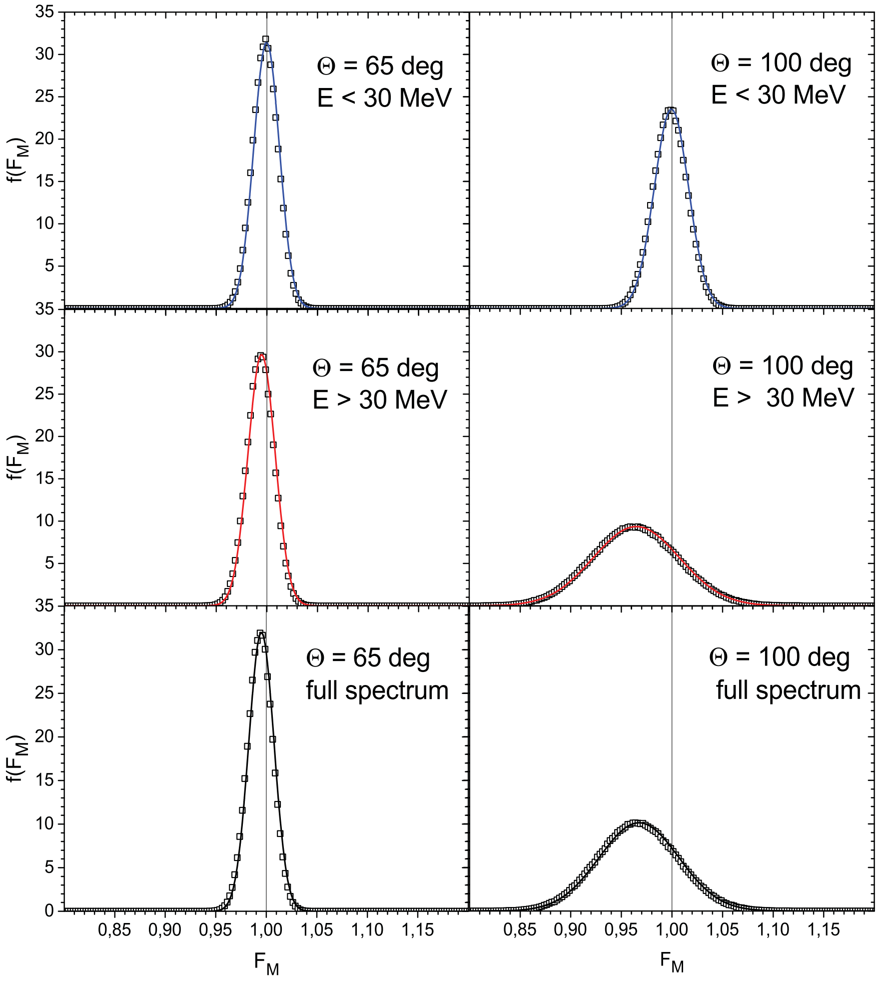

Figure 4.7: Open symbols represent the probability density functions of the F_M deviation factor calculated by Monte Carlo method whereas the lines represent Gauss functions with expectation values $E(F_M)$ and variances $\mathrm{var}(F_M)$ taken from histograms generated by Monte Carlo method. Vertical line present in all panels shows position of $F_M = 1$. The calculations have been done for the data presented in fig. 4.1.

It was not possible to derive the analytical formula for the probability distribution function of the F_M test. Thus the judgment on this subject was done by applying the Monte Carlo method. The histograms for this test were generated in the analogous way as those for previous deviation factors with the one exception: since the logarithm of zero argument cannot be used, only positive cross sections obtained with the Poisson distribution were put in the histograms for poor statistic data.

The histograms are compared in fig. 4.7 with Gaussian functions calculated using the expectation value $E(F_M)$ and variance $\mathrm{var}(F_M)$ determined from the histograms. It turns out that then:

- the histograms are perfectly reproduced, i.e., the Gaussian shape is obtained for all types of data - those with good and bad statistics. This is due to the central limit theorem.
- The centroid of the distribution for good statistic data is close to unity but it shifts significantly to smaller values and the histograms become broader for the bad statistic data.

The reference value for ranking the models by using the F_M - factor is equal to unity as for R^{EC} and R^{CE} factors.

4.1.5 $< F >$ deviation factor

The $< F >$ test is defined by the formula [122]:

$$\boxed{< F >\equiv 10^{\sqrt{\frac{1}{N}\sum\limits_{i=1}^{N}\left\{\log\left(\frac{\sigma_i^{\exp}}{\sigma_i^{cal}}\right)\right\}^2}} \qquad (4.19)}$$

The histograms of $< F >$ deviation factor were generated in the same manner as those for the F_M factor. They are presented in fig. 4.8. As can be seen:

- they all have Gaussian shape, which is due to the central limit theorem and
- they become significantly broader for poor statistic data than for those with good statistic (cf. the middle - right and the lower - right panel with others). As opposite to the F_M factor they are centered around values slightly larger than one and the centroid of the distribution shifts to larger values for poorer statistic of the data.

The reference value of the $< F >$ - factor is equal to unity.

The important positive property of the $< F >$ factor is its symmetry in respect of exchange of experimental and theoretical cross sections. It assures that both, the overestimation and the underestimation of data by models gives the same - positive contribution to the $< F >$ - factor.

The negative feature of the $< F >$ factor is that its behavior is not intuitive because of the use of several non-linear functions in its definition.

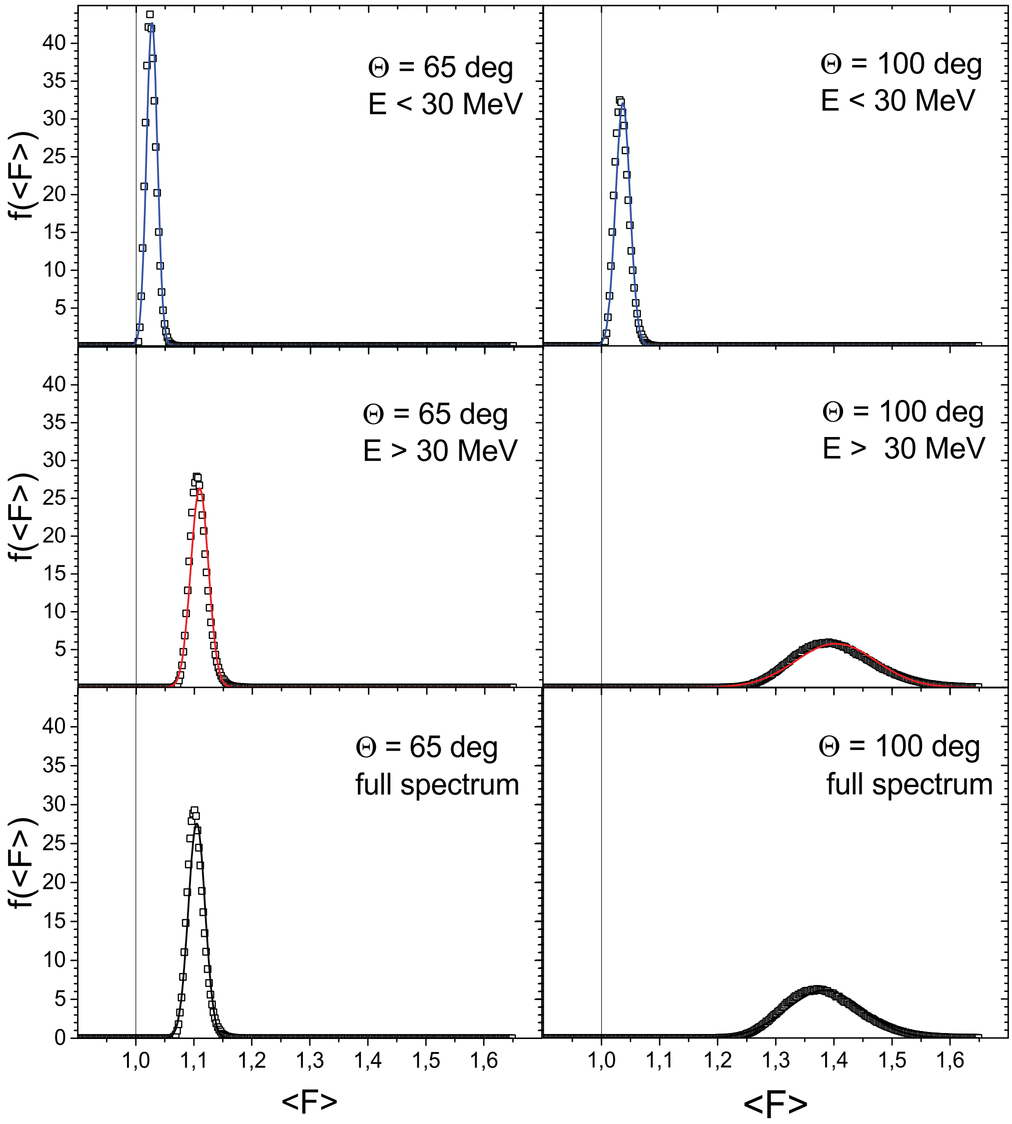

Figure 4.8: Open symbols represent the probability density functions of the $< F >$ deviation factor calculated by Monte Carlo method whereas the lines represent Gauss functions with expectation values $E(< F >)$ and variances $\text{var}(< F >)$ taken from histograms generated by Monte Carlo method. Vertical line present in all panels shows position of $< F >= 1$. The calculations have been done for the data presented in fig. 4.1.

The general properties of the deviation factors are listed in the table 4.1. The following features of the factors were taken into consideration:

- Knowledge of the analytical formulae for the shape of their probability density functions and for the expectation value and variance,

- Sensitivity of the shape and parameters of the probability density function to the poor statistic of data.

The above properties are very important for testing the statistical hypothesis of good agreement of model predictions with data on a given significance level. They can also influence the ranking of various theoretical models in respect to the ability to reproduce well the experimental data.

Table 4.1: Summary of the properties of the deviation factors proposed in literature for ranking and validation of the spallation models. The positive properties of given deviation factor are indicated by the bold text. The knowledge of the shape of the probability density function (p.d.f.) of the deviation factor, knowledge of the formula for its expectation value (the mean value) and variance are among these attractive features. Furthermore, the insensitivity of the above quantities to poor statistic of the experimental data. In the last column the number of positive properties of each deviation factor is given.

Deviation factor	Known analytic formulae for:			Sensitivity to poor statistic of data			Positive features
	p.d.f.	mean	variance	p.d.f.	mean	variance	
H	**yes**	**yes**	**yes**	**no**	**no**	**no**	**6**
R^{EC}	**yes**	**yes**	**yes**	**no**	**no**	yes	**5**
R^{CE}	**yes**	no	**yes**	yes	yes	yes	2
D^{EC}	**yes**	**yes**	**yes**	yes	yes	yes	3
D^{CE}	**yes**	no	no	yes	yes	yes	1
F_M	**yes**	no	no	**no**	yes	yes	2
$< F >$	**yes**	no	no	**no**	yes	yes	2

It is evident that *the H and R^{EC} deviation factors are generally superior to others.* This is because exact formulae are available for probability density function of these deviation factors as well as for their expectation value and variance in the case of the perfect agreement between the model and experimental cross sections. Furthermore, for the H-factor these properties are practically independent of the quality of data. Good statistic and poor statistic data may be treated on the equal footing. Other deviation factors are sensitive to the quality of data, i.e. their expectation value (for all factors except the R^{EC} -factor) and variance (for all factors) change significantly when the relative statistical errors become large.

Only two factors among the considered here have the desirable property to be symmetrical *in respect to exchange of the experimental and model cross sections:* the H - and $< F >$ - factors. This assures that simultaneous overestimation of a part of the data and underestimation of another part of the data by model cross sections does not cancel their contributions, thus the erroneous conclusion on a good agreement cannot be taken.

The H-factor is distinguished among all other factors because only in its definition (4.4) the individual cross sections are weighted taking explicitly into account the experimental errors of the data. Other factors treat as equivalent the data with small and large errors.

Such a unique property of the H-factor together with its robustness to change of the good statistic data to the poor ones is very appealing because the studied cross sections cover usually large range of values which leads to large range of relative uncertainties; from fraction of per cent to tens of per cent. It is obvious that the data biased by large uncertainties should enter the ranking and validation of models with smaller weights and it is highly desirable that their presence does not modify probability distribution of the deviation factor. Both these requirements are fulfilled by the H-factor. ***Thus the present review of the statistical properties of the deviation factors used in literature selects the H-factor as superior to other factors.***

4.2 New deviation factors

The search for new deviation factors should take into consideration following important problems which usually are neglected in the literature:

- Most of the modern theoretical models calculate the cross sections performing event-by-event Monte Carlo imitation of the reaction process which leads to the fact that *the model cross sections are the random variables with non-negligible statistical uncertainty.* Therefore the uncertainty of the model cross sections should be treated on the same footing as the uncertainty of the experimental cross sections.
- The data used as benchmarks for validation and ranking of models cover large range of values. Since the cross sections are proportional to number n_i of registered events their relative uncertainties are proportional to the reciprocal of the square root from number of events:

  $$\Delta(\sigma_i^{exp})/\sigma_i^{exp} \sim 1/\sqrt{n_i}.$$

  Application of deviation factors in which the experimental cross sections are weighted by their uncertainties (like the H-factor) leads to the dominating role of the large cross sections. To be sure that not only the largest experimental values are well reproduced by the model it *is desirable to use also the deviation factors which are not weighted by the errors.*
- The proposed *deviation factor should be symmetrical in respect to the exchange of experimental and theoretical cross sections* to avoid apparent proximity of the factor to its reference value when the overestimation of some data by the model exists together with underestimation of another part of the data.

4.2.1 M - deviation factor

It is interesting and challenging to look for the deviation factor which would have the same advantages as the H-factor but would have the following additional positive properties:

- The expectation value independent of the number of the data.

- The formula for variance simpler than that of the H-factor.

Here it is proposed to use such a new deviation factor - called M-factor ("M" as "modulus") which is the function of the experimental and calculated cross sections:

$$\boxed{\begin{aligned} M &\equiv \frac{1}{N}\sum_{i=1}^{N}\left|\frac{\sigma_i^{\exp}-\sigma_i^{cal}}{\Delta\sigma_i^{\exp}}\right| && (4.20)\\ M &\equiv \frac{1}{N}\sum_{i=1}^{N}\left|\frac{\sigma_i^{\exp}-\sigma_i^{cal}}{\Delta\left(\sigma_i^{\exp}-\sigma_i^{cal}\right)}\right| && (4.21)\end{aligned}}$$

The first of the above equations corresponds to the situation when the calculated cross section is evaluated analytically, i.e., it is not a random variable. The second one (4.21) is the generalization of the equation (4.20) for the case when the theoretical cross section is evaluated by Monte Carlo method, thus it is also a random variable. *Such a character of the theoretical cross sections was not taken into consideration in definitions of the literature deviation factors. In this thesis it is proposed to use this extension whenever it is necessary with the error of the difference* $\sigma_i^{\exp}-\sigma_i^{cal}$ *equal to*

$$\Delta(\sigma_i^{exp}-\sigma_i^{cal}) = \sqrt{(\Delta\sigma_i^{exp})^2+(\Delta\sigma_i^{cal})^2}. \tag{4.22}$$

It is worth to point out that the same generalization may be used in definition of the H*-deviation factor and it is made in the present study .*

Argument M_i of the modulus of each term in the sums (4.20) and (4.21) has the standardized distribution in the case of the perfect agreement of the model and the data cross sections. Assuming the Gaussian character of this distribution it may be shown (see Appendix B) that the probability density function of each term $|M_i|$ in the sums (4.20) and (4.21) is equal to

$$f(|M_i|) = \sqrt{\frac{2}{\pi}}\exp\left(\frac{|M_i|^2}{2}\right) \tag{4.23}$$

with the expectation value $E(|M_i|)$ and variance $var(|M_i|)$ equal to

$$\begin{aligned} E\left(|M_i|\right) &= \sqrt{\frac{2}{\pi}} && (4.24)\\ var\left(|M_i|\right) &= \frac{\pi-2}{\pi} && (4.25)\end{aligned}$$

Since M deviation factor is defined as a sum of independent $|M_i|$ random variables the central limit theorem states that it has a Gaussian probability density function even for different (e.g. Poisson) distributions of individual terms in the sum [2]. The factor $1/N$ assures that expectation value of the M random variable is equal to the expectation value of each term in the sum

$$\boxed{E(M) = \sqrt{\frac{2}{\pi}} \qquad (4.26)}$$

and its variance is equal to

$$\boxed{var(M) = \frac{\pi - 2}{N\pi} \qquad (4.27)}$$

Thus the standardized M-factor should have the asymptotic (for large N) *standard normal probability distribution.*

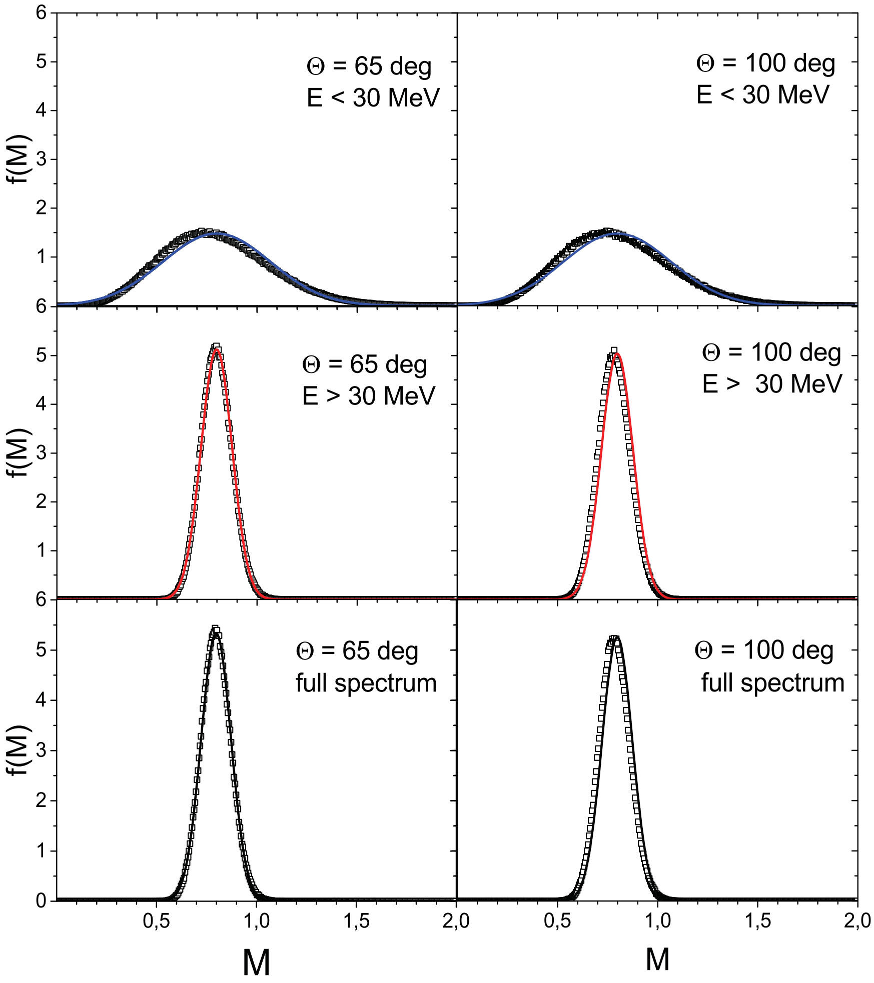

Figure 4.9: Open symbols represent the probability density functions of the M deviation factor calculated by Monte Carlo method whereas the lines represent Gauss function with expectation value and variance given by formulae (4.26) and (4.27). The calculations have been done for the data presented in fig. 4.1.

The histograms of the M-factor values generated by Monte Carlo method for the perfect agreement of model cross sections with the experimental data are presented in fig. 4.9 for the experimental data shown in fig. 4.1. The Gauss functions evaluated with parameters given by equations (4.26) and (4.27) are depicted in the same figure reproducing quite well the histograms.

The M-factor expectation value and the standard deviation depend (in the case of the perfect agreement of the model and experimental cross sections, i.e. , for $E(\sigma_i^{exp}) = \sigma_i^{cal}$) only on the number N of data taken into analysis. This is the same specific property which was found for the H-factor. It is interesting to compare these parameters for both deviation factors. Such a comparison is presented in fig. 4.10.

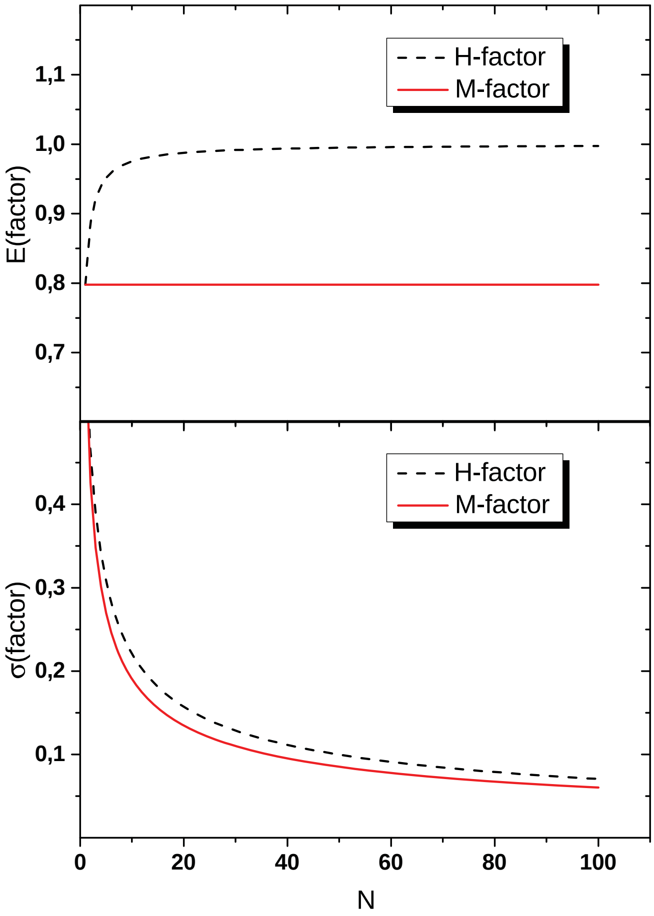

Figure 4.10: Expectation values and standard deviations of the H-factor and M factor are presented in the upper and lower panels of the figure, respectively as functions of number of data used in the analysis.

It can be seen that for small N values (up to around N=20) the expectation value of the H-factor increases quickly from value about 0.8 to value close to unity. The expectation value of the M-factor remains identical for all N-values - equal to $\sqrt{2/\pi} \approx 0.8$. On the other hand the standard deviations of both factors decrease proportionally to

1/N. The standard deviation of the H-factor is systematically larger (about 10 %) than the standard deviation of the M-factor. This indicates that both deviation factors are approximately equivalent when using for validation of the theoretical models. The main difference appears for small samples of the data when the expectation value of the H-factor varies strongly with the dimension of the sample, making values of H-factor less intuitive.

In the case of validity of the hypothesis of the perfect agreement of the model and experimental cross sections (1.1) the observed values of the deviation factors should not be different from their expectation values more than several standard deviations. Since distributions of both deviation factors are identical (or close) to the Gaussian distribution thus it seems reasonable to put three standard deviations as the critical deviation . This would correspond to the significance level of the test smaller than 1% (for exact normal distribution it would be equal to 0.27% [2]).

It should be pointed out that the absolute minimum of both, H and M deviation factors (the reference value for the ranking) is equal to zero. It corresponds to the situation when all experimental cross sections are equal to calculated ones. Thus values of these factors smaller than their expectation value does not contradict the statistical hypothesis (1.1). *The critical values of the deviation factors are only those which are larger than their expectation value by several standard deviations.*

It is thus natural to use for validation the standardized values of the deviation factors for which the expectation value is equal to zero and standard deviation is equal to unity. Then the values of the standardized H-factor or M-factor larger than +3 would contradict the null hypothesis (1.1).

4.2.2 A - deviation factor

As it was stated in the introduction to the present chapter, it is desirable to have possibility to use in the ranking the deviation factor which is independent of the magnitude of the cross sections. This means that such a factor is rather sensitive to the shape of given set of the data (angular distribution, excitation function or energy spectrum) than to absolute value of the data. It is also requested that the deviation factor should be symmetrical in respect to exchange of the experimental and theoretical cross sections.

It is proposed to use the following deviation factor:

$$\boxed{A = \frac{1}{N}\sum_{i=1}^{N}\frac{\left|\sigma_i^{\exp} - \sigma_i^{cal}\right|}{\sigma_i^{\exp} + \sigma_i^{cal}} \qquad (4.28)}$$

It is easy to check that the A - factor has all requested properties:

- It is independent of the magnitude of the cross sections, thus independent of the statistical uncertainties of the data and/or the calculations. Instead of comparing the distance between σ_i^{exp} and σ_i^{cal} to the uncertainty of the cross sections it compares this distance to sum of the cross sections. Thus its values belong to the interval [0,1].

- It is symmetrical in respect to exchange of the experimental and theoretical cross sections.
- Its reference value (absolute minimum obtained in the case when all data are equal to corresponding theoretical values) is equal to zero.
- It has an intuitive interpretation which can be found from inspection of fig. 4.11 where dependence of one term of the sum in the definition of the A-factor is presented as the function of the ratio $\sigma_i^{cal}/\sigma_i^{exp}$ of the calculated to the experimental cross sections.

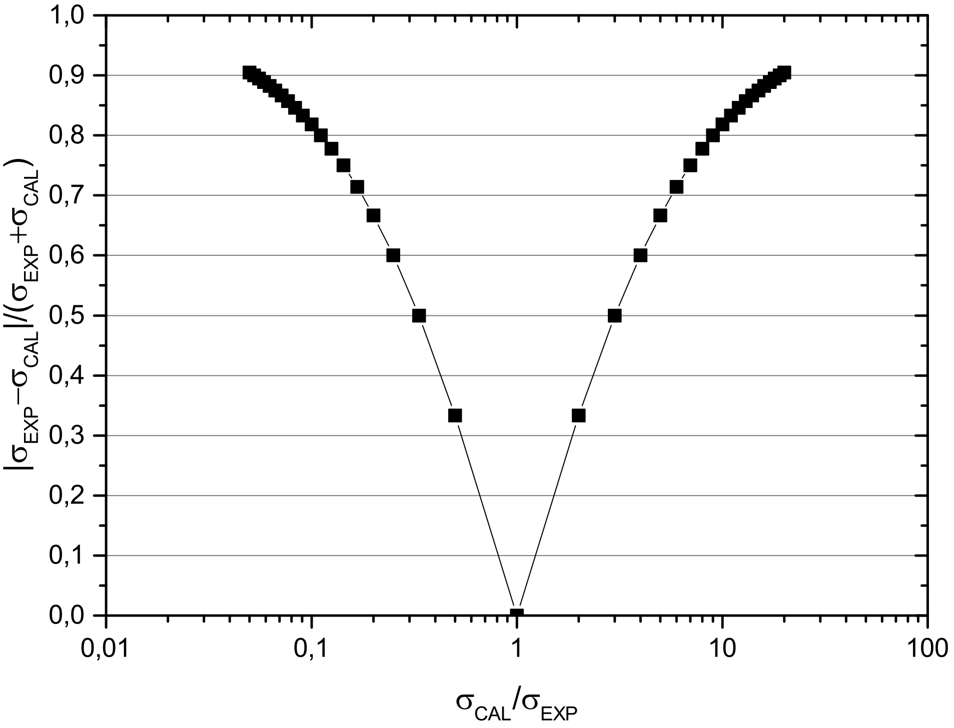

Figure 4.11: Dependence of the A - factor on the ratio of the calculated cross sections to the experimental cross sections $\sigma_i^{cal}/\sigma_i^{exp}$.

As can be seen the dependence of the A-factor on the ratio $\sigma_i^{cal}/\sigma_i^{exp}$ is symmetrical around unit value of this ratio and it is worth remembering that if this ratio is equal to 2 then the A-factor is equal to 1/3, when the ratio is equal to 3 then the A-factor is equal to 0.5, etc. Due to the symmetry the same values of the A-factor appear for the $\sigma_i^{cal}/\sigma_i^{exp}$ equal to 1/2 and 1/3 as those for ratios of the cross sections equal to 2 and 3, respectively. This means that a good agreement of the model cross sections with the data corresponds to values of the A-factor significantly smaller than 1/3.

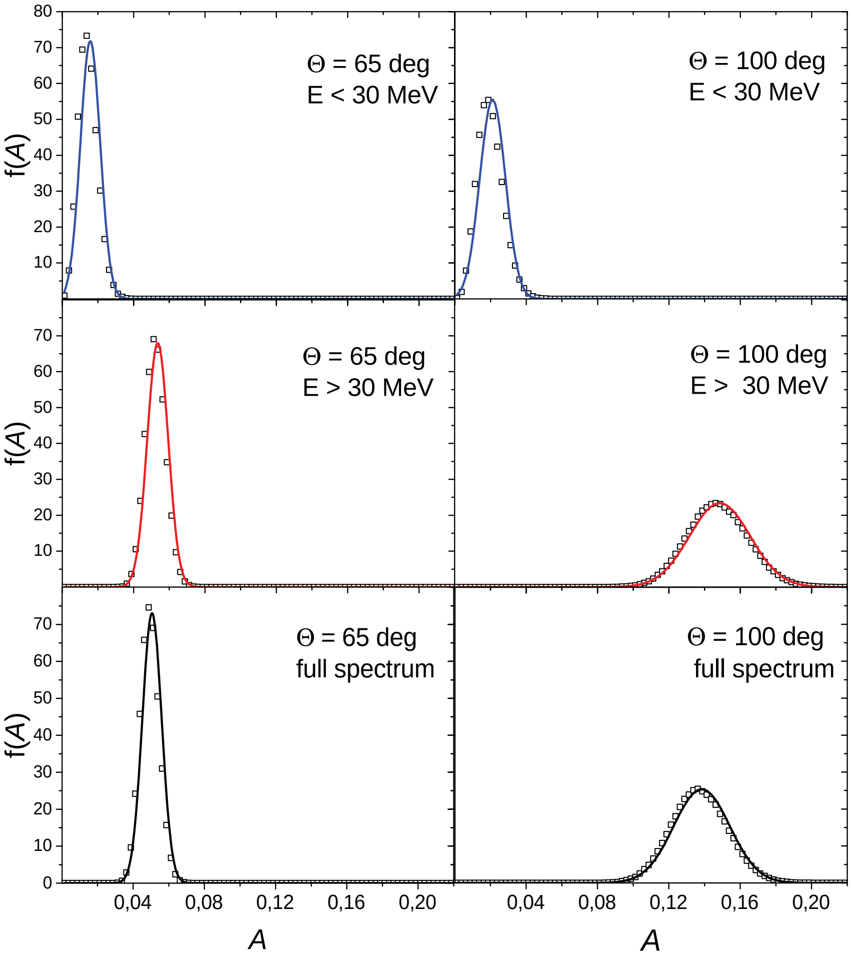

Figure 4.12: Open symbols represent the probability density functions of the A deviation factor calculated by Monte Carlo method whereas the lines represent Gauss function with expectation value and variance estimated from the histograms. The calculations have been done for the data presented in fig. 4.1.

The analytic form of the probability density distribution of the A-factor is not known. The Monte Carlo simulation of values of the A-factor for the case of the perfect agreement of the model and the experimental cross sections presented on fig. 4.12 shows that this distribution can be well reproduced by the Gauss function. The parameters of the Gauss function must be found from histograms. In the simulation it was assumed that the statistical uncertainties of the experimental and calculated cross sections are the same.

Chapter 5

Validation and ranking of spallation models over the wide range of experimental data

5.1 Inclusive observables

In the present section a set of inclusive observables is compared with the predictions of theoretical models which were selected (cf. chapter 2) as the most reliable models. The total isobaric cross sections $\sigma(A)$ measured for p+Al collisions at proton beam energy 180 MeV are discussed in section 5.1.1. The distributions of isotopic cross sections $\sigma(A|Z)$ for emission of sixteen different elements (Z= 41 - 56) from p+Xe collisions at E_p = 500 MeV are analyzed in the section 5.1.2. In the next section the analysis of the forward-backward F/B asymmetry of emission of intermediate mass fragments and heavy residua from p+Au collisions at two energies: 1 and 3 GeV is presented.

5.1.1 Isobaric cross sections $\sigma(A)$ in p+Al reactions at T$_p = 180$ MeV

It was shown in the previous section that the new deviation factor - the M-factor has very similar properties to those of the H-factor when the perfect agreement of the model cross sections with the data is assumed. Thus they both can be used for validation of the models which consists in testing the statistical hypothesis (1.1):

$$E(\sigma^{exp}) = \sigma^{cal}.$$

However, it is important to check whether the both factors lead to the same conclusions also in the case of typical situation when significant deviations of the model cross sections from the data may be expected.

In the present section the M-factor is used for the validation of spallation models when they are applied to description of the isobaric cross sections $\sigma(A)$ measured at proton beam energy equal to 180 MeV on the Al target.

Validation of these models using the H-factor has been recently published by author of this thesis and collaborators [124]. Thus it gives a chance for straightforward comparison of conclusions derived using the M-factor and the H-factor. The atomic mass dependence of the experimental isobaric cross sections measured for p+Al reactions at Tp=180 MeV [88] is shown in figs. 5.1 and 5.2 together with predictions of eight different spallation models [124].

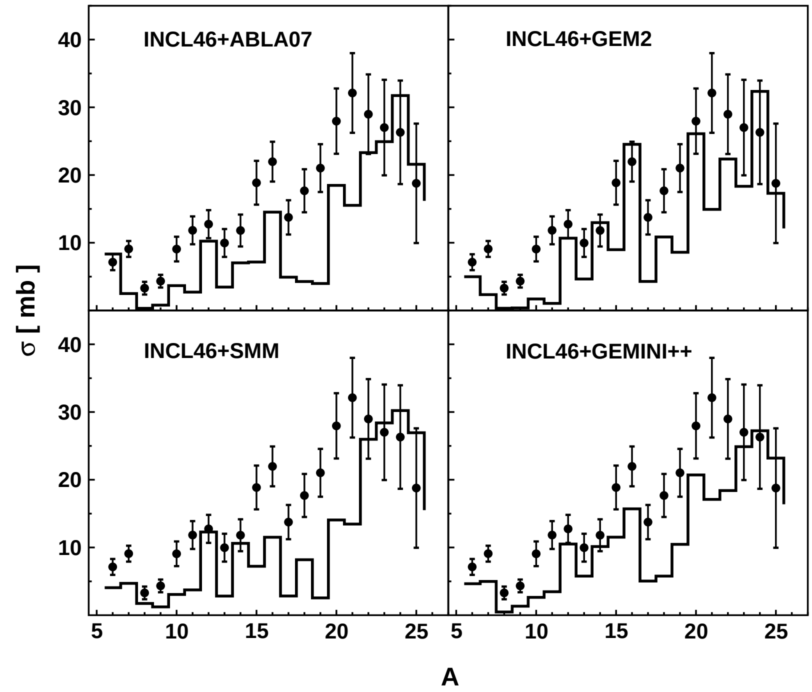

Figure 5.1: Points represent experimental isobaric cross sections σ(A) measured by Kwiatkowski et al. [88], histograms show results of calculations in the frame of four different spallation models. The first stage of the reaction was described by the INCL4.6 model whereas the second stage was evaluated by ABLA07 (left-upper pannel of the figure), SMM (left-lower pannel), GEMINI++(right-lower panel), and by GEM2 (right-upper panel of the figure).

The standardized values of the H-test and of the M-test, i.e. (H-E(H))/σ(H) and (M-E(M))/σ(M), calculated for all these eight models with E(H), E(M), $\sigma(H)$, and $\sigma(M)$ are evaluated for the perfect agreement (1.1) see in table 5.1.

As can be seen the standardized values of H-factor and M-factor are similar. They differ in most cases less than 10% with exception of the SMFSI model for which the H-factor is larger than the M-factor about 13%. Since all values listed in the table are $\sim$ 10 standard deviations larger than the expectation value thus both factors give the same message: *none of the applied models describes perfectly the data.* Thus both deviation factors lead to the same validation of the models.

Table 5.1: The H and M standardized deviation factors and A- factor (non-standardized) calculated for description of isobaric cross sections σ(A) by eight different models. In the first column the name of the model is shown, in the second value of the H-factor, in the third value of the M-factor, in the fourth the A- factor. In the next columns ranks of these models are listed which are determined on the basis of H-test, M-test and A- factor. The tied ranks are listed for close values of the deviation factors.

Model	H	M	A	r(H)	r(M)	r(A)	tied r(H)	tied r(M)	tied r(A)
GEMINI++	9.5	10.6	0.294	1	2	2	1.5	1.5	1.5
GEM2	11.8	12.0	0.345	3	3	4	4	4	4
ABLA07	12.8	13.8	0.367	5	5	6	4	4	6
SMM	12.1	12.9	0.337	4	4	3	4	4	4
SMFSI	21.9	19.1	0.350	8	8	5	8	8	4
CEM	14.5	15.6	0.420	6	7	7-8	6.5	6.5	7.5
BIC	15.4	15.4	0.420	7	6	7-8	6.5	6.5	7.5
PHITS	9.7	9.7	0.292	2	1	1	1.5	1.5	1.5

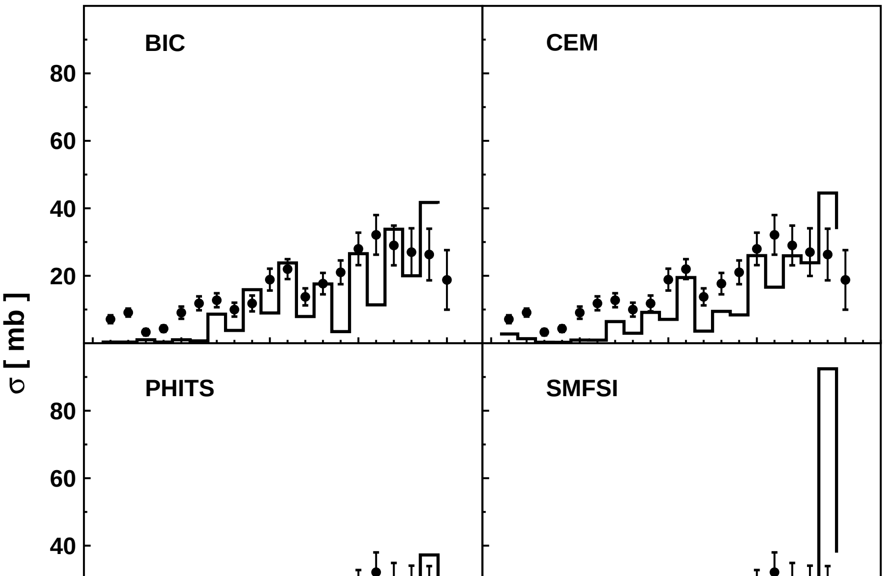

Figure 5.2: Full dots depict the same data as in fig.5.1, histograms present the theoretical values of the cross sections evaluated in the frame of four models BIC, PHITS, SMFSI, and CEM as indicated in different panels of the figure.

The question arises whether both deviation factors, H- and M-factor lead to the same ranking of models. The ranks of individual models which were determined according to value of the H-factor and the M-factor are depicted in the fifth and sixth columns, respectively. The GEMINI++ and PHITS have according to the H-factor the ranks 1 and 2, respectively whereas according to the M-factor the ranks are exchanged, i.e. the rank for GEMINI++ is equal to 2 and that for PHITS is equal to 1. The analogous situation takes place for CEM and BIC models which have ranks 6 and 7 according to H-factor but 7 and 6 according to M-factor. However, its worth emphasizing that the values of the factors for these models differ less than one standard deviation of the factors. Thus, *if one allows for using the tied ranks, i.e. identical ranks for consecutive values which differ less than one standard deviation* then the rankings according to the H-factor and M-factor values become identical (cf. columns 7 and 8 of the table).

The ranking based on values of the A-factor slightly differs from that performed on the basis of H-factor and M-factor values. However, the best two models obtained the same tied ranks as those for H- and M- factors.

5.1.2 Distributions of isotopic cross sections $\sigma(A|Z)$ for heavy residua from p+Xe collisions at T$_p$ = 500 MeV

In this section the analysis of heavy residua from p+Xe collisions at proton beam energy equal to 500 MeV is discussed. These data, published in ref. [89], have been selected because they were measured at proton beam energy higher than that discussed in the previous section and the target has also the larger mass number than aluminium. Furthermore, the present data are more exclusive than those discussed in the previous section because they consist of isotopic distributions $\sigma(A|Z)$ for 16 elements with the atomic number Z ranging from Z=41 to Z=56. It may be thus expected that the analysis of the present data puts more stringent constraints to all theoretical models than the investigation of isobaric cross sections only.

The four pairs of reactions models, i.e. INCL4.6 model for the first stage of the reaction and four models: ABLA07, GEM2, GEMINI++, and SMM for the second stage of the process have been used. Distributions of isotopic cross sections $\sigma(A|Z)$ evaluated with these models for all 16 elements are presented on fig. 5.3 together with the experimental cross sections.

As can be seen all the models produce very similar distributions of the isotopic cross sections, which quite well reproduce the shape of the experimental distributions. The position of maxima of theoretical distributions as well as their width agree well with those for the experimental distributions. However, there are some systematic deviations:

- The data for the elements with atomic Z number in the range from Z=41 (Nb) up to Z=45 (Rh) are underestimated by all models.
- The cross sections for the heaviest isotopes of the elements with atomic Z number in the range from Z=46 (Pd) up to Z=52 (Te) are overestimated by all models.

- The same effect but even more pronounced is visible for the element with the largest atomic number Z=56 (Ba).

Thus the best qualitative agreement is achieved for three elements in the neighborhood of the target nucleus: Z=53 (I), Z=54 (Xe) and Z=55 (Cs).

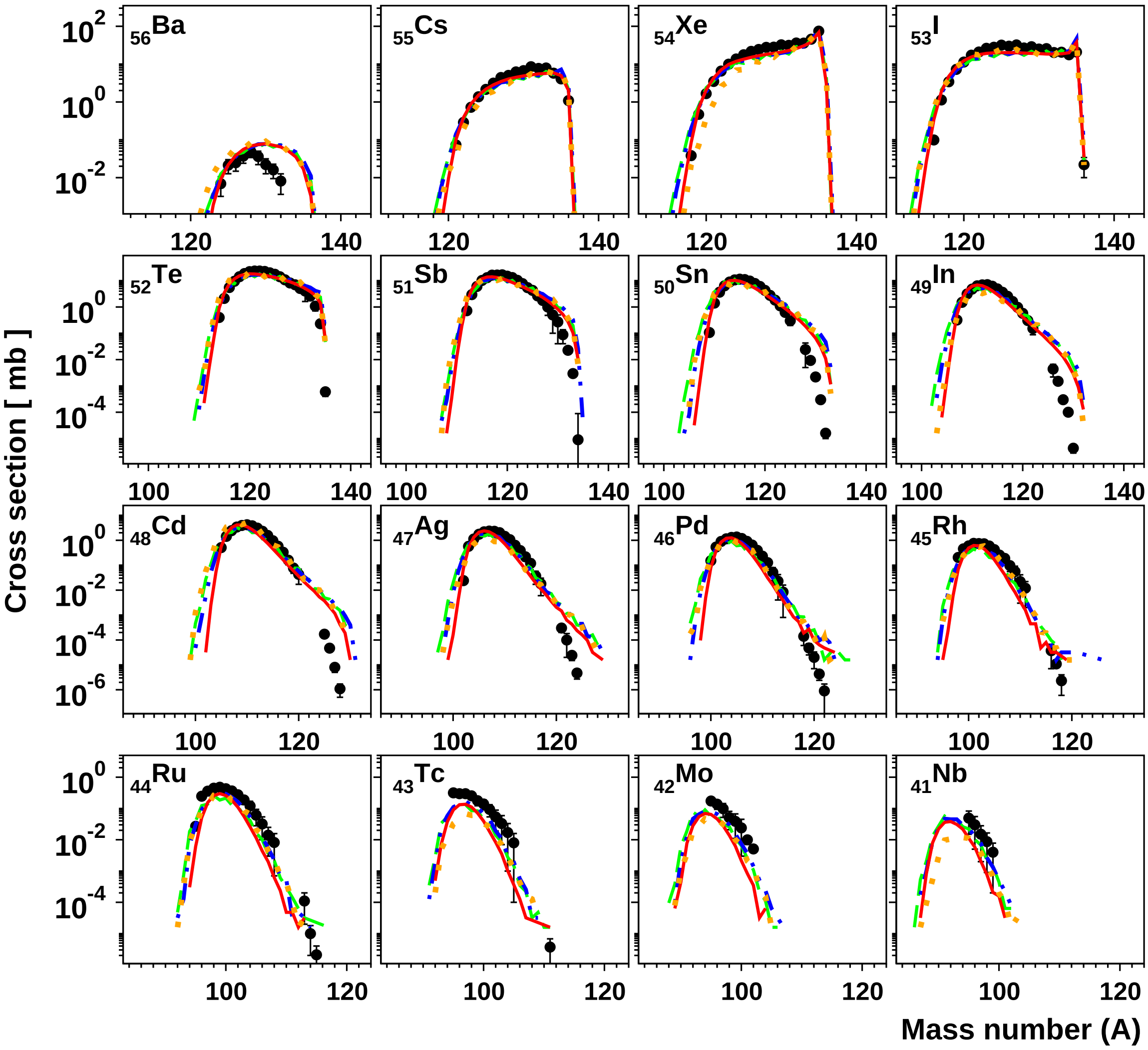

Figure 5.3: The isotopic cross sections from p+^{136}Xe collisions at T$_{p}$=500 MeV [89] (points) together with predictions of the INCL4.6 model for the first stage of the reaction coupled to four models; ABLA07 (green dashed line), GEM2 (orange dots), GEMINI++(blue dash-dotted line) and SMM (red solid line) used for the second step of the reaction.

The H-, M-, and A- deviation factors were considered in the present analysis to achieve the ranking and validation of theoretical models. Their values are collected in table 5.2 and are used to establish the ranking for applied models. These ranks are listed in table 5.3.

Table 5.2: The standardized H- and M-factor as well as non-standardized A-factor values for isotopic distributions of residua from p+Xe collisions at proton beam energy 500 MeV [89]. The INCL4.6 intranuclear cascade model was coupled to four different models of the second stage of the reaction: ABLA07, GEM2, GEMINI++, and SMM. The values of deviation factors smaller than three - written as a bold text - correspond to theoretical cross sections which are so close to the data that the perfect agreement may be assumed.

Ejectile	Non-standardized A				Standardized H				Standardized M			
	ABLA	GEM2	GEMINI	SMM	ABLA	GEM2	GEMINI	SMM	ABLA	GEM2	GEMINI	SMM
$_{41}$Nb	0.46	0.65	0.43	0.76	**-0.66**	**-0.02**	**-0.81**	**0.22**	**-0.20**	**0.53**	**-0.36**	**0.82**
$_{42}$Mo	0.52	0.55	0.41	0.67	9.14	8.76	7.63	11.5	7.46	7.60	5.94	9.29
$_{43}$Tc	0.53	0.66	0.42	0.61	6.07	9.15	4.64	6.06	6.33	9.09	4.86	6.61
$_{44}$Ru	0.47	0.36	0.33	0.53	9.05	7.79	6.23	10.4	9.80	7.30	6.04	10.9
$_{45}$Rh	0.44	0.30	0.32	0.44	8.52	4.84	3.91	7.25	9.70	4.89	4.90	7.82
$_{46}$Pd	0.41	0.36	0.35	0.40	12.1	7.39	7.52	7.21	12.7	8.34	8.13	7.78
$_{47}$Ag	0.37	0.47	0.35	0.39	96.6	33.3	78.2	23.3	42.0	29.2	34.9	18.5
$_{48}$Cd	0.34	0.32	0.31	0.35	36.7	43.9	39.6	26.4	28.5	32.8	27.5	21.5
$_{49}$In	0.36	0.40	0.35	0.34	100	91.8	106	67.7	68.0	63.3	70.5	47.6
$_{50}$Sn	0.38	0.40	0.36	0.33	225	201	232	126	141	131	145	80.7
$_{51}$Sb	0.32	0.34	0.32	0.30	210	204	286	158	97.3	99.3	127	76.9
$_{52}$Te	0.25	0.26	0.24	0.21	87.0	84.6	139	82.3	47.0	50.3	61.8	37.7
$_{53}$I	0.19	0.14	0.19	0.17	63.5	70.9	47.7	30.6	32.6	30.1	27.8	21.5
$_{54}$Xe	0.19	0.32	0.17	0.14	44.2	30.9	29.1	14.9	28.2	28.9	21.0	14.3
$_{55}$Cs	0.17	0.20	0.17	0.13	14.5	14.2	18.0	9.36	14.5	15.4	15.0	9.08
$_{56}$Ba	0.34	0.45	0.34	0.34	20.8	23.7	21.1	19.4	15.2	21.6	15.6	15.0

However, inspection of the table 5.2 indicates that the quantitative agreement is not satisfactory because both, standardized H- and M-factors are significantly larger than the upper limit (three) which can be expected for the perfect agreement. Such values are only achieved for $_{41}$Nb.

Table 5.3: Ranks of various model predictions for isotopic distributions of residua from p+Xe collisions at 500 MeV [89] according to values of non-standardized A-deviation factor as well as of standardized M- and H- deviation factors taking into account both, experimental and Monte Carlo uncertainties.

	Non-standardized A				Standardized H				Standardized M			
Ejectile	ABLA	GEM2	GEMINI	SMM	ABLA	GEM2	GEMINI	SMM	ABLA	GEM2	GEMINI	SMM
$_{41}$Nb	2	3	1	4	**2.5**	**2.5**	**2.5**	**2.5**	**2.5**	**2.5**	**2.5**	**2.5**
$_{42}$Mo	2	3	1	4	2	3	1	4	3.5	2	1	3.5
$_{43}$Tc	2	4	1	3	2	4	1	3	2.5	4	1	2.5
$_{44}$Ru	3	2	1	4	3	2	1	4	3	2	1	4
$_{45}$Rh	3.5	1	2	3.5	4	1	2	3	4	1.5	1.5	3
$_{46}$Pd	3.5	2	1	3.5	4	3	2	1	4	2	2	2
$_{47}$Ag	1.5	4	1.5	3	4	2	3	1	4	2	3	1
$_{48}$Cd	3.5	2	1	3.5	3	4	2	1	3	4	2	1
$_{49}$In	3	4	1.5	1.5	3	2	4	1	4	3	2	1
$_{50}$Sn	3.5	3.5	2	1	3	2	4	1	4	3	2	1
$_{51}$Sb	2	4	2	2	2	3	4	1	4	3	2	1
$_{52}$Te	3	3	3	1	2	3	4	1	4	3	2	1
$_{53}$I	3.5	1	3.5	2	4	3	2	1	3	4	2	1
$_{54}$Xe	3	4	2	1	3	4	2	1	4	3	2	1
$_{55}$Cs	2.5	4	2.5	1	2	4	3	1	3	3	3	1
$_{56}$Ba	2	4	2	2	2	4	3	1	3	4	1.5	1.5
Sum of ranks:	43.5	48.5	28	40	45.5	46.5	40.5	27.5	55.5	46	30.5	28
Average rank:	3	4	1	2	3.5	3.5	2	1	4	3	2	1

The ranks of agreement offered by different models are collected in table 5.3 where the ranks corresponding to the perfect agreement between theory and experiment are written using bold type.

The following summary of the ranking may be formulated:

- According to both deviation factors (H- and M- factor) the best agreement is offered by the SMM model (rank 1).
- The second position (rank 2) is granted by both these deviation factors to GEMINI++. The ranking based on the H-factor indicates large difference between SMM model and GEMINI++ whereas the ranking based on the M-factor shows only small difference between both models.

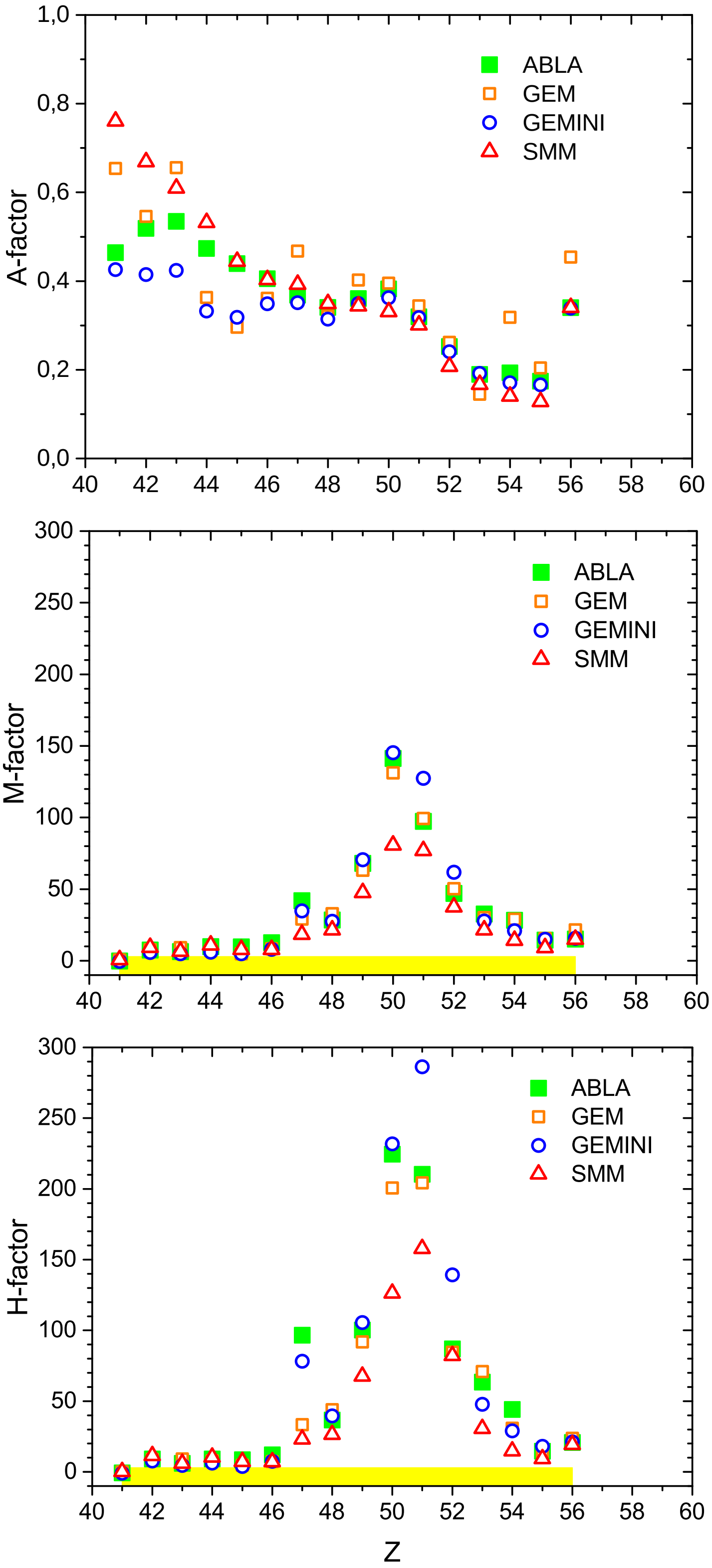

Figure 5.4: A-factor (upper panel), standardized M-factor (middle panel) and standardized H-factor (lower panel) as function of Z of residua from p+Xe reaction at E_p=500 MeV. Full squares (green) represent ABLA07, open squares (orange) - GEM2, circles (blue) - GEMINI++, and triangles (red) - SMM. The yellow bar in the figures for H-factor and M-factor represent values corresponding to perfect agreement of model and data values.

- The difference appears for GEM2 and ABLA07 models which obtained ranks 3 and 4 due to the M-factor, respectively, whereas the H-factor treats both these models as equally good.
- The ranking based on the A-factor is quite different: (1) GEMINI++, (2) SMM, (3) ABLA07, and (4) GEM2.

This difference in ranking performed on the basis of H- and M-factors with respect to the ranking based on A-factor values must have some specific origin. To find it the dependence of the deviation factors on the atomic number Z of the investigated heavy residua was studied. This dependence is shown in fig. 5.4.

The inspection of the figure allows to conclude that the dependence of H-factor and M-factor on the Z number is very similar: it has a maximum in the neighborhood of Z=51 and decreases strongly towards larger and smaller values of Z. Appearing of small values of the H- and M-factors for Z in the neighborhood of the atomic number of the Xe target (Z=54) agrees with the qualitative estimation of the agreement between the data and theoretical cross sections discussed above. However strong decrease of both factors for smallest Z-values does not agree with the qualitative arguments. It seems that such small values of the factors are obtained due to strong increase of the uncertainties of the experimental cross sections as well as those evaluated by models using the Monte Carlo method. The contribution from significant deviations between the data and model cross sections are canceled due to small weights used in the evaluation of the H- and M-factors. Therefore these small values of H- and M-factor cannot be treated as a proof of the good description of the data by applied models.

The dependence of the A-factor on the atomic number is quite different from that of H- and M-factors. The A-factor has the smallest values in the neighborhood of atomic number Z=54 (the target atomic number) and increases almost monotonically with decreasing Z number. This agrees well with the qualitative observations that the theoretical distributions of the isotopic cross sections deviate from the experimental data for Z significantly smaller than Z of the target.

In summary, it may be concluded that:

- the H- and M-factors give the equivalent information on the agreement between the experimental and theoretical cross sections.
- The A-factor which is calculated without weighting the cross sections by their uncertainties offer quite different and important information.
- *The simultaneous application of both types of deviation factors,i.e., these which are calculated using the weights depending on statistical uncertainties (like M-factor) and those which are apparently independent of the uncertainties (like A-factor) may be useful to obtain proper conclusions on the agreement/disagreement of the data and model values.*

5.1.3 Angular asymmetry in F/B emission of recoil nuclides for p+Au reactions at $E_p = 1$ and 3 GeV

One of such observables which corresponds to the angular asymmetry present in the emission of reaction products was reported by Kaufman et al. [90], in the interaction of 1 - 300 GeV protons with a thick Au target(24mg/cm^2). A forward-to-backward ratio (F/B) for large number of nuclides was measured. In the present work, we used the data only for two proton beam energies; 1 GeV and 3 GeV due to the constrain on the applicability of the INCL4.6 model. It is observed that mass dependence of forward-to-backward (F/B) asymmetry of the emitted reaction products varies strongly for proton beam energies in this energy range (cf. Fig. 5.5).

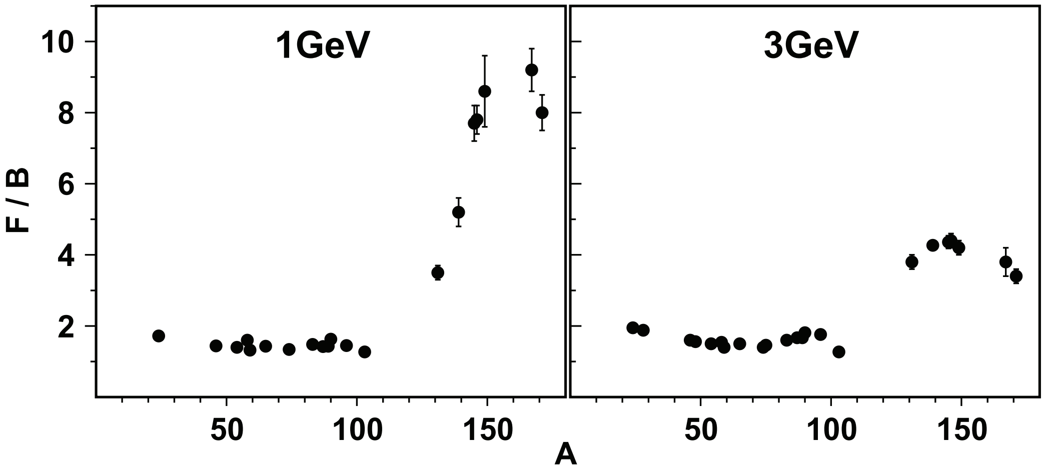

Figure 5.5: Mass and Energy dependence of F/B asymmetry [90].

The present investigation was done mainly for two goals. One, to check the ability of different models in reproducing the mass dependence of reaction products in terms of F/B asymmetry. Second, whether models are also witnessing the same effects as observed in experimental data with varying beam energy from 1 GeV to 3 GeV. Since the target used in the experiment was quite thick it was necessary to take into consideration a fact that the products may be stopped inside the target. To calculate the final predictions of the models for F/B ratio, the reaction products were filtered by performing the following steps:

1. SRIM (Stopping Range of Ions in Matter) was used to evaluate the energy loss and range of different ions in Au material.
2. Since incident proton of GeV energy looses a small amount of energy in passing through the full thickness of Au target, random sampling for the interaction point of proton with Au nucleus was done along its full path through the target.
3. With the information on the direction of emission and knowing the distance of the interacting point to the surface of the target it was possible to decide whether the

ion escapes from the target. The ions which range in the gold material larger than this distance are able to leave the target.

4. Only those ions which qualified to escape from the target were used to calculate the F/B ratio.

It becomes evident by judging the Fig. 5.6 and Fig. 5.7 that all four second stage models ABLA07, SMM, GEMINI++ and GEM2 combined with INCL4.6 are equally good in predicting the F/B ratio up to mass A ∼ 103. The maximal dis-agreement between the different model predictions and with the data is visible for target-like reaction products.

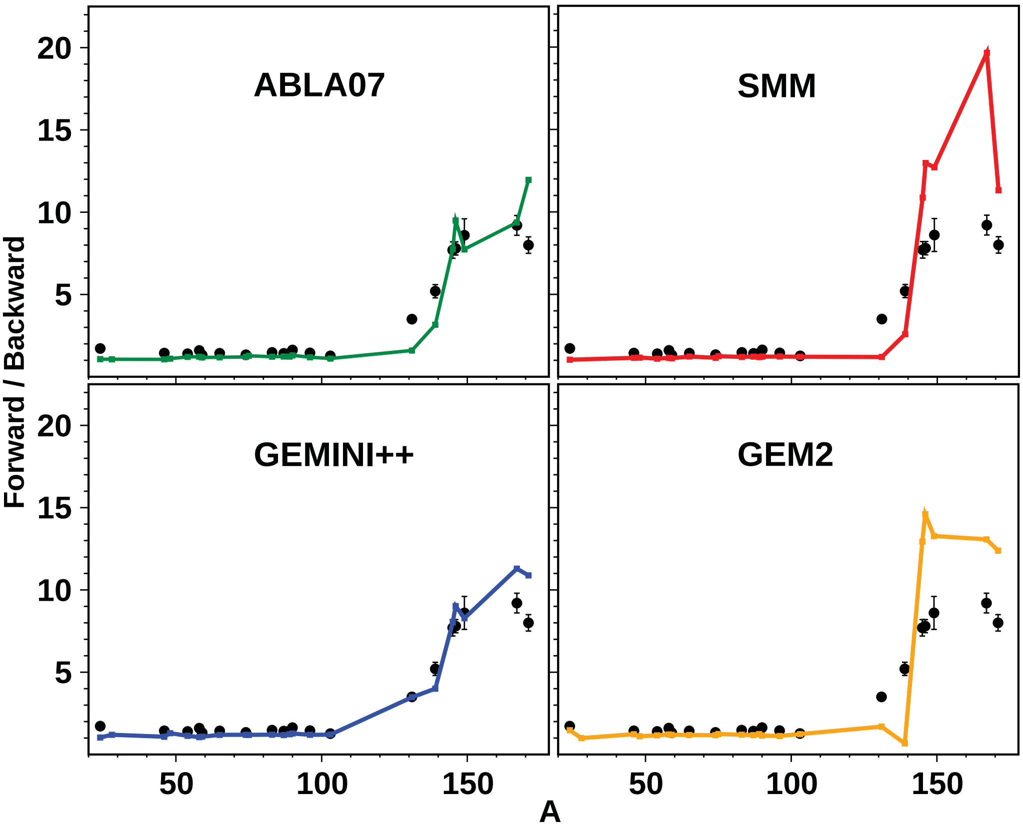

Figure 5.6: Comparison between the measurements (points) for the F/B ratio with four different theoretical models (lines): INCL4.6 coupled with ABLA07 (left upper panel), SMM (right upper panel), GEMINI++ (left lower panel), and GEM2 (right lower panel), at 1 GeV proton beam energy.

A qualitative comparison between model predictions and experimental data shows that the shape and magnitude of mass dependence of F/B asymmetry is best reproduced by GEMINI++ closely followed by ABLA07 for both beam energies. The predictions of SMM and GEM2 codes seem to be improved towards the higher beam energy with exception that GEM2 overestimates magnitude of F/B for one specific nuclide with mass A = 139 at 3 GeV.

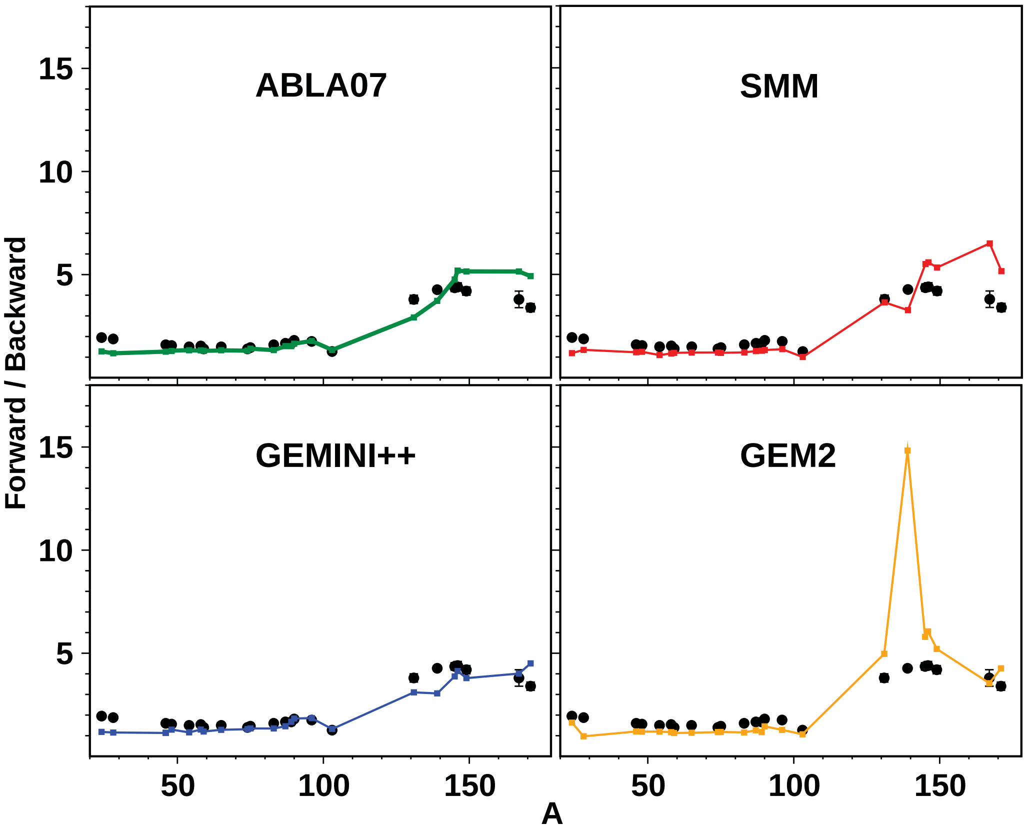

Figure 5.7: same as Fig. 5.6 but at 3 GeV proton beam energy.

In order to give the ranking to different models, the quantification of the comparison was done by using the following form of H-test (5.1), M-test (5.2), and A-test (5.3).

$$H \equiv \left[\frac{1}{N}\sum_{i=1}^{N}\left(\frac{(F/B)_i^{\mathrm{exp}} - (F/B)_i^{calc}}{\Delta(F/B)_i^{\mathrm{exp}}}\right)^2\right]^{1/2} \tag{5.1}$$

$$M \equiv \frac{1}{N}\sum_{i=1}^{N}\frac{\left|(F/B)_i^{\mathrm{exp}} - (F/B)_i^{cal}\right|}{\Delta(F/B)_i^{\mathrm{exp}}} \tag{5.2}$$

$$A \equiv \frac{1}{N}\sum_{i=1}^{N}\frac{\left|(F/B)_i^{\mathrm{exp}} - (F/B)_i^{cal}\right|}{(F/B)_i^{\mathrm{exp}} + (F/B)_i^{cal}} \tag{5.3}$$

Here $(F/B)_i^{\mathrm{exp}}$ symbol represents the experimental and $(F/B)_i^{cal}$ the theoretical F/B asymmetry for ith nuclide whereas $\Delta(F/B)_i^{\mathrm{exp}}$ is the error of experimental values. The following table 5.4 with H, M and A values provides the consistent ranking to different models.

Table 5.4: Ranking of models based on H, M and A test values averaged over two beam energies 1 GeV and 3 GeV. In the calculation of various factors for GEM2 the contribution for A=139 was not taken into consideration.

Model	H	M	A	r(H)	r(M)	r(A)	tied r(H)	tied r(M)	tied r(A)
ABLA07	4.74	3.99	0.099	1	2	2	1.5	1.5	1.5
GEMINI++	5.02	3.95	0.090	2	1	1	1.5	1.5	1.5
SMM	6.99	6.15	0.155	3	3	4	3.5	3.5	3.5
GEM2	7.18	6.16	0.154	4	4	3	3.5	3.5	3.5

5.2 Exclusive observables

5.2.1 Spectra and angular distributions of $d^2\sigma/d\Omega dE$ of IMF from p+Ag collisions at T$_p = 480$ MeV

In the present chapter the application of the A-, H- and M-factors to the ranking of several spallation models is presented when description of spectra of intermediate mass fragments is taken into consideration.

The data of p+Ag reaction, obtained by Green et al. [93] were selected for this analysis because they represent double differential cross sections $d^2\sigma/d\Omega dE$ measured for a large set of intermediate mass fragments at proton beam energy of 480 MeV where the spallation models are claimed to work well. Furthermore, this energy and mass of the target is close to 500 MeV at which the inclusive data from p+Xe collisions were investigated in the chapter 5.1.2.

The intermediate mass fragments are produced with much smaller cross sections than light charged particles therefore both, the data for heaviest products as well as corresponding theoretical cross sections evaluated by means of models which use Monte Carlo method are fluctuating. Thus the H- and M-factors were calculated according to formula (4.21) in which the statistical errors of the theoretical cross sections are also taken into account.

In next ten figures the experimental spectra of Li, Be, B, C, N, O, F, Ne, Na, and Mg isotopes measured by Green et al. [93] for p+Ag collisions at proton beam energy 480 MeV are presented together with predictions of four theoretical models, namely ABLA07, GEM2, GEMINI++, and SMM coupled to INCL4.6 model. Inspection of these figures allows for qualitative estimation of the agreement between the theoretical and experimental cross sections. Below each of these figures the table with standardized H and M factors as well as with non standardized A factor is placed to give possibility to compare the quantitative measure of the agreement offered by these factors with the qualitative judgement.

The following conclusions may be derived from these comparisons:

- Very large values of the standardized deviation factors correspond to poor agreement of the theoretical and experimental cross sections. This is especially obvious for Li, Be and B spectra where two effects give contribution to the disagreement of the experimental and theoretical spectra:

    1. The coalescence model which contributes for IMF with A$\leqslant$ 8 strongly <u>overestimates</u> the data, what is especially visible for ^{8}Li spectra.
    2. The high energy tails of spectra for Be and B isotopes with A$>$ 8, where the coalescence is not introduced are <u>underestimated</u> by the models.

  This means that some kind of a coalescence contribution is very important for light IMF (Li, Be, B and forward scattering angles of C data), however, the present realization of the model is not satisfactory.

- Values of the standardized deviation factors smaller than three appear only for experimental spectra which are very well reproduced by the models.

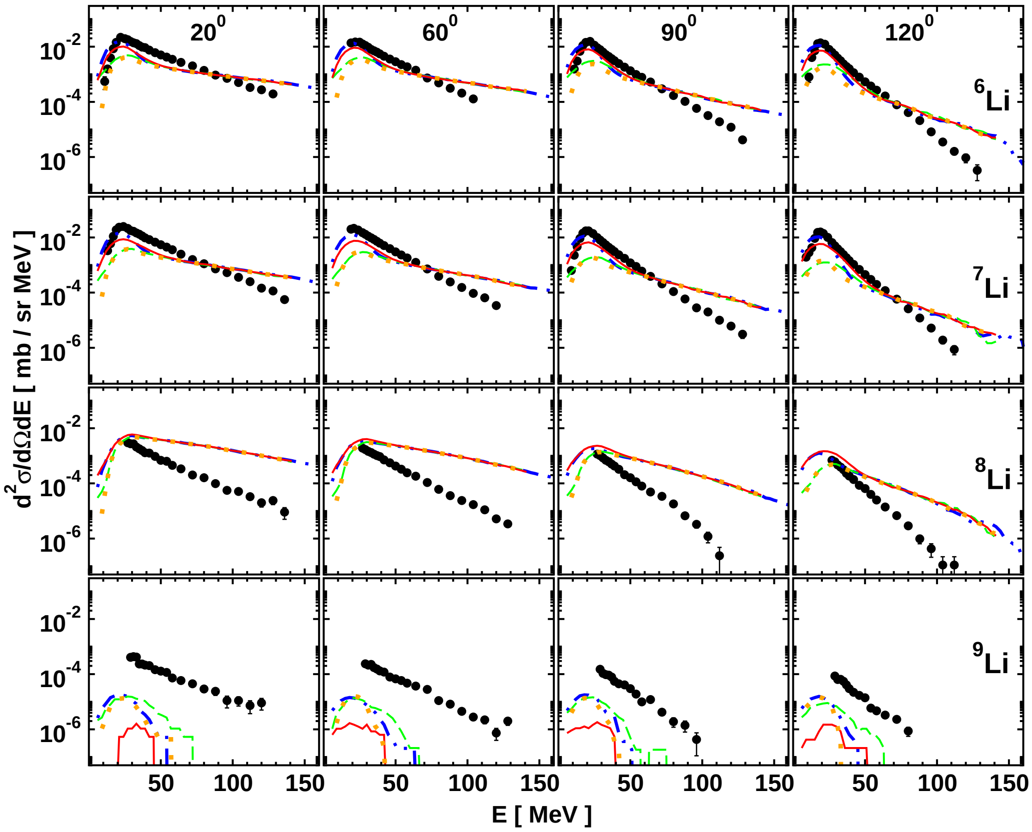

Figure 5.8: Spectra of Li isotopes from p+Ag collisions at proton beam energy 480 MeV [93]. The lines represent the following model calculations: green (dashed) - ABLA07, orange (dotted) - GEM2, dark blue (dash-dotted) - GEMINI++, and red (solid) - SMM.

Table 5.5: The standardized H- and M-factor values as well as non standardized A-factor values for spectra of Li isotopes from p+Ag collisions at proton beam energy 480 MeV [93]. The INCL4.6 intranuclear cascade model was coupled to four different models of the second stage of the reaction: ABLA07, GEM2, GEMINI++, and SMM.

Ejectile	Non-standardized *A*				Standardized H				Standardized M			
	ABLA	GEM2	GEMINI	SMM	ABLA	GEM2	GEMINI	SMM	ABLA	GEM2	GEMINI	SMM
^{6}Li	0.43	0.53	0.39	0.33	621	715	408	335	502	608	386	320
^{7}Li	0.54	0.59	0.42	0.37	834	849	467	463	680	716	437	402
^{8}Li	0.65	0.64	0.65	0.70	315	309	316	349	322	315	324	373
^{9}Li	0.87	-	0.95	0.97	87	59	85	68	91	63	95	75

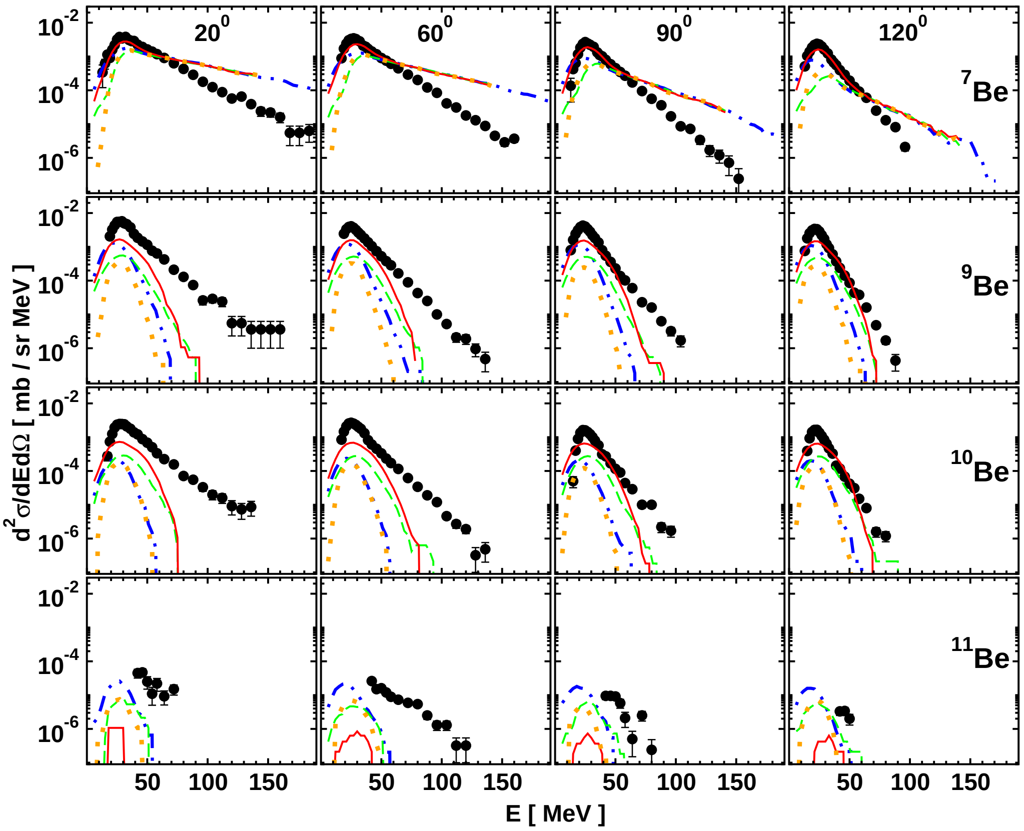

Figure 5.9: Spectra of Be isotopes from p+Ag collisions at proton beam energy 480 MeV [93]. The lines represent the same model calculations as for Li ejectiles (fig. 5.8).

Table 5.6: The standardized H- and M-factor values as well as non standardized A-factor values for spectra of Be isotopes from p+Ag collisions at proton beam energy 480 MeV [93]. The INCL4.6 intranuclear cascade model was coupled to four different models of the second stage of the reaction: ABLA07, GEM2, GEMINI++, and SMM.

	Non-standardized *A*				Standardized H				Standardized M			
Ejectile	ABLA	GEM2	GEMINI	SMM	ABLA	GEM2	GEMINI	SMM	ABLA	GEM2	GEMINI	SMM
^{7}Be	0.54	0.54	0.40	0.28	329	301	230	98	275	262	205	91
^{9}Be	0.71	0.90	0.67	0.42	408	485	356	219	409	524	381	224
^{10}Be	0.67	0.86	0.82	0.41	293	340	334	186	279	359	344	174
^{11}Be	0.56	-	0.75	-	9.2	11.7	14	-	9.1	11.7	15.2	-

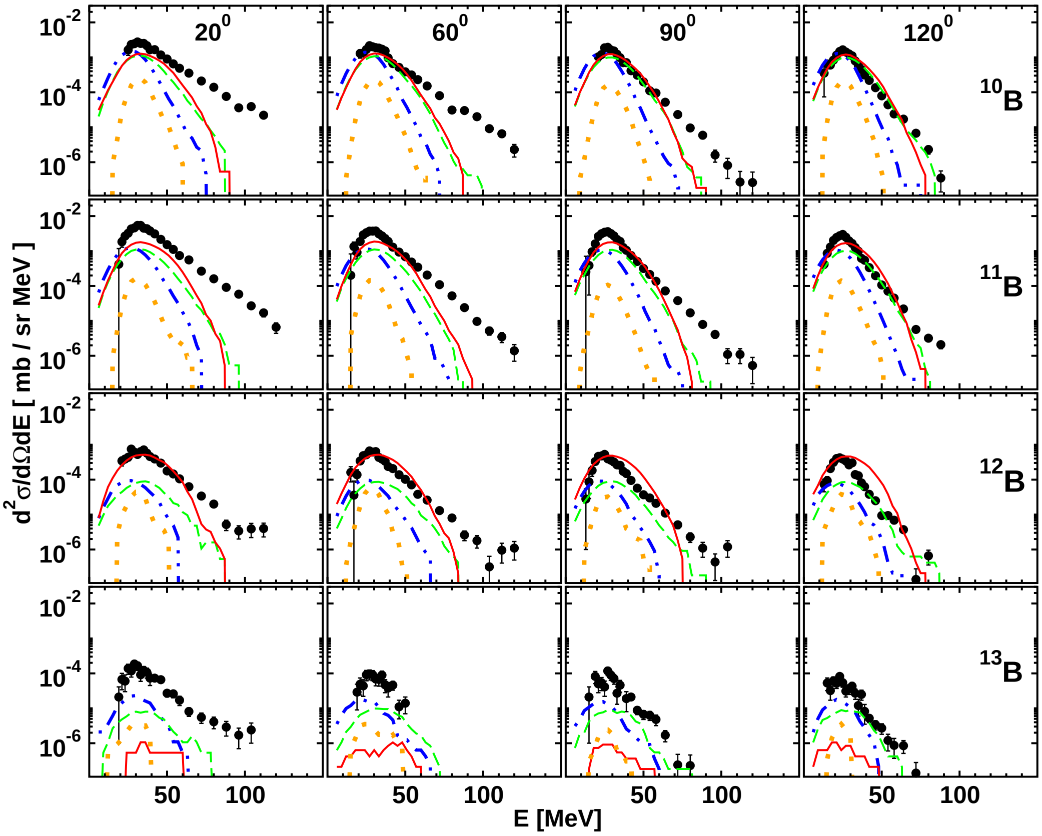

Figure 5.10: Spectra of B isotopes from p+Ag collisions at proton beam energy 480 MeV [93]. The lines represent the same model calculations as for Li ejectiles (fig. 5.8).

Table 5.7: The standardized H- and M-factor values as well as non standardized A-factor values for spectra of B isotopes from p+Ag collisions at proton beam energy 480 MeV [93]. The INCL4.6 intranuclear cascade model was coupled to four different models of the second stage of the reaction: ABLA07, GEM2, GEMINI++, and SMM.

	Non-standardized *A*				Standardized H				Standardized M			
Ejectile	ABLA	GEM2	GEMINI	SMM	ABLA	GEM2	GEMINI	SMM	ABLA	GEM2	GEMINI	SMM
^{8}B	0.94	0.94	0.94	0.94	201	203	203	202	219	220	221	219
^{10}B	0.31	0.88	0.49	0.25	66.5	137	114	56.7	60.8	147	108	49.5
^{11}B	0.46	0.96	0.60	0.29	145	215	208	96.5	143	224	203	91.1
^{12}B	0.57	0.90	0.68	0.26	64.2	72.1	70.9	49.2	64.7	79	73	40.3
^{13}B	0.64	0.90	0.61	0.86	17.1	14.9	17.1	21.4	18.7	18.2	18.6	23.9

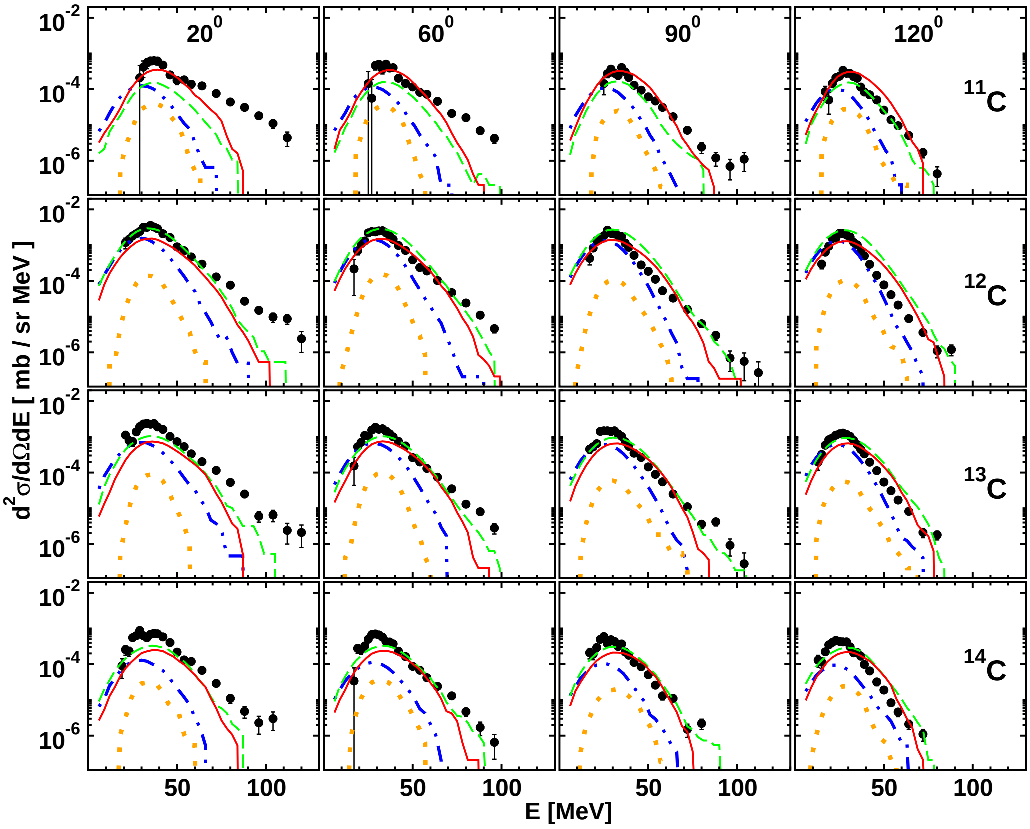

Figure 5.11: Spectra of C isotopes from p+Ag collisions at proton beam energy 480 MeV [93]. The lines represent the same model calculations as for Li ejectiles (fig. 5.8).

Table 5.8: The standardized H- and M-factor values as well as non standardized A-factor values for spectra of C isotopes from p+Ag collisions at proton beam energy 480 MeV [93]. The INCL4.6 intranuclear cascade model was coupled to four different models of the second stage of the reaction: ABLA07, GEM2, GEMINI++, and SMM.

Ejectile	Non-standardized *A*				Standardized H				Standardized M			
	ABLA	GEM2	GEMINI	SMM	ABLA	GEM2	GEMINI	SMM	ABLA	GEM2	GEMINI	SMM
^{11}C	0.38	0.86	0.64	0.24	29.5	44.4	45.5	23.9	28	49.5	47.2	20.4
^{12}C	0.27	0.92	0.41	0.26	95.7	143	89.4	54.1	83	159	89.9	53.2
^{13}C	0.23	0.93	0.46	0.33	42.6	121	117	54.8	40.3	137	98.2	57.6
^{14}C	0.24	0.91	0.65	0.35	20.9	64.8	56.2	30.1	21.7	75.4	62.6	32

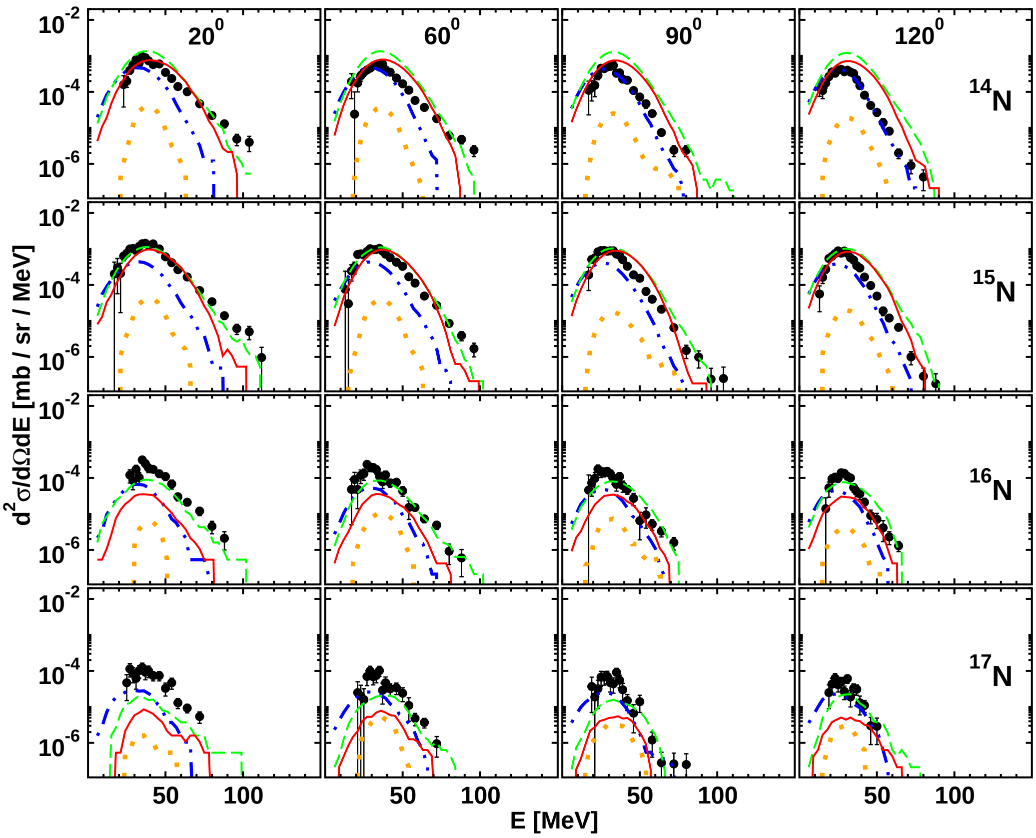

Figure 5.12: Spectra of N isotopes from p+Ag collisions at proton beam energy 480 MeV [93]. The lines represent the same model calculations as for Li ejectiles (fig. 5.8).

Table 5.9: The standardized H- and M-factor values as well as non standardized A-factor values for spectra of N isotopes from p+Ag collisions at proton beam energy 480 MeV [93]. The INCL4.6 intranuclear cascade model was coupled to four different models of the second stage of the reaction: ABLA07, GEM2, GEMINI++, and SMM.

Ejectile	Non-standardized *A*				Standardized H				Standardized M			
	ABLA	GEM2	GEMINI	SMM	ABLA	GEM2	GEMINI	SMM	ABLA	GEM2	GEMINI	SMM
^{14}N	0.47	0.91	0.26	0.30	122	57.1	25.7	66.4	116	66.8	22.2	54.9
^{15}N	0.24	0.95	0.45	0.27	52.3	86.4	57.8	46.5	39.5	100	60.3	38.6
^{16}N	0.26	0.87	0.48	0.54	6.75	22.7	15.8	17.4	7.1	27.2	18.0	19.7
^{17}N	0.45	0.87	0.42	0.74	6.5	12.3	6.0	11.9	7.7	15.6	7.1	14.7

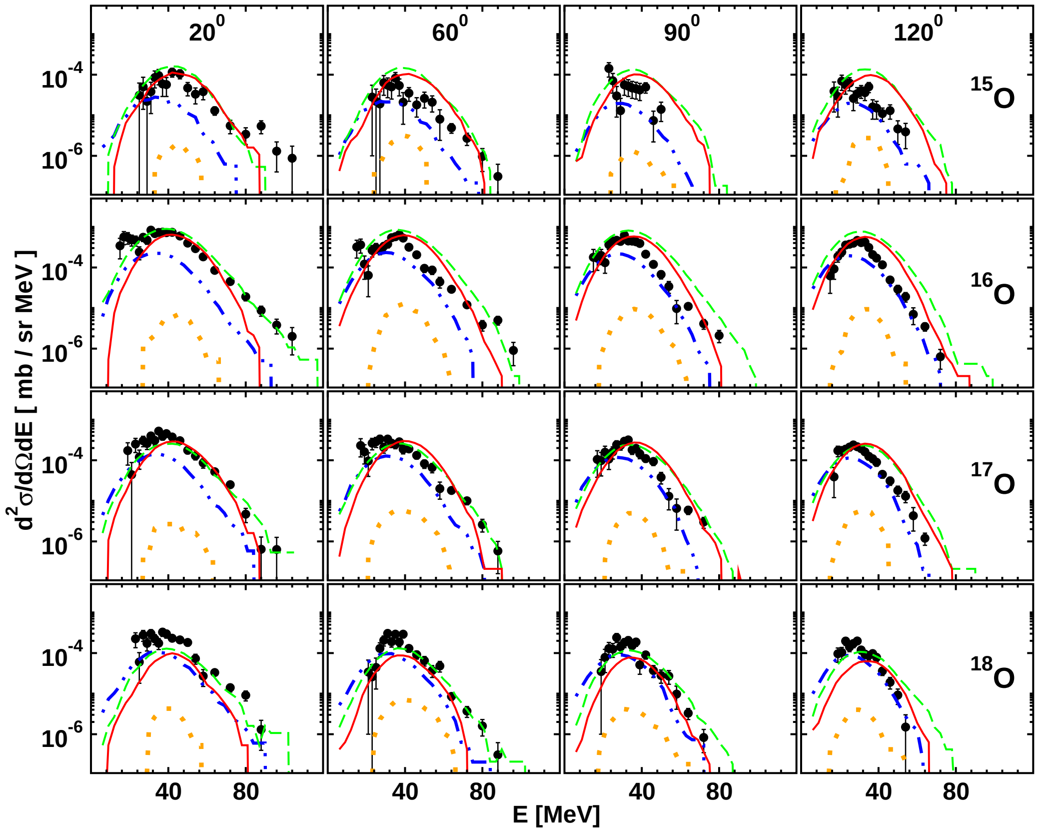

Figure 5.13: Spectra of O isotopes from p+Ag collisions at proton beam energy 480 MeV [93]. The lines represent the same model calculations as for Li ejectiles (fig. 5.8).

Table 5.10: The standardized H- and M-factor values as well as non standardized A-factor values for spectra of O isotopes from p+Ag collisions at proton beam energy 480 MeV [93]. The INCL4.6 intranuclear cascade model was coupled to four different models of the second stage of the reaction: ABLA07, GEM2, GEMINI++, and SMM.

Ejectile	Non-standardized *A*				Standardized H				Standardized M			
	ABLA	GEM2	GEMINI	SMM	ABLA	GEM2	GEMINI	SMM	ABLA	GEM2	GEMINI	SMM
^{15}O	0.43	0.85	0.44	0.37	34.5	10.4	6.2	24	31.9	13	7.0	20.3
^{16}O	0.37	0.96	0.41	0.30	69.8	54.3	33.1	43.2	63.2	63.7	33.4	32.8
^{17}O	0.25	0.95	0.39	0.31	16	35.1	19	23.8	13.5	41.9	20.7	20.9
^{18}O	0.25	0.93	0.38	0.41	7.4	28.4	14	13.7	7.5	34.1	15.7	15.6
^{19}O	0.38	-	0.53	0.38	6.1	10	9.4	6.6	6.3	11.3	10.5	6.2

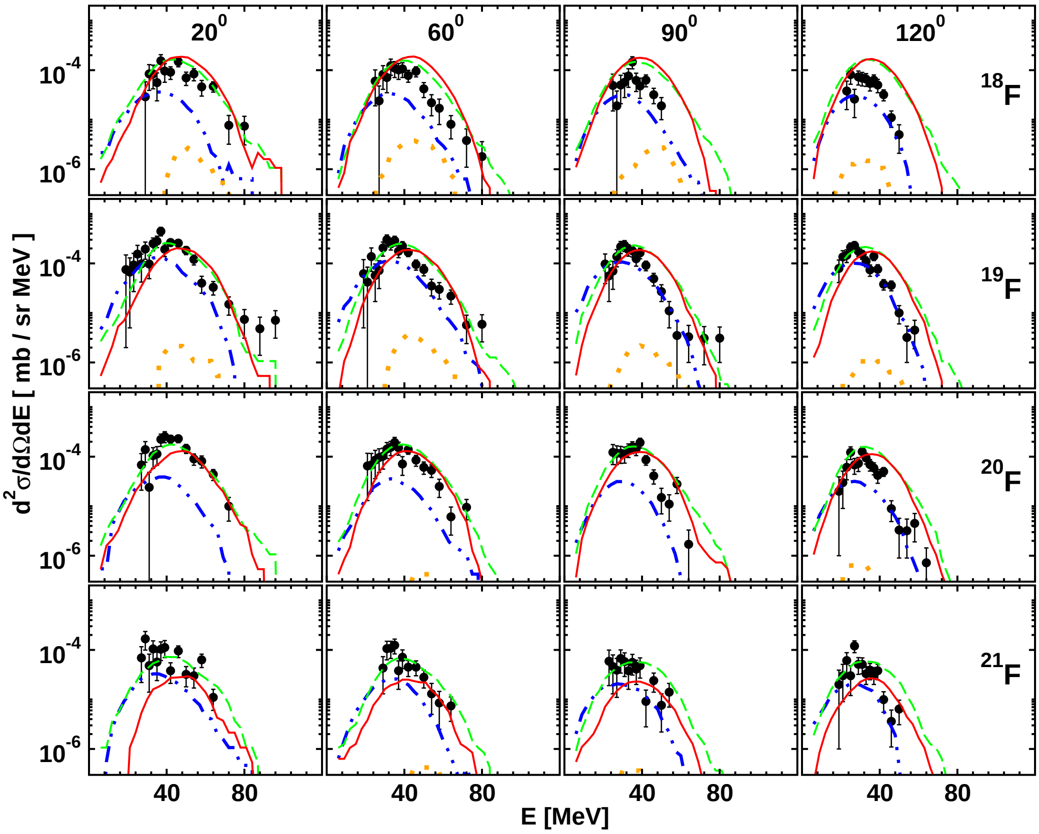

Figure 5.14: Spectra of F isotopes from p+Ag collisions at proton beam energy 480 MeV [93]. The lines represent the same model calculations as for Li ejectiles (fig. 5.8).

Table 5.11: The standardized H- and M-factor values as well as non standardized A-factor values for spectra of F isotopes from p+Ag collisions at proton beam energy 480 MeV [93]. The INCL4.6 intranuclear cascade model was coupled to four different models of the second stage of the reaction: ABLA07, GEM2, GEMINI++, and SMM.

	Non-standardized *A*				Standardized H				Standardized M			
Ejectile	ABLA	GEM2	GEMINI	SMM	ABLA	GEM2	GEMINI	SMM	ABLA	GEM2	GEMINI	SMM
^{18}F	0.34	0.91	0.44	0.38	24.9	22.4	16	19.6	8.9	9.9	32.2	28.8
^{19}F	0.29	0.93	0.27	0.37	21.4	16.6	25.2	29.5	8.4	8.3	22	19.3
^{20}F	0.26	-	0.57	0.32	17.4	12.9	-	-	16.1	17.7	15.2	11.9
^{21}F	0.26	-	0.45	0.42	8.3	5.9	-	-	5.3	6.6	4.44	5.2

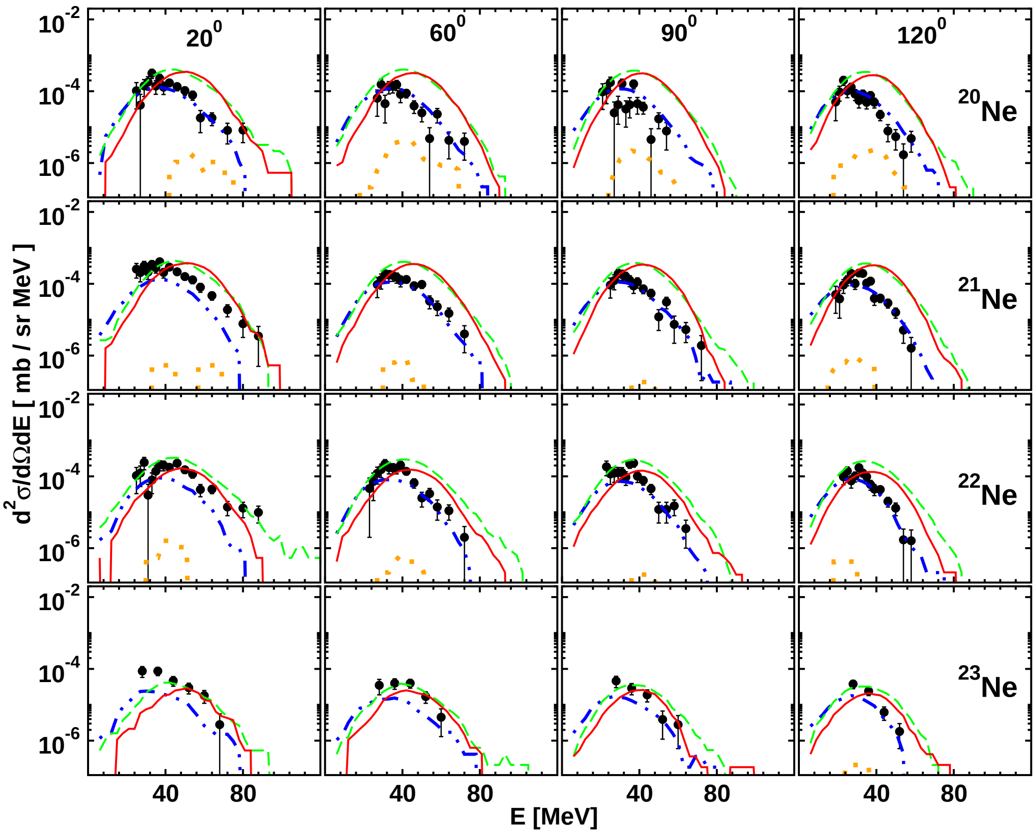

Figure 5.15: Spectra of Ne isotopes from p+Ag collisions at proton beam energy 480 MeV [93]. The lines represent the same model calculations as for Li ejectiles (fig. 5.8).

Table 5.12: The standardized H- and M-factor values as well as non standardized A-factor values for spectra of Ne isotopes from p+Ag collisions at proton beam energy 480 MeV [93]. The INCL4.6 intranuclear cascade model was coupled to four different models of the second stage of the reaction: ABLA07, GEM2, GEMINI++, and SMM.

	Non-standardized *A*				Standardized H				Standardized M			
Ejectile	ABLA	GEM2	GEMINI	SMM	ABLA	GEM2	GEMINI	SMM	ABLA	GEM2	GEMINI	SMM
^{20}Ne	0.56	0.87	0.24	0.53	82.6	13	6.5	76.8	77.3	15.7	5.3	65.2
^{21}Ne	0.48	0.97	0.24	0.44	61.9	18	5.0	65.7	58.9	21.1	4.6	53.9
^{22}Ne	0.42	-	0.31	0.37	46.8	11.6	6.5	23.8	42.4	14.1	6.8	19.4
^{23}Ne	0.27	-	0.38	0.34	3.8	-	4.4	3.6	**2.6**	-	4.9	3.7

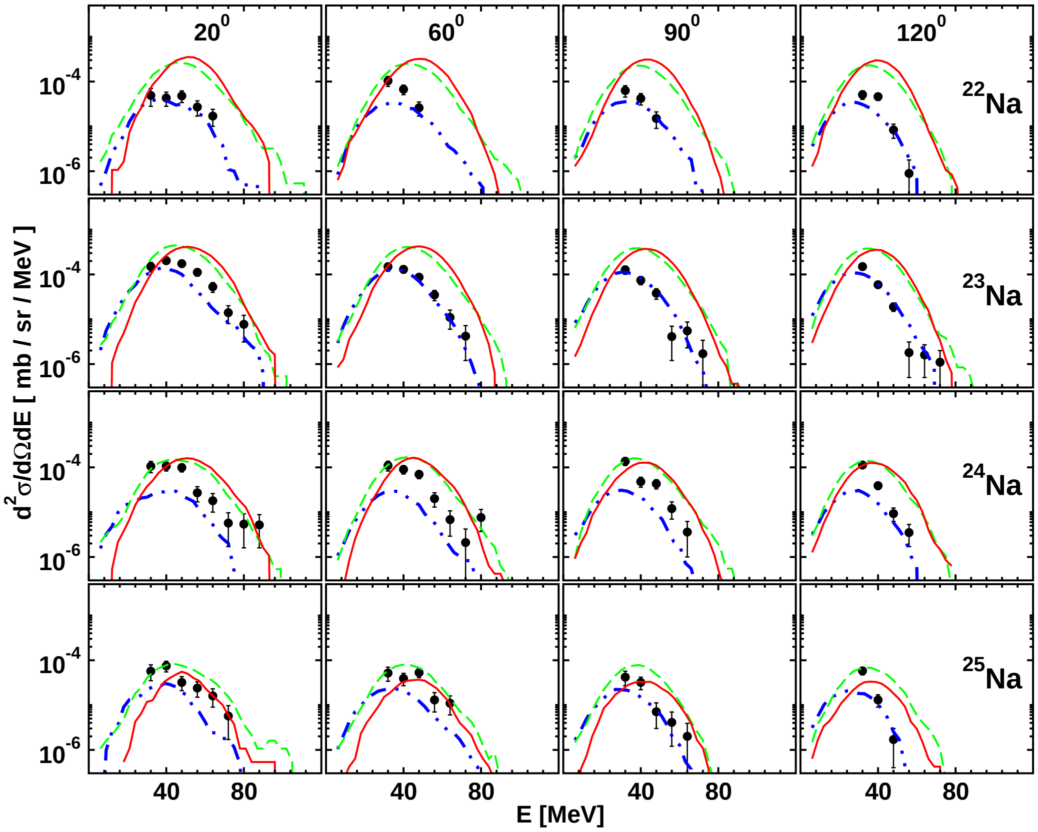

Figure 5.16: Spectra of Na isotopes from p+Ag collisions at proton beam energy 480 MeV [93]. The lines represent the same model calculations as for Li ejectiles (fig. 5.8).

Table 5.13: The standardized H- and M-factor values as well as non standardized A-factor values for spectra of Na isotopes from p+Ag collisions at proton beam energy 480 MeV [93]. The INCL4.6 intranuclear cascade model was coupled to four different models of the second stage of the reaction: ABLA07, GEM2, GEMINI++, and SMM.

	Non-standardized *A*				Standardized H				Standardized M			
Ejectile	ABLA	GEM2	GEMINI	SMM	ABLA	GEM2	GEMINI	SMM	ABLA	GEM2	GEMINI	SMM
^{22}Na	0.67	-	0.21	0.67	44.7	-	**2.5**	57.7	49.4	-	**2.1**	60.1
^{23}Na	0.61	-	0.22	0.60	57.1	-	3.4	64.5	57.6	-	**2.5**	61.4
^{24}Na	0.41	-	0.52	0.50	21.1	-	11.2	25.2	20	-	12.1	25.6
^{25}Na	0.38	-	0.41	0.35	13.3	-	4.5	6.5	12.4	-	4.9	6.5
^{26}Na	0.42	-	0.48	0.56	3.8	-	**2.5**	3.2	3.7	-	**2.6**	3.2

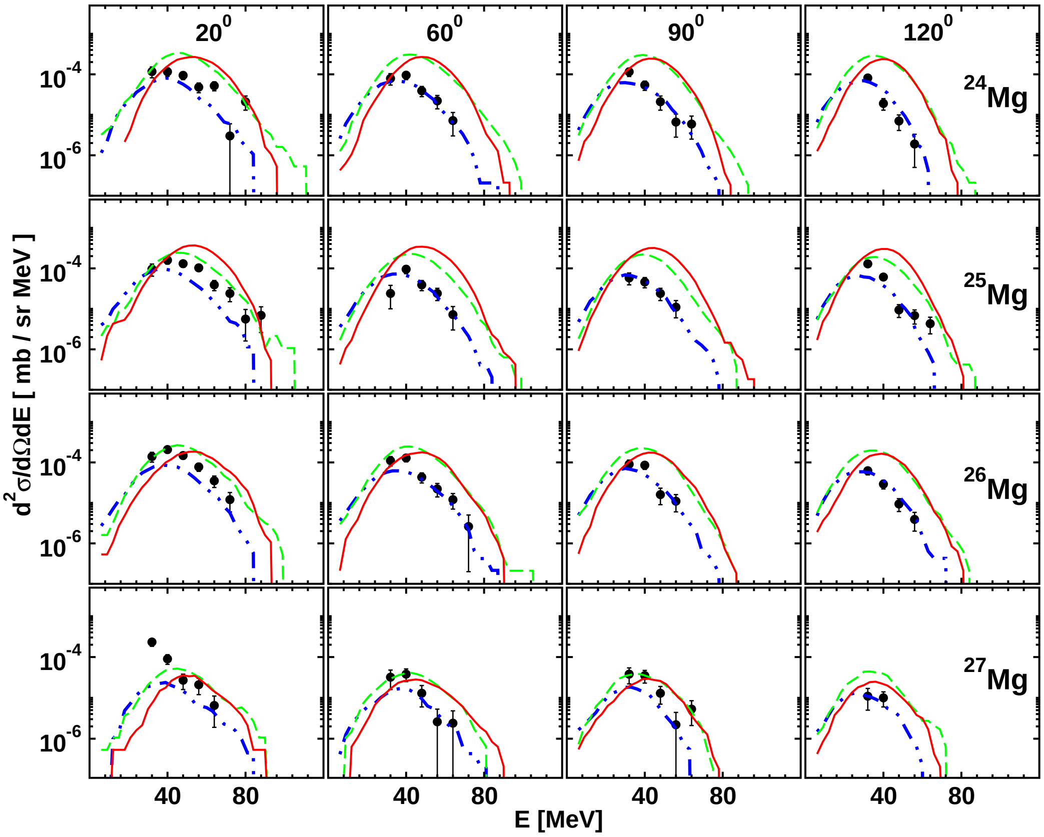

Figure 5.17: Spectra of Mg isotopes from p+Ag collisions at proton beam energy 480 MeV [93]. The lines represent the same model calculations as for Li ejectiles (fig. 5.8).

Table 5.14: The standardized H- and M-factor values as well as non standardized A-factor values for spectra of Mg isotopes from p+Ag collisions at proton beam energy 480 MeV [93]. The INCL4.6 intranuclear cascade model was coupled to four different models of the second stage of the reaction: ABLA07, GEM2, GEMINI++, and SMM.

Ejectile	Non-standardized *A*				Standardized H				Standardized M			
	ABLA	GEM2	GEMINI	SMM	ABLA	GEM2	GEMINI	SMM	ABLA	GEM2	GEMINI	SMM
^{24}Mg	0.63	-	0.21	0.59	53.4	-	**2.2**	5.2	55.6	-	**2.0**	5.1
^{25}Mg	0.47	-	0.25	0.62	33.7	-	5.3	6.2	33.3	-	5.0	6.1
^{26}Mg	0.49	-	0.27	0.50	33.7	-	4.0	3.2	33.6	-	4.1	30.4
^{27}Mg	0.36	-	0.35	0.40	7.8	-	3.3	6.9	7.1	-	**2.6**	6.9

Table 5.15: Ranks of various model predictions for IMF spectra from p+Ag collisions at 480 MeV [93] according to values of non-standardized *A*-deviation factor and standardized H- and M- deviation factors taking into account both, experimental and Monte Carlo uncertainties (to be continued on the next page).

	Non-standardized *A*				Standardized H				Standardized M			
Ejectile	ABLA	GEM2	GEMINI	SMM	ABLA	GEM2	GEMINI	SMM	ABLA	GEM2	GEMINI	SMM
^{6}Li	3	4	2	1	3	4	2	1	3	4	2	1
^{7}Li	3	4	2	1	3	4	2	1	3	4	2	1
^{8}Li	2.5	1	2.5	4	2.5	1	2.5	4	2	1	3	4
^{9}Li	1	3.5	2	3.5	4	1	3	2	3	1	4	2
^{7}Be	4	3	2	1	4	3	2	1	4	3	2	1
^{9}Be	3	4	2	1	3	4	2	1	3	4	2	1
^{10}Be	2	4	3	1	2	4	3	1	2	4	3	1
^{11}Be	1	3.5	2	3.5	1	2	3	4	1	3	2	4
^{8}B	2.5	2.5	2.5	2.5	2.5	2.5	2.5	2.5	2.5	2.5	2.5	2.5
^{10}B	2	4	3	1	2	4	3	1	2	4	3	1
^{11}B	2	4	3	1	2	4	3	1	2	4	3	1
^{12}B	2	4	3	1	2	4	3	1	2	4	3	1
^{13}B	2	4	1	3	2.5	1	2.5	4	2.5	1	2.5	4
^{11}C	2	4	3	1	2	3	4	1	2	4	3	1
^{12}C	2	4	3	1	3	4	2	1	2	4	3	1
^{13}C	1	4	3	2	1	4	3	2	1	4	3	2
^{14}C	1	4	3	2	1	4	3	2	1	4	3	2
^{14}N	3	4	1	2	4	2	1	3	4	3	1	2
^{15}N	1	4	3	2	2	4	3	1	1	4	3	1
^{16}N	1	4	2	3	1	4	2	3	1	4	2	3
^{17}N	2	4	1	3	2	4	1	3	1.5	3.5	1.5	3.5
^{15}O	2	4	3	1	4	2	1	3	4	2	1	3
^{16}O	2	4	3	1	4	3	1	2	3.5	3.5	1.5	1.5
^{17}O	1	4	3	2	1	4	2	3	1	4	2	3
^{18}O	1	4	2	3	1	4	3	2	1	4	2.5	2.5
^{19}O	1.5	4	3	1.5	1.5	4	3	1.5	1.5	3.5	3.5	1.5
^{18}F	1	4	3	2	3	2	1	4	3	2	1	4
^{19}F	2	4	1	3	2.5	4	1	2.5	2	4	1	3
^{20}F	1	4	3	2	3	4	2	1	1.5	4	3	1
^{21}F	1	4	3	2	3	4	2	1	4	2	1	3
^{20}Ne	3	4	1	2	3	4	1	2	4	2	1	3
^{21}Ne	3	4	1	2	3	2	1	4	4	2	1	3
^{22}Ne	3	4	1	2	4	2	1	3	4	2	1	3
^{23}Ne	1	4	3	2	1.5	4	3	1.5	**1**	4	3	2

(Continuation of the Table 5.15: Ranks of various models.)

Ejectile	Non-standardized *A*				Standardized H				Standardized M			
	ABLA	GEM2	GEMINI	SMM	ABLA	GEM2	GEMINI	SMM	ABLA	GEM2	GEMINI	SMM
^{22}Na	2.5	4	1	2.5	2	4	**1**	3	2	4	**1**	3
^{23}Na	2.5	4	1	2.5	2	4	1	3	2	4	**1**	3
^{24}Na	1	4	3	2	2	4	1	3	2	4	1	3
^{25}Na	2.5	4	2.5	1	3	4	1	2	3	4	1	2
^{26}Na	1	4	2	3	3	4	**1.5**	1.5	3	4	**1.5**	1.5
^{24}Mg	3	4	1	2	3	4	**1**	2	3	4	**1**	2
^{25}Mg	2	4	1	3	2	4	1	3	2	4	1	3
^{26}Mg	2.5	4	1	2.5	3	4	1	2	3	4	1	2
^{27}Mg	1.5	4	1.5	3	3	4	1	2	3	4	**1**	2
Sum of ranks	84	165.5	93	87.5	107	146.5	84.0	92.5	103.5	145	85.5	96
Final rank	1	4	3	2	3	4	1	2	3	4	1	2

Inspection of the above table allows to conclude that the H- and M- deviation factors assure the same general ranking:

- The GEMINI++ model assures in average the best description of the experimental spectra of intermediate mass fragments even when the agreement is not satisfactory.
- The GEM2, on the other hand gives in most cases the poorest reproduction of the data, significantly different from other models.
- The ABLA07 and SMM predictions are of the equal quality and only ∼ 7% (in the case of the M-factor) and ∼ 20% (in the case of the H-factor) poorer than those of GEMINI++.
- The agreement between theoretical predictions and the data is satisfactory, i.e., the standardized deviation factors are smaller than three only for heaviest intermediate mass fragments. The ranks corresponding to such values of the deviation factors are denoted by bold numbers. Improvement of the agreements is caused by two effects: (1) The shape and magnitude of the experimental and theoretical spectra indeed become closer one to another, but also (2) The deviation factors become smaller for heavy IMFs because of increasing inaccuracies both, of the data and of the Monte Carlo results.

The non-standardized *A*-factor values lead to different ranking. It only agrees with other rankings in selection of the worst model - GEM2. The sum of ranks for all three other models are much closer one to another than those obtained with H- and M-factors.

Results of the calculations of M-factor values are presented in fig. 5.18 as a function of the mass number of ejectiles. The yellow band in the plots represent the range of standardized M-values which does not contradict the hypothesis of the perfect agreement of the model with the data, i.e. M < 3.0. All points which do not fall in this range contradict the hypothesis of good reproduction of the data by the corresponding model.

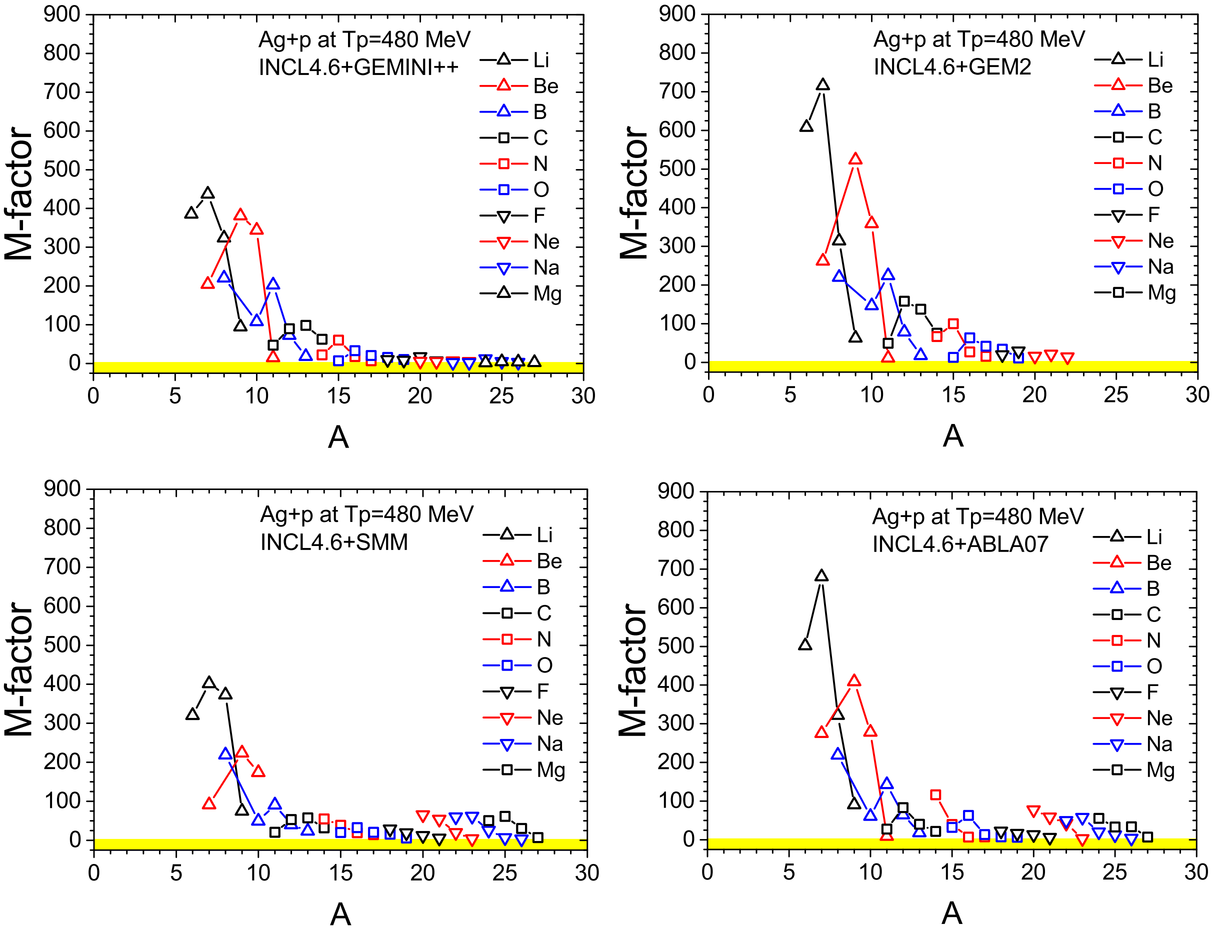

Figure 5.18: The standardized M-factor values calculated for all intermediate mass fragments from the experiment of Green et al. [93] presented as a function of atomic mass of the ejectiles for four models of the second stage of the reaction (ABLA07 - lower, right panel, GEM2 - upper, right panel, GEMINI++ - upper, left panel, and SMM - lower, left panel) coupled with the INCL4.6 which describes the first stage of the process. The yellow band in the plots represent the range of standardized M-values which does not contradict the hypothesis of the perfect agreement of the model with the data.

As can be seen the description of the lightest among intermediate mass fragments, i.e. isotopes of Li, Be, B and C is not good for all the models. However description of heavier ejectiles improves with increasing mass, especially for GEMINI++ and SMM models.

Values of the standardized H-factor calculated for the same data are presented in fig. 5.19.

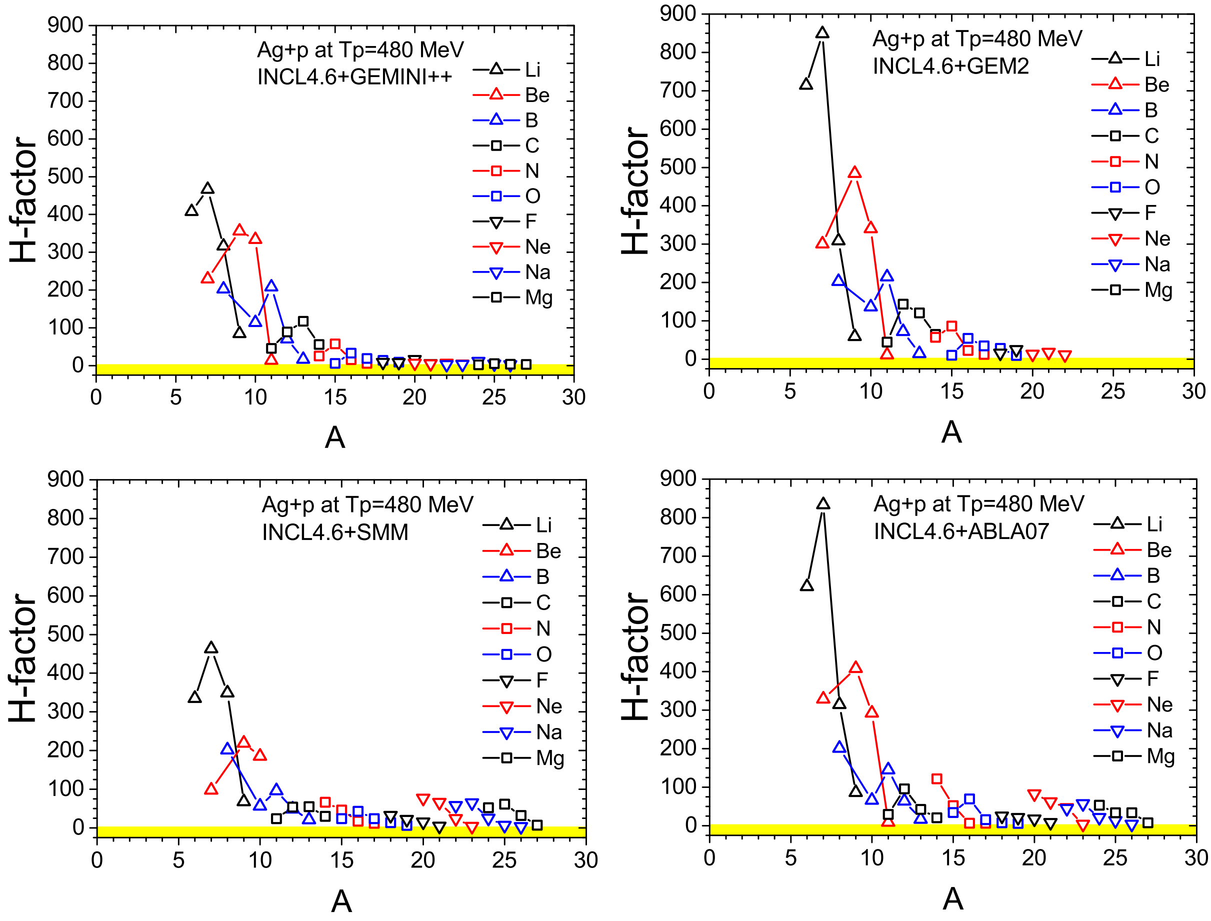

Figure 5.19: The standardized H-factor values calculated for all intermediate mass fragments from the experiment of Green et al. [93] presented as a function of atomic mass of the ejectiles for four models of the second stage of the reaction (ABLA07 - lower, right panel, GEM2 - upper, right panel, GEMINI++ - upper, left panel, and SMM - lower, left panel) coupled with the INCL4.6 which describes the first stage of the process. The yellow band in the plots represent the range of standardized M-values which does not contradict the hypothesis of the perfect agreement of the model with the data.

As it is obvious from comparison of the figs. 5.18 and 5.19 the mass dependence of the H and M deviation factors is very similar, however absolute values of the H-factor are in average larger than those of the M-factor.

The standardization procedure changes relative values of the H and M deviation factors because their expectation values and standard deviations are dependent in different way on the number of compared experimental and theoretical cross sections (cf. fig. 4.10). Thus to examine values of the deviation factors in more transparent way the ratio of non standardized H-factor to M-factor values calculated for comparison of INCL4.6+ABLA07 model with the experimental data is shown in fig. 5.20.

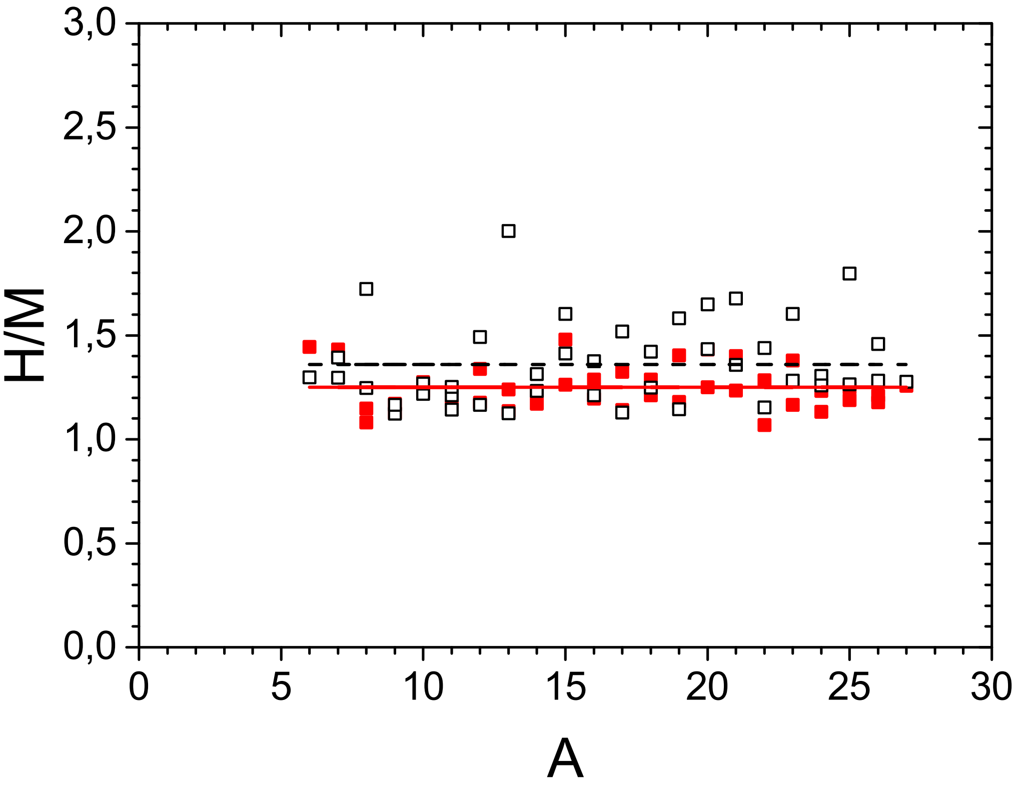

Figure 5.20: The ejectile mass number dependence of ratios of H-factors to M-factors (not standardized) calculated for comparison of the experimental data from p+Ag reactions at proton beam energy 480 MeV [93] with INCL4.6+ABLA07 theoretical cross sections. The calculation of factors was performed with experimental errors only (open squares) and with both, experimental and theoretical uncertainties (full squares). Average values of the ratios are shown as horizontal lines; $< H/M >= 1.36$ for open squares and $< H/M >= 1.25$ for full squares. The standard deviation for individual points was equal to 0.20 and 0.10 for the open and full squares, respectively.

As can be seen in fig. 5.20 values of the H-factor are systematically larger than values of the M-factor. The average value of $< H/M >$ ratio is equal to 1.36(0.03) for factors evaluated with the experimental errors only but it is equal to 1.25(0.02) for factors which were calculated taking into account also fluctuations of the theoretical cross sections inherent in Monte Carlo models. Similar ratios of the H-factor to the M-factor were obtained for other theoretical models. These results are collected in table 5.16.

It seems from this comparison that the not standardized M and H-factors may be used as equivalent in ranking of the models. The same ranking can be obtained using the standardized values of the deviation factors but the latter are also suited for validation of models, i.e., for testing the hypothesis of the perfect agreement of model cross sections with data.

Table 5.16: The averaged over set of data [93] ratios of non-standardized H-factor to M-factor $< H/M >$ and their standard deviations $\sigma(H/M)$ for four theoretical models of the second stage of the reaction coupled to INCL4.6 used as the model of the first stage of the reactions. In the second and third column the deviation factors evaluated with the experimental errors are depicted whereas in the fourth and fifth columns the factors were calculated taking into account also uncertainty of the Monte Carlo theoretical calculations.

	Experimental errors only		Experimental plus MC errors	
Model	$< H/M >$	$\sigma(H/M)$	$< H/M >$	$\sigma(H/M)$
ABLA	1.36	0.20	1.25	0.10
GEM2	1.11	0.14	1.09	0.10
GEMINI++	1.23	0.19	1.19	0.08
SMM	1.37	0.20	1.24	0.11

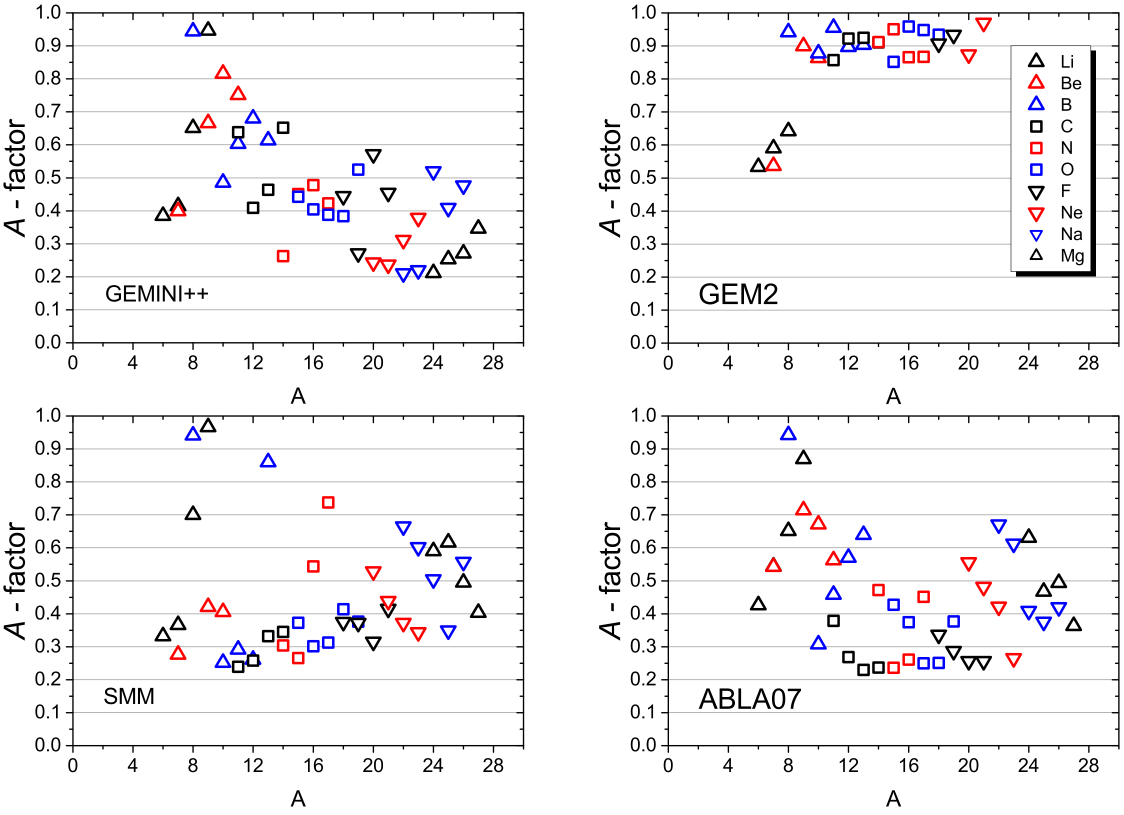

Figure 5.21: The non standardized A-factor values calculated for the same data and the same models as in figures 5.18 and 5.19.

The shape of the atomic mass dependence of the *A*- factor shows that the GEM2 model always gives poorer agreement with data than other models. The GEMINI++ is the best for the heaviest ejectiles, the SMM for the lightest (with exception of Li, Be and B which are always poorly reproduced) and the ABLA07 describes well the products with intermediate mass number.

5.2.2 Spectra and angular distributions of $d^2\sigma/d\Omega dE$ of LCP and IMF for p+Al, p+Ag, and p+Au collisions at 1.2, 1.9, and 2.5 GeV proton beam energy

The data measured by PISA collaboration consist of double differential cross sections $d^2\sigma/d\Omega$ dE measured at several scattering angles from 16° to 100° for three proton beam energies; 1.2, 1.9 and 2.5 GeV and targets which cover full range of masses ; Al [78], Ni [76,77], Ag [125], and Au [74,75,77]. The light charged particles (p, d, t, ^{3}He and ^{4}He) and light intermediate mass fragments ^{6,7,8,9}Li, ^{7,9,10}Be, ^{10,11,12}B have been detected.

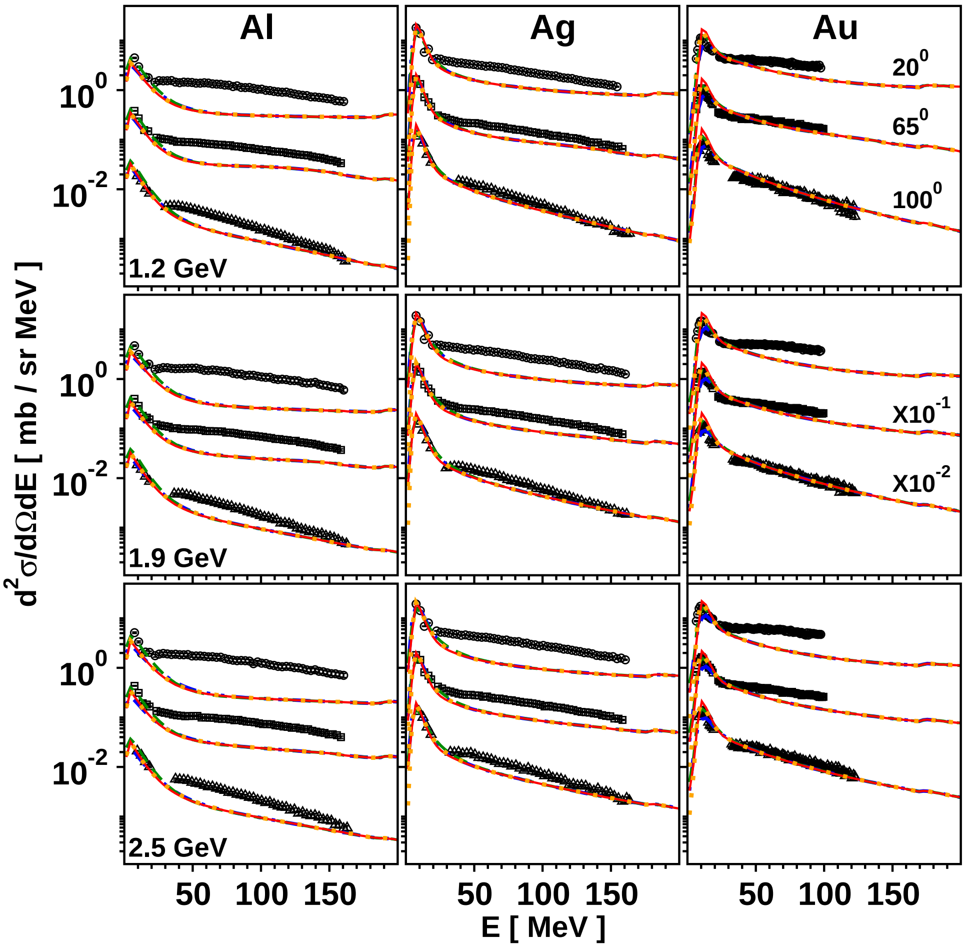

Figure 5.22: Experimental (symbols) and theoretical spectra $d^2\sigma/d\Omega$dE (lines) of protons measured at 20° (circles), 65° (squares) and 100° (triangles) for Al target (left column), Ag target (middle column) and Au target (right column) at three proton beam energies 1.2 GeV (upper row), 1.9 GeV (middle row) and 2.5 GeV (lower row). To distinguish spectra measured at different angles the cross sections measured at 65° were multiplied by factor 0.1 and those at 100° by factor 0.01, respectively. Dashed (green) line represents ABLA07 calculations, dotted (orange) line corresponds to GEM2, Dash-dotted (blue) line depicts GEMINI++ and solid (red) line shows SMM results.

In the present section the analysis of data for Al, Ag and Au is discussed at three proton beam energies mentioned above. The data are compared with theoretical cross sections evaluated by using INCL4.6 as the model of the first stage of the reaction, i.e. the intranuclear cascade, which includes coalescence of the emitted nucleons into complex particles with masses not heavier than A=8 [23]. The emission of particles from excited residua of the first stage of the reaction is described by four different models: ABLA07 [86], GEM2 [52, 53], GEMINI++ [54] and SMM [87].

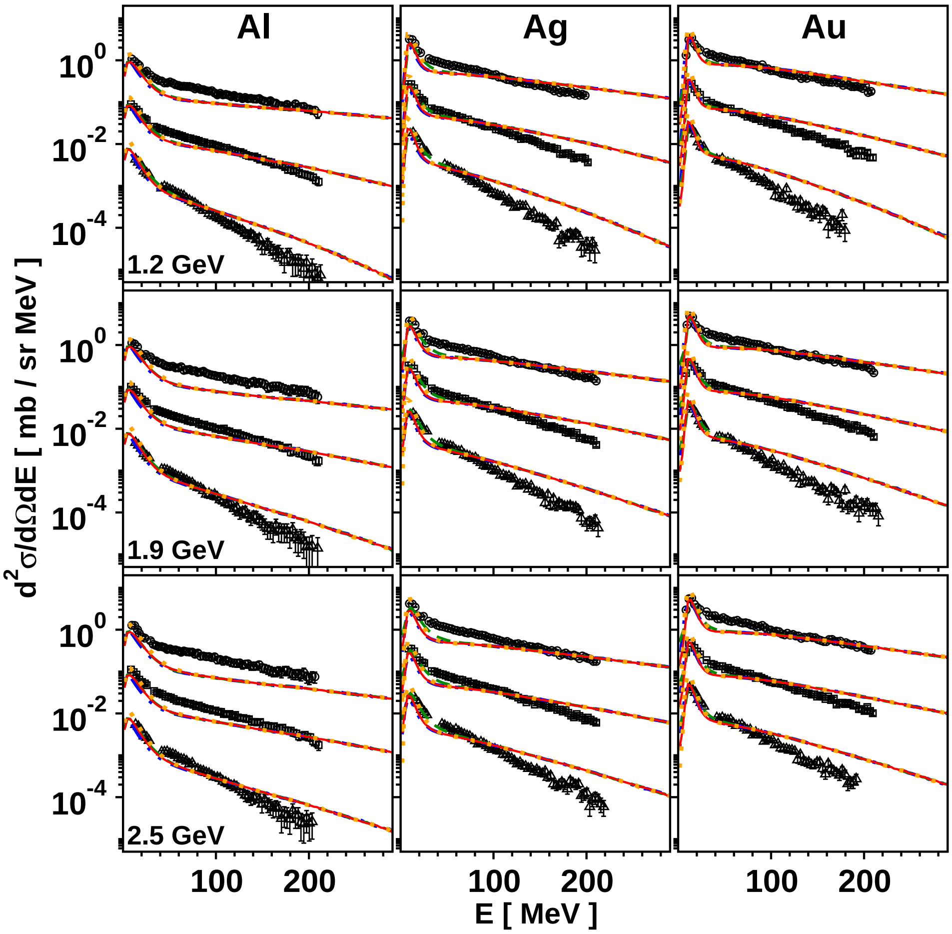

Figure 5.23: The same as in fig. 5.22 but for deuteron spectra.

Results of the calculations are compared with data in figs. 5.22 - 5.34 whereas the standardized values of the M-deviation factor, evaluated with the experimental as well as statistical uncertainties of Monte Carlo calculations are listed in tables 5.17-5.19.

The general conclusion from the comparisons is that the models reproduce main properties of the energy spectra as well as their angular dependence, however, the agreement between model predictions and the data is not satisfactory.

The systematic deterioration of description of proton spectra is clearly visible in fig. 5.22 with increasing the proton beam energy for given target and with decreasing the mass of the target for given beam energy.

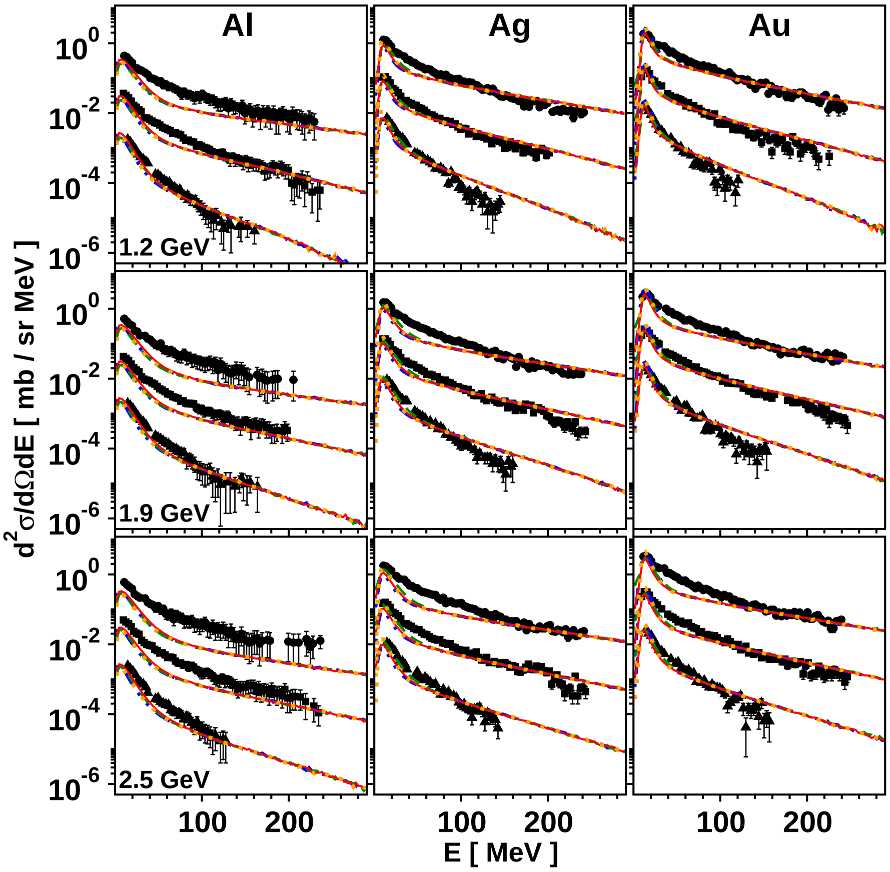

Figure 5.24: The same as in fig. 5.22 but for triton spectra.

The systematic effect of the target mass and the beam energy on the quality of data reproduction which was observed for proton spectra in fig. 5.22 is also present for deuteron spectra in fig. 5.23, however less pronounced than for protons. It should be pointed out that the high energy part of the spectra is here due to the first stage of the reaction, which in the INCL4.6 model produces deuterons by the coalescence of nucleons. The characteristic tendency of the deuteron spectra visible for all scattering angles in fig. 5.23 is too small slope of the theoretical, coalescence spectra in respect to that of the experimental data. The analogous behavior may be observed also for heavier LCP, i.e. for tritons, ^{3}He and ^{4}He as can be seen in the next figures.

The same spectra for protons and other LCP are shown in Appendix E in which the scale is modified offering better distinction between results of different models of the second stage of the reaction. As can be seen the contribution from the second stage of the process is important only for very small energies, i.e., up to 30 - 35 MeV. The spectra at higher energies are completely dominated by contribution from the nucleon-nucleon cascade described by INCL4.6.

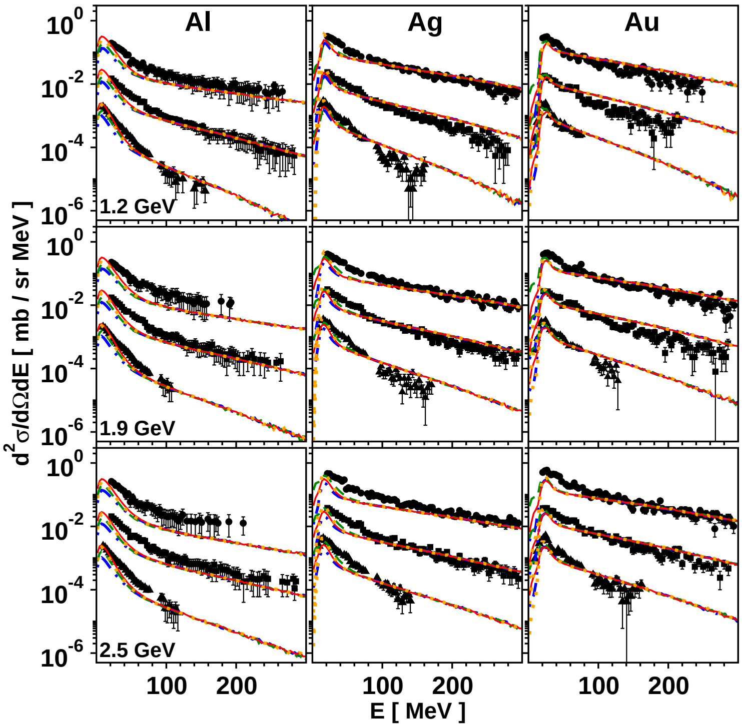

Figure 5.25: The same as in fig. 5.22 but for ^{3}He spectra.

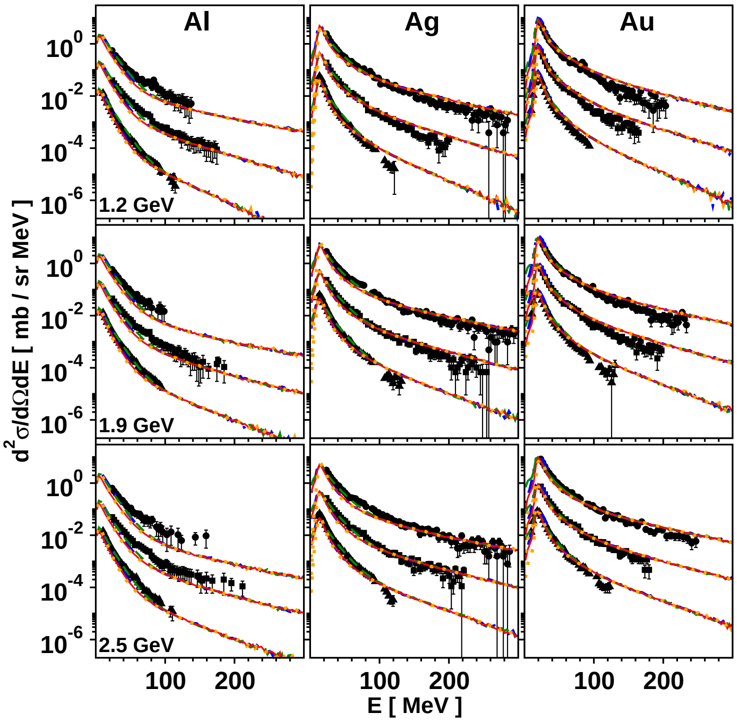

Figure 5.26: The same as in fig. 5.22 but for ^{4}He spectra.

The same systematic effects are observed for tritons and ^{3}He as those for deuterons and protons. The alpha particle spectra (presented in fig. 5.26) seem to be reproduced better than the spectra of lighter LCP. This is especially well visible for silver and gold targets whereas the results for aluminium target are still not quite satisfactory.

Situation changes when particles heavier that ^{4}He are taken into account. In the next two figures the intermediate mass fragments with the atomic mass number six are presented. Three effects are clearly visible:

- Predictions of different models of the second stage of the reaction start to differ significantly,
- The range of energies where the contribution of the second stage of the reaction becomes to be important is broader than for LCP,
- The agreement between data and model predictions is poorer than that for ^{4}He.

This properties of the theoretical spectra indicate that there is a chance to make a meaningful ranking of different models of the mechanism for the second stage of the reaction.

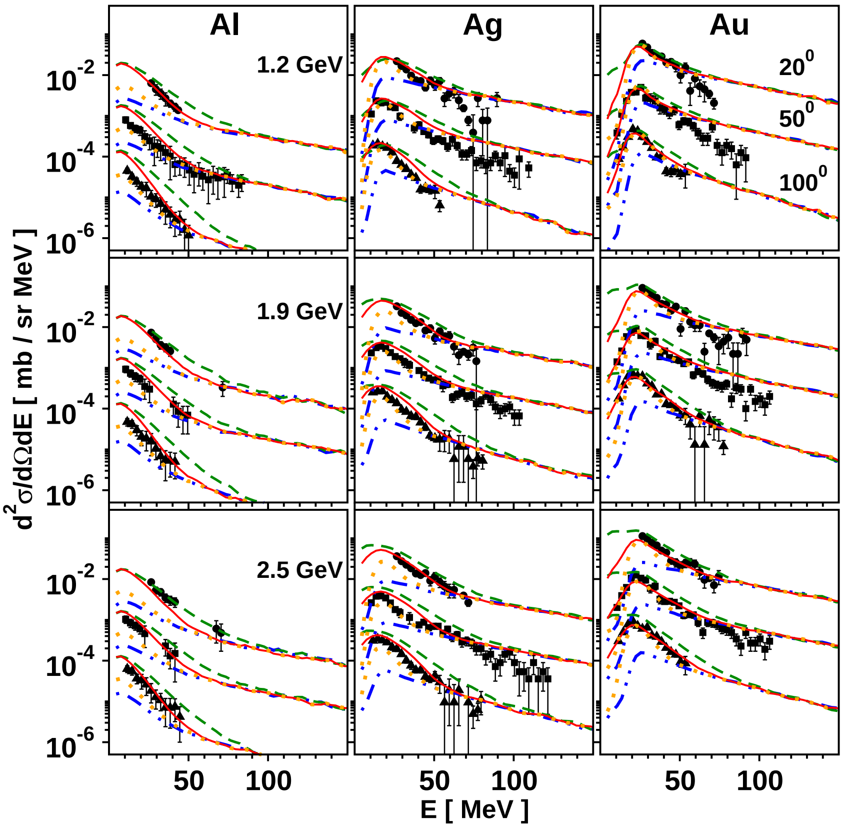

Figure 5.27: The same as in fig. 5.22 but for ^{6}He spectra. Angle 65° is replaced by 50°. NOTE: GEMINI++ underestimates strongly the data.

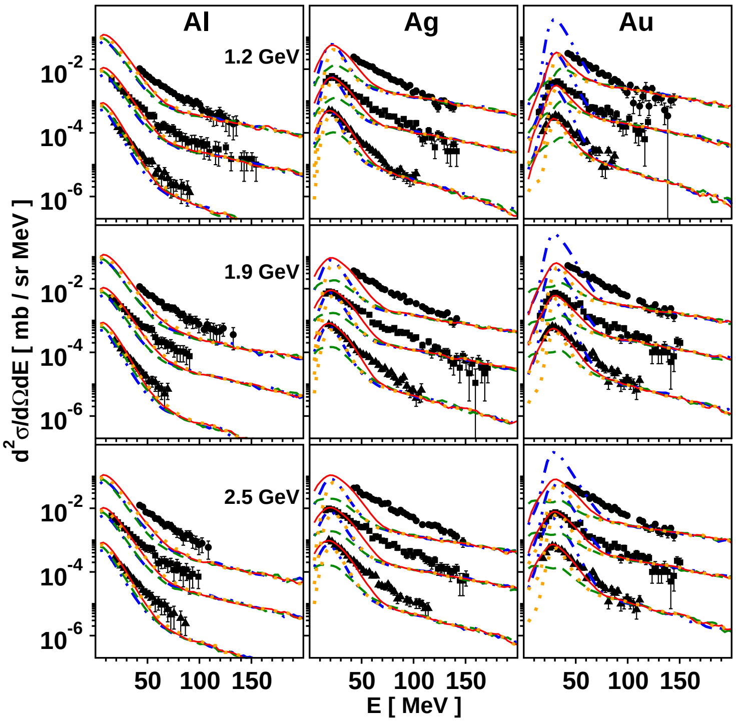

Figure 5.28: The same as in fig. 5.22 but for ^{6}Li spectra. Angle 65° is replaced by 50°.

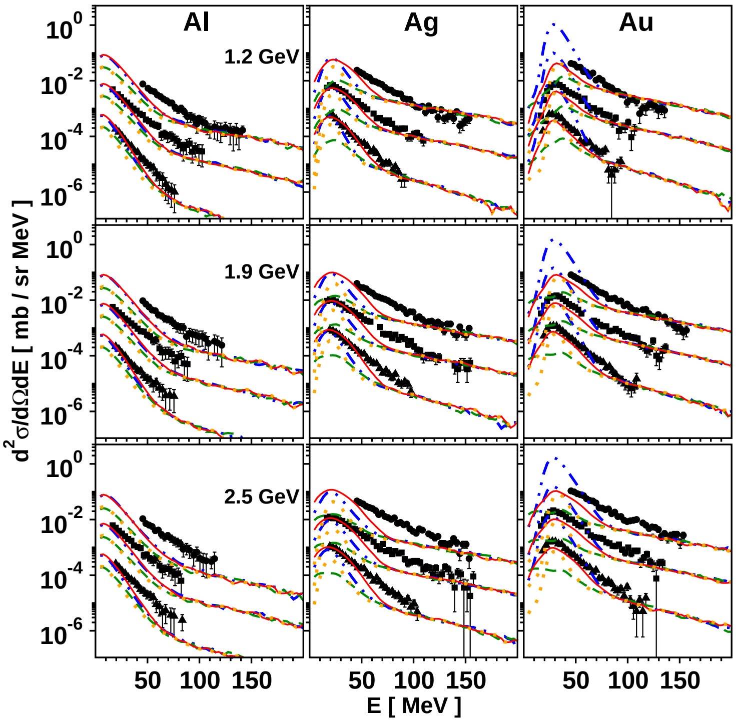

Figure 5.29: The same as in fig. 5.22 but for ^{7}Li spectra. Angle 65° is replaced by 50°.

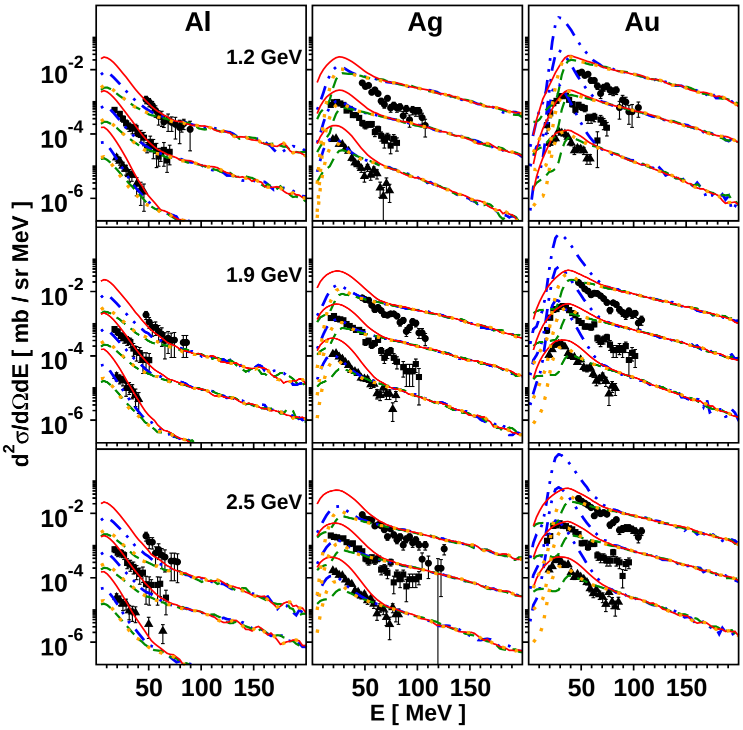

Figure 5.30: The same as in fig. 5.22 but for ^{8}Li spectra. Angle 65° is replaced by 50°.

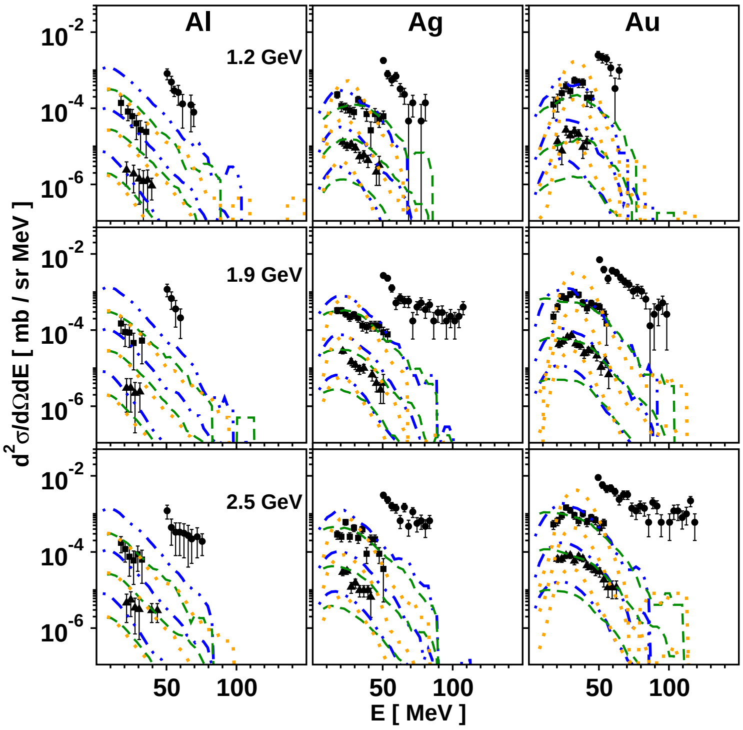

Figure 5.31: The same as in fig. 5.22 but for ^{9}Li spectra. Angle 65° is replaced by 50°. NOTE: SMM does not produce ^{9}Li !.

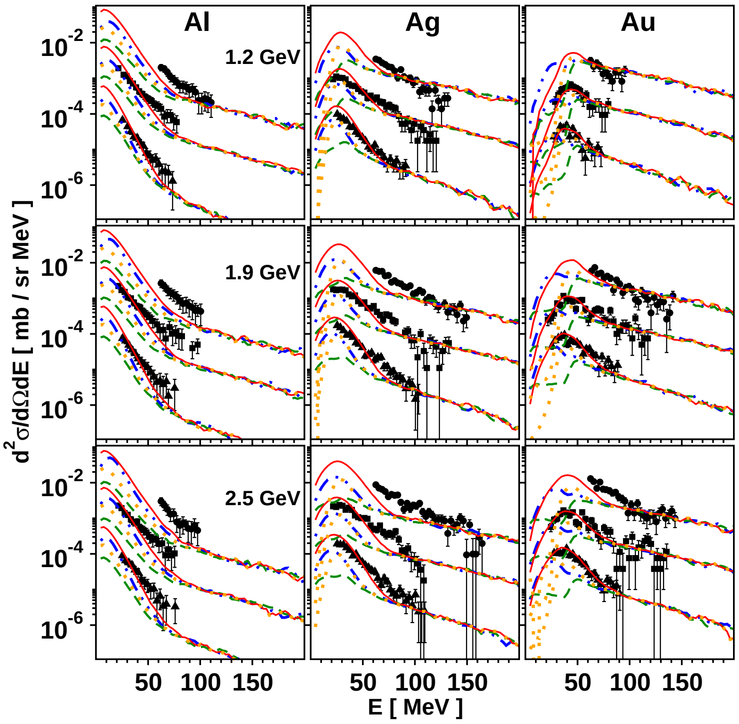

Figure 5.32: The same as in fig. 5.22 but for ^{7}Be spectra. Angle 65° is replaced by 50°.

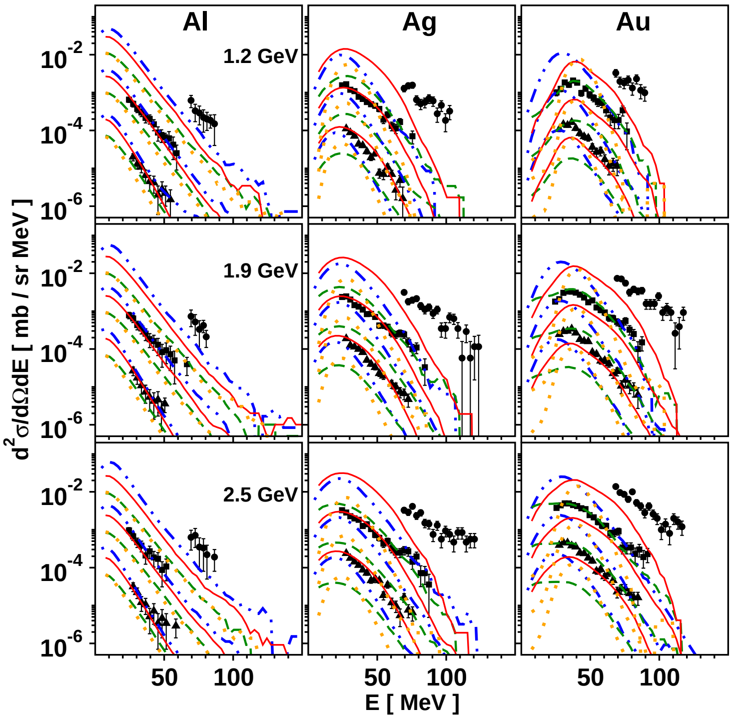

Figure 5.33: The same as in fig. 5.22 but for ^{9}Be spectra. Angle 65° is replaced by 50°.

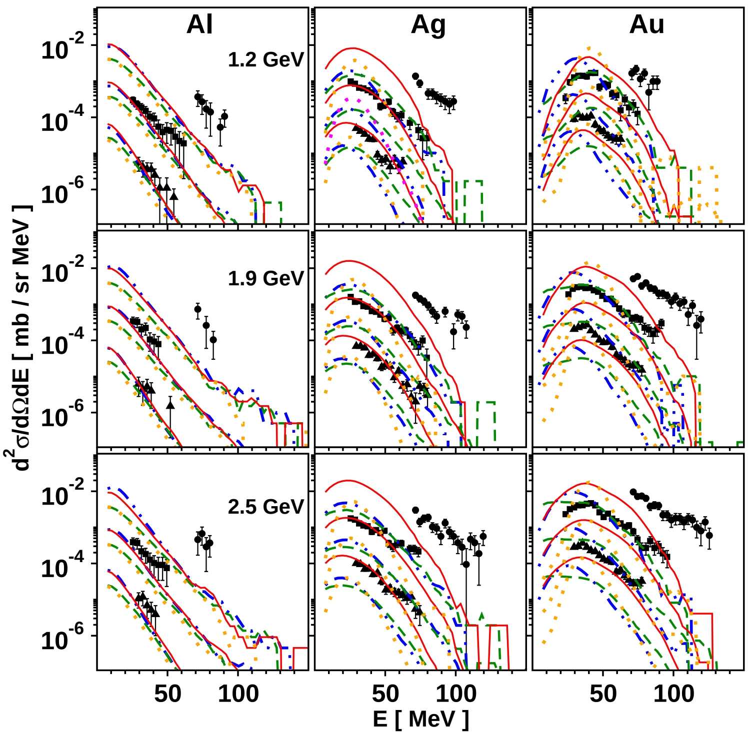

Figure 5.34: The same as in fig. 5.22 but for ^{10}Be spectra. Angle 65° is replaced by 50°.

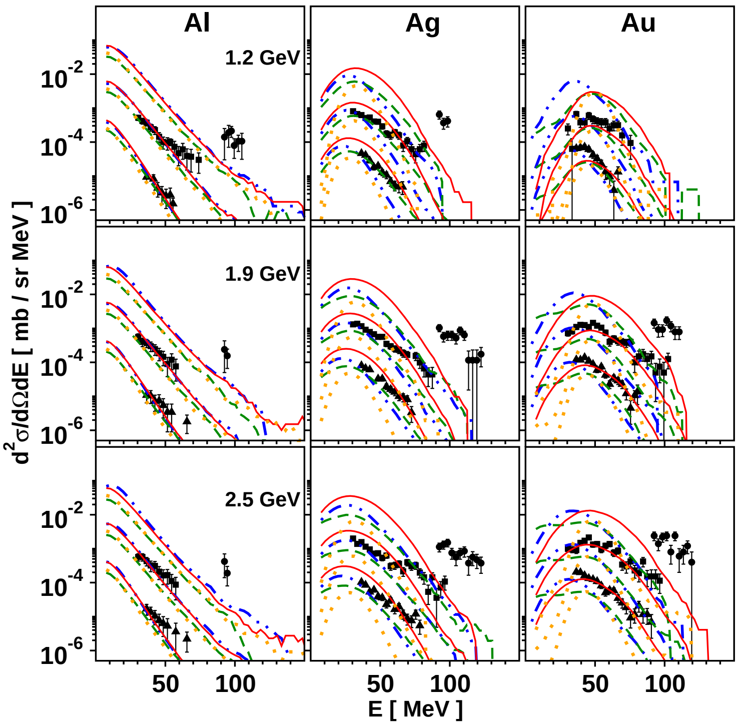

Figure 5.35: The same as in fig. 5.22 but for ^{10}B spectra. Angle 65° is replaced by 50°.

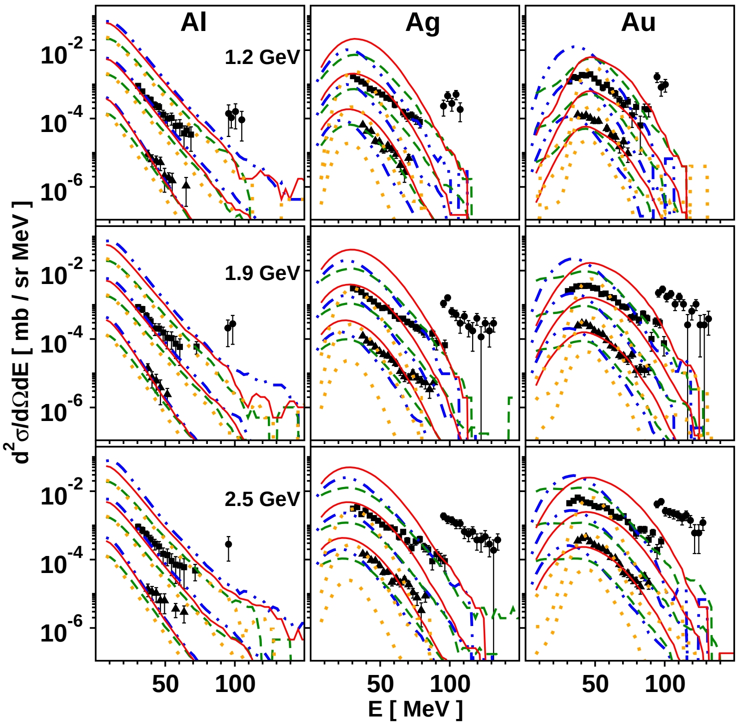

Figure 5.36: The same as in fig. 5.22 but for ^{11}B spectra. Angle 65° is replaced by 50°.

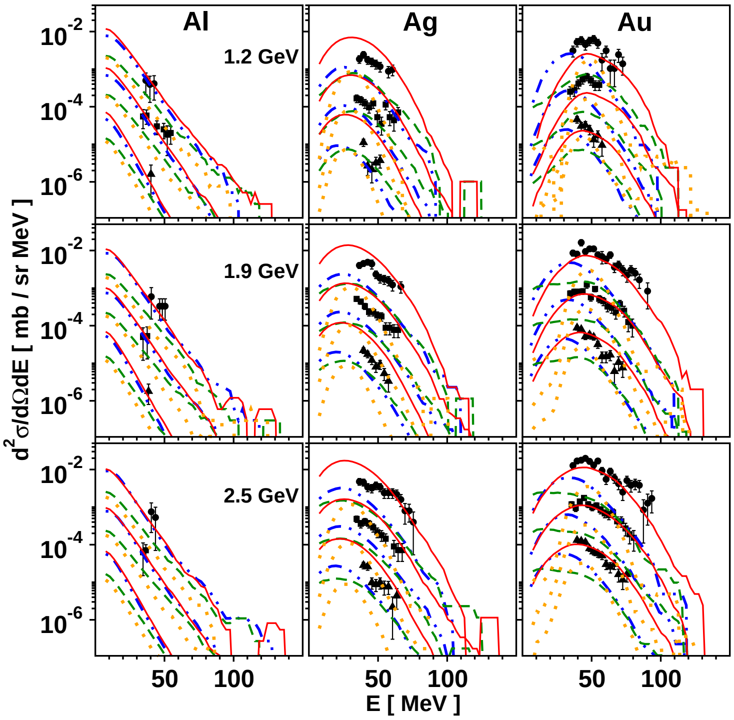

Figure 5.37: The same as in fig. 5.22 but for ^{12}B spectra. Angle 65° is replaced by 50°. Instead spectrum at 20° the spectrum measured at 35° is shown.

The spectra of heavier IMF presented in figures (5.29 - 5.37) are similar to the spectra of mass six ejectiles, i.e.

- *The contribution from the second stage of the reaction is extended to higher energies than that for LCP.*
- *Different models of the second stage produce quite different results.*
- The spectra for ^{9}Be, ^{10}Be, ^{10}B, ^{11}B, and ^{12}B for which the coalescence contribution is not produced by INCL4.6, have wrong shape at high energies and are significantly smaller than the data. *This indicates that the contribution of the first stage of the reaction is important also for IMF with mass number A=9, 10 and 11.*

The qualitative analysis based on inspection of the above figures was extended to quantitative considerations by evaluation of the M-deviation factor. Values of the standardized M-factor calculated with the experimental uncertainties as well as the uncertainties of the Monte Carlo samplings are collected for the investigated PISA data in three tables below: table 5.17, table 5.18 and table 5.19 for the aluminium, silver, and gold targets, respectively. These values allow for ranking of the models and can also indicate the situation when the agreement of the model and experimental cross sections is satisfactory (M-factor smaller than 3).

Table 5.17: Standardized M-factor evaluated for p+Al data [78] taking into account uncertainties of data and Monte Carlo calculations. Values smaller than 3.0 are shown as the bold text.

Model:	ABLA07			GEM2		
Energy:	1.2 GeV	1.9 GeV	2.5 GeV	1.2 GeV	1.9 GeV	2.5 GeV
p	270.53	215.62	224.92	286.21	229.17	243.32
d	66.44	56.30	70.84	89.13	59.05	55.89
t	55.76	51.04	57.18	56.16	51.72	59.91
^{3}He	70.64	70.67	77.95	57.88	58.04	69.15
^{4}He	64.86	56.93	70.87	125.00	113.39	124.52
^{6}He	56.85	26.68	10.96	3.70	8.65	11.11
^{6}Li	28.27	33.87	39.23	19.74	19.30	23.71
^{7}Li	51.03	49.76	51.23	58.38	52.82	53.23
^{8}Li	7.69	11.61	13.01	8.55	11.59	13.01
^{9}Li	6.67	5.73	6.04	7.45	6.01	6.45
^{7}Be	32.03	29.30	30.61	28.14	25.39	26.98
^{9}Be	14.99	13.38	12.96	18.69	15.10	14.30
^{10}Be	8.08	7.12	8.64	10.36	8.26	9.49
^{10}B	11.09	7.93	9.18	10.73	8.94	9.85
^{11}B	14.44	9.94	11.47	17.62	12.47	13.33
^{12}B	9.50	12.80	13.20	10.16	13.52	13.83

Model:	GEMINI++			SMM		
Energy:	1.2 GeV	1.9 GeV	2.5 GeV	1.2 GeV	1.9 GeV	2.5 GeV
p	284.65	230.89	248.08	287.74	230.40	243.67
d	83.75	69.45	82.60	72.06	58.35	72.04
t	53.88	49.65	58.24	39.01	38.23	48.93
^{3}He	87.34	81.55	87.87	46.66	45.87	57.32
^{4}He	75.97	65.47	80.37	137.25	122.65	133.52
^{6}He	10.21	13.98	15.14	15.45	6.52	1.10
^{6}Li	37.40	37.83	41.01	30.02	22.46	22.45
^{7}Li	36.41	35.64	38.34	27.36	29.32	34.48
^{8}Li	**1.25**	5.93	8.09	9.31	1.48	0.10
^{9}Li	**2.28**	**2.47**	3.09	7.50	4.70	4.62
^{7}Be	20.65	18.86	20.15	12.25	9.76	10.36
^{9}Be	4.00	**1.42**	**-0.24**	3.34	4.02	5.10
^{10}Be	5.75	4.19	6.32	4.43	3.97	6.04
^{10}B	7.69	**2.54**	3.65	9.61	**2.41**	3.71
^{11}B	5.93	**2.25**	4.30	8.97	4.55	6.69
^{12}B	7.44	12.27	11.67	7.10	11.98	11.28

Table 5.18: Standardized M-factor evaluated for p+Ag data [78] taking into account uncertainties of data and Monte Carlo calculations. Values smaller than 3.0 are shown as the bold text.

Model:	ABLA07			GEM2		
Energy:	1.2 GeV	1.9 GeV	2.5 GeV	1.2 GeV	1.9 GeV	2.5 GeV
p	427.47	481.00	465.30	458.91	526.90	490.83
d	230.66	202.56	166.77	273.32	261.91	205.55
t	103.23	105.87	101.40	112.09	124.37	119.02
^{3}He	106.89	108.27	105.71	101.88	119.86	121.87
^{4}He	153.44	133.19	137.09	223.55	265.25	280.85
^{6}He	94.18	103.14	84.93	41.22	33.96	31.54
^{6}Li	120.26	148.29	148.16	94.68	113.42	118.07
^{7}Li	143.17	178.51	172.83	125.62	162.52	160.96
^{8}Li	117.77	76.35	48.10	108.05	65.57	42.01
^{9}Li	24.88	33.86	29.91	22.47	31.57	28.41
^{7}Be	51.28	67.19	66.39	36.52	52.72	55.48
^{9}Be	65.16	81.17	74.59	66.50	84.10	76.50
^{10}Be	43.37	56.10	52.99	44.01	59.08	56.19
^{10}B	17.69	35.57	39.41	43.72	56.99	53.39
^{11}B	31.39	52.63	55.49	69.74	90.09	82.14
^{12}B	29.14	44.00	42.75	34.88	51.34	47.46

Model:	GEMINI++			SMM		
Energy:	1.2 GeV	1.9 GeV	2.5 GeV	1.2 GeV	1.9 GeV	2.5 GeV
p	447.54	506.21	476.48	490.72	538.20	505.90
d	287.82	279.95	236.39	262.67	260.59	222.08
t	149.64	165.70	153.33	132.20	144.78	135.39
^{3}He	130.88	155.62	155.87	113.73	134.43	137.10
^{4}He	171.57	208.46	228.88	208.15	240.82	254.06
^{6}He	66.52	61.71	54.58	56.97	41.65	24.37
^{6}Li	83.92	108.76	116.74	48.89	65.97	68.48
^{7}Li	94.26	126.99	131.11	53.00	68.50	75.28
^{8}Li	107.09	60.06	34.47	201.03	176.43	111.35
^{9}Li	24.52	30.80	25.86	10.55	10.40	8.44
^{7}Be	41.20	52.89	54.39	32.60	39.98	36.61
^{9}Be	54.52	58.75	51.98	20.82	29.76	25.25
^{10}Be	50.96	59.34	54.03	17.02	21.08	20.08
^{10}B	31.25	37.32	34.75	38.79	46.49	39.01
^{11}B	47.29	57.75	52.84	42.09	44.74	35.61
^{12}B	31.47	43.21	39.34	65.10	70.71	61.11

Table 5.19: Standardized M-factor evaluated for p+Au data [78] taking into account uncertainties of data and Monte Carlo calculations. Values smaller than 3.0 are shown as the bold text.

Model:	ABLA07			GEM2		
Energy:	1.2 GeV	1.9	2.5 GeV	1.2 GeV	1.9 GeV	2.5 GeV
p	877.84	214.77	226.27	883.47	235.25	250.10
d	153.88	185.65	146.26	225.12	242.94	194.57
t	53.19	82.71	86.21	84.50	115.51	99.02
^{3}He	44.71	62.52	71.71	49.48	72.37	78.02
^{4}He	144.95	109.98	85.00	138.25	147.37	178.76
^{6}He	49.18	101.16	88.66	31.05	44.16	39.00
^{6}Li	60.48	107.87	121.00	51.89	89.91	101.14
^{7}Li	94.11	156.19	168.81	77.95	134.89	150.92
^{8}Li	117.45	125.91	75.24	110.88	115.35	59.07
^{9}Li	22.22	45.99	45.13	13.79	35.85	37.59
^{7}Be	14.17	32.84	35.59	8.85	23.94	27.05
^{9}Be	51.05	88.23	91.80	43.12	79.55	83.95
^{10}Be	45.79	80.65	81.50	35.19	67.23	70.53
^{10}B	20.50	37.01	42.28	28.14	43.62	46.17
^{11}B	35.05	70.17	77.79	48.78	85.92	90.15
^{12}B	34.16	60.76	65.08	28.65	56.44	61.95
Model:	GEMINI++			SMM		
Energy:	1.2 GeV	1.9 GeV	2.5 GeV	1.2 GeV	1.9 GeV	2.5 GeV
p	918.04	210.51	259.75	925.31	279.40	277.23
d	160.95	196.90	157.00	164.97	200.22	159.18
t	69.89	91.80	75.11	63.58	95.62	102.27
^{3}He	50.21	74.52	85.39	54.60	78.57	87.60
^{4}He	251.52	193.90	114.90	95.84	121.46	160.82
^{6}He	51.91	81.25	74.61	27.06	35.19	17.65
^{6}Li	268.96	307.57	241.05	36.12	54.66	65.77
^{7}Li	615.10	677.35	527.81	61.43	92.91	104.70
^{8}Li	689.73	765.77	595.42	122.50	154.15	92.38
^{9}Li	19.67	43.78	42.97	—	—	—
^{7}Be	7.81	23.33	27.05	3.06	6.23	8.34
^{9}Be	36.76	69.95	73.56	33.30	52.42	53.29
^{10}Be	43.92	80.49	80.69	33.83	54.16	53.72
^{10}B	20.31	34.35	38.30	17.07	14.72	14.05
^{11}B	30.87	65.23	70.89	27.37	42.25	44.14
^{12}B	29.22	54.73	59.10	21.12	39.85	34.76

Values of the standardized M-deviation factor smaller than 3 are indicated by the bold text. As can be seen in the above tables that only in several cases for Al target such a situation is realized. This indicates that the overall agreement is not satisfactory.

To gain better insight in the situation the ranks were attributed to each M-value in the tables 5.17 - 5.19. Then, the sum of ranks was calculated for each target/beam-energy/model combination and the obtained results were collected in the tables 5.20, 5.21 and 5.22.

Table 5.20: Sum of ranks of the standardized M-factors from the table 5.17 for p+Al collisions at 1.2, 1.9, and 2.5 GeV.

Energy	Model			
	ABLA07	GEM2	GEMINI++	SMM
1.2 GeV	44	49.5	32.5	34
1.9 GeV	44.5	49	37.5	29
2.5 GeV	43.5	50	39	27.5
Sum of ranks:	132	148.5	109	90
Average rank:	**3**	**4**	**2**	**1**

Table 5.21: Sum of ranks of the standardized M-factors from the table 5.18 for p+Ag collisions at 1.2, 1.9, and 2.5 GeV.

Energy	Model			
	ABLA07	GEM2	GEMINI++	SMM
1.2 GeV	38.5	45	43	33.5
1.9 GeV	39.5	49	41.5	30
2.5 GeV	42	49	39	30
Sum of ranks:	120	143	123.5	93.5
Average rank:	**2**	**4**	**3**	**1**

Table 5.22: Sum of ranks of the standardized M-factors from the table 5.19 for p+Au collisions at 1.2, 1.9, and 2.5 GeV.

Energy	Model			
	ABLA07	GEM2	GEMINI++	SMM
1.2 GeV	43.5	39.5	48	29
1.9 GeV	35.5	37.5	59	28
2.5 GeV	35	37	59	29
Sum of ranks:	114	114	166	86
Average rank:	**2.5**	**2.5**	**4**	**1**

The SMM model has the smallest sum of ranks for all targets when the sum is extended over all energies. Moreover it has the smallest sum of ranks for each single energy with the exception of Al target and 1.2 GeV proton beam where the GEMINI++ is superior.

The situation of other models is not so clear. For example the sum of ranks of the GEMINI++ combined with INCL4.6 is on the second place for Al, on the third for Ag and on the fourth for Au. Thus it seems that the GEMINI++ works in the best way for light targets but its predictions deteriorate with increase of the mass of the target.

Quite opposite result is obtained for ABLA07. This model describes better data obtained for heavier targets. Similar effect is present for GEM2, which has the lowest average rank for Al and Ag targets but for Au target it has the same rank as GEMINI++, just after the best SMM model.

It is interesting to make the ranking of models using A-factor instead of the M-factor. Since the A-factor cannot be used for validation of models according to the same procedure as that for the M-factor, the values of A-factor are not written in the tables but are presented in the following figures for Al, Ag and Au targets, separately. This has an additional advantage to allow for comparison of the quality of description of data for various ejectiles.

It can be stated that

- values of the A-factor are significantly smaller for the LCP than for IMF in the case of the Ag and Au targets. The effect is weaker for Al target, however still visible. This agrees with the fact that for heavy targets the spectra of LCP are in general much better reproduced than IMF data by all models.
- In the case of Al target the SMM model gives the smallest A-factor for ^{6}He and for ^{8}Li among all models and ejectiles. However, the SMM model completely fails in reproduction of ^{9}Li data - the A-factor is practically equal to one. This failure is also true for the Ag and Au targets (cf. fig. 5.31).
- It seems that the SMM model is superior to other models , i.e. it has the smallest A-values (with exception of ^{9}Li isotope as it was mentioned above).
- The A-factor values increase with the beam energy which is most pronounced for the Al target and almost not visible for Au target (at least in the case of LCP).

The conclusions derived from the A-factor values agree with those obtained from the M-factor and with the qualitative comparisons on the basis of figs. 5.22 - 5.37.

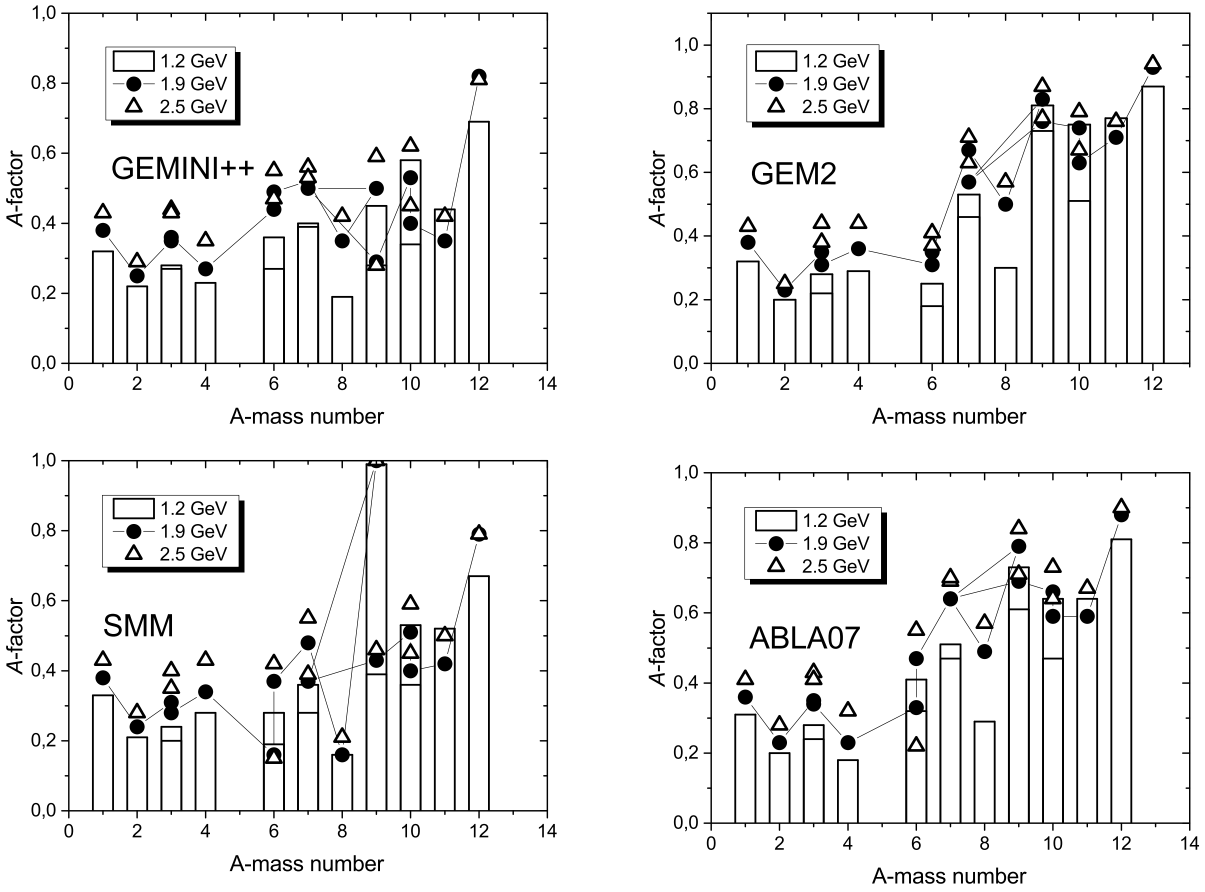

Figure 5.38: The *A*- factor dependence on the mass of ejectiles for p+Al collisions at three proton beam energies: 1.2 GeV, 1.9 GeV and 2.5 GeV. The calculations with ABLA07 are shown in the lower-right panel, the GEM2, GEMINI++, and SMM in the upper-right, upper-left and lower-left panels respectively.

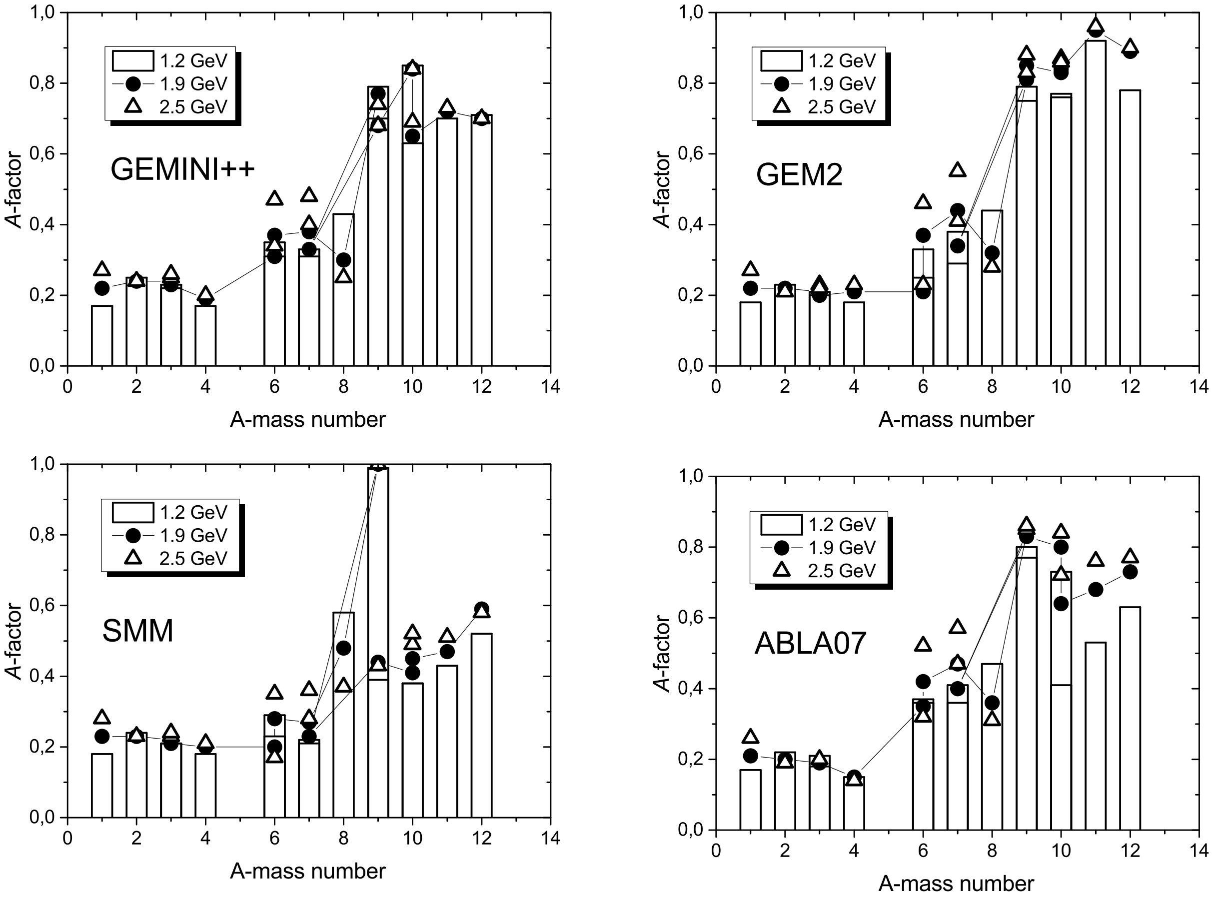

Figure 5.39: The A- factor dependence on the mass of ejectiles for p+Ag collisions at three proton beam energies: 1.2 GeV, 1.9 GeV and 2.5 GeV. The calculations with ABLA07 are shown in the lower-right panel, the GEM2, GEMINI++, and SMM in the upper-right, upper-left and lower-left panels respectively.

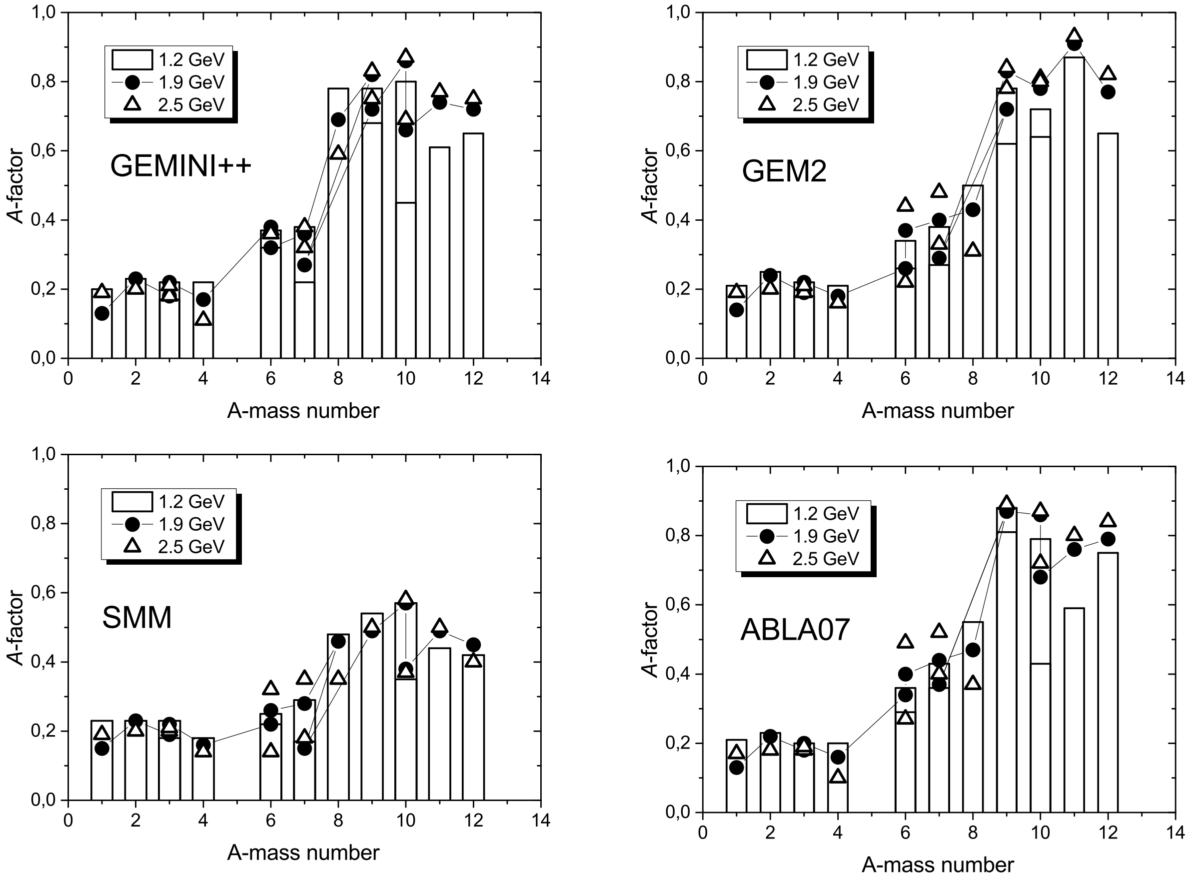

Figure 5.40: The *A*- factor dependence on the mass of ejectiles for p+Au collisions at three proton beam energies: 1.2 GeV, 1.9 GeV and 2.5 GeV. The calculations with ABLA07 are shown in the lower-right panel, the GEM2, GEMINI++, and SMM in the upper-right, upper-left and lower-left panels respectively.

5.2.3 Energy spectra and angular distributions of $d^2\sigma/d\Omega dE$ of neutrons from p+Al, p+In and p+Pb collisions

The largest cross sections for proton induced reactions correspond to the emission of nucleons. It was discussed in the chapter 5.2.2 that the experimental spectra of protons for all studied targets can be reproduced qualitatively by the applied models, however systematic deviations of the cross sections are observed, especially for lightest target (Al) and for the highest beam energy (2.5 GeV). Therefore it is interesting from scientific point of view and very important for many applications of neutrons (e.g. in designing the spallation sources of neutrons) to check quality of reproduction of the neutron cross sections by the theoretical models. In the present chapter the calculations of double differential cross sections $d^2\sigma/d\Omega dE$ of the neutrons produced in collisions of protons with light (Al), intermediate mass (In), and heavy (Pb) atomic nuclei are investigated for broad range of the proton energies from 256 MeV up to 3000 MeV. The results of calculations are compared to the experimental data in three figures below; fig. 5.41, 5.42 and 5.43.

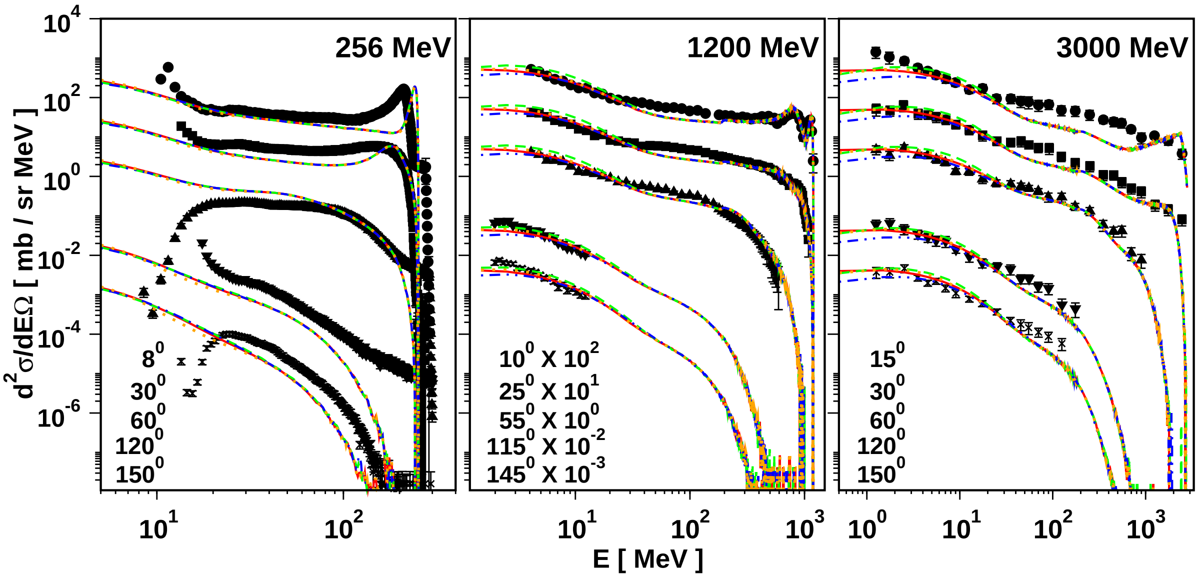

Figure 5.41: The experimental $d^2\sigma/d\Omega dE$ spectra of neutrons measured at three proton beam energies - 256 [91], 1200 [81], and 3000 MeV [91] on the Al target (symbols) together with predictions of INCL4.6 model coupled to ABLA07 (green - dashed line), GEM2 (orange - dotted line), GEMINI++ (blue - dashed-dotted line, and SMM (red - solid line) To distinguish data at different angles the cross sections were multiplied by different scaling factors as listed on the figure.

It can be stated that all models produce very similar energy and angular dependence of the cross sections - the lines corresponding to the different models in the above mentioned figures are almost overlapping even at the lowest neutron energies. There is a visible trend in improving the description of the data from low to intermediate energies and from light to heavier targets. In the best case (Pb target and 1200 MeV proton beam energy) almost full energy range of the spectra as well as the angular dependence seem to be well reproduced (cf. the middle panel of fig. 5.43). Even the quasielastic region of the spectra is satisfactorily described.

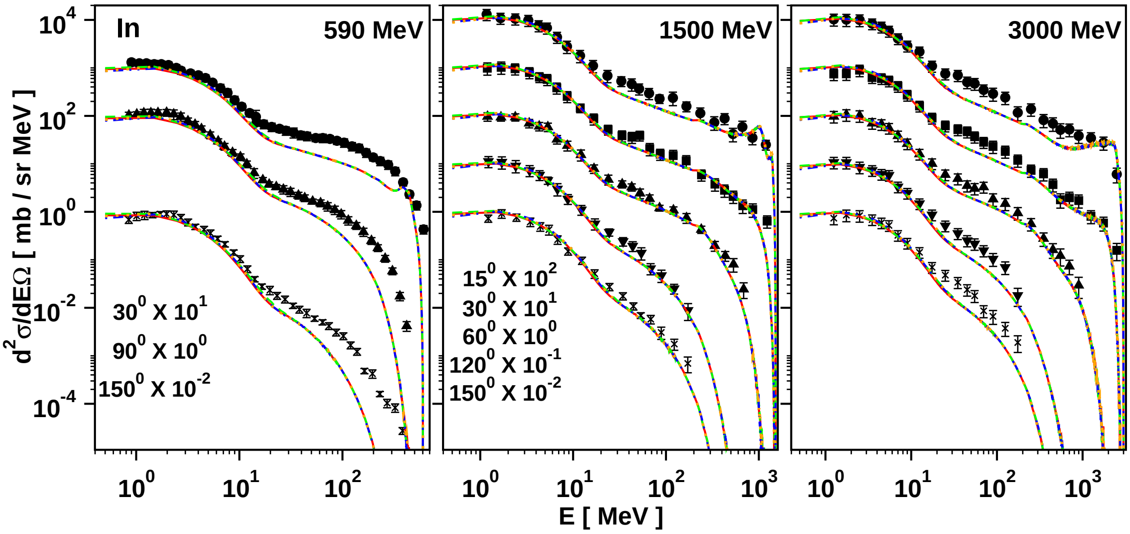

Figure 5.42: The same as on fig. 5.41 but for In target at 590 [92], 1500 [80], and 3000 MeV [80].

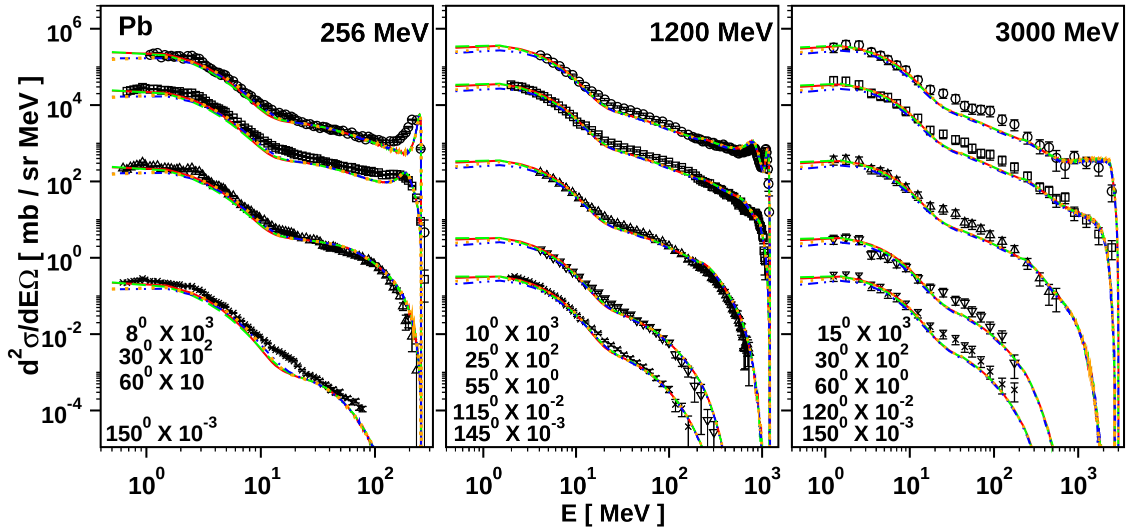

Figure 5.43: The same as on fig. 5.41 but for Pb target at 256 [91], 1200 [81], and 3000 MeV [91].

However, there are systematic deviations of the model predictions from the experimental data. They are most pronounced in the neutron energy range of 30 - 150 MeV - the same as that for the proton and LCP production cross sections at intermediate and high beam energies (cf. fig. 5.22 as well as Appendix E).

Chapter 6

Summary and conclusions

The present work is devoted to validation and ranking of different models of the spallation reactions.

The proposal of validation of spallation models was formulated in the present thesis (cf. In the chapter 5) to be realized as the testing of the statistical hypothesis which claims that the expectation value of the data is equal to the value calculated by the model (1.1). It was for the first time in the literature emphasized that in the case of models which use the Monte Carlo method for numerical calculations the model values are also biased by the statistical errors, therefore the above hypothesis has to be modified to the equality of expectation values of the data and model values (4.1).

To perform the testing of statistical hypothesis the probability density function of used test factors has to be established. As far we know such information is lacking for the factors used in the literature. Therefore the efforts have been undertaken to find statistical properties of these factors. It was found that most of the factors proposed for this purpose do not have the desired features. Especially they are frequently not symmetrical in respect to exchange of the experimental and theoretical values which may result in misleading judgments in providing the ranking to different models.

Only two factors proposed in the literature have the appropriate properties, namely the H-factor (4.4) which is weighting data by their errors and $< F >$-factor (4.19) which compares the experimental and theoretical cross sections without taking errors into consideration.

In the present work the exact formula for the probability density function of the H-factor has been derived for the situation of the perfect agreement of model and experimental cross sections (cf. Appendix A). This enables one to use the H-factor for validation of the models according to prescription discussed in the chapter 5.

It was proposed to introduce new deviation factor (called M-factor (4.2.1)) which has similar properties like the H-factor but is more intuitive. The validation of all data in the present thesis was performed using the M-factor (after proving that it gives the equivalent conclusions like the H-factor).

Furthermore, another new deviation factor (the A-factor (4.28)) was proposed which is independent of the errors of the cross sections, thus it is not biased by larger weights of the ejectiles with larger cross sections (cf. sec. 4.2.2). This factor is much more intuitive than the $< F >$-factor previously used in the literature.

All these considerations were necessary to make the quantitative judgements of the performances of different spallation models.

Such a task has been undertaken by scientific community since more than two decades. The conclusion from those studies is that the goal may be achieved only by iterative procedure which consists in successive development of models and exact measurements of new data which can put additional constraints to all hypothetical reaction mechanisms. Thus, the present investigations have applied the achievements of previous benchmark studies as the starting point:

- The selection of models which are used in the present work is based on the last benchmark of spallation models [82] which showed that the most promising model for the first stage of the reaction is the INCL4.5 model. In the present study the newest version of it, i.e. INCL4.6 has been used. For the models of the second stage of the reaction; ABLA07, GEMINI++, SMM and GEM2 models were applied.

- To obtain new insight in the action of these models in comparison to previous studies several sets of new experimental data were analyzed with special emphasis on LCP and IMF data for broad range of proton beam energies (from 180 MeV up to 3000 MeV). These data are representative to full range of nuclei from Al up to Pb.

- The calculations for the selected data sets have been done with all the models listed above and the qualitative judgment of the obtained results have been performed. The following most important conclusions have been formulated:

    1. The data of composite LCP and IMF up to atomic mass number $\sim$ 13 - 14 (cf. fig. 5.11) show a need to include the mechanism which is responsible for high energy part of the spectra. The present algorithm of the coalescence applied in the INCL4.6 model seems to work reasonably well for light charged particles but it produces too flat tail of the spectra for IMF, especially at beam energies of several hundreds MeV.
    2. The above deficiency seems not to influence significantly the properties of the excited residual nuclei after the first stage of the reactions. However, the analysis of the isotopic cross sections from p+Xe collisions at E_p=500 MeV indicates that their distributions are systematically overestimated (or underestimated) by all models for the heaviest isotopes of given element.
    3. The effect which may be important both, for understanding of the reaction mechanism as well as for numerous applications of the spallation reactions is the fact that the proton and neutron spectra are underestimated by model cross sections in the nucleon energy range from about 30 MeV to 150 MeV. This effect increases systematically with increasing beam energy and is more pronounced for light targets than for heavy ones. This is illustrated by fig. 6.1 in which the spectra of protons measured for Al and Au target at 1.2 GeV and 2.5 GeV are compared with spectra of neutrons obtained at 1.2 GeV and 3.0 GeV on Al and Pb targets.

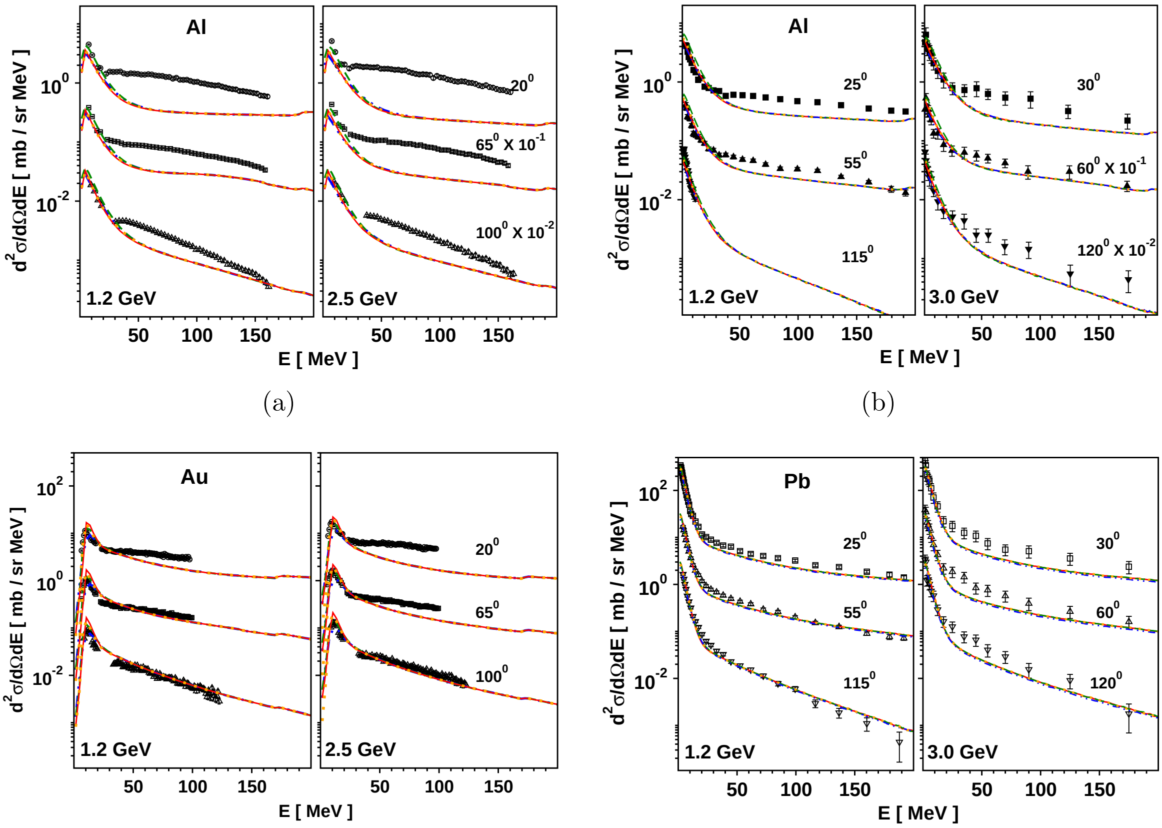

(a)

(b)

(c)

(d)

Figure 6.1: Proton and Neutron $d^2\sigma/d\Omega dE$ representative figures for the qualitative comparison. The data are compared with four different models which give practically the same results for ejectile energies larger than $\approx$ 30 MeV where the contribution from the first stage of the reaction dominates. Subfigures 6.1(a), 6.1(c) represent the proton spectra for two targets Al and Au as shown above. For neutrons, the spectra are depicted in subfigures 6.1(b) and 6.1(d) but instead of Au target, Pb target is chosen and beam energy 2500 MeV is replaced by 3000 MeV.

4. A similar effect, but less pronounced may be observed also in the composite LCP spectra starting from the energy around 30 MeV - cf. Appendix E.

   The source of this systematic underestimation of the data by the model may be the negligence of some important mechanism contributing to the reaction, e.g. possibility of emission of dynamically created unstable clusters during the first stage of the reaction.

5. The analysis of low energy part of LCP spectra, which is dominated by contribution from the second stage of the reaction, indicated that (cf. Appendix E:

   - all the models reproduce position of the maximum of each spectrum,
   - however, the magnitude of the maximum is different for different models. This effect is small for tritons and ^{4}He but it increases significantly for

protons, deuterons and ^{3}He. Therefore, the precise data for low energies of LCP (in the neighborhood of the Coulomb barrier) are desirable to put more stringent constraints to the reaction mechanism of the second stage of the reaction.

There were observed some specific deficiencies of the individual codes which may need immediate attention of the model developers e.g., it was found that ABLA07 was not producing the ^{8}Li. The problem was resolved after discussion with the author of ABLA07. Similarly, GEMINI++ model significantly overestimates the production of ^{6,7,8}Li (cf. ,e.g., fig. 5.28), isotopes for heavier targets (like Au) but on contrary it underestimates strongly the production of ^{6}He for all targets (cf. fig. 5.27). It was also found that the SMM code predicts negligibly small cross section for the ^{9}Li production (cf. fig. 5.31).

To compare the qualitative conclusions with quantitative analysis the ranking of models was done. For this purpose the following activities were undertaken:

- It was tested on three sets of data (isobaric total production cross sections for p+Al reactions at Ep=180 MeV, set of spectra $d\sigma/dEd\Omega$ measured for intermediate mass fragments from Li to Mg in p+Ag reactions at Ep=480 MeV, isotopic cross section for production of residua in p+Xe reactions at Ep=500 MeV) that H- and M-deviation factors lead to almost the same ranking of models, especially when tied ranks are allowed. Application of these two factors for validation of models shows that the H-factor puts in general more stringent constraints to the models. Since the perfect agreement of model and experimental cross sections appears quite rarely the use of less restrictive M-factor seems to be well justified.
- The broad range of observables measured for targets representative for light nuclei (Al), for intermediate mass nuclei (Ag) and for heavy nuclei (Au) has been compared with calculations performed by means of INCL4.6 model (for the first stage of the reaction) coupled to four most popular models of the second stage of the reaction, i.e. ABLA07, GEM2, GEMINI++ and SMM. It was found that all these models produce similar results for light charged particles (LCP) but they give quite different results for intermediate mass fragments (IMF) and heavy residua:
  - The SMM model was in most cases superior in respect to other models.
  - GEMINI++ gave good description of reactions on light target nuclei but the agreement with data deteriorates when the mass of the target nuclei increases.
  - GEM2 and ABLA give poorer description than GEMINI for light nuclei but the agreement of their predictions with data become better and almost equivalent for Au.

The general conclusion of the present investigations is that the recent development of the spallation models leads to improved description over a broad range of the data. However, the agreement of the experimental and theoretical cross sections is still not satisfactory showing some systematic deviations of model predictions from the data. This indicates a need to reexamine the mechanisms implemented in the present form of the theoretical models of the spallation reactions.

Appendix A

Derivation of properties of the H-test

The H-test is defined by the formula [123]:

$$\boxed{H \equiv \left[\frac{1}{N}\sum_{i=1}^{N}\left(\frac{\sigma_i^{\exp} - \sigma_i^{calc}}{\Delta\sigma_i^{\exp}}\right)^2\right]^{1/2} \qquad (A.1)}$$

where $\sigma_i^{\exp}, \sigma_i^{calc}$ and $\Delta\sigma_i^{\exp}$ denote the experimental cross section, the calculated cross sections, and the error of the experimental cross section, respectively.

In the case when the assumptions (1.1) and (4.1)are fulfilled the sum is equal to sum of squares of N independent, standard normal variables N(0,1). Such a random variable is called χ_N^2 (*chi-squared with N degrees of freedom*):

$$\sum_{i=1}^{N}\left(\frac{\sigma_i^{\exp} - \sigma_i^{calc}}{\Delta\sigma_i^{\exp}}\right)^2 = \sum_{i=1}^{N}\left(\frac{\sigma_i^{\exp} - E\left(\sigma_i^{\exp}\right)}{\Delta\sigma_i^{\exp}}\right)^2 \equiv \chi_N^2$$

Then the H-test (A.1) is equal to:

$$H \equiv \sqrt{\frac{\chi_N^2}{N}} \tag{A.2}$$

The χ_N^2 probability density function has the following form [126]:

$$f(y) = \begin{cases} \frac{1}{2^{N/2}\Gamma(N/2)} \exp\left(-\frac{y}{2}\right) \cdot y^{N/2-1} & \text{for } y \geq 0 \\ 0 & \text{for } y < 0 \end{cases} \tag{A.3}$$

where symbol y is used instead χ_N^2.

Let us first find probability distribution of the x variable defined as the square root of the chi-square variable: $x \equiv \sqrt{y}$. For continuous monotonic function $x(y)$ the probability distribution function $g(x)$ may be expressed by the probability distribution function $f(y)$ of variable y as follows:

$$g(x) = f(y(x)) \left| \frac{dy(x)}{dx} \right| \tag{A.4}$$

i.e.

$$\begin{aligned} g(x) &= \frac{1}{2^{N/2}\Gamma(N/2)} \cdot \exp(-y(x)^2/2) \cdot y(x)^{N/2-1} \cdot \left| \frac{dy(x)}{dx} \right| = \\ &= \frac{1}{2^{N/2}\Gamma(N/2)} \cdot \exp(-x^2/2) \cdot (x^2)^{N/2-1} \cdot |2x| = \\ &= \frac{1}{2^{N/2-1}\Gamma(N/2)} \cdot \exp(-x^2/2) \cdot x^{N-1} \end{aligned}$$

thus

$$\boxed{g(x) = \begin{cases} \frac{1}{2^{N/2-1}\Gamma(N/2)} \cdot \exp(-x^2/2) \cdot x^{N-1} & \text{for } x \geq 0 \\ 0 & \text{for } x < 0 \end{cases} \qquad \text{(A.5)}}$$

The above distribution is usually called χ_N-distribution (*chi-distribution with N degrees of freedom*) [126]. Now it is straightforward to find distribution of H-variable which is equal to the above x variable divided by $\sqrt{N}$, i.e.,

$$x(H) = \sqrt{N} \cdot H.$$

$$f(H) = g(x(H)) \left| \frac{dx}{dH} \right| = g(x(H)) \cdot \sqrt{N}$$

$$\begin{aligned} f(H) &= \frac{1}{2^{N/2-1}\Gamma(N/2)} \exp(-x(H)^2/2) \cdot (x(H))^{N-1} \cdot \sqrt{N} \\ &= \frac{\sqrt{N}}{2^{N/2-1}\Gamma(N/2)} \exp(-NH^2/2) \cdot (\sqrt{N}H)^{N-1} = \\ &= \frac{N^{N/2}}{2^{N/2-1}\Gamma(N/2)} \exp\left(-\frac{NH^2}{2}\right) \cdot H^{N-1} \end{aligned}$$

The probability distribution function of the H-test reads finally as:

$$\boxed{h(H) = \frac{N^{N/2}}{2^{N/2-1}\Gamma(N/2)} \exp\left(-\frac{NH^2}{2}\right) \cdot H^{N-1} \qquad \text{(A.6)}}$$

The expectation value $E(H)$ and standard deviation $\sigma(H) \equiv \sqrt{var(H)}$ may be calculated using the probability distribution function (A.6) but they may be even more easily found by scaling $E(x)$ and $E(x^2)$, i.e. $H \equiv x/\sqrt{N}$ thus

$$\begin{aligned} E(H) &= E(\frac{1}{\sqrt{N}} \cdot x) = \frac{1}{\sqrt{N}} \cdot E(x) \\ E(H^2) &= E(\frac{1}{N} \cdot x^2) = \frac{1}{N} \cdot E(x^2) \end{aligned}$$

The mode x_m (i.e. the position of the maximum of the χ_N probability density function), its expectation value $E(x)$, and its variance $var(x)$ are equal to [126], p.73:

$$\begin{aligned} x_m &= \sqrt{N-1} \quad \text{for} \quad N \geq 1 \\ E\left(x\right) &= \sqrt{2}\,\frac{\Gamma\left(\frac{N+1}{2}\right)}{\Gamma\left(\frac{N}{2}\right)} \\ var\left(x\right) &= N - E\left(\chi_N x\right)^2 \end{aligned}$$

therefore the mode H_m, the expectation value $E(H)$, and the variance $var(H)$ are:

$$\boxed{\begin{aligned} H_m &= \sqrt{\frac{N-1}{N}} && \text{(A.7)} \\ E(H) &= \sqrt{\frac{2}{N}} \cdot \frac{\Gamma\left(\frac{N+1}{2}\right)}{\Gamma\left(\frac{N}{2}\right)} && \text{(A.8)} \\ var(H) &= 1 - E(H)^2 && \text{(A.9)} \end{aligned}}$$

Appendix B

Probability density function of $t \equiv \sigma|z|$ for standard normal z

$$f(z) = \frac{1}{\sqrt{2\pi}} \exp\left(-\frac{z^2}{2}\right)$$

To find probability distribution function $g(t)$ for $t \equiv \sigma|z|$ we would like to use the standard prescription valid for monotonic, continuous functions:

$$g(t) = f(z(t)) \left|\frac{dz(t)}{dt}\right|$$

However the function $t \equiv \sigma|z|$ is monotonic only in two separate ranges of z: (1) $z \in (-\infty, 0]$ and (2) $z \in [0, +\infty)$ thus the resulting $g(t)$ should be equal to sum of two contributions corresponding to these separate ranges of z.

$$\begin{aligned} g(t) &= f(t = -\sigma z) \left|\frac{d(-t/\sigma)}{dt}\right| + f(t = \sigma z) \left|\frac{d(t/\sigma)}{dt}\right| = \\ &= \frac{1}{\sqrt{2\pi}\;\sigma} \exp\left(-\frac{t^2}{2\sigma^2}\right) + \frac{1}{\sqrt{2\pi}\;\sigma} \exp\left(-\frac{t^2}{2\sigma^2}\right) = \\ &= \sqrt{\frac{2}{\pi\sigma^2}} \exp\left(-\frac{t^2}{2\sigma^2}\right) \end{aligned}$$

Thus, finally

$$\boxed{g(t) = \sqrt{\frac{2}{\pi\sigma^2}} \exp\left(-\frac{t^2}{2\sigma^2}\right) \quad \text{for } \; t \geq 0 \qquad \text{(B.1)}}$$

The expectation value $E(t)$ and variance $var(t)$ may be found by integration:

$$\begin{aligned}
E(t) &= \sqrt{\frac{2}{\pi\sigma^2}} \int\limits_0^\infty t \, \exp\left(-\frac{t^2}{2\sigma^2}\right) dt = \\
&= \sqrt{\frac{2}{\pi\sigma^2}} \int\limits_0^\infty \sigma(2y)^{1/2} \, \exp\left(-y\right) \; \sigma(2y)^{-1/2} dy = \\
&= \sqrt{\frac{2}{\pi}} \, \sigma \int\limits_0^\infty y^0 \, \exp\left(-y\right) dy = \\
&= \sqrt{\frac{2}{\pi}} \, \sigma \, \Gamma(1) = \\
&= \sqrt{\frac{2}{\pi}} \, \sigma
\end{aligned}$$

where the following substitution was done:

$$y \equiv t^2/(2\sigma^2) \rightarrow t = \sigma(2y)^{1/2}, \quad dt = \sigma dy (2y)^{-1/2}$$

To find variance $var(t) \equiv E(t^2) - E(t)^2$ one should evaluate integral for $E(t^2)$ using the same substitution.

$$\begin{aligned}
E(t^2) &= \sqrt{\frac{2}{\pi\sigma^2}} \int\limits_0^\infty t^2 \, \exp\left(-\frac{t^2}{2\sigma^2}\right) dt = \\
&= \sqrt{\frac{2}{\pi\sigma^2}} \int\limits_0^\infty \sigma^2(2y) \, \exp\left(-y\right) \sigma(2y)^{-1/2} dy = \\
&= \sqrt{\frac{2}{\pi}} \cdot \sigma^2 \sqrt{2} \int\limits_0^\infty y^{1/2} \, \exp\left(-y\right) dy = \\
&= \frac{2}{\sqrt{\pi}} \sigma^2 \Gamma\left(\frac{3}{2}\right) = \\
&= \frac{2}{\sqrt{\pi}} \sigma^2 \Gamma\left(\frac{1}{2}\right) \cdot \frac{1}{2} = \\
&= \sigma^2
\end{aligned}$$

Finally

$$E(t) = \sqrt{\frac{2\sigma^2}{\pi}} \tag{B.2}$$

$$\operatorname{var}(t) = \sigma^2 \left(\frac{\pi - 2}{\pi} \right) \tag{B.3}$$

Appendix C

Probability density function of $y = x_0/x$ for normal x

The probability density function of $y = x_0/x$ where the random variable x has normal distribution with expectation value $E(x) = x_0$ and standard deviation σ:

$$f(x) = \frac{1}{\sqrt{2\pi}\sigma} \exp\left[-\frac{(x - x_0)^2}{2\sigma^2}\right]$$

can be found from formula (A.4) writing

$$y = \frac{x_0}{x} \to x = \frac{x_0}{y}, \quad \frac{dx}{dy} = -\frac{x_0}{y^2}$$

thus

$$\boxed{g(y) = \frac{x_0}{\sqrt{2\pi}\sigma} \exp\left[-\frac{x_0^2\,(1/y - 1)^2}{2\sigma^2}\right] \cdot \frac{1}{y^2} \qquad \text{(C.1)}}$$

To get a qualitative understanding of the properties of this distribution values of two probability density functions have been calculated for $x_0 = 10,\ \sigma = 1$ and $x_0 = 10,\ \sigma = 2$. Results of the calculations are presented on fig. C.1 as the solid and the dashed line, respectively. As can be seen the distribution is similar to the Gaussian distribution for the ratio $x_0/\sigma = 10$ but it becomes evidently asymmetric with the tail of the distribution extended towards large values of y when $x_0/\sigma = 5$. Furthermore, the mode (position of the maximum) of the probability distribution function $f(y)$ is in both cases lower than one and shifts to smaller y values when σ increases. Numerically calculated expectation value $E(y)$ of $y \equiv 10/x$ is equal to ≈ 1.01 for $\sigma = 1$ and to ≈ 1.04 for $\sigma = 2$ whereas the standard deviation $\sigma(y) \approx 0.10$ and ≈ 0.24, respectively.

This means that the expectation value of the ratio $\sigma^{cal}/\sigma^{exp}$ is in general case different from unity even in the case of perfect agreement of model and experimental data ($E(\sigma^{exp}) = \sigma^{cal}$) and, moreover, it depends on the relative error of the experimental data $\Delta(\sigma^{exp})/\sigma^{exp} \equiv \sigma/x_0$.

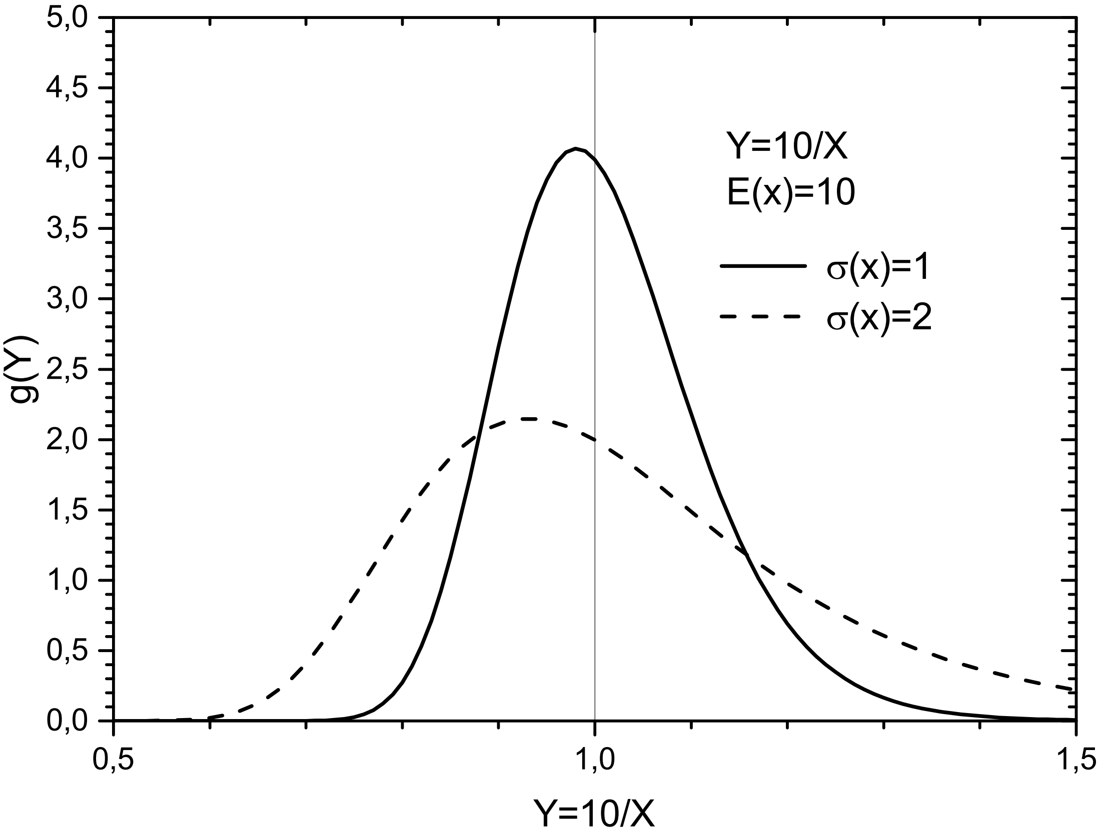

Figure C.1: The solid line represents probability density function of random variable $y \equiv 10/x$ where x has the Gaussian distribution with the expectation value $E(x) = 10$ and the standard deviation of $\sigma = 1$. The dashed line corresponds to the same variable $y = 10/x$ but for the case when standard deviation of x is larger ($\sigma = 2$).

Appendix D

Details of Monte Carlo simulations

The following assumptions have been done for Monte Carlo simulation of the statistical properties of the deviation factors:

1. The experimental cross section value σ^{exp} has been used as the estimate of the expectation value of the experimental cross section:

   $$\sigma^{exp} \rightarrow E\left(\sigma^{exp}\right) \tag{D.1}$$

   The same was done for the theoretical cross sections when it was calculated by the Monte Carlo procedure:

   $$\sigma^{cal} \rightarrow E\left(\sigma^{cal}\right) \tag{D.2}$$

2. The statistical experimental error $\Delta\left(\sigma^{exp}\right)$ has been used as the estimate of the standard deviation of the experimental cross section:

   $$\Delta(\sigma^{exp}) \rightarrow \sigma\left(\sigma^{exp}\right) \tag{D.3}$$

   The same assumption concerns the standard deviation of model calculations when they were done using the Monte Carlo method:

   $$\Delta(\sigma^{cal}) \rightarrow \sigma\left(\sigma^{cal}\right) \tag{D.4}$$

The above assumptions allow to simulate by Monte Carlo method the probability density function for the deviation factor in the case when the perfect agreement of data with model values is assumed (1.1):

$$E(\sigma^{exp}) = \sigma^{cal} \tag{D.5}$$

(valid in the case when only data are random variables).

Let us consider Monte Carlo sampling of the H-factor defined by formula (A.1) as an example:

$$H \equiv \left[\frac{1}{N}\sum_{i=1}^{N}\left(\frac{\sigma_i^{\mathrm{exp}} - \sigma_i^{calc}}{\Delta\sigma_i^{\mathrm{exp}}}\right)^2\right]^{1/2}$$

Due to equalities (D.5) and (D.3) each term in the sum above is equal to

$$\frac{\sigma_i^{\mathrm{exp}} - E(\sigma_i^{exp})}{\sigma(\sigma_i^{exp})} \equiv z$$

where $\sigma(\sigma_i^{exp})$ is used to represent the standard deviation of the experimental cross section σ_i^{exp}. Such a "z" variable is called *standardized random variable* and in the case when the experimental cross section can be treated as a gaussian variable (measurements with "good statistics"), its probability distribution is well known:

$$f(z) = \frac{1}{\sqrt{2\pi}} \exp\left(-\frac{z}{2}\right)^2 .$$

It has the expectation value $E(z) = 0$ and the standard deviation $\sigma(z) = 1$ independent of the expectation value $E(\sigma_i^{exp})$ and the standard deviation $\sigma(\sigma_i^{exp})$ of the cross sections. Values of this variable was generated by the standard FORTRAN subroutine RGAUS listed below.

The situation is more complicated in the case of data measured with poor statistics. Then the Poisson distribution should be used to sample values of the cross sections. For this purpose the number of events N which were stored in the experiment to determine the cross section value $\sigma_i^{\mathrm{exp}} = N \cdot FACTOR$ and the normalizing factor $FACTOR$ have to be known. If the experimental errors are of the statistical nature only then the determination of the N - value is straightforward from the relation:

$$\frac{\Delta\sigma_i^{\mathrm{exp}}}{\sigma_i^{\mathrm{exp}}} = \frac{FACTOR \cdot \sqrt{N}}{FACTOR \cdot N} = \frac{1}{\sqrt{N}}$$

The $FACTOR$ value may be found by comparing the cross sections measured at different ejectile energies in the same spectrum because they should differ only by N-values but must have the same normalizing $FACTOR$. Due to the approximation (D.1) the N-value may be treated as the expectation value of the number of events stored in the experiment to obtain the cross sections. Thus using the same $FACTOR$ and generating number of events by Monte Carlo method according to Poisson distribution with its parameter equal to N allows us to generate values of the cross sections and their statistical errors. For this purpose the standard FORTRAN subroutine RPOIS, listed below has been used.

The Gauss distribution was used as an approximation to the Poisson distribution when number of events N corresponding to the studied cross section was larger than 36. This corresponds to the ratio of standard deviation of gaussian variable to its expectation value $\Delta\sigma_i^{\mathrm{exp}}/\sigma_i^{\mathrm{exp}} = 1/6$, i.e. the negative values of the cross section could not practically appear in such a sampling.

The FORTRAN subroutines applied in the present calculations to sample Gauss and Poisson distributions use the RIBM subroutine listed below for generation of uniformly distributed variable in [0,1] range.

The random numbers with uniform, Gauss and Poisson distributions were sampled using the following FORTRAN routines: RIBM, RGAUS and RPOIS listed below.

```
C
CCC   IBM standard random number
C     starting seed e.g. IAL=22032203
C
      SUBROUTINE RIBM(RNDM,IAL)
      INTEGER*4 IAL
      REAL AL,RNDM
      IAL=IAL*65539
      IF(IAL)1187,1188,1188
1187  IAL=IAL+2147483647+1
1188  AL =IAL
      RNDM=AL*0.4656613E-9
      RETURN
      END
C
CCC   GAUSSIAN random number generator
C
      SUBROUTINE RGAUS(XG,IAL)
      INTEGER*4 IAL,J
      REAL XG,XXG
      XG =0.0
      DO J=1,12
      CALL RIBM(XXG,IAL)
      XG=XG+XXG
      ENDDO
      XG=XG-6.0
      RETURN
      END
C
```

```
C
CCC  POISSON random number generator
C    IN: IAL - seed for RIBM random number generator
C    XLMBDA - parameter λ of the Poisson distribution
C    OUT: NP - integer variable distributed according to Poisson p.d.
C
     SUBROUTINE RPOIS(NP,XLMBDA,IAL)
     INTEGER*4 IAL,K,NP
     REAL A,EXPML,XPOMO,XLMBDA
     EXPML =EXP(-XLMBDA)
     K=1
     A=1.0
1    CALL RIBM(XPOMO,IAL)
     A=XPOMO*A
     IF (A.LT.EXPML) THEN
     NP=K-1
     ELSE
     K=K+1
     GOTO 1
     ENDIF
     RETURN
     END
```

Appendix E

LCP spectra for p+Al and p+Au at Ep=1.2 and 2.5 GeV with expanded scale

In the present appendix the same LCP data and calculations are presented as those discussed in chapter 5.2.2 but with the modified scale of the differential cross sections as well as scale of the energy offering better distinction between results of different models of the second stage of the reaction.

The systematic underestimation of the experimental cross sections for LCP by the models is evident on figs. 5.22 - 5.26 for ejectile energies in the range from about 30 MeV to about 150 MeV. For these energies the contribution from the second stage of the reaction becomes much smaller than that from the intranuclear cascade describing the first stage of the process. Furthermore, the contribution of the second stage models to the theoretical cross sections is practically negligible for ejectile energies larger than 50 MeV. To have better insight in behavior of the spectra evaluated in the frame of various models of the second stage of the reactions the data for p+Al and p+Au collisions at the lowest (1.2 GeV) and the highest (2.5 GeV) proton beam energy are presented in figs. E.1 - E.10.

As can be seen on these figures all models reproduce position and shape of the maximum in the spectra, however different models predict different magnitude of the maximum. The difference in model predictions is relatively small for tritons and ^{4}He but it becomes as large as factor 2 for protons, deuterons and ^{3}He.

This result shows that exact data of LCP, measured for small energies of the ejectiles (in the neighborhood of the Coulomb barrier) may be very important for selection of the model offering the most realistic mechanism of the second stage of the reaction. Such a selection must be, however, accompanied by improved description of the first stage of the reaction which at present predicts the cross sections significantly different from data at LCP energies in the range of 30 - 150 MeV.

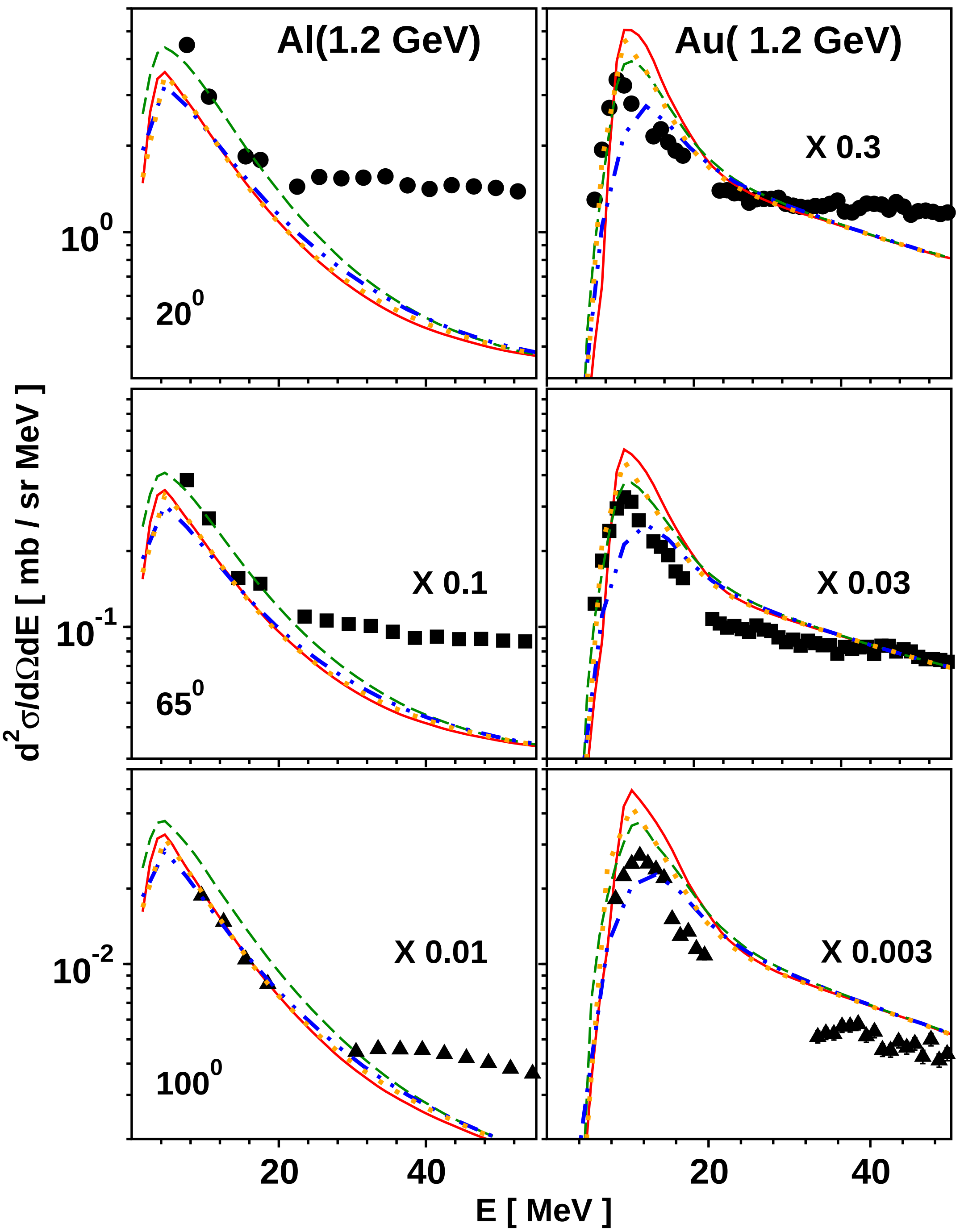

Figure E.1: Experimental spectra of **protons** measured at 20° (upper panels), 65° (middle panels) and 100° (lower panels) for Al target (left column of panels) and Au target (right column of panels) at proton beam energy of 1.2 GeV. This is expanded fig. 5.22 (without data for Ag target and proton beam energies 1.9 and 2.5 GeV).

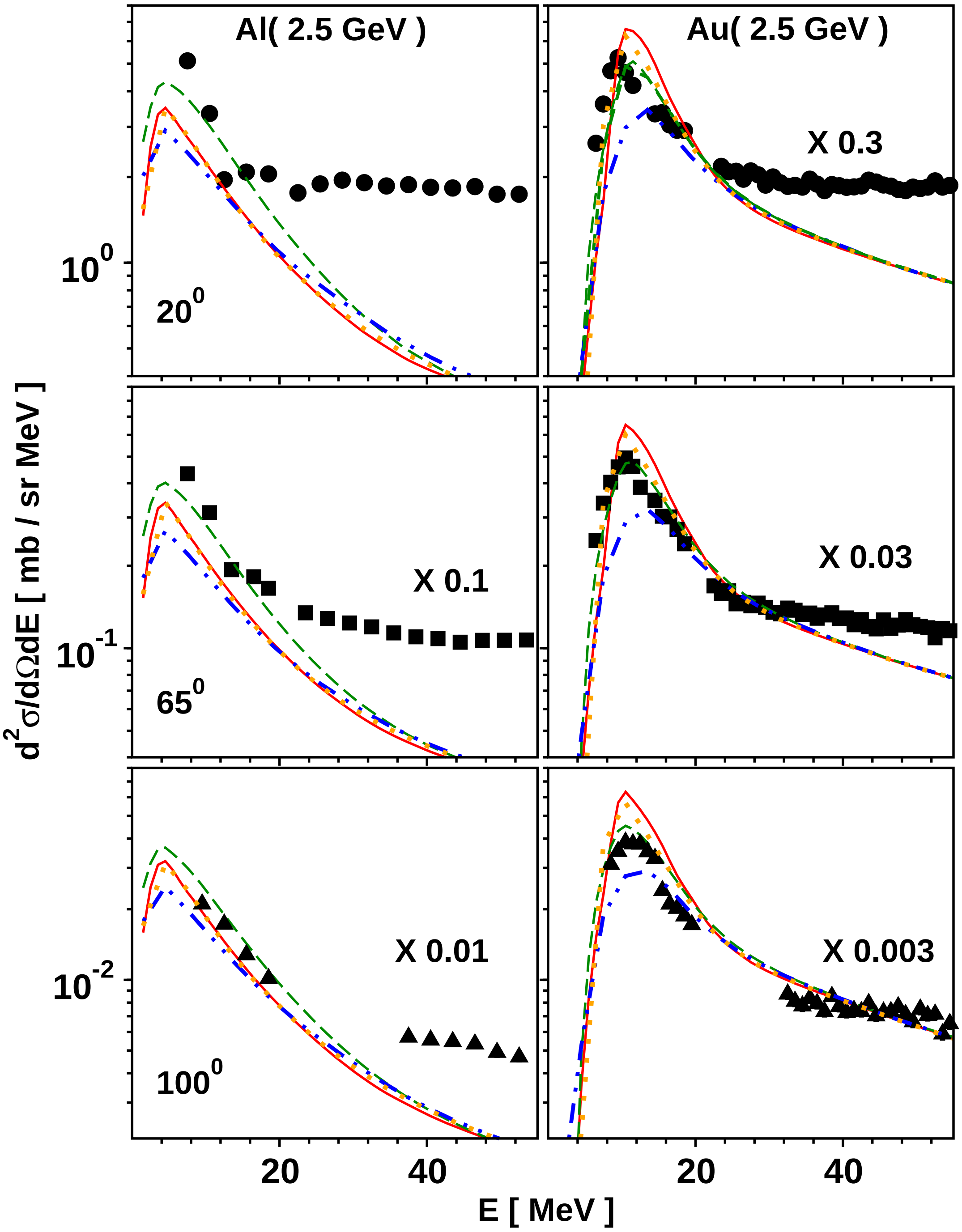

Figure E.2: Experimental spectra of **protons** measured at 20° (upper panels), 65° (middle panels) and 100° (lower panels) for Al target (left column of panels) and Au target (right column of panels) at proton beam energy of 2.5 GeV. This is expanded fig. 5.22 (without data for Ag target and proton beam energy 1.2 and 1.9 GeV).

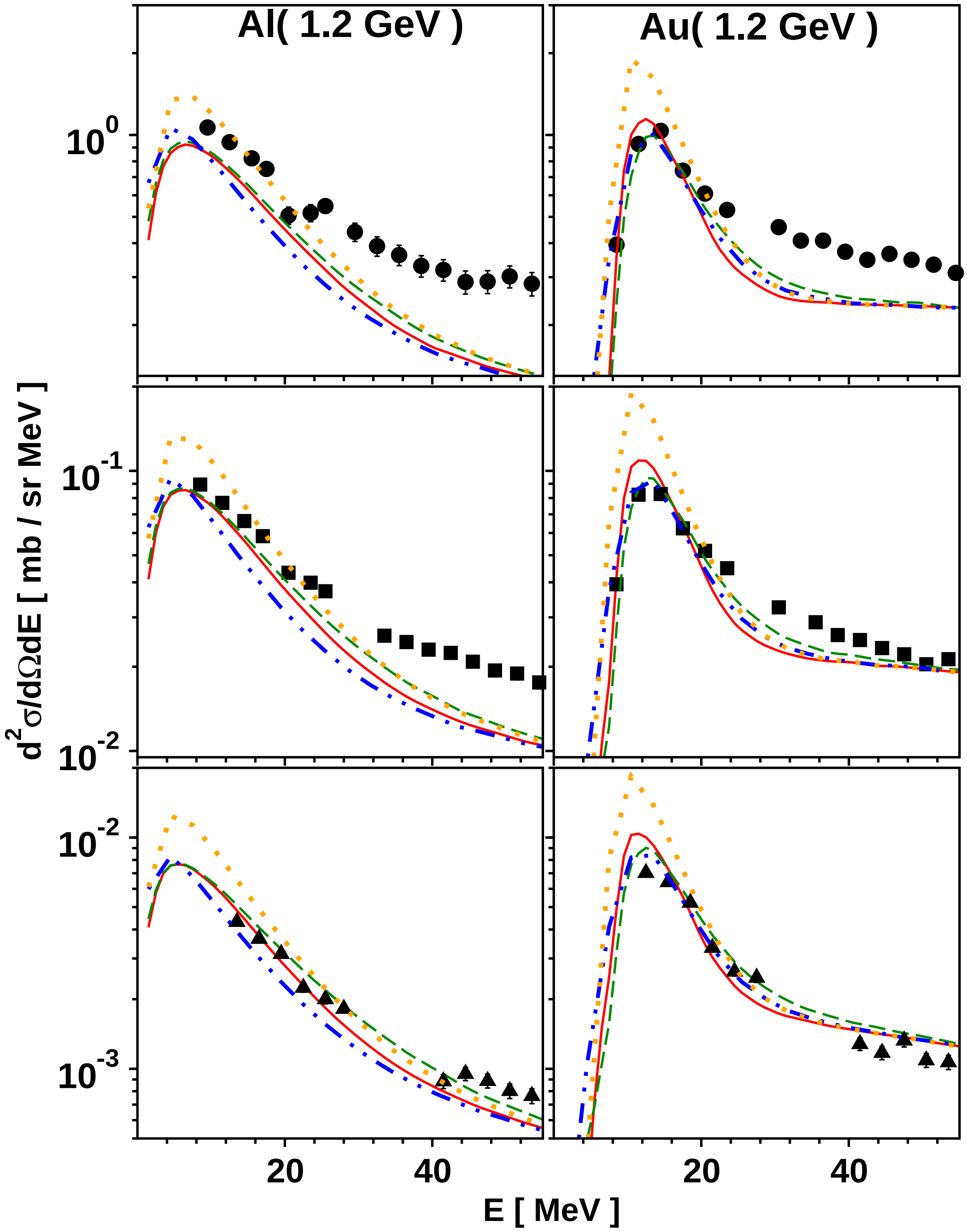

Figure E.3: Experimental spectra of **deuterons** measured at 20° (upper panels), 65° (middle panels) and 100° (lower panels) for Al target (left column of panels) and Au target (right column of panels) at proton beam energy of 1.2 GeV. This is expanded fig. 5.23 (without data for Ag target and proton beam energies 1.9 and 2.5 GeV). The same scaling factors for the cross sections at different angles and targets were used as for the protons (fig. E.1).

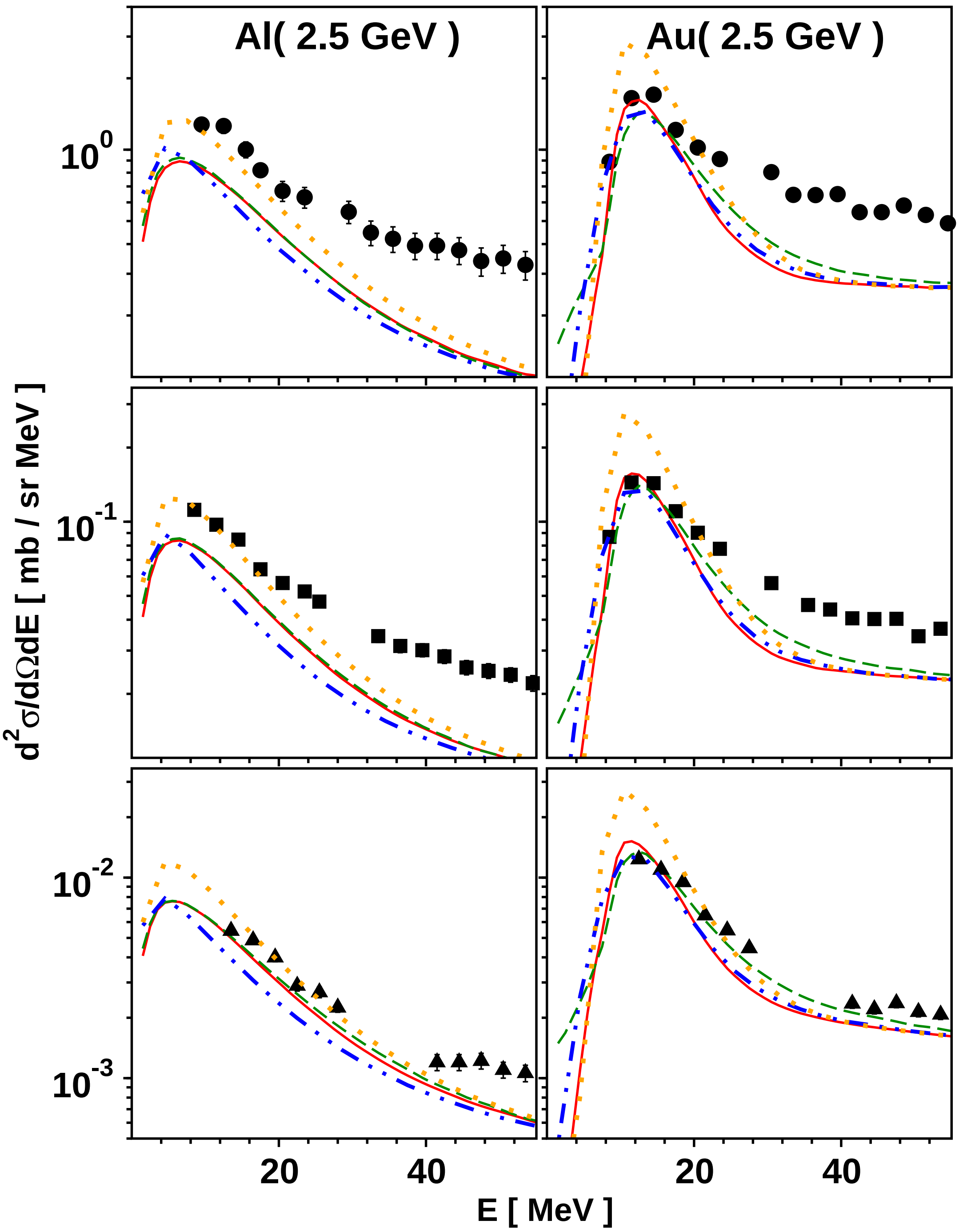

Figure E.4: Experimental spectra of **deuterons** measured at 20° (upper panels), 65° (middle panels) and 100° (lower panels) for Al target (left column of panels) and Au target (right column of panels) at proton beam energy of 2.5 GeV. This is expanded fig. 5.23 (without data for Ag target and proton beam energy 1.2 and 1.9 GeV). The same scaling factors for the cross sections at different angles and targets were used as for the protons (fig. E.2).

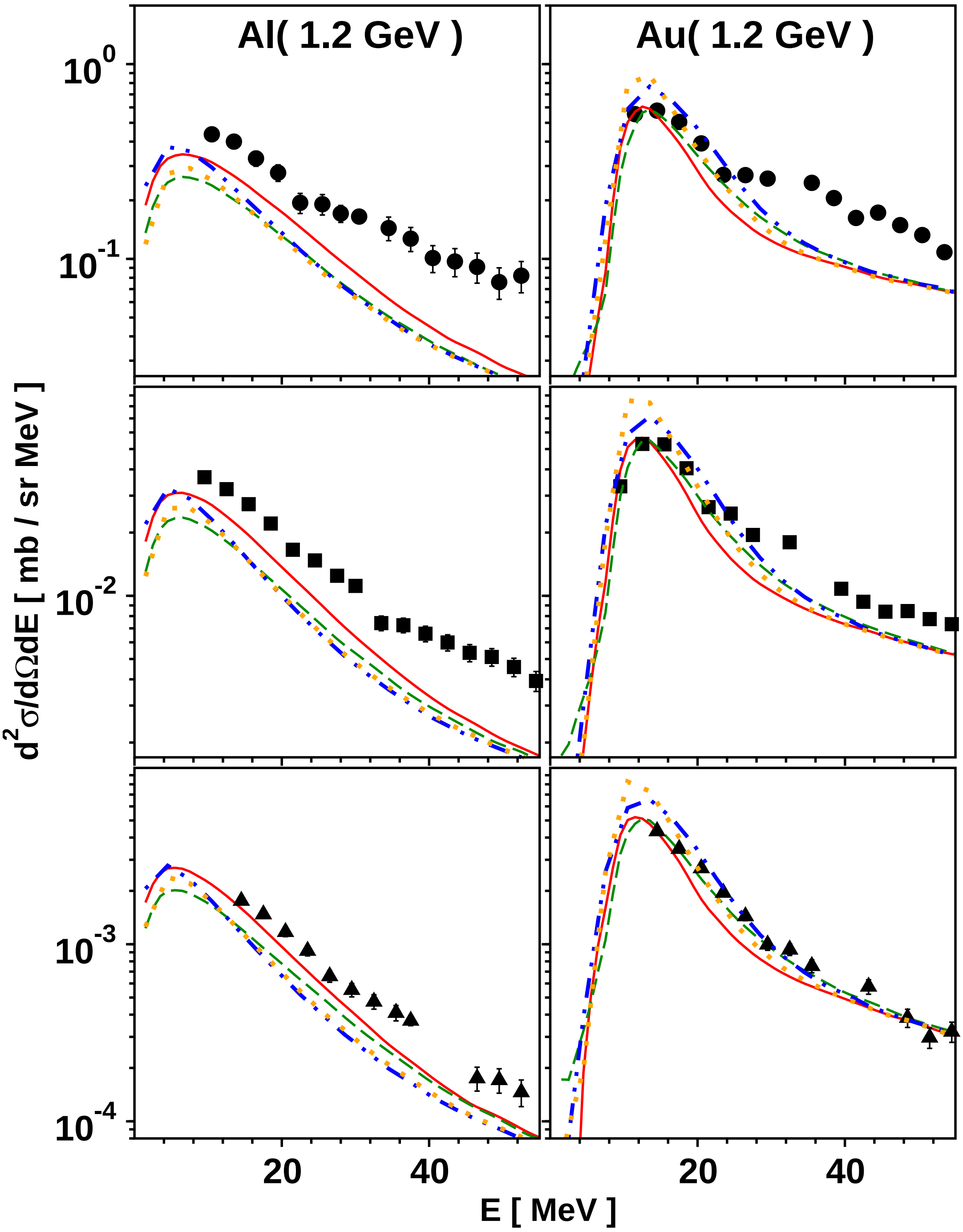

Figure E.5: Experimental spectra of **tritons** measured at 20° (upper panels), 65° (middle panels) and 100° (lower panels) for Al target (left column of panels) and Au target (right column of panels) at proton beam energy of 1.2 GeV. This is expanded fig. 5.24 (without data for Ag target and proton beam energies 1.9 and 2.5 GeV). The same scaling factors for the cross sections at different angles and targets were used as for the protons (fig. E.1).

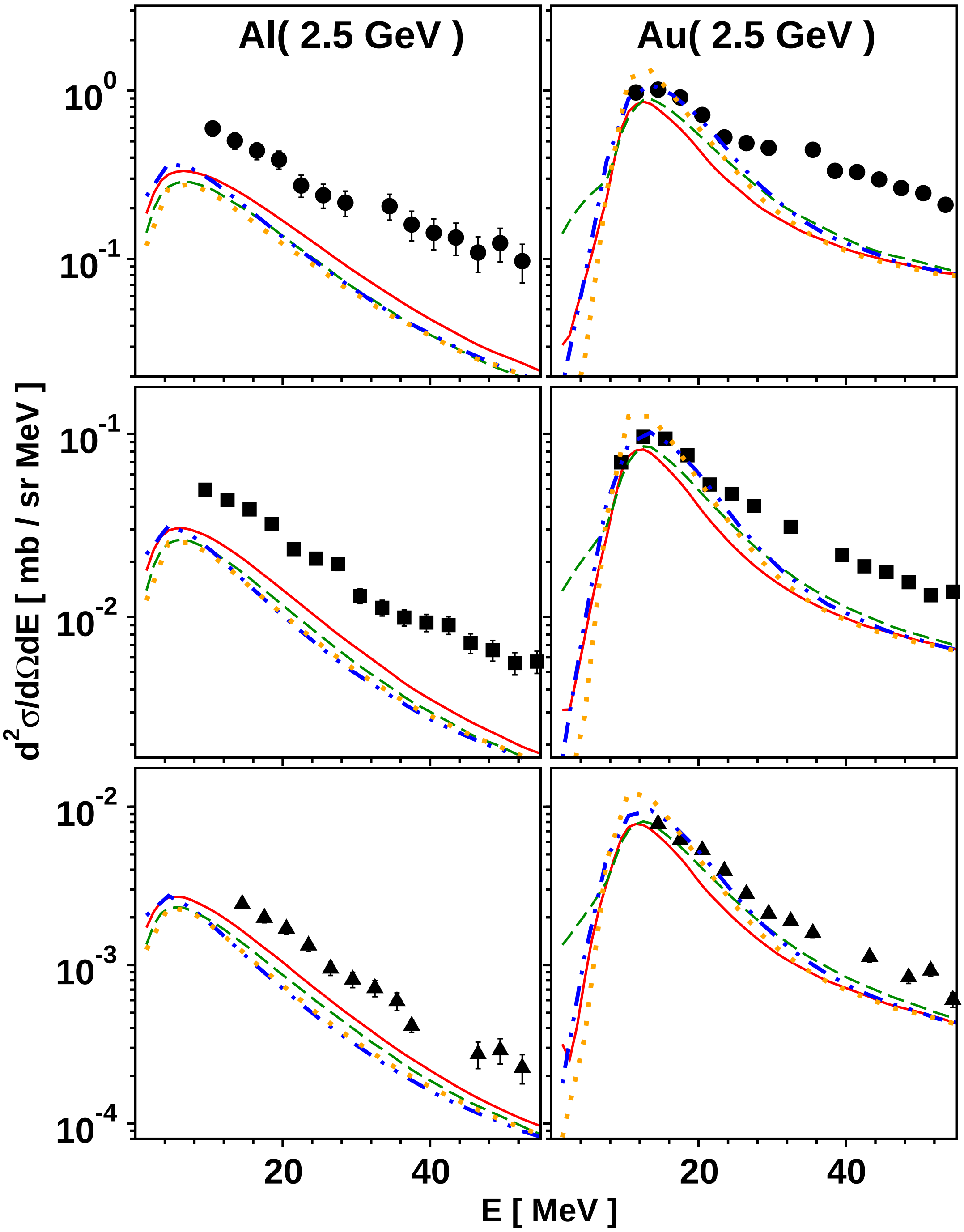

Figure E.6: Experimental spectra of **tritons** measured at 20° (upper panels), 65° (middle panels) and 100° (lower panels) for Al target (left column of panels) and Au target (right column of panels) at proton beam energy of 2.5 GeV. This is expanded fig. 5.24 (without data for Ag target and proton beam energy 1.2 and 1.9 GeV). The same scaling factors for the cross sections at different angles and targets were used as for the protons (fig. E.2).

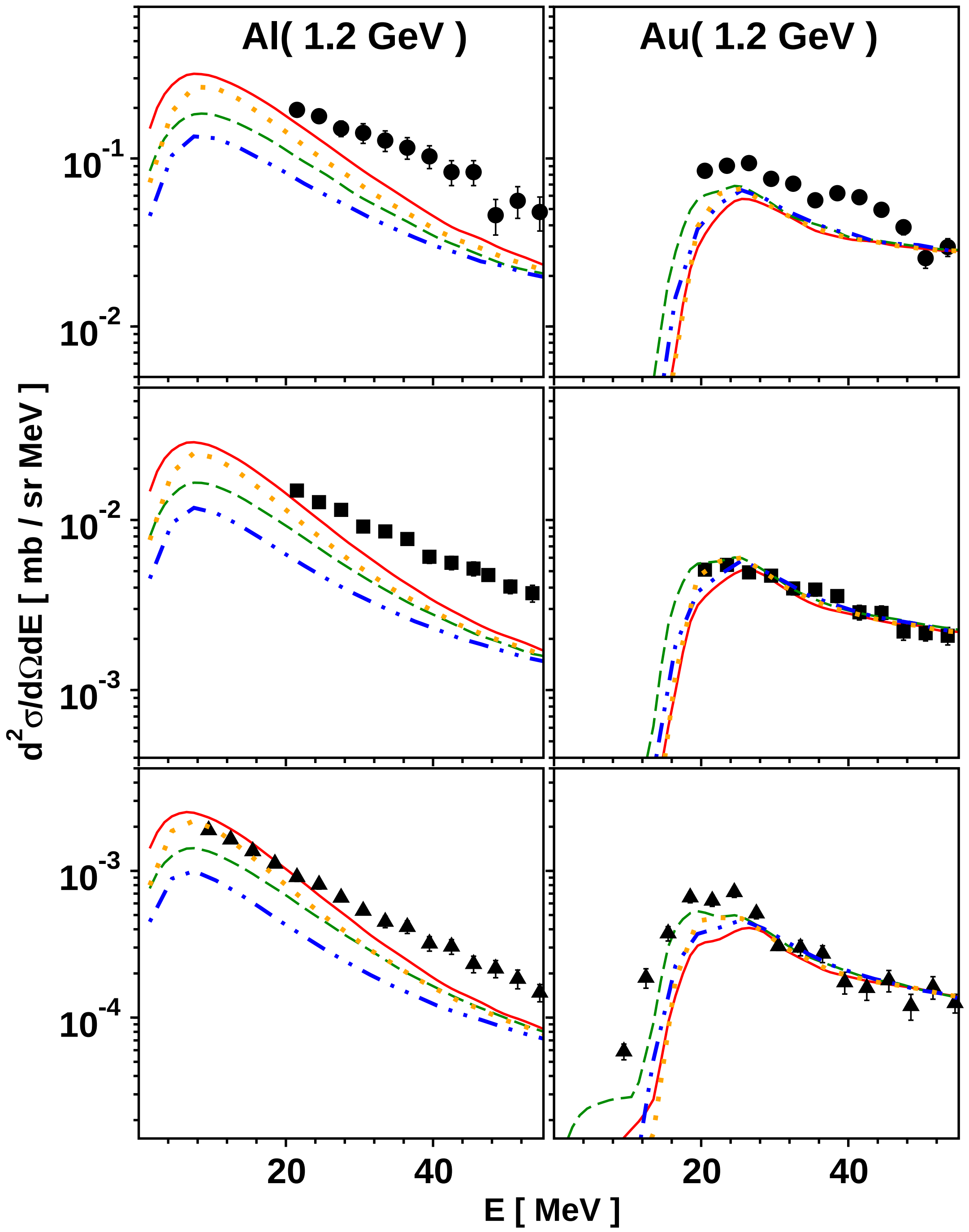

Figure E.7: Experimental spectra of $^3\mathbf{He}$ measured at 20° (upper panels), 65° (middle panels) and 100° (lower panels) for Al target (left column of panels) and Au target (right column of panels) at proton beam energy of 1.2 GeV. This is expanded fig. 5.25 (without data for Ag target and proton beam energies 1.9 and 2.5 GeV). The same scaling factors for the cross sections at different angles and targets were used as for the protons (fig. E.1).

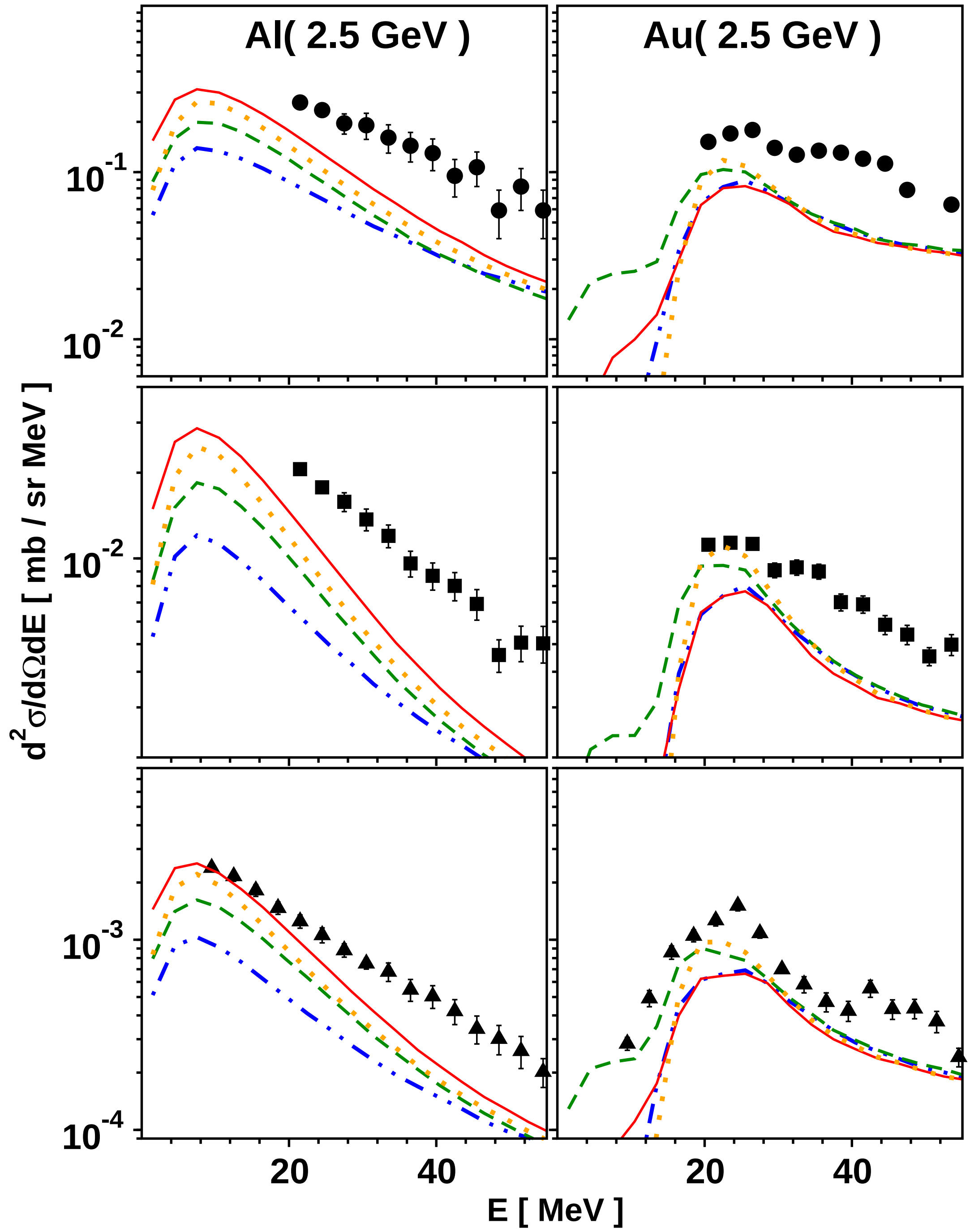

Figure E.8: Experimental spectra of ^{3}**He** measured at 20° (upper panels), 65° (middle panels) and 100° (lower panels) for Al target (left column of panels) and Au target (right column of panels) at proton beam energy of 2.5 GeV. This is expanded fig. 5.25 (without data for Ag target and proton beam energy 1.2 and 1.9 GeV). The same scaling factors for the cross sections at different angles and targets were used as for the protons (fig. E.2).

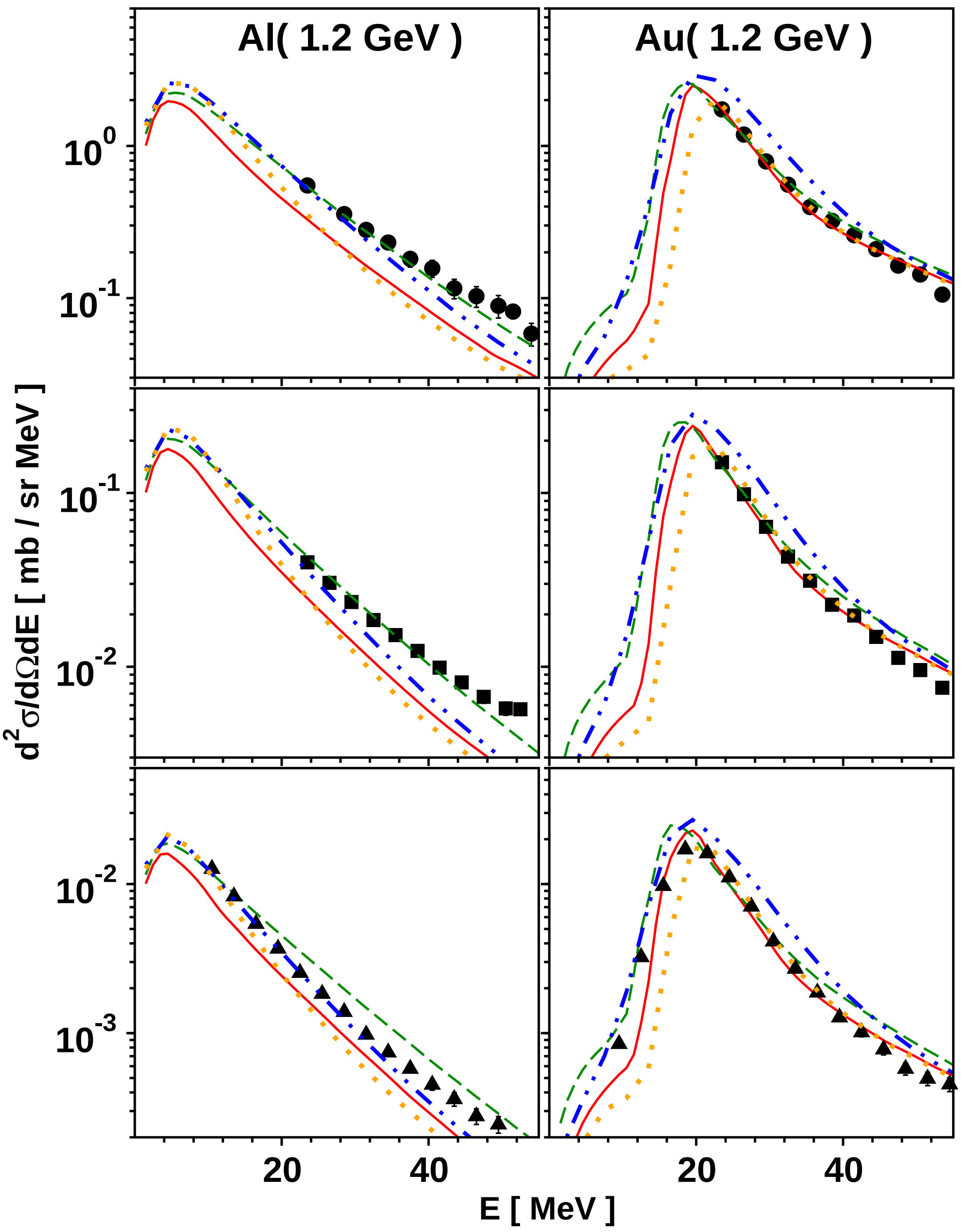

Figure E.9: Experimental spectra of ^{4}**He** measured at 20° (upper panels), 65° (middle panels) and 100° (lower panels) for Al target (left column of panels) and Au target (right column of panels) at proton beam energy of 1.2 GeV. This is expanded fig. 5.26 (without data for Ag target and proton beam energies 1.9 and 2.5 GeV). The same scaling factors for the cross sections at different angles and targets were used as for the protons (fig. E.1).

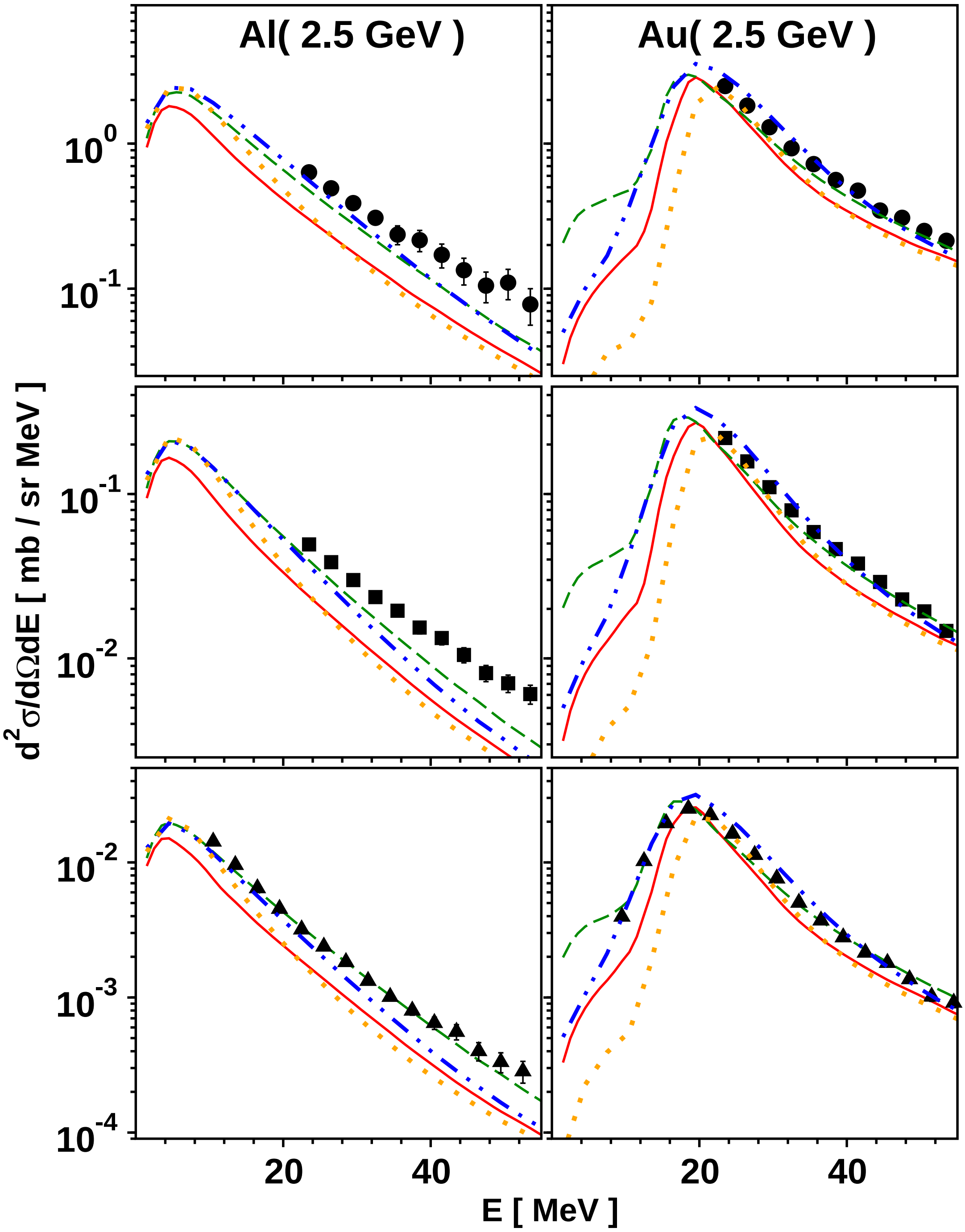

Figure E.10: Experimental spectra of ^{4}**He** measured at 20° (upper panels), 65° (middle panels) and 100° (lower panels) for Al target (left column of panels) and Au target (right column of panels) at proton beam energy of 2.5 GeV. This is expanded fig. 5.26 (without data for Ag target and proton beam energy 1.2 and 1.9 GeV). The same scaling factors for the cross sections at different angles and targets were used as for the protons (fig. E.2).

Acknowledgements

It is hard to overstate my gratitude to my mentor and PhD supervisor, Professor Bogusław Kamys. Without his inspirational guidance in all the time of research and writing of this thesis, his encouragements, hours of constructive discussions about the deep aspects of spallation physics and last but not the least his faith in me, I could never finish my dissertation work. For me, he is not only a teacher, but also a life time inspiration and advisor.

I would also like to express my sincere gratitude to Dr. hab. Frank Goldenbaum and Professor Detlef Filges for their hospitality and fruitful discussions to keep and accelerate my investigations on track to achieve the maximal output.

It gives me great pleasure in acknowledging the support and help of Professor Paweł Moskal in all these years for providing the instant solutions to many problems which could hinder my studies. A special thanks goes to him for providing a scientific environment and opportunities to co-organize many scientific conferences which greatly help me to explore the horizons of my knowledge about various advancements in the fields of research.

I am indebted to Professor Lucjan Jarczyk , Professor Zbigniew Rudy, Professor Andrzej Magiera for their motivation and willingness to help in the times of need.

I am also thankful to all my colleagues (Indians, Polish, Pakistanis, Iranians, Egyptians, Germans) for the nice atmosphere of work and discussions on broad range of subjects especially to introduce me the native views of the great ancient culture of their countries.

I gratefully acknowledge the support by the Foundation for Polish Science - MPD program, co-financed by the European Union within European Regional Development Fund making it possible for me to study here.

I would like to thank my beloved wife Neha who was always there cheering me up and stood by me through all the challenges I faced. Finally, I would like to thank my parents, elder brother, sisters, bhabhi and kids for supporting me and encouraging me with their best wishes.

Bibliography

[1] *MYRRHA: Multi-purpose hybrid research reactor for high-tech applications* http://myrrha.sckcen.be/

[2] W.T. Eadie, D. Drijard,F.E. James, M. Roos, B. Sadoulet; *Statistical Methods in Experimental Physics, North-Holland Publishing Company, 1971.*

[3] R. Serber; *Nuclear Reactions at High Energies*, Phys. Rev. **72** (1947) 1114.

[4] Hugo W. Bertini; *Low-Energy Intranuclear Cascade Calculations,* Phys. Rev. **131** (1963) 1801 ; Erratum Phys. Rev. **138** (1965) AB2.

[5] H. Bertini et al.; *Intranuclear cascade calculations of the secondary nucleon spectra from nucleon-nucleus interactions in energy range 340 - 2900 MeV and comparision with experiment,* Phys. Rev. **188** (1969) 1711.

[6] H. Bertini et al.; *High energy (E≤1000 GeV) intranuclear cascade model for nucleons and pion incident on nuclei and comparison with experimental data,* Phys. Rev. C **17** (1978) 1382.

[7] Y.Yariv and Z. Fraenkel, Phys. Rev. C **20** (1979) 2227; Phys. Rev. C **24** (1981) 488.

[8] J. Cugnon, T. Mizutani and J. Vandermeulen; *Equilibration in relativistic nuclear collisions: A Monte Carlo calculation,* Nucl. Phys. A **352** (1981) 505.

[9] J. Cugnon, D. KINET and J. Vandermeulen; *Pion production in central high energy nuclear collisions,* Nucl. Phys. A **379** (1982) 553.

[10] J. Cugnon; *Proton-nucleus interaction at high energy,* Nucl. Phys. A **462** (1987) 751.

[11] J. Cugnon and M. -C. Lemaire; *Medium effects in pion production,* Nucl. Phys. A **489** (1988) 781.

[12] P. Cugnon, P. Deneye and J. Vandermeulen; *Multipion dynamics following antiproton annihilation on nuclei,* Nucl. Phys. A **500** (1989) 701.

[13] J. Cugnon, D.L'Hôte and J. Vandermeulen; *Simple parametrization of cross-sections for nuclear transport studies up to the GeV range,* Nucl. Inst. and Meth. in Phys. Res. B **111** (1996) 215.

[14] J. Cugnon, C. Volant, S. Vuillier; *Improved intranuclear cascade model for nucleon-nucleus interactions,* Nucl. Phys. A **620** (1997) 475.

[15] J. Cugnon, S. Leray, E. Martinez, Y. Patin, and S. Vuillier; *New constraints on the* Δ *production cross section,* Phys. Rev. C **56** (1997) 2431.

[16] A. Boudard, J. Cugnon, S. Leray and C. Volant; *Intranuclear cascade model for a comprehensive description of spallation reaction data,* Phys. Rev. C **66** (2002) 044615.

[17] J. Cugnon and P. Henrotte; *The low-energy limit of validity of the intranuclear cascade model,* Eur. Phys. J. A **16** (2003) 393.

[18] A. Boudard, J. Cugnon, S. Leray, C. Volant; *A new model for production of fast light clusters in spallation reactions,* Nucl. Phys. A **740** (2004) 195.

[19] Th. Aoust and J. Cugnon; *Effects of isospin and energy dependences of the nuclear mean field in spallation reactions,* Eur. Phys. J. A **21** (2004) 79.

[20] Thierry Aoust, Alain Boudard, Joseph Cugnon,....et. al.; *Recent extensions of the INCL4 model for spallation reactions,* Nucl. Inst. and Meth. in Phys. Res. A **562** (2006) 810.

[21] Th. Aoust and J. Cugnon; *Pion physics in the Liège intranuclear cascade model,* Phys. Rev. C **74** (2006) 064607.

[22] J.-C. David, A. Boudard, et al.,; *Spallation Modeling - What's new on Nuclei production with INCL4.5 - ABLA07?,* Mem. S.A.It. Vol. **75** (2008) 282.

[23] A. Boudard, J. Cugnon, J. -C. David, S. Leray and D. Mancusi; *New potentialities of the Liège intranuclear cascade model for reactions induced by nucleons and light charged particles,* Phys. Rev. C **87** (2013) 014606.

[24] C. Villagrasa-Cantn, PhD thesis; *Etude de la production de noyaux rsiduels dans la raction de spallation Fe+p 5 nergies (300-1500 MeV/A) et applications au calcul de dommages sur une fentre de systme hybride,* Universit Paris XI Orsay, December 2003. Phys. Rev. C **75** (2007) 044603.

[25] B. Fernandez-Dominguez, PhD thesis; *Etude de la production des fragments de fission de la raction 208Pb+p 500 AMeV,*, Universit de Caen, March 2003. Nucl. Phys. A **747** (2005) 227.

[26] G. F. Bertsch, H. Kruse and S. Das Gupta; *Boltzmann equation for heavy ion collisions,* Phys. Rev. C **29** (1984) 673.

[27] G. F. Bertsch and S. Das Gupta; *A guide to microscopic models for intermediate energy heavy ion collisions,* Phys. Rep. **160** (1988) 189.

[28] W. Cassing, V. Metag, U. Mosel, K. Niita; *Production of energetic particles in heavy-ion collisions,* Phys. Rep. **188** (1990) 363.

[29] E. A. Uehling and G. E. Uhlenbeck; *Transport Phenomena in Einstein-Bose and Fermi-Dirac Gases,* Phys. Rev. **43** (1933) 552.

[30] K. Niita, W. Cassing, U. Mosel, *Hard-photon production within a self-consistent transport approach to heavy ion collisions,* Nucl. Phys. A **504** (1989) 391.

[31] T. Kodama, S. B. Duarte, K. C. Chung, R. Donangelo and R. A. M. S. Nazareth; *Causality and relativistic effects in intranuclear cascade calculations,* Phys. Rev. C **29** (1984) 2146.

[32] K. Niita, S. Chiba, T. Maruyama, T. Maruyama, H. Takada, T. Fukahori, Y. Nakahara, A. Iwamoto; *Analysis of the (N , x N 1)reactions by quantum molecular dynamics plus statistical decay model,* Phys. Rev. C **52** (1995) 2620.

[33] S. Chiba, M. B. Chadwick, K. Niita, T. Maruyama, T. Maruyama and A. Iwamoto; *Nucleon-induced pre-equilibrium reactions in terms of quantum molecular dynamics,* Phys. Rev. C **53** (1996) 1824.

[34] S. Chiba, O. Iwamoto, T. Fukahori, K. Niita, T. Maruyama, T. Maruyama and A. Iwamoto; *Analysis of proton-induced fragment production cross sections by the quantum molecular dynamics plus statistical decay model,* Phys. Rev. C **54** (1996) 285.

[35] J. Aichelin; *Quantum Molecular Dynamics - A dynamical microscopic n-body approach to investigate fragment formation and the nuclear equation of state in heavy ion collisions,* Phys. Rep. **202** (1991) 233.

[36] T. H. R. Skyrme; *The effective nuclear potential,* Nucl. Phys. **9** (1959) 615.

[37] S. R. Souza, L. de Paula, S. Leray, J. Nemeth, C. Ngo and H. Ngo; *A dynamical model for multifragmentation of nuclei,* Nucl. Phys. A **571** (1994) 159.

[38] A. Bohr and B. R. Mottelson; *Nuclear Structure - W. A. Benjamin, New York, 1969, Vol. 1.*

[39] K. K. Gudima, S. G. Mashnik, and V.D Toneev; Nucl. Phys. A **401** (1983) 329.

[40] S. G. Mashnik; *Physics of the CEM92M code: Intermediate Energy Nuclear Data: Models and Codes,* Proc. of a Specialists Meeting, 30 May-1 June, Issy-Les-Moulineaux, France, pp. 107-120, 1994.

[41] S. G. Mashnik, A. J. Sierk, O. Bersillon, T. A. Gabriel; *Cascade-exciton model detailed analysis of proton spallation at energies from 10 MeV to 5 GeV,* Los Alamos Report **LA-UR-97-2905**, 1997.

[42] S. G. Mashnik, A.J. Sierk,O. Bersillon, T. Gabriel; *Cascade-exciton model analysis of proton induced reactions from 10 MeV to 5 GeV,* Nucl. Inst. Meth. Phys. Res. Sec. A **414** (1998) 68.

[43] S. G. Mashnik and A. J. Sierk; *Improved cascade-exciton mdoel of nuclear reactions,* LANL Report **LA-UR-98-5999**, 1998.

[44] Stepan G. Mashnik, Arnold J. Sierk, Konstantin K. Gudima; *Complex particle and light fragment emission in the cascade-exciton model of nuclear reactions,* arXiv:**nucl-th/0208048**, 2002.

[45] S. G. Mashnik, K. K. Gudima and A. J. Sierk; *Merging the CEM2K and LAQGSM codes with GEM2 to describe fission and light-fragment production,* arXiv:**nucl-th/0304012** [nucl-th], 2003.

[46] S. G. Mashnik, K. K. Gudima, A. J. Sierk, R. E. Prael; *Improved intranuclear cascade models for the codes CEM2k and LAQGSM,* arXiv: **nucl-th/0502019** [nucl-th], 2005

[47] S.G. Mashnik, A. J. Sierk,K. K. Gudima and M. I. Baznat; *CEM03 and LAQGSM03 - new modeling tools for nuclear applications,* J. of Phys. : Conference Series **41** (2006) 340.

[48] S. G. Mashnik, K. K. Gudima, R. E. Prael, A. J. Sierk, M. I. Baznat, N. V. Mokhov; *CEM03.03 and LAQGSM03.03 event generators for the MCNP6, MCNPX, and MARS15 transport codes,* arXiv: **0805.0751 [nucl-th]**, 2008.

[49] V.D. Toneev, K.K. Gudima; *Particle emission in light and heavy ion reactions,* Nucl. Phys. A **400** (1983) 173.

[50] K. K. Gudima, G. A. Ososkov, and V. D. Toneev; *Model for Pre-Equilibrium Decay of Excited Nuclei,* colorYad. Fiz. **21** (1975) 260 [Sov. J. Nucl. Phys. **21** (1975) 138].

[51] S. G. Mashnik et al.,; *MODEX - the Program for Calculation of the Energy Spectra of Particles Emitted in the Reactions of Pre-Equilibrium and Equilibrium Statistical Decays,* JINR Communication P4 - 8417, Dubna, 1974.

[52] S. Furihata; *Statistical analysis of light fragment production from medium energy proton-induced reactions,* Nucl. Inst. and Meth. in Phys. Res. B **71** (2000) 251.

[53] S. Furihata and T. Nakamura; Calculation of Nuclide Productions from Proton Induced Reactions on Heavy Targets with INC/GEM", Jour. of Nucl. Scie. and Tech. Supp. **2**, 758 (2002).

[54] R. J. Charity; in *Proceedings of the Joint ICTP-IAEA Advanced Workshop on Model Codes for Spallation Reactions, ICTP Trieste, Italy, 4-8 February, 2008)* edited by D. Filges et al., INDC(NDS)- 530, (IAEA, Vienna, 2008), p. 139.

[55] M. Blann, H. Gruppelaar, P. Nagel, J. Rodens, *International Code Comparison for Intermediate Energy Nuclear Data*, NSC/DOC(94)-2, NEA/OECD (1993).

[56] R. Michel, P. Nagel, *International Codes and Model Intercomparison for Intermediate Energy Activation Yields*, NSC/DOC(97)-1, NEA/OECD (1997).

[57] P. Armbruster, J. Benlliure, M. Bernas, A. Boudard, E. Casarejos, S. Czajkowski, T. Enqvist, S. Leray, P. Napolitani, J. Pereira, F. Rejmund, M.-V. Ricciardi, K.-H. Schmidt, C. Stephan, J. Taieb, L.Tassan-Got, and C. Volant, *Measurement of a Complete Set of Nuclides, Cross Sections, and Kinetic Energies in Spallation of* ^{238}*U 1A GeV with Protons*, Phys. Rev. Let. **93** (2004) 212701.

[58] L. Audouin, L. Tassan-Got, P. Armbruster, J. Benlliure, M. Bernas, A. Boudard, E. Casarejos, S. Czajkowski, T. Enqvist, B. Fernandez-Dominguez, B. Juradob, R.Legraind, S. Leray, B. Mustapha, J. Pereira, M. Pravikoff, F. Rejmund, M.-V. Ricciardi, K.-H. Schmidt, C. Stephan, J. Taieb, C. Volant, W. Wlazlo, *Evaporation residues produced in spallation of* ^{208}*Pb by protons at 500A MeV*, Nucl. Phys. A. **768** (2006) 1.

[59] M. Bernas, P. Armbruster, J. Benlliure, A. Boudard, E. Casarejos, T. Enqvist, A. Kelic, R. Legraind, S. Leray, J. Pereira, F. Rejmund, M.-V. Ricciardi, K.-H. Schmidt, C. Stephan, J. Taieb, L. Tassan-Got, C. Volant, *Very heavy fission fragments produced in the spallation reaction* ^{238}*U +p at 1A GeV*, Nucl. Phys. A **765** (2006) 197.

[60] J. Benlliure, P. Armbruster, M. Bernas, A. Boudard, J.P. Dufour, T. Enqvist, R. Legraind, S. Leray, B. Mustapha, F. Rejmundc, K.-H. Schmidt, C. Stphanc, L. Tassan-Got, C. Volant, *Isotopic production cross sections of fission residues in* ^{197}*Au-on-proton collisions at 800 A MeV*, Nucl. Phys. A **683** (2001) 513.

[61] T. Enqvist, j. Benlliure, E Farget, K.-H. Schmidt, P. Armbruster, M. Bernas, L. Tassan-Got, A. Boudard, R. Legrain, C. Volant, C. B6ckstiegel, M. de Jong, J.P. Dufour, *Systematic experimental survey on projectile fragmentation and fission induced in collisions of 238U at 1 A GeV with lead*, Nucl. Phys. A **658** (1999) 47.

[62] T. Enqvist, W. Wlazob, P. Armbruster, J. Benlliure, M. Bernas, A. Boudard, S. Czajkowski, R. Legraina, S. Leray, B. Mustapha, M. Pravikoff, F. Rejmund, K.-H. Schmidt, C. Stephan, J. Taieba, L. Tassan-Got, C. Volant, *Isotopic yields and kinetic energies of primary residues in 1 A GeV* ^{208}*Pb+ p reactions*, Nucl. Phy. A **686** (2001) 481.

[63] P. Napolitani, K.-H. Schmidt, A. S. Botvina, F. Rejmund, L. Tassan-Got, and C. Villagrasa, *High-resolution velocity measurements on fully identified light nuclides produced in* ^{56}*Fe+hydrogen and* ^{56}*Fe+titanium systems*, Phys. Rev. C **70** (2004) 054607.

[64] P. Napolitani, K.-H. Schmidt, L. Tassan-Got, P. Armbruster, T. Enqvist, A. Heinz, V. Henzl, D. Henzlova, A. Kelic, R. Pleskac, M. V. Ricciardi, C. Schmitt, O. Yordanov, L. Audouin, M. Bernas, A. Lafriaskh, F. Rejmund, C. Stephan, J. Benlliure, E. Casarejos, M. Fernandez Ordonez, J. Pereira, A. Boudard, B. Fernandez, *Measurement of the complete nuclide production and kinetic energies of the system* ^{136}*Xe+hydrogen at 1 GeV per nucleon*, Phys. Rev. C **76** (2007) 064609.

[65] M. V. Ricciardi, P. Armbruster, J. Benlliure, M. Bernas, A. Boudard, S. Czajkowski, T. Enqvist, A. Kelic, S. Leray, R. Legrain, B. Mustapha, J. Pereira, F. Rejmund, K.-H. Schmidt, C. Stephan, L. Tassan-Got, C. Volant, and O. Yordanov, *Light nuclides produced in the proton-induced spallation of* ^{238}U *at 1 GeV*, Phys. Rev. C **73** (2006) 014607.

[66] F. Rejmund, B. Mustapha, P. Armbruster, J. Benlliure, M. Bernas, A. Boudard, J.P. Dufour, T. Enqvist, R. Legrain, S. Leray, K.-H. Schmidt, C. Stphan, J. Taieba, L. Tassan-Got, C. Volant, *Measurement of isotopic cross sections of spallation residues in 800 A MeV* $^{197}Au+p$ *collisions*, Nucl. Phys. A **683** (2001) 540.

[67] W. Wlazlo, T. Enqvist, P. Armbruster, J. Benlliure, M. Bernas, A. Boudard, S. Czjkowski, R. Legrain, S. Leray, B. Mustapha, M. Pravikoff, F. Rejmund, K.-H. Schmidt, C. Stphan, J. Taieb, L. Tassan-Got, and C. Volant, *Cross Sections of Spallation Residues Produced in 1A GeV* ^{208}Pb *on Proton Reactions*, Phys. Rev. Let. **84** (2000) 5736.

[68] C.-M. Herbach, D. Hilscher, U. Jahnke, V. Tishchenko, W. Bohne, J. Galin, A. Letourneau, B. Lott, A. Pghaire, F. Goldenbaum, and L. Pienkowski, *A combination of two* $4\pi-$ *detectors for neutrons and charged particles.: Part II. The Berlin silicon ball BSiB for light- and heavy-ion detection,* Nuclear Instruments and Methods in Physics Research Section A: Accelerators, Spectrometers, Detectors and Associated Equipment, **508** (2003) 315.

[69] C.-M. Herbach, D. Hilscher, U. Jahnke, V. Tishchenko, J. Galin, A. Letourneau, A. Pghaire, D. Filges, F. Goldenbaum, L. Pienkowski, W. Schrder, and J. Tke, *Charged-particle evaporation and pre-equilibrium emission in 1.2 GeV proton-induced spallation reactions,* Nuclear Physics A, **765** (2006) 426.

[70] U. Jahnke, C.-M. Herbach, D. Hilscher, V. Tishchenko, J. Galin, A. Letourneau, B. Lott, A. Pghaire, F. Goldenbaum, and L. Pienkowski, *A combination of two* 4π *detectors for neutrons and charged particles.: Part I. The Berlin neutron balla neutron multiplicity meter and a reaction detector*, Nuclear Instruments and Methods in Physics Research Section A: Accelerators, Spectrometers, Detectors and Associated Equipment **508** (2003) 295.

[71] A. Letourneau, A. Bhm, J. Galin, B. Lott, A. Pghaire, M. Enke, C.-M. Herbach, D. Hilscher, U. Jahnke, V. Tishchenko, D. Filges, F. Goldenbaum, R. Neef, K. Nnighoff, N. Paul, G. Sterzenbach, L. Pienkowski, J. Tke, and U. Schrder, *Composite-particle emission in the reaction p+Au at 2.5 GeV*, Nuclear Physics A, **712** (2002) 133.

[72] R. Barna, V. Bollini, A. Bubak, A. Budzanowski, D. D. Pasquale, D. Filges, S. Frtsch, F. Goldenbaum, A. Heczko, H. Hodde, A. Italiano, L. Jarczyk, B. Kamys, J. Kisiel, M. Kistryn, S. Kistryn, S. Kliczewski, A. Kowalczyk, P. Kulessa, H. Machner, A. Magiera, J. Majewski, W. Migda, H. Ohm, N. Paul, B. Piskor-Ignatowicz, K. Pysz, Z. Rudy, H. Schaal, R. Siudak, E. Stephan, G. Steyn, R. Sworst, T. Thovhogi, M. Wojciechowski, and W. Zipper, *PISA - an experiment for fragment spectroscopy*

at the internal beam of COSY: application of an Axial Ionization Chamber, Nuclear Instruments and Methods in Physics Research Section A: Accelerators, Spectrometers, Detectors and Associated Equipment, **519** (2004) 610.

[73] V. Bollini, *Proton Induced Fragmentation of Gold Nuclei at Incident Energy of 2.5 GeV.* PhD thesis. Wuppertal University, 2004.

[74] A. Bubak, A. Budzanowski, D. Filges, F. Goldenbaum, A. Heczko, H. Hodde, L. Jarczyk, B. Kamys, M. Kistryn, St. Kistryn, St. Kliczewski, A. Kowalczyk, E. Kozik, P. Kulessa, H. Machner, A. Magiera, W. Migda, N. Paul, B. Piskor-Ignatowicz, M. Puchaa, K. Pysz, Z. Rudy, R. Siudak, M. Wojciechowski, and P. Wüstner; *Non-equilibrium emission of complex fragments from p + Au collisions at 2.5 GeV proton beam energy,* Phys. Rev. C **76** (2007) 014618

[75] A. Budzanowski, M. Fidelus, D. Filges, F. Goldenbaum, H. Hodde, L. Jarczyk, B. Kamys, M. Kistryn, St. Kistryn, St. Kliczewski, A. Kowalczyk, E. Kozik, P. Kulessa, H. Machner, A. Magiera, B. Piskor-Ignatowicz, K. Pysz, Z. Rudy, R. Siudak, and M. Wojciechowski; *Competition of coalescence and fireball processes in nonequilibrium emission of light charged particles from p + Au collisions,* Phys. Rev. C **78** (2008) 024603

[76] A. Budzanowski, M. Fidelus, D. Filges, F. Goldenbaum, H. Hodde, L. Jarczyk, B. Kamys, M. Kistryn, St. Kistryn, St. Kliczewski, A. Kowalczyk, E. Kozik, P. Kulessa, H. Machner, A. Magiera, B. Piskor-Ignatowicz, K. Pysz, Z. Rudy, R. Siudak, and M. Wojciechowski, *Variation of nonequilibrium processes in the p + Ni system with beam energy,* Phys. Rev. C **80** (2009) 054604

[77] A. Budzanowski, M. Fidelus, D. Filges, F. Goldenbaum, H. Hodde, L. Jarczyk, B. Kamys, M. Kistryn, St. Kistryn, St. Kliczewski, A. Kowalczyk, E. Kozik, P. Kulessa, H. Machner, A. Magiera, B. Piskor-Ignatowicz, K. Pysz, Z. Rudy, R. Siudak, and M. Wojciechowski; *Comparison of nonequilibrium processes in p + Ni and p + Au collisions at GeV energies* Phys. Rev. C **82** (2010) 034605

[78] M. Fidelus, D. Filges, F. Goldenbaum, H. Hodde, A. Jany, L. Jarczyk, B. Kamys, M. Kistryn, St. Kistryn, St. Kliczewski, E. Kozik, P. Kulessa, H. Machner, A. Magiera, B. Piskor-Ignatowicz, K. Pysz, Z. Rudy, Sushil K. Sharma, R. Siudak, and M. Wojciechowski; *Sequential and simultaneous emission of particles from p + Al collisions at GeV energies,* Phys. Rev. C **89** (2014) 054617.

[79] B. Piskor-Ignatowicz, *Energy Dependence of Proton Induced Fragmentation of Atomic Nuclei.* PhD thesis. Jagellonian University, Cracow, 2009.

[80] Kenji ISHIBASHI, Hiroshi TAKADA, Tatsushi NAKAMOTO, Nobuhiro SHIGYO, Keisuke MAEHATA, Naruhiro MATSUFUJI, Shin-ichiro MEIGO, Satoshi CHIBA, Masaharu NUMAJIRI, Yukinobu WATANABE and Takashi NAKAMURA, *Measurement of Neutron-Production Double-Differential Cross Sections for Nuclear Spallation Reaction Induced by 0.8, 1.5 and 3.0 GeV Protons*, Journal of NUCLEAR SCIENCE and TECHNOLOGY, **34** (1997) 529.

[81] S. Leray, F. Borne, S. Crespin, J. Frehaut, X. Ledoux, E. Martinez, Y. Patin, E. Petibon, P. Pras, A. Boudard, R. Legrain, Y. Terrien, F. Brochard, D. Drake, J. C. Duchazeaubeneix, J. M. Durand, S. I. Meigo, G. Milleret, D. M. Whittal, W. Wlazlo, D. Durand, C. Le Brun, F. R. Lecolley, J. F. Lecolley, F. Lefebvres, M. Louvel, C. Varignon, F. Hanappe, S. Menard, L. Stuttge, J. Thun, *Spallation neutron production by 0.8, 1.2, and 1.6 GeV protons on various targets*, Phys. Rev. C **65** (2002) 044621.

[82] http://www-nds.iaea.org/spallations. *IAEA Benchmark of Spallation Models*

[83] Jean-Christophe David, Detlef Filges et al.,; *Benchmark of Spallation Models,* Prog. in Nucl. Scie. and Tech. Vol. **2** (2011) 942.

[84] S. Leray, J. C. David, M. Khandaker et al.,; *Results from the IAEA Benchmark of Spallation Models,* Jour. of the Korean. Phys. Soci. **59** (2011) 791.

[85] https://www-nds.iaea.org/spallations/2010ws/michel-report.pdf.

[86] A.Kelić, M.V. Ricciardi and K.-H. Schmidt; *ABLA07- towards a complete description of the decay channels of a nuclear system from spontaneous fission to multifragmentation*, in Proceedings of the Joint ICTP-IAEA Advanced Workshop on Model Codes for Spallation Reactions, ICTP Trieste, Italy, 4-8 February 2008, edited by D. Filges et al. INDC(NDS)-530 (IAEA, Vienna, 2008), p. 181

[87] J. P. Bondorf, A. S. Botvina, A. S. lljinov, I. N. Mishustin, and K. Sneppen; *Statistical multifragmentation of nuclei,* Phys. Rep. **257** (1995) 133.

[88] K. Kwiatkowski, S. H. Zhou, T. E. Ward, V. E. Viola Jr., H. Breuer, G. J. Mathews, A. Gökmen and A. C. Mignerey ; *Energy Deposition in Intermediate-Energy Nucleon-Nucleus Collisions*, Phys. Rev. Lett. **50** (1983) 1648.

[89] L. Giot, J.A. Alcantara-Nunez, J. Benlliure, D. Perez-Loureiro, L. Audouin, A. Boudard, E. Casarejos, T. Enqvist, J.E. Ducret, B. Fernandez-Dominguez, M. Fernandez Ordonez, F. Farget, A. Heinza, V. Henzl, D. Henzlova, A. Keliċ-Heil, A. Lafriaskh, S. Leray, P. Napolitani, C. Paradela, J. Pereira, M.V. Ricciardi, C. Stephan, K.-H. Schmidt, C. Schmitt, L. Tassan-Got, C. Villagrasa, C. Volant, O. Yordanov, *Isotopic production cross sections of the residual nuclei in spallation reactions induced by 136Xe projectiles on proton at 500 AMeV*, Nucl. Phys. A 899, 116 (2013)

[90] S. B. Kaufman, E. P. Steinberg, and M. W. Weisfield; *Recoil properties of radionuclides formed in the interaction of 1-300-GeV protons with gold*, Phys. Rev. C **18** (1978) 1349

[91] S. Stamer, W. Scobel, W. B. Amian, R. C. Byrd, R. C. Haight, J.L.Ullmann, R. W. Bauer, M. Blann, B. A. Pohl, J. Bisplinghoff, R. Bonetti; *Double differential cross sections for neutron emission induced by 256 MeV and 800 MeV protons,* Phys. Rev. C **47** (1993) 1647.

[92] http://www.oecd-nea.org/janisweb/search/exfor.

[93] R.E.L. Green, R.G. Korteling, K.P. Jackson; *Inclusive production of isotopically resolved Li through Mg fragments by 480 MeV p+Ag reactions* Physical Review C **29**, 1806 (1984).

[94] Sophie Pedous, Joseph Cugnon; *Extension of the Liège intranuclear cascade model at incident energies between 2 and 12 GeV: Aspects of pion production,* Nucl. Phys. A **866** (2011) 16.

[95] S. T. Butler and C. A. Pearson; *Deuterons from High-Energy Proton Bombardment of Matter,* Phys. Rev. **129** (1963) 836.

[96] V. F. Weisskopf and D. H. Ewing; *On the Yield of Nuclear Reactions with Heavy Elements,* Phys. Rev. **57** (1940) 472.

[97] F. Atchison; *Jül-conf-34: Proc. of Mtg. on Targets for Neutron Beam Spallation Source*, KFA-Jülich, Germany, June 1979, **17** (1980).

[98] A. Gilbert and A. G. W. Cameron; Can. J. Phys. **43** (1965) 1446.

[99] R. Vandenbosch and J. R. Huizenga; *Nuclear Fission,* Academic Press, New York (1973).

[100] R. J. Charity, Phys. Rev. C 61 (2000) 054614

[101] A. S. Botvina, A. S. Iljinov, I. N. Mishustin, Sov. J. Nucl. Phys. **42** (1985) 217

[102] A. S. Botvina, and I. N. Mishustin; *Statistical description of nuclear break-up,* Eur. Phys. J. A **30** (2006) 121.

[103] A. S. Botvina, A. S. lljinov, I. N. Mishustin.; *Statistical simulation of the break-up of highly excited nuclei,* Nucl. Phys. A **475** (1987) 663.

[104] Niels Bohr, John Archibald Wheeler; *The Mechanism of Nuclear Fission,* Phys. Rev. **56** (1939) 426.

[105] W.D. Myers and W.J. Swiatecki; Nucl. Phys. A **601** (1996) 141.

[106] W. Hauser and H. Feshbach; *The Inelastic Scattering of Neutrons,* Phys. Rev. **87** (1952) 366.

[107] Luciano G. Moretto and Gordon J. Wozniak; *The role of the compound nucleus in complex fragment emission at low and intermediate energies,* Prog. in Part. and Nucl. Phys. **21** (1988) 401.

[108] Arnold J. Sierk; *Mass-Asymmetric Fission of Light Nuclei,* Phys. Rev. Lett. **55** (1985) 582.

[109] A. Raduta, F. Gulminelli, Phys. Rev. C **75** (2007) 024605.

[110] D. Henzlova, A.S. Botvina, K.-H. Schmidt, V. Henzl, P. Napolitani, M.V. Ricciardi, *Symmetry energy of fragments produced in multifragmentation*, nucl-ex/0507003

[111] A. S. Goldhaber; *Statistical models of fragmentation processes,* Phys. Lett. B **53** (1974) 306.

[112] Wolfgang Bauer; *Temperatures of fragment kinetic energy spectra,* Phys. Rev. C **51** (1995) 803

[113] Jan Toke, Jun Lu, and W. Udo Schröder; *Surface entropy in statistical emission of massive fragments from equilibrated nuclear systems,* Phys. Rev. C **67** (2003) 034609.

[114] K. C. Chung, Rio de Janeiro, and H. Schechter; *Dynamical effects in the Coulomb expansion following nuclear fragmentation,* Phys. Rev. C **36** (1987) 986.

[115] R. Bass, *Nuclear Reactions with Heavy Ions*, Springer, Berlin, 19080

[116] J. Benlliure, A. Grewe, M. de Jong, K.-H.Schmidt, S. Zhdanov; *Calculated nuclide production yields in relativistic collisions of fissile nuclei,* Nucl. Phys. A **628** (1998) 458.

[117] K. Kruglov, A. Andreyev, B. Bruyneel et al.,; *Yields of neutron-rich isotopes around Z = 28 produced in 30 MeV proton-induced fission 238U,* Eur. Phys. J. A **14** (2002) 365.

[118] K.-H. Schmidt, A.Kelić and M. V. Ricciardi; *Experimental evidence for the separability of compound-nucleus and fragment properties in fission,* Euro. Phys. Lett **83** (2008) 32001.

[119] B. Jurado, K.-H.Schmidt and J. Benlliure; *Time evolution of the fission-decay width under the influence of dissipation,* Phys. Rev. B **533** (2003) 186.

[120] B. Jurado, C. Schmitt, K.-H. Schmidt, J. Benlliure, A.R. Junghans; *A critical analysis of the modelling of dissipation in fission,* Nucl. Phys. A **747** (2005) 14.

[121] B. Jurado, C. Schmitt, K.-H. Schmidt, J. Benlliure, A.R. Junghans; *Conditions for the manifestation of transient effects in fission,* Nucl. Phys. A **757** (2005) 329.

[122] A. Yu. Konobeyev, U. Fischer, A. J. Koning, H. Leeb, S. Leray and Y. Yariv; *What Can We Expect from the Use of Nuclear Models Implemented in MCNPX at Projectile Energies below 150 MeV? Detailed Comparison with Experimental Data,*Journal of the Korean Physical Society **59** (2011) 927.

[123] N.V. Kurenkov, V.P. Lunev, Yu.N. Shubin; Appl. Radiat. Isot. **50** (1999) 541.

[124] Sushil K. Sharma, B. Kamys, F. Goldenbaum and D. Filges; *Validation of Spallation Models for p+Al Reactions at 180 MeV Incident Proton Beam Energy,* Acta Physica Polonica B **45** (2014) 1963.

[125] M. Wojciechowski, PhD thesis (2015), Jagiellonian University and to be published

[126] C. Forbes, M. Evans,N. Hastings, and B. Peacock; *Statistical Distributions, John Wiley and Sons, Inc. Publication, 2011.*